Optical Microsystems for Static and Dynamic Tactile Sensing: Design, Modeling, Fabrication and Testing

Roozbeh Ahmadi

A Thesis

in

the Department

of

Mechanical and Industrial Engineering

Presented in Partial Fulfillment of the Requirements

for the Degree of

Doctor of Philosophy (Mechanical and Industrial Engineering) at

Concordia University

Montreal, Quebec, Canada

December 2011

CONCORDIA UNIVERSITY
SCHOOL OF GRADUATE STUDIES

This is to certify that the thesis prepared

By: **Roozbeh Ahmadi**

Entitled: **Optical Microsystems for Static and Dynamic Tactile Sensing: Design, Modeling, Fabrication and Testing**

and submitted in partial fulfillment of the requirements for the degree of

Doctor of Philosophy (Mechanical and Industrial Engineering)

complies with the regulations of the University and meets the accepted standards with respect to originality and quality.

Signed by the final examining committee:

Dr. Maria Elektorowicz Chair

Dr. Ash Parameswaran External Examiner

Dr. Zahangir Kabir External to Program

Dr. Narayanswamy Sivakumar Examiner

Dr. Rolf Wüthrich Examiner

Dr. Muthukumaran Packirisamy Co-Supervisor

Dr. Javad Dargahi Co-Supervisor

Approved by

Dr. Martin D. Pugh Chair of Department

Dr. Robin Drew Dean of Faculty

January 2012

Abstract

Minimally invasive surgical operations encompass various surgical tasks ranging from conventional endoscopic/laparoscopic methods to recent sophisticated minimally invasive surgical techniques. In such sophisticated techniques, surgeons use equipment varying from robotic-assisted surgical platforms for abdominal surgery to computer-controlled catheters for catheter-based cardiovascular surgery. Presently, the countless advantages that minimally invasive surgery offers for both patients and surgeons have made the use of such surgical operations routine and reliable. However, in such operations, unlike conventional surgical operations, surgeons still suffer from the lack of tactile perception while interacting with the biological tissues using surgical instruments. To address this issue, it is necessary to develop a tactile sensor that can mimic the fingertip tactile perceptions of surgeons. In doing so and to satisfy the needs of surgeons, a number of considerations should be implemented in the design of the tactile sensors.

First, the sensor should be magnetic resonance compatible to perform measurements even in the presence of magnetic resonance imaging (MRI) devices. Currently, such devices are in wide-spread use in surgical operation rooms. Second, the sensor should be electrically-passive because introducing electrical current into the patients' body is not desirable in various surgical operations such as cardiovascular operations. Third, the sensor should perform measurements under both static and dynamic loading conditions during the sensor-tissue interactions. Such a capability of the sensor ensures that surgeons receive tactile feedback even when there is continuous static contact between surgical tools and tissues. Essentially, surgeons need such feedback to make surgical tasks safer. In addition, the size of the sensor should be miniaturized to address the size restrictions. In fact, the combination of intensity-based optical fiber sensing principles and microsystems technology is one of the limited choices that address all the required considerations to develop such tactile sensors in a variety of ways.

The present thesis deals with the design, modeling, manufacturing, testing, and characterizing of different tactile sensor configurations based on detection and integration methods. The various stages of design progress and principles are developed into different design configurations and presented in different chapters. The main sensing principle applied is based on the intensity modulation principle of optical fibers using micro-systems technology. In addition, a hybrid sensing principle is also studied by integrating both optical and non-optical detection methods. The micromachined sensors are categorized into five different generations. Each generation has advantages by comparison with its counterpart from the previous generation. The initial development of micromachined sensors is based on optical fiber coupling loss. In the second phase, a hybrid optical-piezoresistive sensing principle is studied. The success of these phases was instrumental in realizing a micromachined sensor that has the advantage of being fully optical. This sensor measures the magnitude of concentrated and distributed force, the position of a concentrated force, the variations in the force distribution along its length, the relative hardness of soft contact objects, and the local discontinuities in the hardness of the contact objects along the length of the contact area. Unlike most electrical-based commercially-available sensors, it performs all of these measurements under both static and dynamic loading conditions. Moreover, it is electrically passive and potentially MRI-compatible. The performances of the sensors were experimentally characterized for specific conditions presented in this thesis. However, these performances are easily tunable and adjustable depending upon the requirements of specific surgical tasks. Although the sensors were initially designed for surgical applications, they can have numerous other applications in the areas of robotics, automation, tele-display, and material testing.

Acknowledgements

Obtaining a Doctorate is arduous and full of twists and turns. Along the way, though doctoral work is supposed to represent the achievement of a single person, no one is able to complete the work without the immense support of many other people. In my case, my advisors, Dr. Javad Dargahi and Dr. Muthukumaran Packirisamy, offered me constant and sustained help and support. First and most, I would like to thank them from the bottom of my heart for all their contributions, guidance, remarkable/practical ideas, and encouragement. Their gentle nature is a constant inspiration for their students encouraging them to work harder than ever before and to seek their own creative solutions. Indeed, whenever I felt lost, stressed, or lacking the confidence to continue, I could always depend on them to provide direction, help, and support.

Moreover, I would like to thank Dr. Renzo Cecere at the Division of Cardiothoracic Surgery, McGill University, for his thoughtful and useful advice. I would also like to thank the members of my defence committee, Dr. Ash Parameswaran, Dr. Narayanswamy Sivakumar, Dr. Rolf Wüthrich, and Dr. Zahangir Kabir, for taking their valuable time to examine my thesis.

Also I would like to thank Jonathan Farber at the Concordia Office of Research, Natacha Mongeau and Valérie Lavoie at Valeo Management L.P. all of whom provide support and assistance in patent filing. In particular, I would like to thank Manuel Fortin, an experienced patent agent, for writing the patent application.

Special thanks to the administrative staff at Concordia University: Leslie Hossien, Arlene Zimmerman, Sophie Mérineau, and Maureen Thuringer. I would also like to thank Dainius Juras for assistance in setting up experiments. Also I would like to thank Dr. Matthieu Nannini, Don Berry, and John Li at McGill Nanotools-Microfab facility for their training in micro-machining processes. Also thanks to Philippe Plamondon at École Polytechnique de Montréal for his assistance with scanning electron microscopy.

Very special thanks go to all my friends and lab-mates in the Tactile Sensing and Medical Robotics Laboratory and the Optical-Bio Microsystems Laboratory of Concordia University: Ashkan, Ali, Ahmad, Siamak, Davoud, Jayan, Kamal, Arvind, Hamid, Amir, Mahmoud, Carlos, Stefan, Shakawat, Simona, Pierre, Gino, and all others. Particularly, I would like to thank Masoud, Reza, and Saeed, all three of whom helped me with the experimental setups. Definitely, I could not have had better friends and colleagues.

My deepest heartfelt gratitude goes out to my wife, Azadeh, my mother, Sedigh, and my father, Dr. Ahmad Ahmadi. Words simply cannot express my gratitude for their love and support. They have been with me every step of the way and I could not have achieved it without them. They provided the best possible network of love and support and help and kindness and understanding without which I would not have been able to carry on my studies to the doctoral level.

To

the love of my life, Azadeh,

my mother, and my father

Table of Contents

List of Figures

List of Tables

Nomenclature

3D	Three Dimensional
BHF	Buffered Hydrofluoric acid
BOE	Buffered Oxide Etch
CBT	Catheter-based Technique
DAQ	Data Acquisition system
DC	Direct Current
FBG	Fiber Bragg Grating
FEM	Finite Element Method
FSR	Force sensitive resistor
FWHM	Full-width-half-maximum
Hz	Hertz
MEMS	Micro Electro Mechanical Systems
MIS	Minimal Invasive Surgery
MIRS	Minimally Invasive Robotic Surgery
MR	Magnetic Resonance
MR	Mitral Valve Regurgitation
MRI	Magnetic Resonance Imaging
N	Newton
Pa	Pascal
PDMS	Polydimethylsiloxane
PVDF	Polyvinylidene Fluoride
rms	Root Mean Square

SEM	Scanning Electron Microscopy
SLD	Superluminescent Diode
TMAH	Tetramethylammonium hydroxide
μm	micrometer

List of Symbols

E	Young’s modulus / Modulus of elasticity
κ	Bulk modulus
V	Voltage
W	Strain energy function
$\mathbf{F}$	Deformation gradient tensor
$\mathbf{S}$	First Piola-Kirchhoff stress tensor
C_{10}	Mooney-Rivlin material constant
C_{01}	Mooney-Rivlin material constant
I_i	Principal invariants
X	Position of the concentrated force
y_A	Deflection of the beam at Point A
y_B	Deflection of the beam at Point B
y_C	Deflection of the beam at Point C
J	Determinant of the elastic deformation gradient tensor
μ	Initial shear modulus
d	Material incompressibility parameter
ν	Poisson’s ratio
$\lambda_1, \lambda_2, \lambda_3$	Principal stretches
η	Coupling efficiency between two adjacent optical fibers
k	Propagation constant of the gap medium between the optical fibers

w_A	Gaussian mode field-radius of Fiber A
w_B	Gaussian mode field-radius of Fiber B
$\Delta\theta$	Angular misalignment between the axis of optical fibers
n_0	Refractive index of the air
n_{core}	Refractive index of the fiber core
$n_{cladding}$	Refractive index of the fiber cladding
λ	Wavelength of the light
a	Radius of the fiber core
f_L	Force per length applied to the sensor
I	Moment of inertia of the sensor beam’s cross section around its neutral axis
L	Length of the sensor beam
Q	Gap between the optical fibers
P_A	Power of the light source coupled into Fiber A
P_B	Power of the coupling light into Fiber B
V_{OUT}	Output voltage of the sensor
R	Resistance
F	Force
$\Delta\ell$	Lateral displacement between the axis of the fibers
A	Area

Chapter 1: Introduction and Literature Review

1.1 Introduction

In late 1980s, the technology development for minimally invasive surgery (MIS) allowed surgeons to perform surgery without directly using their hands in the operation sites. A few years later, the progress of robotic technology led to the first use of robots in the operating rooms [1]. At present, recent advances in robotic technology have made it possible to use minimally invasive robotic surgery (MIRS) systems in common. By comparison with traditional surgical techniques, MIRS have significant advantages for both patients and surgeons. For instance, reducing trauma and pain, less complication, less blood loss, fewer transfusions, less risk of wound infection, less scarring, less hospitalization time, reducing recovery time, and making remote surgical procedures possible are some considerable advantages of MRIS for the patients. On the other hand, improvement of surgeon dexterity (by scaling down hand motions of surgeon and adding extra degreed of freedom to surgical instruments) and visualization (by providing 3D vision from the site of operation), and reduction of surgeon fatigue are some significant advantages of MIRS for the surgeons [2, 3]. Figure 1-1 compares a conventional open surgical operation with a minimally invasive surgical operation. In conventional operations, surgeons cut large invasive incisions on patients' body, as sown in Figure 1-1-a, to access the internal organs. However, in MIRS, surgeons access the live organs through a few keyhole incisions. The figure itself illustrates the advantages of MIRS over conventional surgical techniques. Due to these significant advantages, MIS and especially MIRS are growing fast and this growth is anticipated to expand over the next decades [4].

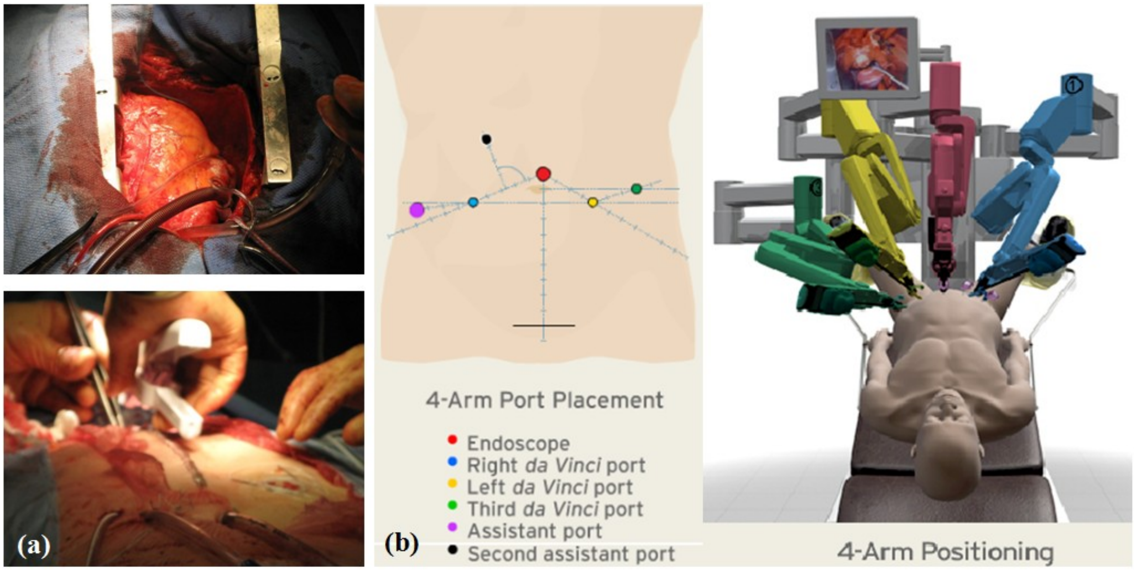

Figure 1-1: Comparison between a conventional invasive open surgical operation (a) and a minimally invasive robotic surgical operation performed by the da Vinci Surgical System (b); image (b) is the courtesy of Intuitive Surgical Inc. (http://www.intuitivesurgical.com), ©[2011] Intuitive Surgical, Inc. [5].

In fact, despite the superiorities of MIS and MIRS over traditional open surgery techniques, there are a few unsolved shortcomings involved in MIS and MIRS. One of the important shortcomings is the lack of haptic (force and tactile) feedback to surgeons. For instance, the da Vinci Surgical System (Intuitive Surgical, Inc., Sunnyvale, CA) shown in Figure 1-2, which is one of the widespread MIRS systems, does not provide the surgeon with haptic feedback during tissue manipulation [6]. Such haptic feedback is a sensory feedback that results from kinesthetic or tactile feedback [7] while the surgical instruments are interacting with tissues. Providing tactile feedback to the surgeon in MIS and MIRS, like palpation during open surgical procedures, helps the surgeon to characterize the contact tissues, to investigate anatomical structures of tissues, and to distinguish between different types of tissues [8]. Such different types of tissues can be an abnormal tissue (e.g. a tumorous lump) [9], an artery [10], a vein, a ureter, etc. surrounded with background tissues. In addition, tactile feedback from the interaction between surgical instruments and tissues allow the surgeons to apply appropriate interacting forces to avoid tissue damage during tissue manipulations [11]. Generally, providing such feedback to the surgeons leads to better performance in MIS and MIRS [3, 12, 13]. It is experimentally proved that providing tactile feedback reduces grasping force in MIRS performed by the da Vinci [14]. Consequently, the development of a tactile sensor with the capability of measuring the tactile information is crucial to mimic the perception of the surgeon's fingertips in MIS and MIRS systems. During tool-tissue interaction, such tactile information includes: the amplitude of contact force, the distributed force information, the degree of hardness for the contact tissue, and the local discontinuities in the hardness of contact tissue. In fact, the degree of hardness indicates the degree of softness for biological tissues. In other words, decreasing the hardness will result in increasing the softness. Similar to surgeons' fingertips, the tactile sensor should measure the relative degree of hardness/softness to characterize the tissues based on their degree of hardness. In fact, different tissues exhibit different degrees of hardness.

Figure 1-2: Photograph of a surgical operating room featuring the da Vinci Surgical System. This photograph is the courtesy of Intuitive Surgical Inc. (http://www.intuitivesurgical.com), ©[2011] Intuitive Surgical, Inc. [5]. The system comprises one surgical robot, two surgeon consoles, one patient cart, and one vision cart.

As shown in Figure 1-3, in MIRS operated by da Vinci, the movements of surgeons' hands on the master controls of the main console is transferred to surgical instruments through keyhole incisions on patients' body. In MIRS, unlike conventional surgical methods, surgeons do not feel any tactile perception while interacting with tissues via surgical instruments.

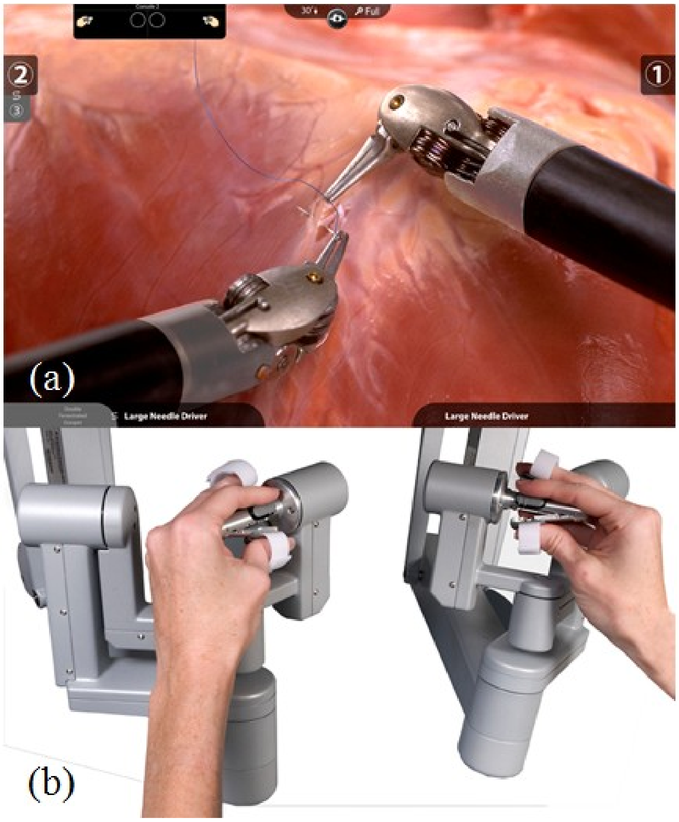

Figure 1-3: Showing hands on the master controls of the surgeon console; and (b) showing the operative split screen; the images are the courtesy of Intuitive Surgical Inc. (http://www.intuitivesurgical.com), ©[2011] Intuitive Surgical, Inc. [5].

As shown in Figure 1-4, the Canadian competitor of the da Vinci is the Amadeus Surgical Robot, which was introduced by Titan Medical Inc. (Toronto, ON, Canada). In addition, Artisan Extend Control Catheter introduced by Hansen Medical Inc. (Mountain View, CA, USA) as well as TactiCath catheter ablation introduced by Endosense SA (Geneva, Switzerland) are among the common examples of catheter-based techniques (CBT) in which tactile sensors are required. In these MIRS and CBT, tactile sensors are useful in measuring the tactile information while surgical tools interact with tissues [8]. In general, providing surgeons with such tactile information results in a better performance in MIRS and CBT [3, 12-14]. Therefore, the development of a sensor with the ability to measure the tactile information is crucial for use in MIRS systems such as the da Vinci and the Amadeus as well as CBTs such as Artisan [15] and TactiCath.

Figure 1-4: The Amadeus® Robotic Surgical System is a 4-armed robotic surgical platform developed by Titan Medical Inc. in Canada; This image is the courtesy of Titan Medical Inc. (http://www.titanmedicalinc.com), ©[2011] Titan Medical, Inc. [16].

In nature, tissue is a viscoelastic material. Therefore, during MIRS, due to the viscoelastic properties of the tissues, tool-tissue interactions involve both dynamic and static loading conditions. For instance, while tissue is grasped, it exhibits a strong dynamic behavior for a short time. However, as time passes, the rate of change in the interacting force between the grasper's jaws and tissue decreases. As a result, a force feedback from the tool-tissue interaction involves both dynamic and static loading conditions [17]. It means that the tactile sensor must be able to measure the dynamic contact forces as well as the static ones. However, on the one hand, existing electrical-based tactile sensors, such as piezoelectric-based ones [18], mostly perform only under dynamic loading conditions. On the other hand, sensors that perform under static conditions are usually simple force sensors that cannot measure distributed tactile information [19]. Consequently, there is a need to develop a tactile sensor that can measure distributed tactile information and can also perform under static loading conditions.

In fact, surgeons sometimes need to perform MIS and MIRS under the presence of strong electro-magnetic fields [20]. For instance, magnetic resonance imaging (MRI) devices are one of the common sources of such electro-magnetic fields. Currently, such devices are commonly used during MIS and MIRS for various applications [21, 22]. However, existing electrical-based tactile sensors such as strain gauges, piezoelectric, and piezoresistive sensors are not practical in MRI environments. In addition, a tactile sensor must be electrically passive to avoid disrupting the electrical activities of the heart [23] for minimally invasive cardiovascular surgery. Consequently, there is a need to develop a tactile sensor which is MRI-compatible and electrically-passive. In fact, optical micro-systems are one of the few choices that can address such conditions [24].

To design a tactile sensor, size constraint is another important factor. Due to the limitation of available space at the tips of surgical instruments used in MIS and MIRS, tactile sensors must be sufficiently miniaturized to be integrated into such limited spaces. Advances in micro electro mechanical system (MEMS) technology have caused a new opportunity for the development of such sensors [25]. Optical micro-system based devices are compatible for tactile sensing. The sensing principles of such optical micro-systems are divided into three categories: fiber Bragg grating (FBG) based, interferometry based, and intensity-modulated optical waveguide based [26]. Among these three categories, it is the intensity-modulated devices that offer unique advantages such as less complexity, less expensive equipment, and less sensitivity to thermal-induced strain [27]. Moreover, these sensors can be miniaturized and can also perform under both static and dynamic conditions.

The above mentioned factors are some of the most important challenges to design an optical MEMS device for tactile sensing in MIS and MIRS. Such challenges can be addressed by the development of smart surgical instruments equipped with MEMS-based tactile sensors that would be necessary for MIS and MIRS. Accordingly, the present thesis investigates the feasibility of various MEMS-based tactile sensors.

1.2 Literature Review

1.2.1 Related Work in Articles

In recent years, in order to respond to the inadequacies of MIS and MIRS systems, a large number of tactile sensors with different sensing principles have been proposed [8, 11]. Nevertheless, the majority of these proposed or developed tactile sensors have practical limitations. For instance, recently, Sokhanvar et al. [18, 28] have proposed a MEMS endoscopic tactile sensor, which is electrically passive, but not MRI compatible because of its electrical-based sensing elements. Although their developed tactile sensors can measure both force and the hardness/softness of grasped tissues, they are based on piezoelectric Polyvinylidene fluoride (PVDF), which cannot perform under static loading conditions. In addition, Tholey et al. [29] have proposed a modular grasper integrated with a three-dimensional force sensor for use in MIS. However, although their sensor accurately measures tool-tissue interaction forces, it is neither MRI-compatible nor electrically passive because of its use of strain gages as the sensing elements. More recently, in 2009, King et al. [6] used a commercially available FlexiForce sensor to investigate the effects of tactile feedback on grasping forces in surgery performed by da Vinci. The commercial force sensor used in their work is a piezoresistive-based sensor that is not electrically passive.

One of the common optical waveguide is optical fiber. In fact, optical fiber sensing technology, which has offered insensitivity to electromagnetic disturbances and miniaturization capabilities, has been widely accepted for use in medical applications [23]. For instance, Patriciu et al. [30] have proposed a new robotic system to perform brachytherapy seed placement under MRI guidance. In their proposed surgical system, position feedback was obtained by optical fiber sensors. However, they have not used any force sensors in their proposed surgical system. As another example, Takahashi et al. [31] have developed an optical-based force sensor for brain function analysis in MRI environments. However, the structural design of their sensor does not allow the measurement of distributed tactile information. In fact, a very limited number of optical fiber based force and tactile sensors have been proposed for use in MIS and MIRS. However, for use in catheter-based techniques (CBT) and catheterization procedures, a large number of optical fiber force sensors have been proposed and developed [32]. For instance, using 3 optical fibers to measure micro-deformations of a catheter tip, a contact sensor has been proposed [33]. As shown in **Error! Reference source not found.** this sensor was incorporated into a commercially available ablation catheter (TactiCath, Endosence SA). To provide an idea about the size of such surgical instruments, it can be mentioned that the diameter of the TactiCath catheter is 7 French [33], which is approximately 2.3

mm. In addition, in 2010, Althoefer et al. [34, 35], proposed two different miniaturized MRI-compatible optical fiber sensors, one for use in MRI-guided MIS and the other for use in cardiac catheterization procedures [35]. Although their proposed sensors are optical-fiber based, they only can measure the magnitude and direction of contact force and they cannot measure distributed tactile information.

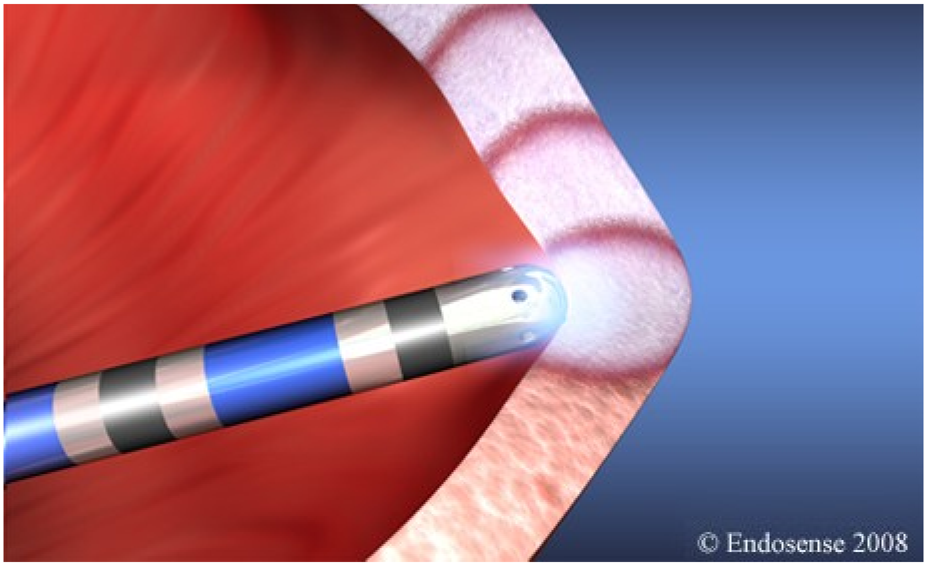

Figure 1-5: TactiCath force sensing catheter (with the diameter of 7 Fr. and 3.5 mm diameter tip electrode [33]) developed by Endosense SA during ablation in the atrium; the image is the courtesy of Endosense SA (http://www.endosense.com) [36].

1.2.2 Related Work in Patents

Nowadays, tactile sensors are being widely utilized in medical applications. For instance, recently, for the examination of breasts or any other soft tissue, a method and a tactile sensor device have been invented [37]. This tactile breast imager measures the pressure distribution on the contact area resulting in measuring the local discontinuities in the hardness/softness of the contact object. However, it is neither an MRI-compatible nor a hardness-measuring sensor. In addition, in 2007, a force sensor [38] was invented for providing force and torque sensing and feedback to the surgeons performing operations with minimally invasive robotic surgery systems such as the da Vinci robot. Since this force/torque sensor uses strain gauges as the measuring elements, it is not insensitive to electromagnetic interferences. In addition, it does not convey any information to surgeons from the interaction between the surgical tools and the tissue.

In fact, due to their significant advantages, optical-based micro-systems have been utilized to develop state-of-the-art tactile sensor inventions for measuring different tactile information, such as force, pressure, acceleration, vibration, etc., in the contact object. These optical-based micro-systems are utilized not only in medical applications, but in other various applications. One of the applications in which optical-based sensors play an important role is robotic applications. For instance, in 2010, Obinata et al. [39] invented an optical tactile sensor to obtain a gripping force between robot hands and the gripped objects. Their invention consists of a tactile portion made of an optically transparent elastic material that has a marker portion on its convex curved surface. This elastic material deforms due to any force applied to it. Then a CCD camera and image-processing techniques are utilized to extract the contact force applied to the sensor. In fact, although they have utilized optical imaging techniques in their invention, they have not used fiber optic technology. As another similar example, in 2008, Mizota et al. [40] invented another optical tactile sensor for reconstructing force vector distribution by using image-based techniques.

Besides image-based optical techniques, optical fiber technology also provides a good opportunity for inventors to develop new tactile sensors due to its unique features. For instance, fiber Bragg grating (FBG) is one of the recent optical fiber-based technologies that allow the precise measurement of various physical parameters such as pressure, force, or temperature especially in harsh environments [41]. In addition, optical coupling fiber optic sensors are also one of the choices to develop new tactile sensors. For instance, Wise [42] have developed an array of optical fiber sensors to measure the force distribution on a mounting plate of robot manipulators. By measuring the force distribution of the grasped or moved object on a robot arm, Wise's invention can determine the size, location of the object. Similarly, Thiele et al. [43] have invented a crossed fiber optic tactile sensor that consists of a row of transmitting optical fibers as well as a column of detecting optical fibers overlapping each other. Their invention can measure only the spatial distribution of the contact forces involved in gripping an object. In addition to the above-mentioned optical methods, optical fiber interferometry is another technique to develop various optical-fiber-based tactile sensors. For instance, Duncan et al. [44] invented a fiber optic sensor apparatus for measuring the pressure of media. Their sensor includes a light source, a reflective sensor, a diaphragm, which deflects in accordance with the pressure applied in a medium, and an optical fiber coupled to the light source and a detector and a spectrometer. However, it can measure only the pressure in a medium and it cannot provide any information about the hardness of the medium.

Although purely optical sensing principles, used in these sensors, make them MRI-compatible, none of them can sense the hardness or softness of contact objects. As an example, Aeby et al. [45] have invented a catheter for the diagnosis or treatment of a vessel or an organ. At the tip, their invented catheter consists of a tri-axial optical fiber force sensor. Although their invention measures the contact force, it cannot measure the hardness/softness of the contact tissue. Moreover, in 2008, Leo et al. [46] invented a medical apparatus system for measuring loads applied from an organ or a vessel using catheter-based systems for diagnosing or treating purposes. Their invention uses at least two optical fiber sensors which permit the computation of a multi-dimensional force vector resulting from contact between the distal extremity of the apparatus and the contact organ or tissue. Similarly, Kane [47] has invented an optical pressure sensor for measuring blood pressure in catheter-based systems. Like all other existing optical tactile sensors, his invention cannot measure the local hardness or softness of contact objects.

1.3 Thesis Motivation

The da Vinci Surgical system developed by Intuitive Surgical Inc. located in Sunnyvale, CA, USA, is an example of MIRS systems. The Amadeus Surgical Robot introduced by the Titan Medical, Inc. in Toronto, Ontario, is the Canadian competitor of the da Vinci. In fact, the da Vinci robot does not provide surgeons with tactile cutaneous feedback during tool-tissue interactions [6, 48]. Similarly, robotic catheter systems such as the one developed by the Hansen Medical Inc. in California, USA, does not provide surgeons with tactile feedback while the tip of the catheters interacts with vessel walls or cardiac tissues. However, surgeons need this feedback to enhance the performance of minimally invasive surgical operations. Consequently, there is a need to develop a tactile sensor that can be integrated into the end-effectors of such systems and measure the tactile information during the sensor-tissue interactions. Being MRI compatible and electrically passive, and performing under both static and dynamic loading conditions are the required features that the tactile sensor should have in order to address the important issues involved in surgical applications. In the present thesis, tactile sensors based on optical micro-systems are proposed, designed, simulated, fabricated, and tested for use in MIS and MIRS. The sensing principles of the developed tactile sensors in this work are MRI-compatible.

In fact, the platforms of five developed sensors in the present work are made of silicon material, which is not hundred percent MRI-compatible since silicon material is semi-conductive. However, the sensor platforms could be made of any non-conductive materials such as polymeric materials. In other word, the challenge to have an MRI-compatible sensor is to come up with an MRI-compatible sensing principle. Once an MRI-compatible sensing principle is available, the platform of the sensor could be made of MRI-compatible materials. In the present work, silicon-based sensor platforms have been developed because it requires simpler micromachining process. However, based on the proposed designs, other micromachined platforms that are totally MRI-compatible, such as SU-8 platform, can also be implemented.

1.4 Thesis Objective and Scope

Basically, the *objective* of the present thesis is to design and develop a fully optical tactile sensor that mimic the tactile/touch perceptions of human fingertips considering certain constraints required for medical applications. Such constraints include being magnetic resonance compatible, being electrically passive, and ability to perform under static and dynamic loading conditions. The primary application of such sensor is in performing minimally invasive surgical tasks whether they are conventional laparoscopic/endoscopic tasks or sophisticated robotic-assisted surgical tasks. To do so, various sensor configurations representing different stages of development are studied in the present thesis. In order to meet the *objective*, specific sub-objectives are detailed as follow:

1. Using optical fiber bend-type sensing principle to design and develop a macro-scale tactile sensor for the integration into surgical graspers
2. Design and develop a catheter-tip tactile sensor for use in catheter based cardiovascular surgical operations
3. Study the effects of important tissue parameters on a beam-type sensor structure during sensor-tissue interaction
4. Implementing an intensity-modulated optical fiber sensing principle toward the design and development of an optical force sensor
5. Add force distribution sensing feature to the force sensor developed in the previous step
6. Implementing fully optical methods to design and develop a hardness/softness sensor suitable for both static and dynamic measurements
7. Study on using a novel optical/non-optical hybrid principle to design and develop a relatively less-complex hardness/softness sensor
8. Finally, develop, test, and characterize a fully-optical multi-functional sensor for simultaneously measuring multiple tactile information under both static and dynamic

loading conditions for tissue manipulation and palpation in minimally invasive robotic surgery

To achieve the objective, the following steps were implemented individually for each sensor: (a) design and modeling; (b) simulation; (c) development and prototyping; (d) testing; ultimately, (e) characterization.

1.5 Thesis Contribution

As the main contribution of this thesis, for the first time, an innovative microsystem based sensor that measures tactile information and combines numerous unique features is designed, developed, tested, and characterized. The tactile information includes force, force distribution, relative hardness, and local discontinuities in the hardness of soft objects. The unique sensor features comprise of being potentially MRI-compatible, being electrically passive, and having the ability to perform under both static and dynamic loading conditions. Based on this contribution, both an International PCT Patent (with the reference number of PCT/CA2011/001192, Oct. 26, 2011) and a provisional U.S. Patent (with the Serial Number of 61/344,859, Oct. 26, 2010) were filed. The sub-contributions are categorized as follows:

1. A new approach for measuring distributed tactile information based on the optical fiber bending principle
2. A novel catheter-tip hybrid sensor to measure the relative hardness of cardiovascular tissues
3. Modeling of the sensor-tissue interaction and studying the effects of important tissue parameters on the sensor response

4. An innovative approach to measure force with high-sensitivity and high-resolution based on an optical sensing principle using optical fiber coupling
5. Design and develop a new miniaturized force distribution optical sensor
6. Propose and implement an innovative approaches to measure relative hardness of soft objects based on optical fiber coupling
7. Using an innovative concept to develop an optical microsystem sensor to simultaneously measure multiple parameters in both static and dynamic modes

In addition to the US and International PCT patents, the content of this thesis is written based on one published journal article [49], three peer-reviewed conference papers [50-52], three under review journal article [53-55], and three journal articles [56-58] to be submitted in the next few months. In addition, two more journal articles [59, 60] and nine more conference papers [61-69] have been published based on the expertise developed as part of the thesis.

1.6 Organization of the Thesis in Manuscript-based Format

This manuscript-based thesis is organized in ten chapters. In the present chapter, a brief introduction about the use of tactile sensing in MIS and MIRS, literature review, motivation of the thesis, and scopes/objectives of the thesis are presented. The literature review includes a brief comprehensive survey of the recently developed sensors for use in surgical applications. Even though the literature review is not elaborated in Chapter 1, a detailed literature review corresponding to topics will be covered in respective chapters as this thesis is prepared in manuscript-based format. Chapter 2 to Chapter 9 are duplicated from three published conference articles, one published journal article, one international PCT patent, one provisional US patent, and six submitted (or to be submitted) journal articles. Chapter 10 presents the summary and conclusions of the thesis as well as the recommendations for the future study. To address the objectives of the thesis defined in Section 1.4, the chapters are organized in a cohesive manner. Moreover, the structure of the thesis is formatted according to the "Thesis Preparation and Thesis Examination Regulations (version-2011)" of the School of Graduate Studies at Concordia University. In doing so, the sections, figures, equations, and tables of the duplicated articles are accordingly numbered to address the regulations of the thesis preparation. At the end of the chapters, rather than individual reference lists of the papers, a single comprehensive reference list is presented in the Bibliography section.

Chapter 2, entitled "Tactile Sensing Based on the Optical Fiber Bending Principle", covers Sub-objective 1 of the "Thesis Objective and Scope" in Section 1.4. This chapter is based on a manuscript published in IEEE Sensors Journal [49] and a conference paper [50] presented by the author at the IEEE 7th International Workshop on Fibre Optics and Passive Components (WFOPC2011) in Montreal in July 2011. The conference presentation won the best student presentation award. In fact, Chapter 2 is compiled from the following papers:

R. Ahmadi, M. Packirisamy, J. Dargahi and R. Cecere, "Discretely-loaded beam-type optical fiber tactile sensor for tissue manipulation and palpation in minimally invasive robotic surgery," *IEEE Sensors Journal,* vol. 12, no. 1, pp. 22–32, January 2012.

R. Ahmadi, M. Packirisamy and J. Dargahi, "Optical fiber sensor array for Artery/Lump detection," in *Proc. IEEE 7th International Workshop on Fibre Optics and Optical Passive Components (WFOPC)*, Montreal, Canada, July 2011, pp. 13–15. *(Won Canadian Institute for Photonics Innovation Award for the best student presentation)*

Chapter 3, entitled "Catheter-Tip Tactile Sensing for Catheter-Based Techniques", covers Sub-objective 2 of the "Thesis Objective and Scope" in Section 1.4. Chapter 3 is based on a conference paper [51] presented by the author at IEEE Sensors Conference in Hawaii in November 2010 as follows:

R. Ahmadi, J. Dargahi, M. Packirisamy and R. Cecere, "A new hybrid catheter-tip tactile sensor with relative hardness measuring capability for use in catheter-based heart surgery," in *Proc. IEEE International Conference on Sensors*, Hawaii, USA, November, 2010, pp. 1592–1595.

Chapters 4 to 9 cover Sub-objective 3 to Sub-objective 8 of the "Thesis Objective and Scope" in Section 1.4. These chapters are based on a U.S. and an International PCT patent applications as follow:

M. Packirisamy, R. Ahmadi, and J. Dargahi, S*ystem for sensing a mechanical property of a sample*, International PCT Patent filed on Oct. 26, 2011, Application Number: PCT/CA2011/001192 and Provisional U.S. Patent filed on Oct. 26, 2010, Serial Number: 61/344,859.

More specifically, Chapter 4, entitled “Modeling and Parametric Study of Sensor-tissue Interaction for Minimally Invasive Surgical Tasks”, covers Sub-objective 3 of the “Thesis Objective and Scope” in Section 1.4. Chapter 4 is based on a manuscript to be submitted to a journal [56] as follows:

R. Ahmadi, M. Packirisamy and J. Dargahi, “Modeling and parametric study of sensor-tissue interaction for minimally invasive surgical tasks,” *The International Journal of Medical Robotics and Computer Assisted Surgery*, to be submitted.

Chapter 5, entitled “Fully Optical High Sensitive Force Sensing”, covers Sub-objective 4 of the “Thesis Objective and Scope” in Section 1.4. Chapter 5 is based on a manuscript [53] submitted to the ASME Journal of Medical Devices as follows:

R. Ahmadi, M. Packirisamy and J. Dargahi, “High sensitive force sensing based on the optical fiber coupling loss,” *ASME Journal of Medical Devices*, Under Review, Submitted on October 27, 2011, Paper No. MED-11-1096.

Chapter 6, entitled “Optical Array-based Force Distribution Sensing for Lump/Artery Detection”, covers Sub-objective 5 of the “Thesis Objective and Scope” in Section 1.4. In fact, Chapter 6 is based on a manuscript [54] submitted to a journal as follows:

R. Ahmadi, M. Packirisamy and J. Dargahi, "Optical array-based force distribution sensing suitable for lump/artery detection," *IEEE Trans. Biomed. Eng.*, Under Review, Submitted on January 09, 2012, Manuscript ID: TBME-00033-2012.

Chapter 7, entitled “Fully Optical Microsystem for Static and Dynamic Relative Hardness Sensing”, covers Sub-objective 6 of the “Thesis Objective and Scope” in Section 1.4. Chapter 7 is based on a manuscript [55] submitted to a journal as follows:

R. Ahmadi, M. Packirisamy and J. Dargahi, "An Innovative optical microsystem for static and dynamic tissue diagnosis in minimally invasive surgical operations," *J. Biomed. Opt.,* Under Review, Submitted on Dec. 14, 2011, Manuscript #11755SS.

Chapter 8, entitled “Optical-Piezoresistive Hybrid Relative Hardness Sensing”, covers Sub-objective 7 of the “Thesis Objective and Scope” in Section 1.4. In fact, Chapter 8 is based on a manuscript [57] to be submitted to a journal as follows:

R. Ahmadi, M. Packirisamy and J. Dargahi, “Design and development of an optical-piezoresistive hybrid tactile sensor for use in minimally invasive surgery,” *Biosensors and Bioelectronics*, to be submitted.

Chapter 9, entitled “Multi-Purpose Optical Microsystem for Static and Dynamic Tactile Sensing”, covers Sub-objective 8 of the “Thesis Objective and Scope” in Section 1.4. Chapter 9 is based on a manuscript [58] to be submitted to a journal as follows:

R. Ahmadi, M. Packirisamy and J. Dargahi, “Multi-purpose optical microsystem: toward hardness measurement and lump/artery detection in minimally invasive surgical tasks,” *Journal of Biomedical Microdevices*, to be submitted.

Chapter 2: Tactile Sensing Based on the Optical Fiber Bending Principle

In the present chapter, an optical fiber tactile sensor based on a novel design is proposed, designed, simulated, fabricated, and tested for use in MIS and MIRS. In 2010, a preliminary version of this work was presented at a conference [52]. To simulate the output of the sensor, a theoretical model of the sensor and a finite-element (FE) model of the sensor-tissue interaction have been developed. A prototype of the sensor was fabricated. Using elastomeric materials, the sensor has been tested and validated experimentally.

2.1 Introduction

In traditional open surgery, surgeons use their fingertip palpation to investigate the hidden anatomical structures of tissue. However, in the current commercially available minimally invasive robotic surgery (MIRS) systems, while surgical instruments interact with tissues, surgeons do not sense any tactile information. Therefore, tactile sensors are required to be integrated into the tips of surgical instruments to mimic the perception of the surgeon's fingertips. The electrical-based tactile sensors that exist at present cannot usually operate under static loading conditions. In addition, they are not compatible with magnetic resonance imaging (MRI) devices.

Therefore, this research was aimed at restoring tactile information by developing an MRI compatible optical fiber tactile sensor. The sensor consists of only one single moving part. Thanks to this novel design, the sensor does not require the use of an array of sensors to measure the distributed tactile information. This capability simplifies the integration of the sensor into any suitable space available at the tips of surgical instruments. In addition, the sensor performs under both static and dynamic loading conditions. A theoretical model of the sensor and a finite-element model of the sensor-tissue interaction were developed. To validate the sensor, a prototype of the sensor was fabricated and tested.

2.2 Sensor Design

For our purposes, a number of conditions must be considered in the design of the proposed tactile sensor. First, the sensor should be able to measure accurately the value and the position of a concentrated force so as to identify the size and the location of different types of hidden tissues within surrounding background tissues. Second, the sensor should measure the amount of force interacting between tissues and surgical tools. These forces can be either distributed contact forces or concentrated contact forces, or can be in combination. Third, the sensor should perform such measurements under both static loading conditions and dynamic loading conditions to address the following needs: a) to maintain the contact stability during tool-tissue interaction; and b) at the same time, to avoid tissue damage caused by excessive contact force [17]. Fourth, the sensor should also be insensitive to electromagnetic interference in order to be compatible with MRI devices, which are currently in widespread use in surgical operating rooms. Fifth, the sensor should be electrically passive for particular applications such as cardiac surgeries so as to avoid disrupting the normal electrical activities of the heart [71]. Sixth, the sensor must be waterproof to perform in-situ and in-vivo measurements. Seventh, the sensor should be made of non-metallic materials so as to avoid creating artifacts in ultra-sound images since, in some MIS and MIRS applications, such ultra-sound imaging techniques might be utilized for guiding surgical instruments inside the body [71]. Ultimately, the sensor should be small enough so that it can be integrated into any suitable space available at the tips of surgical tools such as da Vinci graspers. Thanks to their unique characteristics, optic fiber sensors prove to be attractive for our purposes because they satisfy all the above-mentioned requirements. For example, they are insensitive to electromagnetic fields and are also electrically passive.

Size limitation is one of the important design constraints. It is indeed difficult to integrate an array of sensors with moving parts into the tips of surgical instruments. Because of this constraint, the proposed sensor consists of only one single moving part, which is a flexible beam. In fact, the novel part of the sensor is that to measure the force and the position of the force, the sensor uses this single moving part. Thanks to this novel design, the sensor does not require the use of an entire array of sensors to measure the distributed tactile force. This capability simplifies the integration of the sensor into the narrow space available at the tips of surgical instruments. Presenting a variety of different views, Figure 2-1 shows the structural design of the proposed tactile sensor. The moving part of the sensor is a beam. This beam behaves like a Euler/Bernoulli beam with fixed-fixed boundary conditions. The sensing principle of the sensor depends on measuring the deflection of this beam at three points: Point A, Point B, and Point C. To carry out this type of measurement and to satisfy the above-mentioned design constraints, a single-mode optical fiber sensing based on bending principle is implemented.

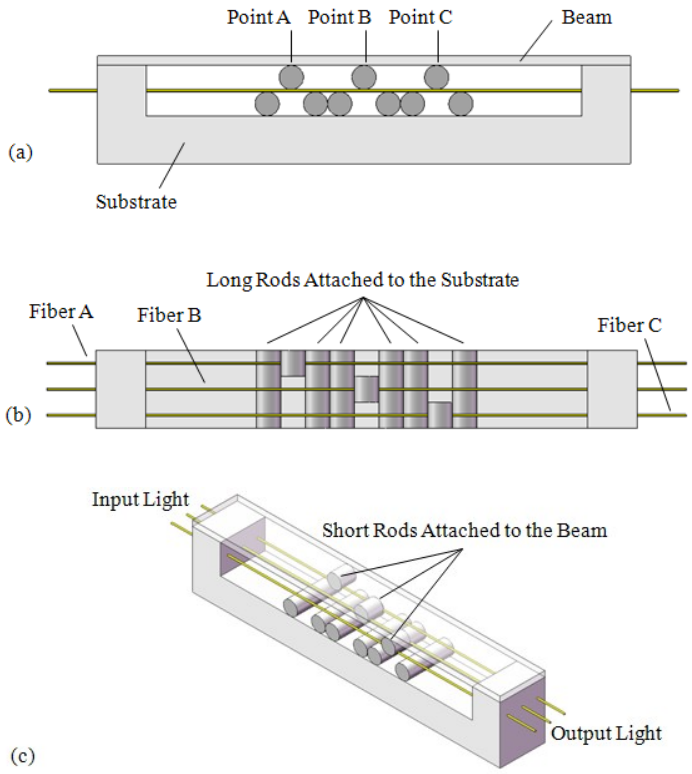

Figure 2-1: The structure of the tactile sensor: (a) front view; (b) top view in which the beam is transparent for demonstration purposes; and (c) 3-D view in which the beam is translucent for demonstration purposes.

As shown in Figure 2-1, at Point A, Point B, and Point C, three short movable rods are attached to the bottom surface of the beam. In addition, six long rods are fixed to the substrate accordingly. Three single-mode optical fibers (Fiber A, Fiber B, and Fiber C) with 250 µm coating diameters are embedded between the short rods and the long rods. The optical fibers are initially stretched by fixing them to the supports of substrate at the sides of the sensor. On the one hand, the fibers are coupled to a laser light source. On the other hand, the other ends of fibers are coupled to photodetectors, which can measure the intensity of the light inside the fibers. In their initial conditions, the fibers are straight. Any subsequent deflection of the beam then causes the straight fibers to be subjected to a single small-radius bend. Such fiber bending results in a power loss in each fiber. Then, by measuring the power loss on each fiber, the deflection of the beam can be measured at Point A, Point B, and Point C. By analyzing the deflection of the beam at these three points, a measurement of the distributed tactile information on the beam can be obtained. In the next section, the theoretical relation between the applied force and the resulting power loss is discussed.

2.3 Sensor Modeling

The proposed sensor should measure discrete force information while interacting with tissues. In order to simulate the output of the sensor, two different models must be introduced. First, the model of the sensor must be developed. Second, the interaction between the sensor and tissues must be modeled. In the present work, the theoretical model of the proposed bend-type optical fiber sensor is developed. In addition, a finite-element model of soft objects, which represent tissues, is introduced. Moreover, the interaction between the sensor and such soft objects is modeled to simulate the output of the sensor.

2.3.1 Theoretical Model of the Sensor

During MIS and MIRS, surgeons need to identify the location of hidden tissue abnormalities within surrounding tissue. Such tissue abnormalities such as an embedded lump are usually harder than the background tissue. Figure 2-2 demonstrates such a condition, when the sensor touches a tissue with an embedded lump. As shown in this figure, during the interaction between the sensor and such tissue, the lump, which is harder than the surrounding tissue, causes a concentrated force to be applied to the sensor at Point X. Therefore, identifying the position of this concentrated force causes the detection of the position of the lump. A novel method is proposed to measure this position.

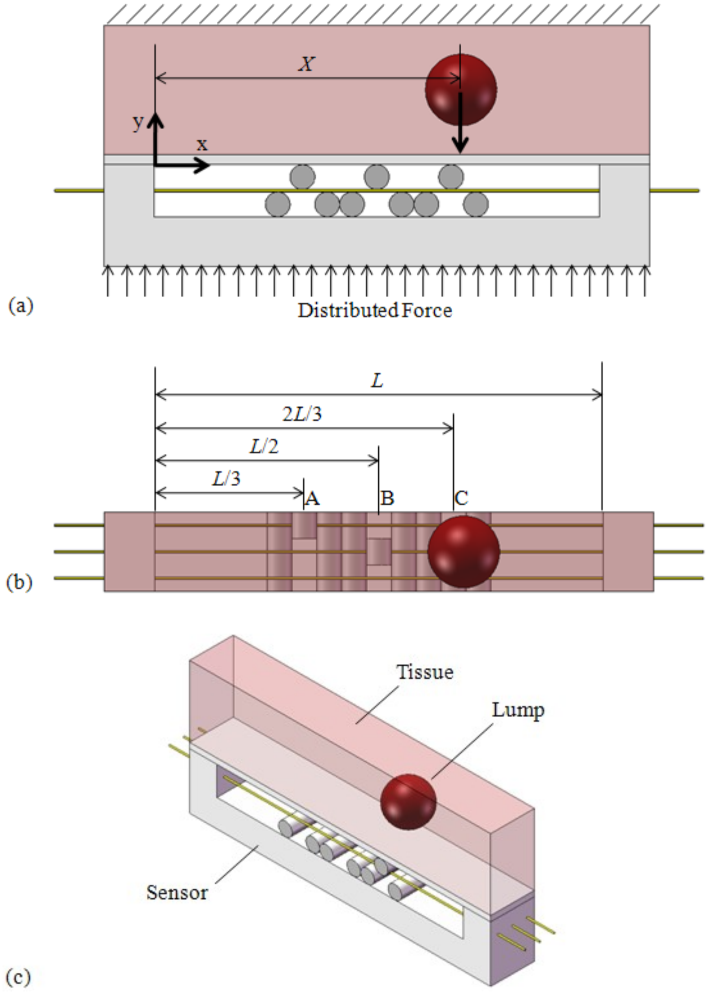

Figure 2-2: Tissue abnormalities such as lumps, which are usually harder than the background tissues, cause a concentrated force to be applied to the sensor. The sensor measures the position of such concentrated force (X) by having only one single moving part. This force position represents the position of the embedded lump inside the tissue. In (b), the beam was drawn transparent and the tissue was drawn translucent for demonstration purposes.

In order to measure the position of Point X, the deflection of the beam at Point A, Point B, and Point C must be measured. Figure 2-3 demonstrates the configuration of the rods and fibers at one of the three measurement points of the sensor. The deflection of the beam at Point A, Point B, or Point C is equal to the displacement of the movable rod at the same point. In order to model the output of the sensor with respect to the applied force, the relation between the applied force and the resulting power loss in the fibers must be modeled. In order to do that, the relation between the concentrated applied force at Point X and the resulting deflection of the beam at Point A, Point B, and Point C must be extracted. For the sensor's beam, which is assumed as a Euler/Bernoulli beam with fixed-fixed boundary conditions, this relation is extracted as follows [72]:

$$y(X) = \frac{P}{EI}\left[-\frac{X(L-X)^2}{2L^2} l^2 + \frac{(L-X)^2(L+2X)^2 l^3}{L^3} - \frac{1}{6}\langle l-X \rangle^3 \right] \tag{2.1}$$

where *y(X)* is the deflection of the beam at point l, when a concentrated force, *P*, applies on the beam at position *X* (Figure 2-2-a). *E* is the beam's modulus of elasticity. *I* is the moment of inertia of the beam's cross section about its neutral axis. *L* is the length of the beam which is 45 mm in this case. *X* is the position of the concentrated force which represents the position of the lump. *P* is the amount of the concentrated force. < > is the singularity function [73]. l is the position of Point A, Point B, and Point C which is defined as follow:

$$l = \begin{cases} L/3 & \text{for Point A} \\ L/2 & \text{for Point B} \\ 2L/3 & \text{for Point C} \end{cases} \tag{2.2}$$

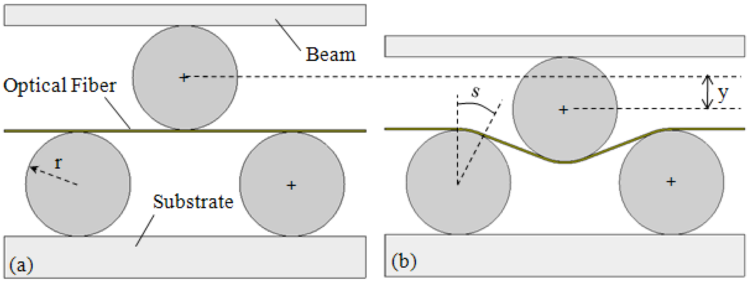

Figure 2-3: The configurations of the rods are the same at Point A, Point B, or Point C of the sensor. One short movable rod is attached to the sensor beam whereas two fixed rods are attached to the sensor substrate. An optical fiber is stretched in its initial position between these rods. The displacement of the movable rod (y) causes a bend arc length (s) on the fiber. The total bend arc length of the fiber is four times s.

In the modeling, the dimensions of the beam are chosen as the dimensions of the real fabricated sensor. The length, the width, and the thickness of the beam are 45 mm, 8 mm, and 1 mm respectively. The beam should be made of a non-metallic material. In the present work, a Hi-Impact PolyStyrene is selected as the material of the beam. The modulus of elasticity of such material is 3000 MPa. In the modeling, the amount of the concentrated force, *P*, is assumed to be 3.0 N. The deflection of the beam at Point A, Point B, and Point C equals the displacement of the corresponding movable rods at those points. This displacement is called y for a movable rod. Now, the relation between the displacement of a movable rod and resulting power loss must be found. It has been shown that the relation between the total bend arc length of the fiber and the resulting power loss of the fiber is linear [73]. In other words, the total bend arc lengths of Fiber A, Fiber B, and Fiber C linearly represent the power loss on the same fiber. Therefore, the output of the sensor can be modeled by finding the relation of the total arc lengths of the Fiber A, Fiber B, and Fiber C with the displacement of the movable rod at Point A, Point B, and

Point C respectively. The total arc length of each fiber, *S*, is four times of bend arc length, *s*, shown in Figure 2-3:

$$S = 4s(r, y) \tag{2.3}$$

The arc length, s, is extracted through geometrical considerations [73] as follows:

$$s(r, y) = r \arccos\left[\frac{2r(\Delta^2/4 + r\Delta)^{1/2}}{r^2 + \Delta^2/4 + r\Delta}\right] \tag{2.4}$$

where r is the bend of radius, which is equal to the radius of each rod. In this case, the radius of each rod is 1.25 mm. In addition, Δ is defined as:

$$\Delta = (8r^2 + y^2 - 4ry)^{1/2} - 2r \tag{2.5}$$

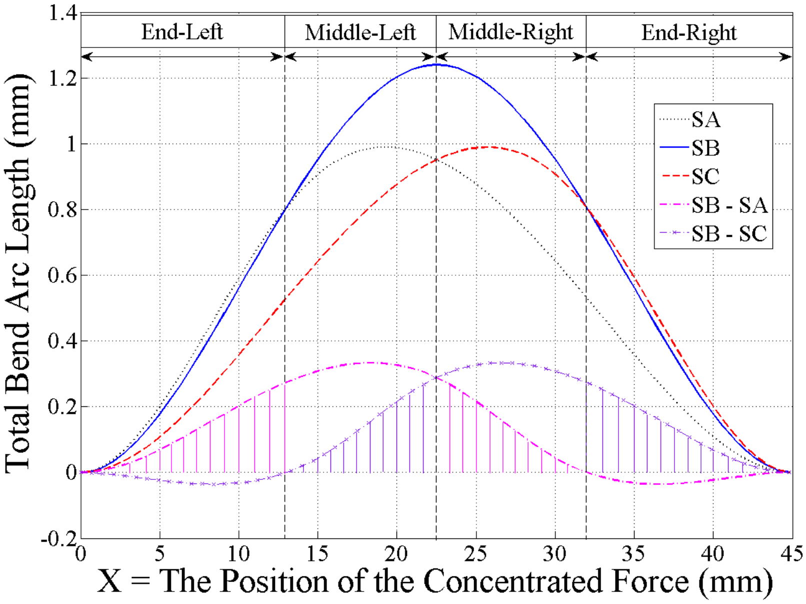

Figure 2-4: The relation between the position of a concentrated force (X) applied to the sensor and resulting bend arc lengths on the optical fibers. SA, SB, and SC represent the total bend arc length of Fiber A, Fiber B, and Fiber C respectively. SB-SA and SB-SC represent the difference between SB and SA and the difference between SB and SC respectively.

Based on these theoretical considerations, the relation between the position of the concentrated force, *X*, and the total bend arc length of each fiber of the sensor can be found. Figure 2-4 demonstrates the simulated total arc length of Fiber A, Fiber B, and Fiber C caused by a 3.0 N concentrated force applied at Point X. As shown in Figure 2-4, by comparing the total arc lengths of these three fibers, the position of the concentrated force, *X*, can be obtained by using the algorithm shown in Figure 2-5. Using this algorithm, the position of the concentrated force can be identified among the four sections of the beam of the sensor: End-Left, Middle-Left, Middle-Right, and End-Right. *SA*, *SB*, and *SC* represent the total bend arc length of Fiber A, Fiber B, and Fiber C respectively. More accurately, as demonstrated in Figure 2-4, by finding *SB-SA* and *SB-SC*, the exact position of *X* can be obtained within each of these four sections. It is now clear that the position of the concentrated force is on a specific pre-defined section. Now, on each of these pre-defined sections, the output of Fiber B can be used to measure the magnitude of the force. In other words, on each pre-defined section, the greater the *SB*, the greater the magnitude of the concentrated force applied to the sensor. The positions of Point A, Point B, and Point C are chosen in a way that will result in four pre-defined sections having approximately equal lengths.

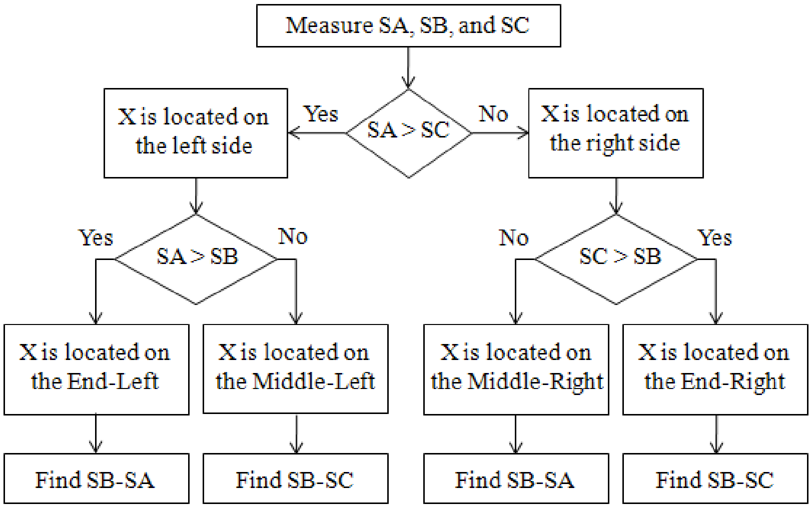

Figure 2-5: Block diagram of the algorithm to measure the position of the concentrated force (X).

The position of the concentrated force represents the location of the lump. For the application of the sensor in MIS and MIRS, the amount of total force applied to the sensor, which is a combination of concentrated and distributed forces, is important to avoid tissue damage. This force can be measured by measuring the output of the sensor from Fiber B. Based on the required range of force measurement and the required resolution for different types of surgical applications, the sensor can be calibrated accordingly by changing the dimensions and the material of the sensor's beam.

2.3.2 Modeling of the Interaction between Sensor and Tissue

In order to model the sensor-tissue interaction, the tissue must be modeled. In the present work, elastomeric materials with similar mechanical properties to biological tissues are used to model the sensor-tissue interaction. The behavior of such materials, which undergo large deformations, can be described by nonlinear elasticity theory. Using hyperelastic models is one of the common methods to model such materials [74].

Hyperelastic materials are described by a strain energy function, W, which is a scalar function. The stress component of the material as a result of applied strain is obtained from [75]:

$$\mathbf{S} = \frac{\partial W(\mathbf{F})}{\partial \mathbf{F}} \tag{2.6}$$

where **F** is the deformation gradient tensor and **S** is the first Piola-Kirchhoff stress tensor. To describe the strain energy function, Mooney-Rivlin model is selected. This model is widely used to model rubber-like elastomeric materials as well as biological tissues. Based on 2 parameters Mooney-Rivlin model, the strain energy function for an isotropic and an incompressible material is defined by [75]:

$$W = C_{10}(I_1 - 3) + C_{01}(I_2 - 3) \tag{2.7}$$

where C_{10} and C_{01} are the Mooney-Rivlin material constants. I_i are the principal invariants in most common use in the literature [75].

Table 2-1: Mooney-Rivlin parameters of elastomeric materials

	C_{10} (kPa)	C_{01} (kPa)
H1N Material	-10.6544	43.2938
ICF Material	-0.9667	2.0829

In the experimental setup, two different elastomeric materials, named H1N and ICF, with different mechanical properties were chosen to represent the biological tissues. Using ElectroForce 3200 test instrument (Bose, Minnesota, USA), the stress-strain data for these elastomeric materials were obtained in compression tests. Using curve fitting methods [76] and based on the obtained experimental stress-strain data, the Mooney-

Rivlin material constants for H1N and ICF were calculated. The calculated material constants for these two materials are given in Table 2-1. The sizes of the tested elastomeric materials were selected with respect to the size of the fabricated sensor. Based on the calculated material constants and considering the sizes of the tested elastomeric materials, the FE model of the materials are developed in COMSOL Multiphysics software v3.4. The model is developed in 2-D space dimensions mode of the structural mechanics module of the software. The plain strain mode with parametric analysis and large deformations is used in the model. The Lagrange-Quadratic triangular elements are used in the FE solution. This type of element has hyperelasticity, large deflection, and large strain capabilities. Comparisons between the simulated stress-strain curves and those curves obtained from experiments for H1N and ICF verify that the obtained material constants are accurate enough to model the sensor-tissue interaction. Results show that H1N is harder than ICF.

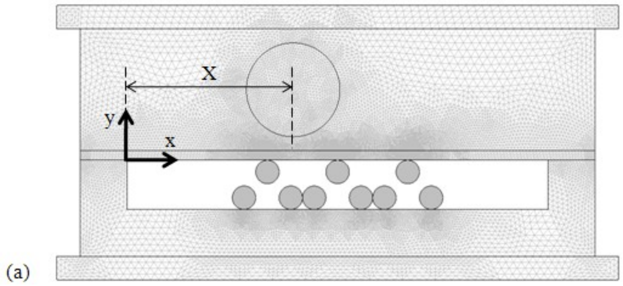

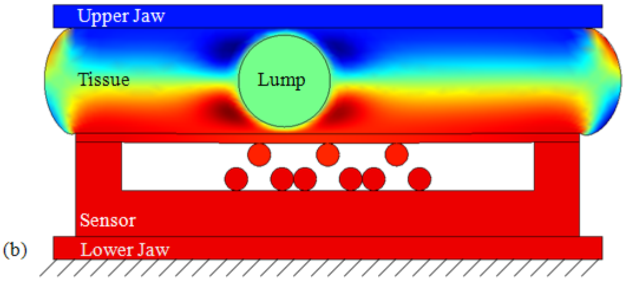

Figure 2-6: The finite element model of tool-tissue interaction. The tissue contains an embedded lump at position X. (a) meshed structure of the model; (b) the deformation of tissue, embedded lump, and sensor beam. The model undergoes large deformations. The tissue is modeled as a hyperelastic material.

In the next step, the obtained material constants for H1N and ICF are used to model the interaction between the sensor and elastomeric materials used in the experiments. Figure 2-6 shows the developed FE model of the interaction between the sensor and an elastomeric material containing an embedded lump. The embedded lump is assumed as a rigid material. The position of the embedded lump is defined by *X*. The elastomeric material is modeled twice based on the previously calculated material constants for H1N and ICF. The material properties of the sensor are chosen similar to the fabricated one. As shown in Figure 2-6-b, the sensor is located on the top of the fixed Lower Jaw of the ElectroForce test instrument. The elastomeric material, which represents biological tissue, is located on the top of the sensor. A lump is embedded inside the elastomeric material at position *X*. In the model, the Upper Jaw is lowered by using the parametric solver of COMSOL as the negative *y* displacement. The displacement goes from 0 mm to -1.5 mm with 0.1 mm intervals. In the experimental test, it is observed that the friction between the elastomeric materials and the upper jaw as well as the sensor's beam is large enough to avoid any lateral sliding movements between them. Consequently, the same conditions are assumed in the FE model by gluing the upper and lower parts of the tissue to the Upper Jaw and to the sensor beam respectively. As discussed in the following section, the developed model is used to simulate the output of the sensor when it interacts with the tissue containing an embedded lump.

2.3.3 Simulation Results

Figure 2-7 and Figure 2-8 demonstrate the simulation results of the sensor-tissue interaction models with different conditions. Figure 2-7-a demonstrates the deflection of the sensor's beam at Point A, Point B, and Point C when the elastomeric material is modeled as H1N and the lump is located on the End-Left section of the beam. Figure 2-7-b demonstrates the same simulation results when the location of the lump is moved on the Middle-Left section of the beam.

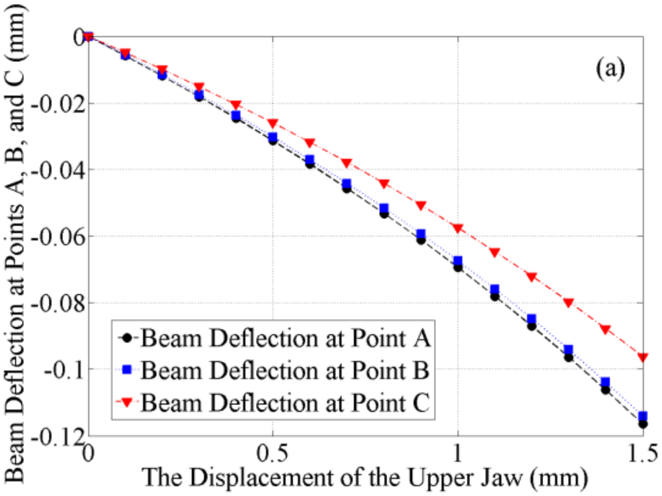

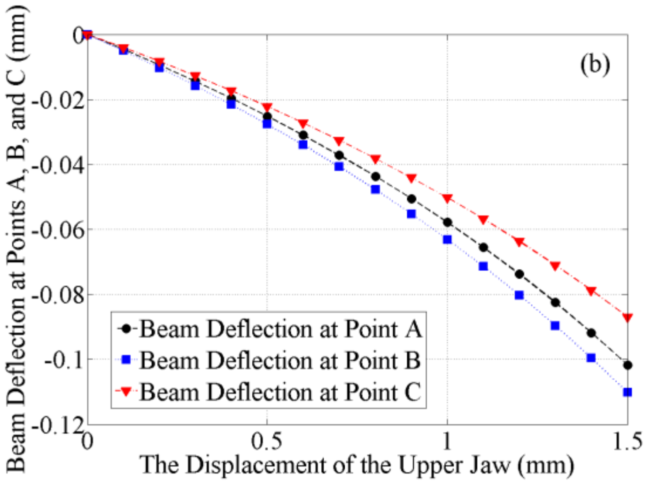

Figure 2-7: The simulation results for the deflection of the sensor's beam at Point A, Point B, and Point C for the following conditions: a) a lump is located on the End-Left section of the beam; and b) a lump is located on the Middle-Left section of the beam. The surrounding background tissue is modeled as H1N material.

Figure 2-8 shows the simulation results when the mechanical properties of the elastomeric material are selected as the mechanical properties of ICF material. Figure 2-8-a and Figure 2-8-b demonstrate such results when the lump is located on the End-Left and Middle-Left sections of the sensor's beam respectively. In these simulations, H1N represents a hard tissue whereas ICF represents a softer one. For the both of these materials, simulation results confirm that the location of the embedded lump can be obtained by using the proposed algorithm in Figure 2-5 and also by considering the following fact: a greater the deflection of the beam at Point A (y_A), at Point B (y_B), and at Point C (y_C) causes a greater *SA*, *SB*, and *SC* respectively. For instance, in Figure 2-7-a, and Figure 2-8-a, the relation between the absolute value of the beam deflections is written in this way: $y_A > y_B > y_C$. This means that *SA* > *SB* > *SC*. Consequently, based on the same algorithm, the latter relation means that the location of the lump is on the

End-Left section. Similar methodology can be used for Figure 2-7-b and Figure 2-8-b to find that the position of the lump is on the Middle-Left section. In fact, the proposed algorithm is obtained based on the output of the sensor for a concentrated force applied to the sensor. However, in the simulated model, similar to the real surgical situations, a combination of a concentrated force and a distributed force applies to the sensor's beam. On the one hand, a concentrated force applies to the beam at point X, where the lump is located. On the other hand, distributed force applies to the beam because of the interaction between the beam and the elastomeric material. Because of the principle of superposition for deflection of the beam [72], this added distributed applied force will not affect the relative deflections of the beam at Point A, Point B, and Point C. Therefore, the same algorithm can be used to measure the position of the embedded lump in real surgical situations. Simulated results also verify this ability of the sensor.

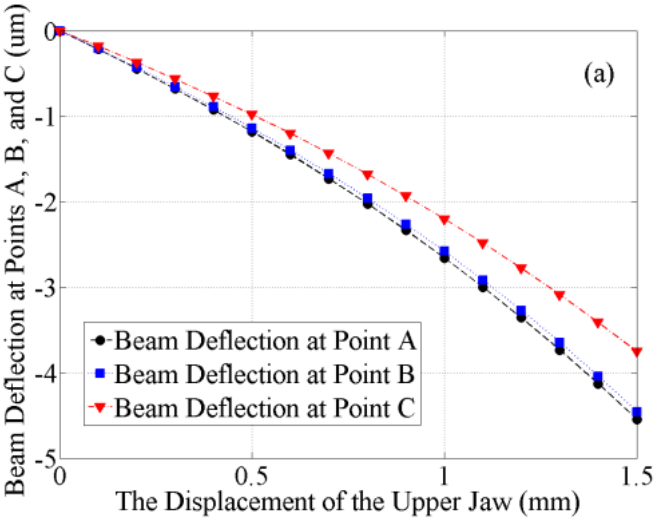

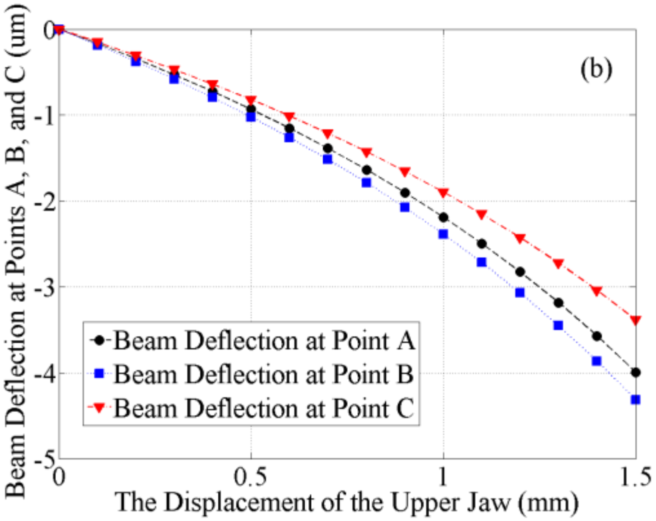

Figure 2-8: The simulation results for the deflection of the sensor's beam at Point A, Point B, and Point C for the following conditions: a) a lump is located on the End-Left section of the beam; and b) a lump is located on the Middle-Left section of the beam. The surrounding background tissue is modeled as ICF material.

2.4 Sensor Fabrication and Experimental Setup

Figure 2-9 demonstrates the configuration of experimental setup. The optical fibers are single-mode with 250 μm coating diameters. The light source (FOSS-01 form OZ Optics, Ottawa, Canada) injects 635 nm light into the fibers. This light source has ± 0.05 dB optical power stability, 9 Volts input power, and 1 mW optical power. The photodetectors are high-speed Si detectors (DET02AFC from Thorlabs, NJ, USA) with the wavelength range of 400 to 1100 nm. Three photodetectors are used to convert the light intensity of Fiber A, Fiber B, and Fiber C to electrical signals at the same time. Using a DAQ (NI PCI-6225), the converted electrical signals are transferred to a computer and are recorded using LabVIEW software. The Bose ElectroForce® device is used to apply different force configurations to the sensor. The reference force applied to the sensor is measured by the force transducer of the ElectroForce device.

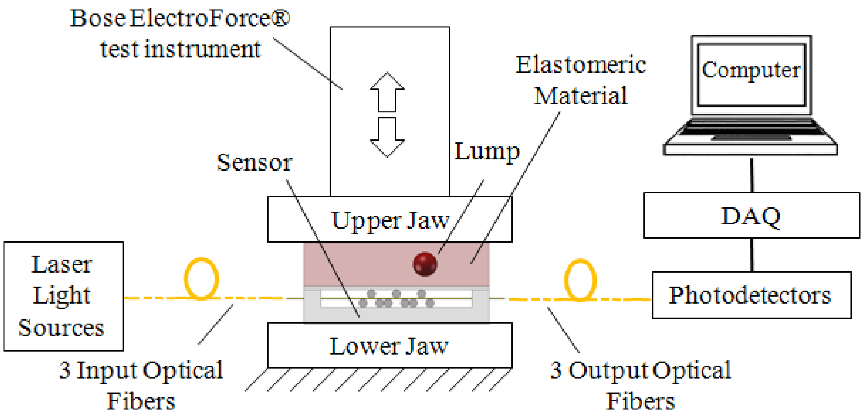

Figure 2-9: The schematic diagram of the experimental setup. The Lower Jaw is fixed whereas the Upper Jaw is movable. The force and displacement applied from the Upper Jaw to the Elastomeric Material is controlled by the Bose ElectroForce test instrument. The Photodetectors convert the light intensity of the fibers into the voltage. The output voltage of photodetectors is recorded on the computer. By analyzing the recorded data, the unknown position of the embedded lump will be identified.

The sensor was made of non-metallic materials to satisfy the design constraints. The lower part and the upper part of the sensor were fabricated separately. Then these two parts were assembled together. Figure 2-10-a demonstrates the lower part and the upper part before the assembly. The lower part consists of the substrate, fixed rods, optical fibers, and half of the supports on each side of the substrate. The substrate was made of a Lexan polycarbonate sheet. The fixed rods were glued to the substrate. The optical fibers are integrated inside the narrow grooves made on the supports. In their initial conditions, fibers are stretched and are glued to the supports. The upper part of the sensor consists of a beam fixed on the other half parts of the supports on each side. The beam was made of

Hi-Impact PolyStyrene material. Three short movable rods were glued to the beam in pre-defined locations. For sensor assembly, the upper part of the sensor was glued on the top of the lower part. Figure 2-10-b demonstrates the assembled structure of the sensor.

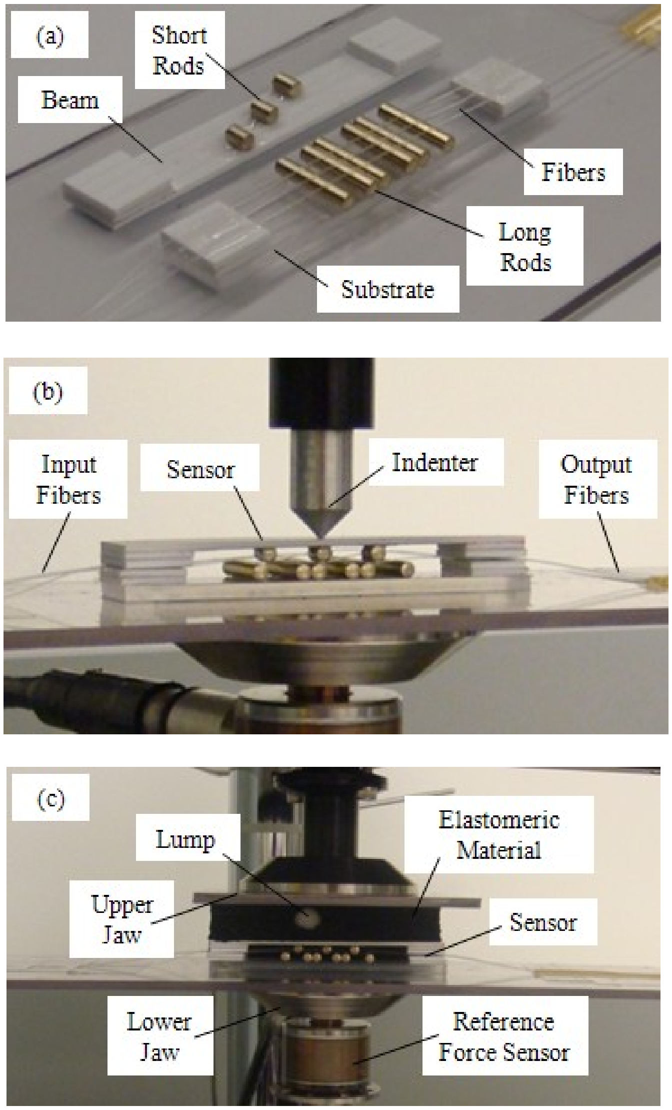

Figure 2-10: The photograph of the fabricated sensor. The beam and substrate of the sensor are made of non-metallic materials. a) the sensor before assembly; b) illustrates the assembled sensor under the test with a concentrated force applied to the beam; and c) illustrates the assembled sensor under compression test to measure the unknown position of a hard spherical lump embedded inside a soft elastomeric material.

The sensor was tested under two different conditions. First, the sensor was tested by applying a concentrated force at different locations. Figure 2-10-b demonstrates the sensor under a test with concentrated force. A conical-shaped aluminum indenter was used to apply concentrated force to the sensor. Second, the sensor was tested under similar conditions as explained in the FE model of the interaction between the sensor and elastomeric materials.

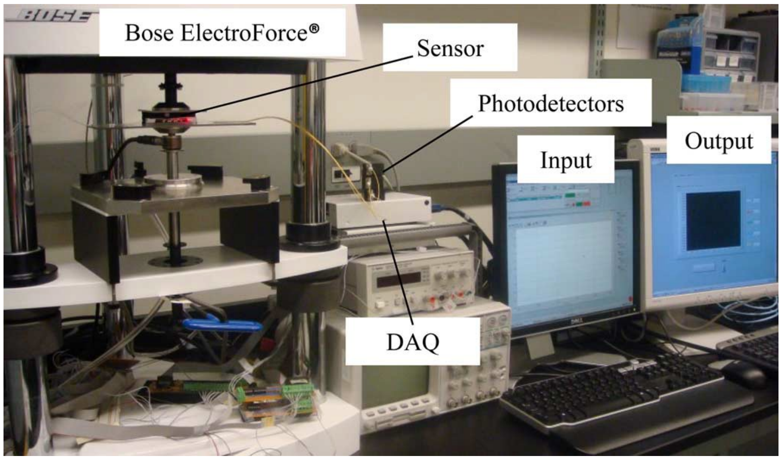

Figure 2-11: The experimental setup to test the sensor. On the one hand, the reference force and displacement applied to the sensor is controlled and is recorded on the Input screen. On the other hand, the response of the sensor to the applied reference force is recorded by the LabVIEW software on the Output screen. Laser light sources are not illustrated in this figure.

As shown in Figure 2-10-c, the sensor was fixed on the Lower Jaw of the ElectroForce device. An elastomeric material (ICF in this case) was sandwiched between the sensor's beam and the Upper Jaw of the ElectroForce device. A rigid spherical lump was embedded inside the elastomeric material. The force applied from the Upper Jaw. This force was measured by the ElectroForce device. Simultaneously, the output of the sensor was measured and was recorded on the computer. Figure 2-11 demonstrates the testing setup. On the one hand, the reference force applied to the sensor was measured on the Input screen. On the other hand, the outputs of the sensor from Fiber A, Fiber B, and Fiber C were recorded on the Output screen. These Input and Output date were compared to characterize the sensor.

2.5 Experimental Test Results

In the first test, a concentrated force, equals to the force used in simulations, is applied at two different points of the sensor. This concentrated force is a step function with the frequency of 0.025 Hz and the amplitude of 3.0 N. Figure 2-12-a and Figure 2-12-b demonstrate the response of the sensor to this concentrated force applied to the End-Left section and to the Middle-Left section of the sensor's beam respectively. In Figure 2-12, the outputs of the sensor are the output voltages of each photodetectors connected to Fiber A, Fiber B, and Fiber C. When the applied force is zero, the initial output voltages for the fibers are equally set in the LabVIEW (13.380 Volts in this case). In Section 2.3.1, it has been shown that the relation between the total bend arc length of the fiber and the resulting power loss of the fiber is linear. In addition, according to the specifications of photodetectors, the difference between the output voltage under loading conditions and the initial output voltage is linearly proportional to the fiber power loss. Therefore, the more total bend arc length in a fiber, the more output voltage difference for the same fiber. In other words, the difference in output voltage for each fiber is linearly proportional to the total bend arc length of the corresponding fiber. Considering this fact, and using the algorithm of Figure 2-5 to compare the outputs of the sensor in Figure 2-12, the position of the concentrated force, which represents the position of a lump, can be identified among the four pre-defined sections on the sensor's beam. The results confirm the capability of the sensor to identify the location of the concentrated force. In addition, during the 20 seconds period of applying the constant force, the drift of the sensor is negligible. Presented results show that the sensor can perform under static loading conditions with negligible amount of drift. In MIS and MIRS, this capability of the sensor helps the surgeons to maintain the stable contact between surgical instruments and biological tissues. For instance, tissue relaxation occurs very slowly. Therefore, during the tissue relaxation, changes in force-displacement data between surgical tools and tissue occur in very small rates which are near to static conditions than dynamic. Such a sensor is required to measure these slow-rate and nearly-static changes to keep a stable contact.

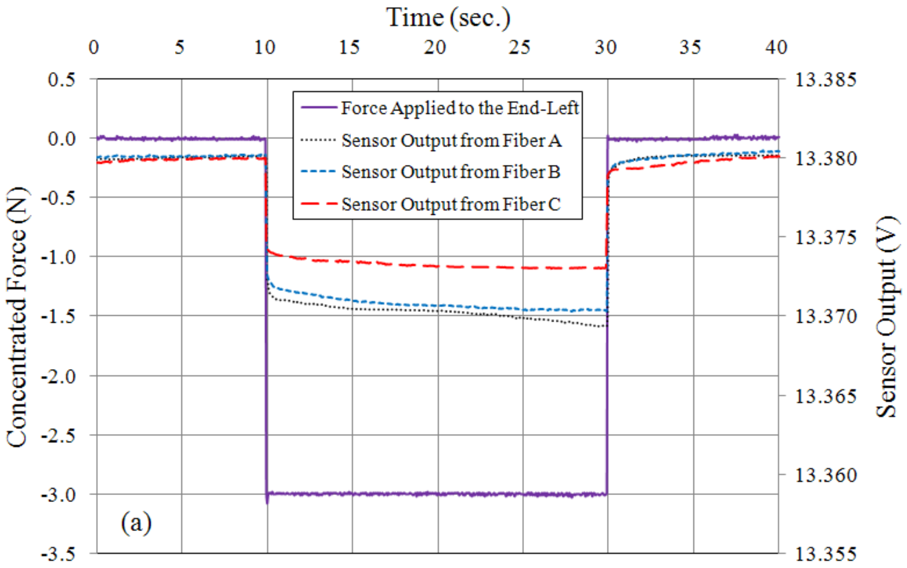

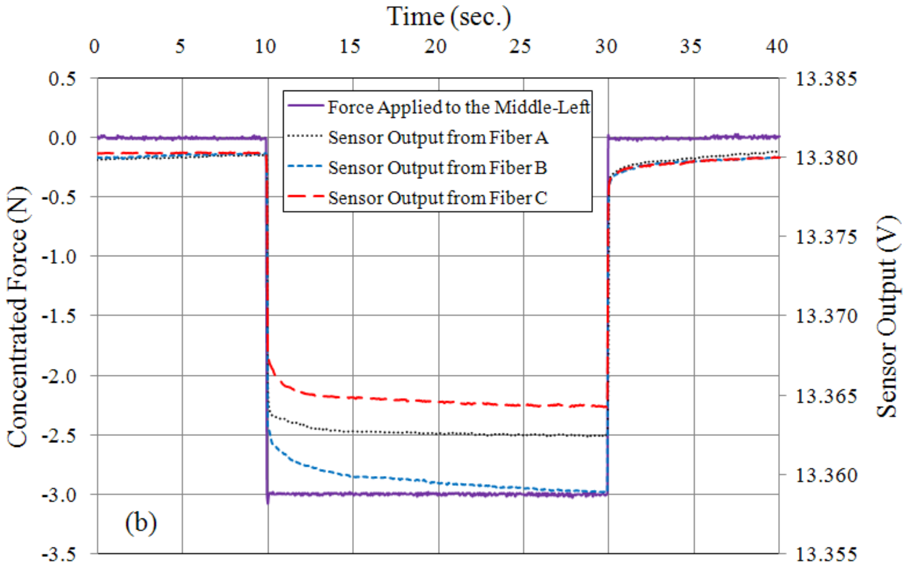

Figure 2-12: The response of the sensor to a concentrated force applied on: a) the End-Left section, and b) the Middle-Left section of the sensor's beam.

In the second test, the interaction between the sensor and the ICF material is considered. A rigid spherical lump is embedded inside the ICF material on the Middle-Left section of sensor's beam. Figure 2-10-c demonstrates the configuration of the setup for this test. In this test, a distributed force function is applied from the Upper Jaw to the system. This force is a step function with the amplitude of 7 N and with the frequency of 0.05 Hz. Figure 2-13 shows the applied reference force as well as the response of the sensor in such testing conditions from Fiber A, Fiber B, and Fiber C. Again, using the proposed algorithm, the position of the lump can be identified. The outputs of the sensor validate the capability of the sensor to identify the location of the lump among the four pre-defined sections of the sensor. As shown in Figure 2-13, during the static period of the test, the output of the sensor is gradually changing mainly because of the time-dependant behavior of the elastomeric material. In the meantime, the creep behavior of the bended optical fibers also affects the output. However, results confirm that the position of the embedded lump can accurately be located during this period. In the all of the experimental tests, the sensor is tested when the location of the concentrated force and the embedded lump are in the left-half part of the sensor's beam. Based on the results for the left-half part, the sensor's outputs are predictable for right-half part because of the symmetry of the sensor's structure.

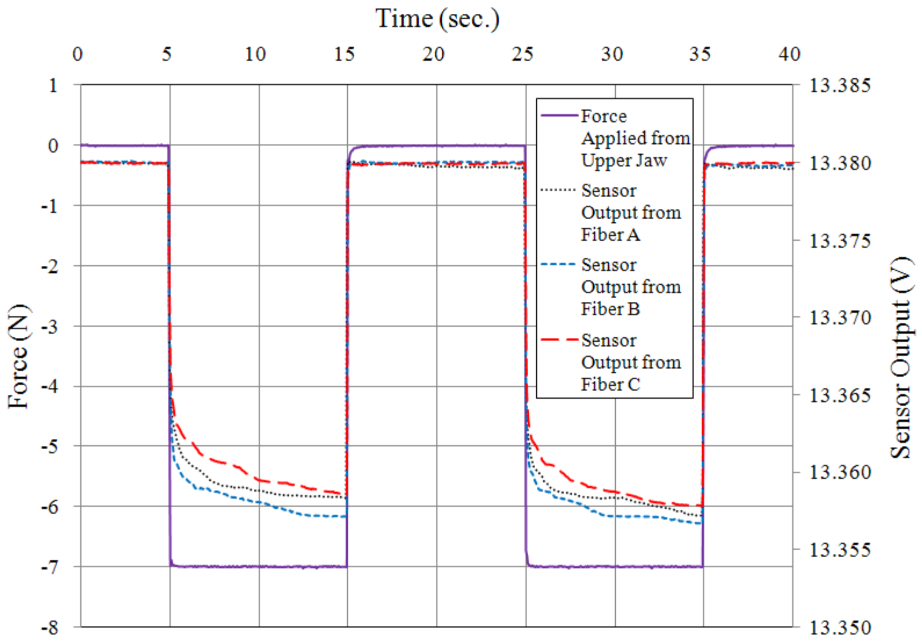

Figure 2-13: The output of the sensor under the test with ICF material with an embedded lump on the Middle-Left section of sensor's beam. The force applies from the upper jaw of the test instrument.

In order to analyze the linearity of the output of the sensor, eight different discrete concentrated forces, between 0.5 N to 4.0 N were applied to the center of the beam. The range of interacting forces between surgical tools and tissues are reported in different studies [29, 77]. Based on these studies, the range of testing force is chosen for this experiment. For each amount of these contact forces, the output of the sensor was recorded. These measurements were performed for the number of 20 tests for each force.

Figure 2-14 represents the statistical descriptor of sensor outputs under these tests. Figure 2-14-a and Figure 2-14-b demonstrate the box plot and the average of the output of the sensor from Fiber B respectively. As shown in the box plot, for forces less than 2.0 N, the inter-quartile ranges are generally smaller than the ones for larger forces. This indicates the better repeatability of the sensor for input forces less than 2.0 N, although the repeatability is in quite similar range for all force intervals. In addition, it is observed that the error of the sensor will increase by increasing the amount of contact force.

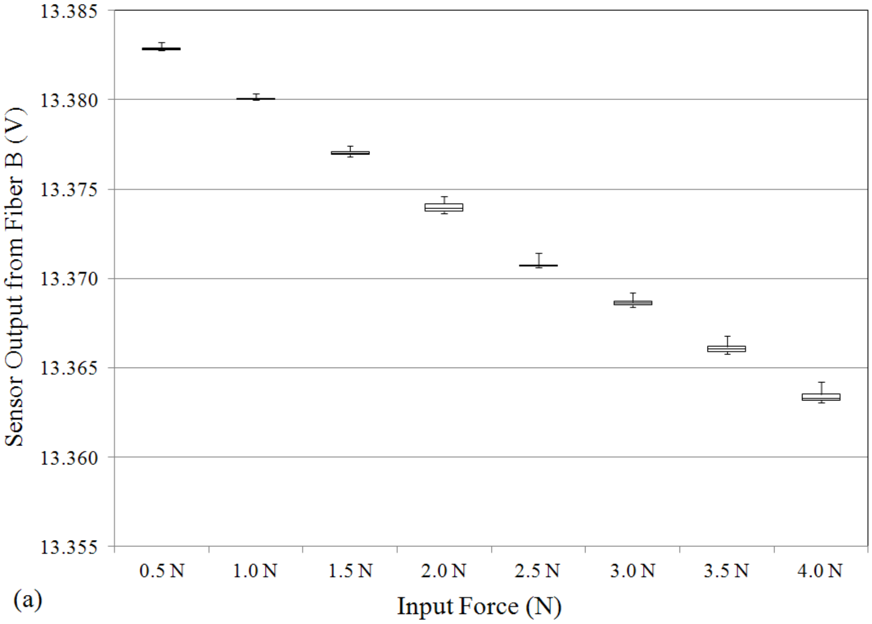

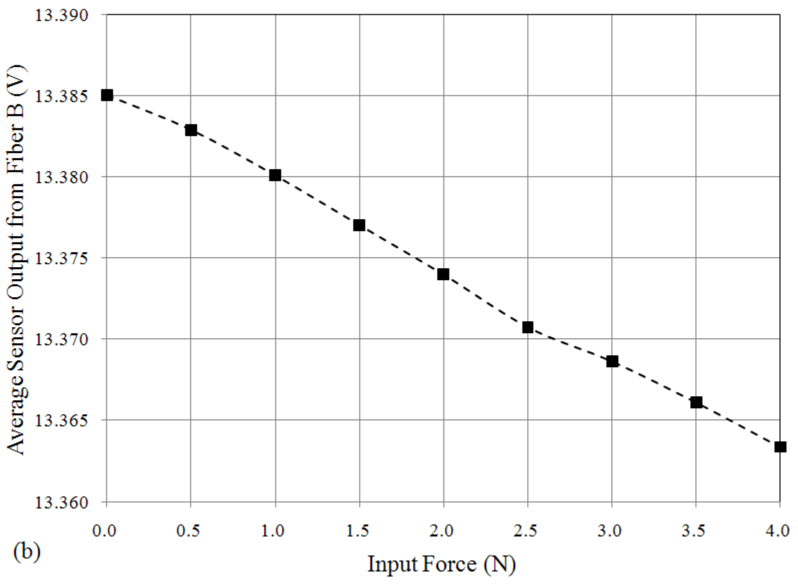

Figure 2-14: (a) The statistical descriptor of sensor outputs with respect to a reference concentrated force applied to the center point of sensor's beam for the numbers of 20 measurements are represented in a boxplot. (b) The average of sensor output with respect to the applied reference concentrated force to the middle of sensor's beam for the number of 20 measurements.

2.6 Conclusions

In conclusion, the feasibility and the performance of an innovative beam-type optical fiber tactile sensor for use in MIS and MIRS were investigated in the present chapter. The novelty of the proposed sensor lies in its measuring the discrete force distribution by using only one single moving part, which is a beam. Thanks to this novel design, the sensor can be fitted into narrow spaces available at the tips of surgical tools. The results from experimental tests demonstrate the capability of the sensor to measure discrete tactile information. It was demonstrated that this information can be utilized to locate a hard lump embedded in soft elastomeric materials. Based on this feasibility study of such materials, the conclusion is that the sensor is capable of identifying tissue abnormalities in real MIS operations and also in real MIRS operations. In addition, the test results verified the capability of the sensor to perform under both static and dynamic loading conditions. This capability allows surgeons to avoid damaging tissue and also to maintain a stable contact between surgical tools and tissues while tissue relaxations occur during tissue manipulations. Moreover, the sensor is MRI-compatible and electrically-passive. In various MIS and MIRS procedures, these two features are essential for the performance of safe operations.

The fabricated sensor measures 45 mm in length, 8 mm in width and 8 mm in height. The sensor is made of ultrasound-friendly and MRI-compatible materials. Further miniaturization of the sensor is needed. This will be accomplished by using MEMS technology. This study has already confirmed the feasibility of such a sensor, which can be used in MIS and MIRS. In fact, the beam-type structure of the sensor will facilitate its MEMS miniaturization, which will render the sensor even more useful. To achieve this micro-fabrication, one could, for instance, use the biocompatible polymer, SU-8. The experimental tests have demonstrated that the output of the sensor is linear for the forces in the range of 0 to 4 N. The present study proved that this novel single-beam design can experimentally locate a lump relative to the four pre-defined sections on the beam of the sensor. In addition, according to the results of the theoretical modeling of the sensor, it is possible to locate the lump even more precisely within each pre-defined section. However, by contrast with the results of this sensor modeled in simulation, the results from the test showed that the fabricated sensor cannot in fact measure the position of the lump within each section of the beam. Fortunately, this inadequacy of the fabricated sensor can be solved by creating an even smaller and more accurate sensor fabricated by using MEMS technology. Moreover, as a future improvement in this miniaturized MEMS sensor, micro-mirrors could be utilized to reflect the output light of the sensor back into the output optical fibers, which would be oriented in the same direction as the input optical fibers. This configuration would allow the sensor to be integrated more easily into the tip of surgical tools such as graspers since the entrance point of the input fibers and the exit point of the output fibers would be located at only one end of the sensor. Furthermore, a graphical interface could be utilized to give the surgeons a visual rendering of the mapped locations of any tissue abnormalities.

The proposed sensor is intended to be miniaturized enough so that it can be integrated into the MIS or MIRS graspers. After comparing the size of such graspers with the size of real tumorous lumps, it was concluded that only one lump could potentially be located on the top of the sensor. The beam of the proposed sensor has only three measurement points. It was demonstrated that these three measurement points are adequate to measure the discrete force distribution on the sensor's beam, thereby resulting in the identification of the position of a potential lump. However, the resolution of the sensor to characterize such discrete force distribution can be increased by adding more measurement points to the sensor's beam. In addition, the range and the sensitivity of the sensor in various surgical uses can be easily fine-tuned by changing the size and/or the material of the sensor beam.

Chapter 3: Catheter-Tip Tactile Sensing for Catheter-Based Techniques

Mitral valve regurgitation (MR) is one of the common heart valve diseases. It can be fixed by surgical mitral valve repair. Currently, this type of surgery is performed using open heart bypass methods. If it would be performed using catheter-based techniques (CBT), it would offer both patients and surgeons many advantages. To perform it via CBT, it is necessary to include, on the tip of a catheter, tactile sensors that measure the relative hardness of contact tissues. The present chapter discusses the design, modeling, and fabrication of a novel hybrid (Piezoresistive-Optical Fiber) catheter-tip tactile sensor that differentiates between the hardness of different kinds of elastomeric materials. In addition, finite element models of elastomeric materials, contacted at the tip of the catheter, were developed to verify the output of the sensor. Similarly, the experimental results confirm the relative hardness measurement of contact elastomeric materials.

3.1 Introduction

Mitral valve regurgitation (MR) is a condition in which the mitral valve of the heart does not close completely, thereby reducing the performance of the heart. Surgical mitral valve repair is the treatment of choice for this condition [78]. In this surgery, at the site of the operation, there are different types of tissues. If this surgery is performed via catheter-based techniques (CBT), it is necessary to measure the relative hardness of these different tissues by using catheters although the surgeons also use the conventional imaging techniques. Hence, it is required to integrate tactile sensors at the tip of a catheter†. Most such sensors can measure only the contact force, and not the relative hardness of the contact tissues. For instance, recently, an optical contact force has been developed to measure the contact force between the catheter and the heart tissue [33]. This recently developed sensor was incorporated into the distal part of a commercially available ablation catheter. By using three optical fibers, this sensor measures micro-deformation of the catheter tip. In addition, in 2009, Howe et al. [23] developed a force sensor to accurately measure the contact forces for force stabilization during beating heart intracardiac surgery. Moreover, Althoefer et al. [79] have proposed a fiber optic catheter-tip sensor to measure the contact forces between blood vessel walls and the catheter tip.

By contrast, the proposed tactile sensor offers contact force measurement as well as the relative hardness measurement, which is required for mitral valve repair via CBT. Although two different optical fiber tactile sensors recently have been proposed by Althoefer et al. [80, 81], they use different methodologies compared to the proposed sensor in the present work.

In the present work, a novel hybrid catheter-tip tactile sensor is designed, modeled, fabricated and tested. The proposed sensor not only measures the contact forces, but also measures the relative hardness of different soft objects. Using finite element analysis, the

---

† Private communication with a noted cardiovascular surgeon:
Dr. Renzo Cecere, MD, FRCSC
Staff Surgeon, The Royal Victoria Hospital
Staff Surgeon, The Montreal Children's Hospital
Assistant Professor of Surgery, McGill University
The Royal Victoria Hospital
687 Pine Ave. West, Suite S8-44
Montreal, Quebec H3G 1A1, Canada
Office: (514) 842-1231 ext. 3
Fax: (514) 843-1602
E-mail: renzo.cecere@muhc.mcgill.ca

tool-tissue interaction between the catheter tip and different elastomeric materials is modeled and is simulated. In addition, the sensor was fabricated and the experimental tests were performed with different elastomeric samples. Finally, simulation results were compared with the experimental results.

3.2 Design of the Sensor

In Figure 3-1, the design of the proposed innovative hybrid sensor at the tip of a catheter is clearly illustrated. An optical fiber is integrated into the tubular feature of the catheter. A cap with a flexible diaphragm at the end is located at the tip of the catheter. The inner surface of the flexible diaphragm is reflective. In addition a ring of thin piezoresistive film is integrated close to the end of the catheter. The sensing principle to measure the relative hardness of contact soft objects relies on, simultaneously, measuring the contact force applied from the tip of catheter to such objects as well as measuring the resulted objects deformation. In fact, the deformation of contact objects is obtained by measuring the small deflection of the flexible diaphragm resulted by the contact. On the other hand, the contact force is measured by the integrated piezoresistive film. With such a hybrid measurement, force-deformation data for the contact object is obtained. The obtained force-deformation data is used to measure the relative hardness of the contact soft objects. For instance, for the same amount of contact force measured by the piezoresistive film, the more deflection of the diaphragm is, the softer the contact object is.

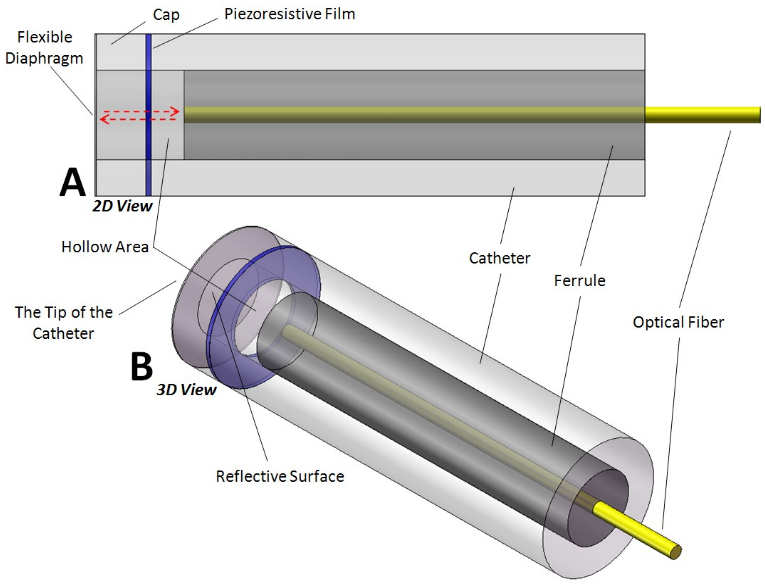

Figure 3-1: The schematic representation of the proposed concept to measure the relative hardness of the contact tissues at the tip of the catheter: (A) 2D View; (B) 3D View.

Figure 3-2 illustrates the schematic diagram of the proposed setup. A cap with the flexible diaphragm is attached at the tip of the catheter. Therefore, a small gap is provided between the bare end of the optical fiber and the reflective surface of the flexible diaphragm. The bare end of the optical fiber is flat-cleaved. The other end of the optical fiber is coupled to one of the ports of a fiber optic circulator. In addition, as illustrated in Figure 3-2, a laser light source and a photodetector are coupled to the other ports of the circulator. The reflected light from the reflective surface of the diaphragm is coupled back to the optical fiber. This reflected light is directed through the circulator to the photodetector. With this configuration, the deflection of the diaphragm, resulted by a soft contact object, modifies the intensity of the reflected light detected by the photodetector through the optical fibers. The photodetector converts the reflected light intensity to the voltage. Using LabVIEW software, the output voltage of the photodetector is recorded by a computer. Nilsson et al.

[82] have proposed a similar concept to develop a displacement sensor. In the meantime, the contact force is measured by the integrated piezoresistive film.

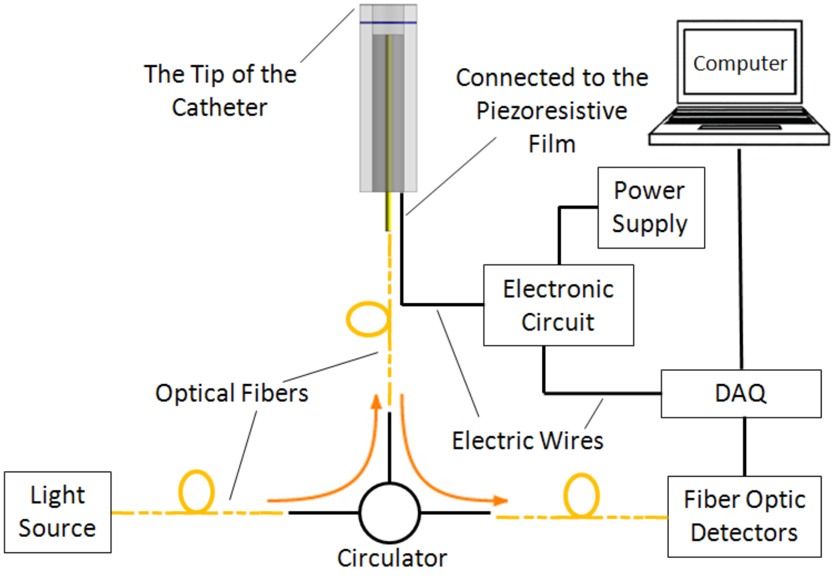

Figure 3-2: The schematic diagram of the experimental setup. Different elastomeric materials were contacted at the tip of the catheter for the relative hardness measurement.

The integrated piezoresistive film acts as a force sensor. The ring of piezoresistive film is sandwiched between the cap and the catheter. In the proposed design, the piezoresistive force sensor is attractive because it has a thin layer, which makes it suitable for integrating into the tiny space available at the tip of catheter. In addition, it has a quick response with a linear output in the required range. The integrated force sensor consists of a pair of input and output ports, which are electrically connected to the computer via a buffer electric circuit (Figure 3-2). The wiring of the integrated force sensor is guided through the inner part of the catheter to the circuit. The sensor is fed by an external DC power supply. Using LabVIEW software, the output voltage of the force sensor, which represents the contact force, is recorded by the computer and is compared by the recorded output voltage of the photodetector. Hence, by comparing the output of force sensor and the output of photodetector, the contact force and the resulting deformation of soft contact objects at the tip of the catheter can be measured simultaneously. This hybrid measurement results in relative hardness measurement of the contact object.

3.3 Modeling the Interaction between the Sensor and the Soft Object

Using COMSOL Multiphysics software, the finite element (FE) model of the interaction between the tip of the catheter and soft objects is developed. The soft objects can be modeled according to their elasticity and compressibility, based on different modeling methods such as: linear elastic material, nonlinear hyperelastic material, or viscoelastic material [83]. In the present work, the soft objects are assumed to be a hyperelastic material. Hyperelastic material refers to materials with large strain, in which stress component equals to the derivative of the strain energy function (*W*). The strain energy function is a scalar function of deformation tensors, or the strain component [75]. It defines the relation between the strain energy density of the hyperelastic material and its deformation gradient. The stress component is defined by the Piola-Kirchhoff stress tensor [76]:

$$\mathbf{S} = \frac{\partial W(\mathbf{F})}{\partial \mathbf{F}} \tag{3.1}$$

In isotropic materials, the strain energy function can only be a function of the strain invariants. One of the popular models to model a hyperelastic materials is the Mooney-Rivlin model (COMSOL Software user's guide). The following equation shows the 2-parameters strain energy function defined by the Mooney-Rivlin model:

$$W = C_{10}(I_1 - 3) + C_{01}(I_2 - 3) + \frac{1}{2}\kappa(I_3 - 1)^2 \tag{3.2}$$

in which, C_{10} and C_{01} are Mooney-Rivlin constants, κ is the bulk modulus of the material, and I_1, I_2, I_3 are three invariants of the Right Cauchy-Green Deformation tensors which are defined as follow:

$$I_1 = \lambda_1^2 + \lambda_2^2 + \lambda_3^2 \tag{3.3}$$

$$I_2 = (\lambda_1\lambda_2)^2 + (\lambda_2\lambda_3)^2 + (\lambda_1\lambda_3)^2 \tag{3.4}$$

$$I_3 = (\lambda_1\lambda_2\lambda_3)^2 \tag{3.5}$$

where $\lambda_1, \lambda_2, \lambda_3$ are principal stretches.

Using an Electroforce 3200 device from Bose Company, stress-strain data in compression tests is obtained for three elastomeric samples. These samples, which are different in terms of their hardness, are named as ICF-400, A2-3/4, and EVA-1/2. Based on the obtained stress-strain data in the experiments, the curve-fitting techniques in MATLAB is used to calculate the Mooney-Rivlin parameters for these elastomeric samples. The calculated parameters were used in the developed model to simulate the soft objects with different mechanical properties.

As illustrated in Figure 3-3, the soft object is fixed from the top part. The tip of the catheter contacts the soft object. Similar to the real surgery conditions, a distributed force applies from the bottom part of the catheter. As a result, the tip of the catheter deforms the soft object. The interaction force between the tip of catheter and the soft object results in the deflection of the flexible diaphragm located at the tip of catheter.

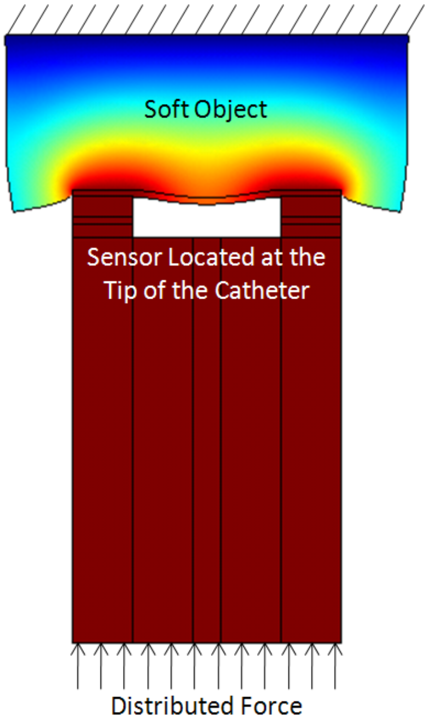

Figure 3-3: The simulated interaction between the tip of catheter and a hyperelastic object. A distributed force applies from the bottom of the catheter results in large deformation in the object. In addition, the interact force between the catheter tip and the object results in the deformation of the flexible diaphragm at the tip.

In the simulation, the same distributed force is applied to the bottom of catheter for two different cases: case 1 with a soft object (i.e. A2-3/4), and case 2 with a softer object (i.e. ICF-400). The resulting measured contact force by the integrated piezoresistive films will be the same for both case 1 and case 2 since the applied force to the catheter is the same in both cases. However, simulation results confirm that with the same amount of contact force in both cases, the resulting deflection of the center of diaphragm for case 1 is less than that deflection for case 2. In other words, for the same amount of contact force, the more the detected deflection of the flexible diaphragm is, the softer the contact object is. Hence, by a simple comparison, relative hardness of contact objects can be measures. However, the absolute hardness measurement of samples by the proposed sensor requires a specific calibration of the sensor. In fact, for mitral valve repair surgery, only relative hardness measurement will be enough and there is no need for absolute hardness measurement for such application.

3.4 Fabrication and Experimental Results

Finite element modeling (FEM) results verify that the correlation between the contact force measurement and the diaphragm deflection measurement results in relative hardness measurement. In order to compare the FEM results with the experimental results, a prototype of the sensor is fabricated. Figure 3-4 shows the photograph of the fabricated catheter-tip sensor. As illustrated in this figure, a cap is located at the tip of a phantom catheter. A thin ring of piezoresistive force sensor is sandwiched between the cap and the rest of the catheter close to the tip. The wiring of the force sensor is guided from the inner part of the catheter to the electric circuit. An optical fiber with a flat bare end is integrated at the middle part of the catheter. A flexible diaphragm is attached at the tip of the cap. The inner surface of the cap has a reflective surface. The diaphragm is made of Hi-Impact PolyStyrene with 3000 MPa Young's modulus. Inside the cap, a small gap is provided between the bare end of optical fiber and the reflective surface of the diaphragm.

Using the fabricated sensor, the relative hardness of sample elastomeric materials were measured. Table 3-1 compares the results obtained by the sensor with a standard method of hardness measurement by a durometer on the same samples. In addition, in the table, the FEM results are compared with both durometer results and the experimental results. This comparison verifies the capability of the proposed tactile sensor to measure the relative hardness of soft objects. This capability allows surgeons to localize different heart tissues at the site of operation.

The fabricated catheter in the present work has a 30 Fr. diameter. Compared with smaller commercially available catheters, the fabricated catheter-tip sensor has relatively larger dimensions. However, it is fabricated only to prove the proposed concept for relative hardness measuring. Using micro-machining techniques, the sensor has a potential to be miniaturized and to be integrated into the tiny space available at the tip of current commercial catheters.

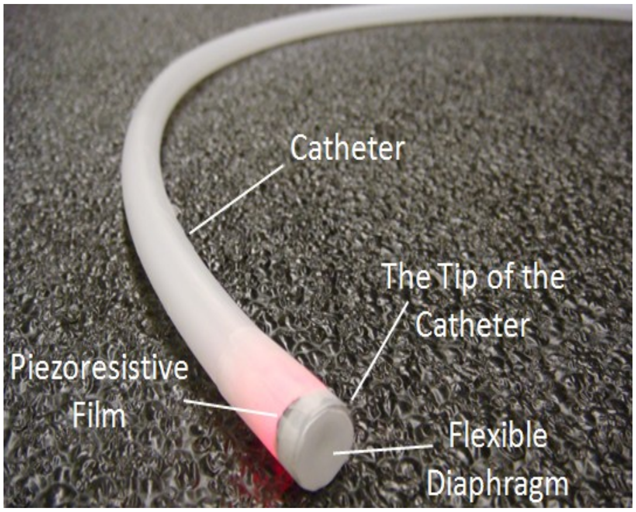

Figure 3-4: The photograph of the tactile sensor integrated at the tip of a phantom catheter.

Table 3-1: Comparison between the output of the hybrid sensor, the output of the durometer, and the simulation results by the Comsol Multiphysics software

Name of the Elastomeric Materials	**ICF-400**	**A2-3/4**	**EVA-1/2**
Results obtained by the durometer	***Softer***	***Soft***	***Harder***
Results obtained by the simulation	***Softer***	***Soft***	***Harder***
Results obtained by the tactile sensor at the tip of the catheter	***Softer***	***Soft***	***Harder***

3.5 Discussion

Mitral valve regurgitation (MR) is a common heart valve disease. MR results in chronic volume overload on the left ventricle, with a reduction in cardiac function. Surgical mitral valve repair is often the treatment of choice for such patients. Currently, mitral valve repair is performed using open heart surgical methods in which surgeons use direct palpation to assess the different types of tissues available at the site of operation. However, unlike surgeon's fingertips, catheters do not provide surgeons with any tactile perception. Consequently, providing surgeons with a tactile feedback from the interaction between catheter-tips and tissues, although the surgeons also use the conventional imaging techniques, would help surgeons to perform such surgery via catheter-based techniques (CBT). In fact, CBT would offer numerous advantages for both patients and surgeons.

To provide such tactile feedback, it is necessary to integrate tactile sensors at the tip of catheters. In the present study, an innovative hybrid catheter-tip tactile sensor is proposed for use in CBT. The proposed sensor is modeled, simulated, fabricated and tested. Using finite element method, the tool-tissue interaction between the catheter-tip sensor and the soft objects is modeled.

The sensor not only measures the contact forces, but also measures the relative hardness/softness of biological tissues. The experimental results confirm the ability of the sensor to distinguish between three different soft elastomeric materials, named as ICF-400, A2, and EVA. Among these three materials, ICF-400 is the softer one, which resembles the leaflet tissue; EVA is the harder one, which resembles the annulus tissue; and ICF-400 with medium softness resembles the atrium tissue. The sensor consists of an optical-fiber and a piezoresistive-film integrated into a catheter. The optical-fiber measures the tissue deformation while at the same time the piezoresistive-film measures the contact force. By comparing these measurements, the relative softness of the contact tissue can be obtained. These three different soft materials represent the left atrium, mitral valve annulus and mitral valve leaflet available at the site of a MR-treatment operation.

3.6 Conclusions

In brief, mitral valve regurgitation (MR), which is one of the common heart valve diseases, can be treated by surgical mitral valve repair. In order to perform such treatment via catheter-based techniques (CBT), tactile sensors with relative hardness measuring capabilities must be integrated into the tip of catheters. In the present chapter, based on a novel concept, a hybrid (Piezoresistive-Optical Fiber) catheter-tip tactile sensor is designed, modeled, and fabricated. Finite element models of three different elastomeric materials, contacted at the tip of the catheter, were developed. Simulation results were compared with the experimental results. This comparison proves the capability of the proposed sensor for relative hardness measuring of soft elastomeric materials. Based on the required hardness measuring range and sensitivity, the sensor can be tuned for particular use in catheter-based cardiac surgeries. However, using micro electro mechanical system (MEMS) technology, the sensor would be capable of being miniaturized and integrated into commercially available catheters. For future work, the sensor will be miniaturized and calibrated with respect to the required force and hardness range, and resolution for surgical applications. In short, the sensor in this work was designed based on an idea proposed in a patented instrument[‡].

[‡] R. Cecere, and T. Azar, *Instrument including a movement sensor and method of using same*, U. S. Patent US 2011/0160596 A1, Filing date: Dec 17, 2010.

Chapter 4: Modeling and Parametric Study of Sensor-tissue Interaction for Minimally Invasive Surgical Tasks

In minimally invasive surgical tasks, tactile sensors that are integrated into the tips of surgical tools measure the information of tool-tissue interaction. Based on this information, surgeons can investigate hidden tissue structures in the same way they use palpation techniques in conventional surgical operations. In order to investigate the performance of the tactile sensors, the tool-tissue interaction should be modeled under conditions similar to real surgical conditions. The present chapter investigates the effects of important parameters on the tool-tissue interaction. Being similar to practical conditions, the list of such parameters includes the size, the location, and the mechanical properties of lumps or blood vessels surrounded by background tissues with different mechanical properties. To carry out this investigation, the finite element model of the interaction between a typical beam-type tactile sensor and biological tissues was developed. The simulation results are useful for the development of an inverse model of the sensor-tissue interactions. Based on this inverse model, fundamental information such as the size, depth, location, and mechanical properties of any hidden lump, blood vessel, or ureter can be extracted.

4.1 Introduction

During conventional surgical tasks, surgeons use their direct tactile perceptions via their fingertips to investigate tissues. However, in minimally invasive surgical (MIS) tasks, surgeons' tactile perceptions are restricted to indirect access to tissues via surgical instruments. To compensate for the lack of such perception, it is necessary to put a tactile sensor between the surgical instruments and the tissues. Such a tactile sensor should mimic the fingertip tactile perceptions of surgeons during the sensor-tissue interaction.

In the present thesis, various tactile sensors are proposed. Although the proposed sensors are different from each other in terms of design, sensing principle, and performance, they all have one common characteristic. This common characteristic is that they have a beam-type structure. In fact, in each of the proposed sensors, the sensor-tissue interactions result in the deflection of the sensor beams. In surgical applications, the important parameters that should be measured are tissue properties such as tissue hardness, size, location, and hardness of any abnormal tissue (e.g. cancerous lumps) located inside the background tissue. In all of the proposed sensors, these important parameters affect the sensor beam deflection. In the next step, the resulting beam deflections or slopes are measured by using the sensing elements of the proposed sensors. Consequently, the effects of the parameters on the sensor beam deflection are of great importance.

The present chapter provides a parametric study of the effects of important parameters on the sensor beam deflection. To do so, a finite element (FE) model of the interaction between a beam-type sensor and tissue was developed. The effects of the important parameters on the sensor beam deflection were investigated. It was assumed that the size of the modeled sensor beam equals the size of the sensor beam presented in Chapter 9. However, the simulation results can also be useful for the sensors presented in the other chapters since all these sensors consist of a beam-type structure with fixed-fixed boundary conditions.

4.2 Tissue Modeling: Hyperelastic Theory under Uni-axial Compression

In the present research, the theory of elasticity is used to model the behavior of tissues while they are interacting with surgical tools. Basically, an object has elastic behavior when the following two conditions are applicable: first, the stress in the object must be a unique function of the strain and, secondly, the deformed object must exhibit the property of complete recovery to its initial shape upon the removal of the applied forces. If these two conditions are not satisfied, the material is inelastic. The elastic behavior of a material may be linear or non-linear during the loading and unloading paths.

Technically, biological tissues are soft materials that undergo large deformations and exhibit non-linear and time-dependent behavior. In the present thesis, artificial tissues made of silicone rubber materials were used to represent real biological tissues during the experimental tests. During the tests, it was observed that the viscoelastic behavior of the artificial tissues has a negligible effect on the sensor-tissue interaction. Consequently, the time-dependent behavior of the tissue was not considered in the modeling. Moreover, it was observed that these artificial tissues undergo large and nearly incompressible deformation. As a result, they were modeled as isotropic, nearly incompressible hyperelastic materials. To do so, the theoretical consideration for such hyperelastic material is summarized in this work. The background theory for the stress-strain behavior of hyperelastic materials is explained in [75, 84, 85]. For a hyperelastic material, the second Piola-Kirchhoff stress tensor is defined by the derivative of a strain energy function to strain components. In a reference configuration, the stress component of the material as a result of applied strain is obtained as

$$\mathbf{S} = 2\frac{\partial W(\varepsilon)}{\partial \mathbf{B}} \tag{4.1}$$

where W and $\mathbf{B}$ are the strain energy function and the right Cauchy-Green deformation tensor respectively. In fact, the strain energy function is an isotropic function of the strain in the form of I_1, I_2, and I_3 that are the deformation tensor invariants

$$W = W(I_1, I_2, I_3) \tag{4.2}$$

Moreover, the second Piola-Kirchhoff stress tensor, $\mathbf{S}$, is related to Cauchy stress tensor, $\boldsymbol{\sigma}$, by the following equation

$$\mathbf{S} = J\mathbf{F}^{-1} \cdot \boldsymbol{\sigma} \cdot \mathbf{F}^{-\mathrm{T}} \tag{4.3}$$

where

$$J = \det \mathbf{F} \tag{4.4}$$

in which $\mathbf{F}$ is the deformation gradient tensor. Basically, the right Cauchy-Green deformation tensor can be expressed with the deformation gradient as

$$\mathbf{B} = \mathbf{F}^{\mathrm{T}} \cdot \mathbf{F} \tag{4.5}$$

Thus, using mathematical manipulation, the elements of Cauchy (true) stress can be described as

$$\sigma_{ij} = -p\delta_{ij} + 2\frac{\partial W\left(\varepsilon_{ij}\right)}{\partial I_1} B_{ij} - 2\frac{\partial W\left(\varepsilon_{ij}\right)}{\partial I_2} B_{ij}^{-1} \tag{4.6}$$

where p is the hydrostatic pressure, δ_{ij} is the kronecker delta, I_1, I_2, (and I_3) are invariants of the right Cauchy-Green deformation tensor, and B_{ij} is the component of the right Cauchy-Green deformation tensor. In the conditions applied to the performed tests of this work, the hydrostatic pressure is zero. The three invariants of the right Cauchy-Green deformation tensor are expressed as

$$I_1 = \lambda_1^2 + \lambda_2^2 + \lambda_3^2 = \mathrm{tr}(\mathbf{B}) \tag{4.7}$$

$$I_2 = (\lambda_1\lambda_2)^2 + (\lambda_2\lambda_3)^2 + (\lambda_1\lambda_3)^2 = \frac{1}{2}\left[I_1^2 - \mathrm{tr}(\mathbf{B}^2)\right] \tag{4.8}$$

$$I_3 = (\lambda_1\lambda_2\lambda_3)^2 = \det\left(\mathbf{B}\right) \tag{4.9}$$

where λ_1, λ_2, and λ_3 are the principal stretches that are defined by

$$\lambda_i = 1 + \varepsilon_i \tag{4.10}$$

For incompressible materials, the third deformation invariant is expressed as

$$I_3 = (\lambda_1\lambda_2\lambda_3)^2 = 1 \tag{4.11}$$

In the proposed work, the Mooney-Rivlin (M-R) formulation is used to express the energy function [86]. In such formulation, the strain energy function, *W*, is expressed as a general polynomial in terms of I_1 and I_2 as

$$W(I_1, I_2) = \sum_{i=0}^{\infty}\sum_{j=0}^{\infty} c_{ij}(I_1 - 3)^i (I_2 - 3)^j \tag{4.12}$$

where c_{ij} are M-R constants that depend on the properties of the material. Basically, these constants are obtained by applying curve-fitting methods on the stress-strain data of the material. Therefore, they do not convey any physical meaning. Technically, in a stress free condition, the strain energy function equals zero. Thus, considering $i = 0$ and $\mathrm{j} = 0$ will cause the c_{00} constant to be equal to zero too. In this thesis, the artificial tissues were initially modeled by using M-R formulation with two constants. In this regard, $i = 0, j = 1$ and $i = 1, j = 0$ are set in Equation 4.12 to obtain the two terms M-R energy function as

$$W(I_1, I_2) = c_{10}\left(I_1 - 3\right) + c_{01}(I_2 - 3) \tag{4.13}$$

For this equation, c_{10} and c_{01} can be extracted from the material's stress-strain date. To obtain the stress-strain data of the artificial tissues, uni-axial compression tests were conducted on the tissues. By applying a curve-fitting method [76], the M-R constants were extracted for the tested tissues.

Due to the incompressible material properties of the tested artificial tissues, their behaviors under uni-axial compression and equibiaxial tension are identical. In other words, for an incompressible hyperelastic material, the material deformation does not vary in the presence of a tensile or compressive hydrostatic stress [87, 88]. As a result, for a tissue with an isotropic material property under an unconstrained compression test, the applied stretches are expressed as

$$\lambda_1 = \lambda_2 = \lambda^{-1/2} \tag{4.14}$$

$$\lambda_3 = \lambda \tag{4.15}$$

Consequently, the deformation gradient, and the right Cauchy-Green deformation tensor are described as

$$[\mathbf{F}]=\begin{bmatrix}\lambda^{-1/2} & 0 & 0\\ 0 & \lambda^{-1/2} & 0\\ 0 & 0 & \lambda\end{bmatrix}\Rightarrow[\mathbf{B}]=[\mathbf{F}]^{\mathrm{T}}\bullet[\mathbf{F}]=\begin{bmatrix}\lambda^{-1} & 0 & 0\\ 0 & \lambda^{-1} & 0\\ 0 & 0 & \lambda^{2}\end{bmatrix} \tag{4.16}$$

Accordingly, the deformation invariants are derived as

$$I_1 = \lambda^2 + 2\lambda^{-1} \tag{4.17}$$

$$I_2 = 2\,\lambda + \lambda^{-2} \tag{4.18}$$

$$I_3 = 1 \tag{4.19}$$

Hence, according to Equation 4.6, the principal stresses of the material are obtained as

$$\sigma_{33} = -p + 2\left(\frac{\partial W(\varepsilon_{ij})}{\partial I_1}\right)\lambda^2 - 2\left(\frac{\partial W(\varepsilon_{ij})}{\partial I_2}\right)\lambda^{-2} = 2\left(\lambda^2 - \lambda^{-1}\right)(c_{10} + c_{01}\lambda^{-1}) \tag{4.20}$$

$$\sigma_{11} = \sigma_{22} = -p + 2\left(\frac{\partial W(\varepsilon_{ij})}{\partial I_1}\right)\lambda^{-1} - 2\left(\frac{\partial W(\varepsilon_{ij})}{\partial I_2}\right)\lambda = 0 \tag{4.21}$$

In fact, σ_{33} is the principal stress on the uni-axial direction of the compression test performed on the artificial tissues.

Although M-R formulation was used to obtain the hyperelastic material constants of the tested artificial tissues, a different formulation (Neo-Hookean) [75, 89] was used to model them using the finite element method. In other words, Neo-Hookean (N-H) formulation was chosen to describe the strain energy function for the tissue domain in COMSOL. To do so, the tissue in the N-H model is described as a nearly incompressible material instead of a totally incompressible material. Hence, the modeled tissue can undergo larger deformations in COMSOL. This is why the N-H model was used in the finite element analysis. In general, the N-H model is widely acceptable for modeling silicone rubber materials as well as biological tissues. As mentioned before, the tested artificial tissues are assumed as isotropic and nearly-incompressible materials. Based on the N-H model, the strain energy function for an isotropic and nearly-incompressible hyperelastic material is expressed as [75, 89]

$$W = \frac{1}{2}\mu(I_1 - 3) + \frac{1}{d}(J-1)^2 \tag{4.22}$$

where I_1 is the first deformation invariant, J is the determinant of the elastic deformation gradient tensor (**F**), μ is the initial shear modulus of the material, and d is the material incompressibility parameter. The initial shear modulus and the incompressibility parameter are described as [89, 90]

$$\mu = 2(C_{10} + C_{01}) \tag{4.23}$$

$$d = \frac{1-2\nu}{C_{10} + C_{01}} \tag{4.24}$$

where C_{10} and C_{01} are the material constants of the M-R model as described previously in this section. These material constants were obtained by using curve fitting methods applied to the stress-strain data of the tested tissues under uni-axial compression conditions. ν is the Poisson's ratio of the tissues, which is assumed as 0.49 for the nearly-incompressible tested tissues. Accordingly, the initial bulk modulus of the material is defined as

$$\kappa = \frac{2}{d} \tag{4.25}$$

4.3 Finite Element Modeling

For the finite element modeling of sensor-tissue interaction, three steps should be followed. First, the tissue should be modeled. Second, the sensor structure should be modeled. Finally, the interaction between the sensor and the tissue should be modeled. To do so, COMSOL Multiphysics (formerly FEMLAB) software was chosen. COMSOL is a finite element analysis software for various physics and engineering applications. In the present chapter, the structural mechanics module of COMSOL Multiphysics v3.4 (http://www.comsol.com) was used for the finite element modeling of the problem. This module of the software performs classical stress-strain analysis with full multiphysics capabilities [76]. The model was developed in the 2-D space dimensions mode of the module. The plain strain mode with parametric analysis and large deformations was used in the model.

To model the tissue, three silicone rubber materials were chosen as artificial tissues with three different degrees of hardness equal to 10 Shore[§] OO (10-OO), 30 Shore OO (30-OO), and 20 Shore A (20-A). Figure 4-1 shows these artificial tissues made by Smooth-On (PA, USA).

[§] Shore (Durometer) type A and type OO scales are used to measure the hardness of soft materials such as silicone rubbers

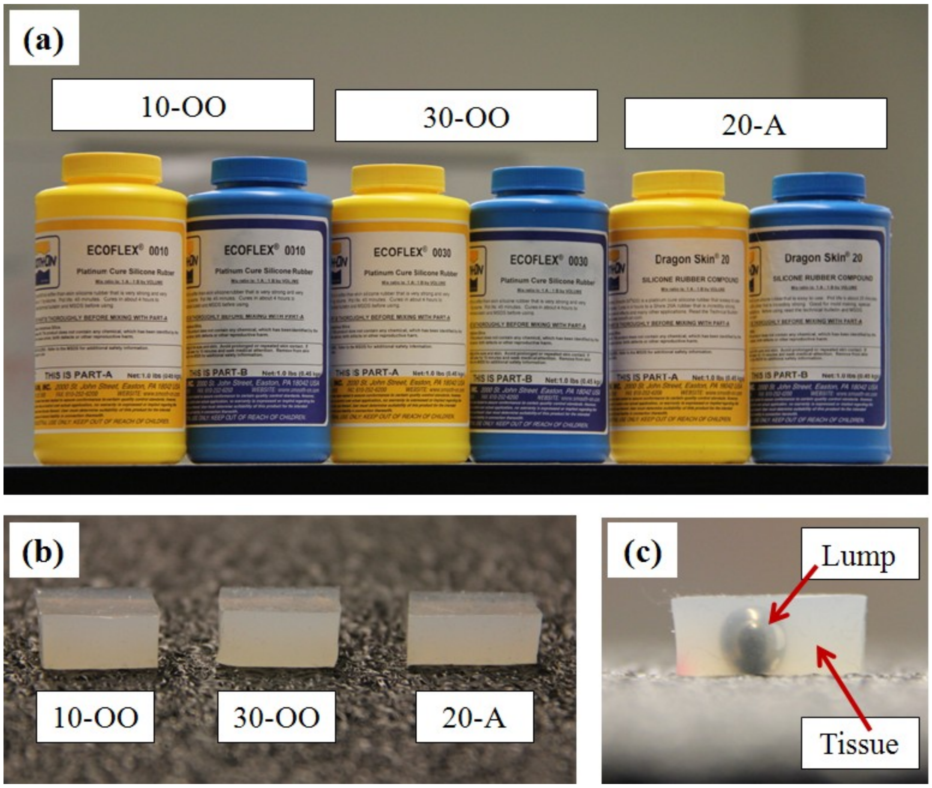

Figure 4-1: For 10-OO, 30-OO, and 20-A silicone rubber materials, the corresponding Parts A (yellow bottles) and Parts B (blue bottles) shown in (a) were mixed together with the ratio of 1 Part A: 1 Part B by volume to make artificial tissue samples shown in (b). In (c), a sample of tissue containing an embedded solid lump is shown.

As in real surgical operations, these artificial tissues represent biological tissues with different degrees of softness. During surgical tasks, such tissues undergo large deformations. Thus, their behaviors can be modeled by hyperelastic theory. To extract the hyperelastic material properties of the tissues, it is necessary to obtain their stress-strain data under compression tests. Only compression tests were chosen because in real surgical tasks the tool-tissue interactions mostly involve compressions rather than tensions. To obtain the stress-strain data, an ElectroForce 3200 test instrument (Bose Inc., Minnesota, USA) shown in Figure 4-2-a was used. As shown in Figure 4-2-b, the artificial tissue samples were placed between the lower jaw and the upper jaw of the test instrument. Then their stress-strain data were recorded under uni-axial compression tests. To derive the M-R hyperelastic material constants of the tissues, curve-fitting methods were applied to this data. Then, as described in Section 4.2, based on the derived M-R constants, the N-H constants [76] were calculated using Equations 4.23 to 4.25. The calculated N-H material constants are summarized in Table 4-1. These material constants were used in the finite element model.

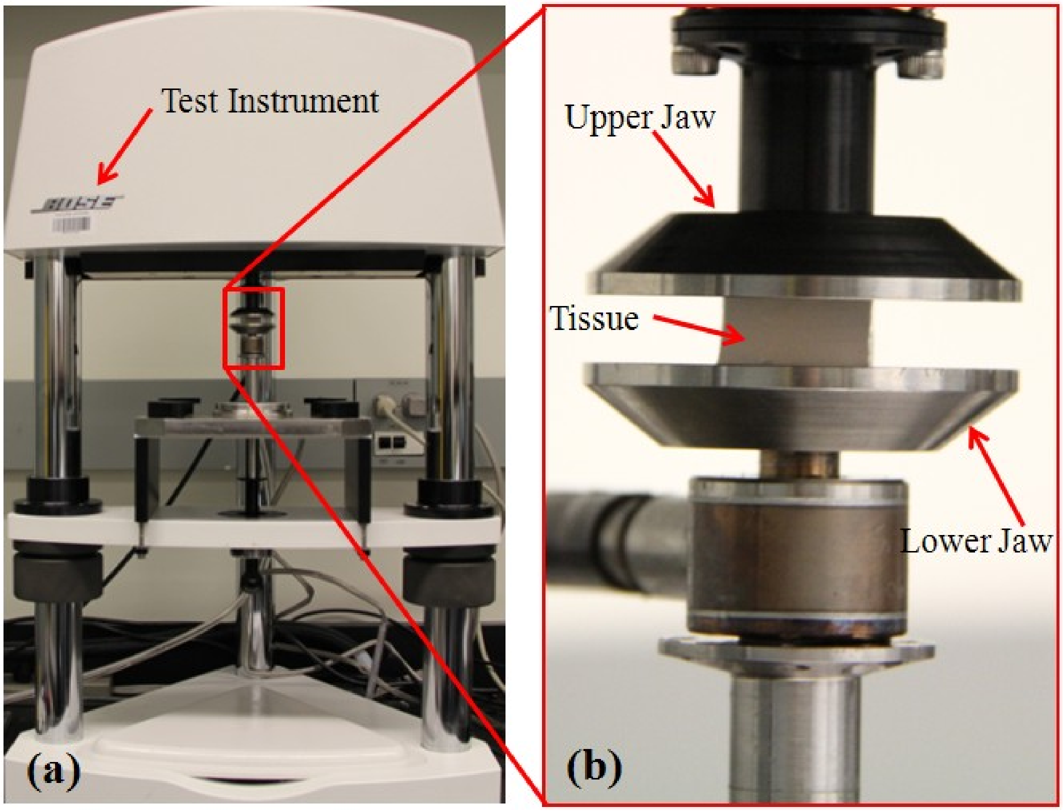

Figure 4-2: The artificial tissue sample under uni-axial compression test using Bose ElectroForce 3200 test instrument. The magnified view of (a) is shown in (b).

Table 4-1: Neo-Hookean parameters of the artificial tissues

	μ (kPa)	κ (kPa)
10-OO Material	2.743	137.149
30-OO Material	9.542	477.123
20-A Material	63.293	3164.638

To verify whether the derived material constants were accurate or not, the experimental stress-strain data were compared with the simulated stress-strain behavior for the tested tissues. Figure 4-3, Figure 4-4, and Figure 4-5 show the comparison of the experimental and M-R model stress-strain data for 10-OO, 30-OO, and 20-A materials respectively.

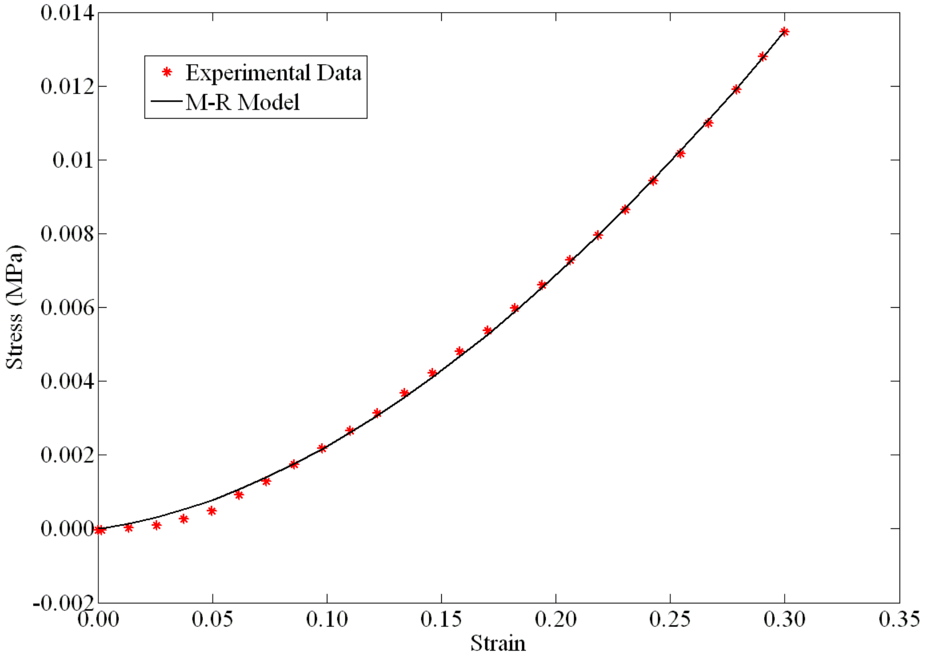

Figure 4-3: Comparison of the experimental data and the M-R model's stress-strain data obtained by a uniaxial compression test for 10-OO material at C_{10} = 27.147 kPa and C_{01} = -25.776 kPa.

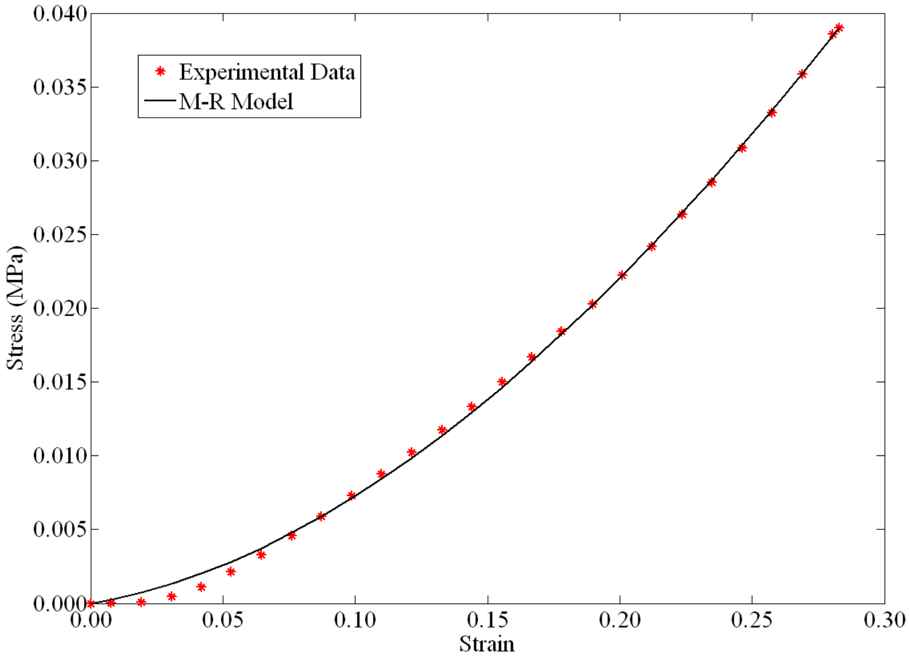

Figure 4-4: Comparison of the experimental data and the M-R model's stress-strain data obtained by a uniaxial compression test for 30-OO material at C_{10} = 85.157 kPa and C_{01} = -80.385 kPa.

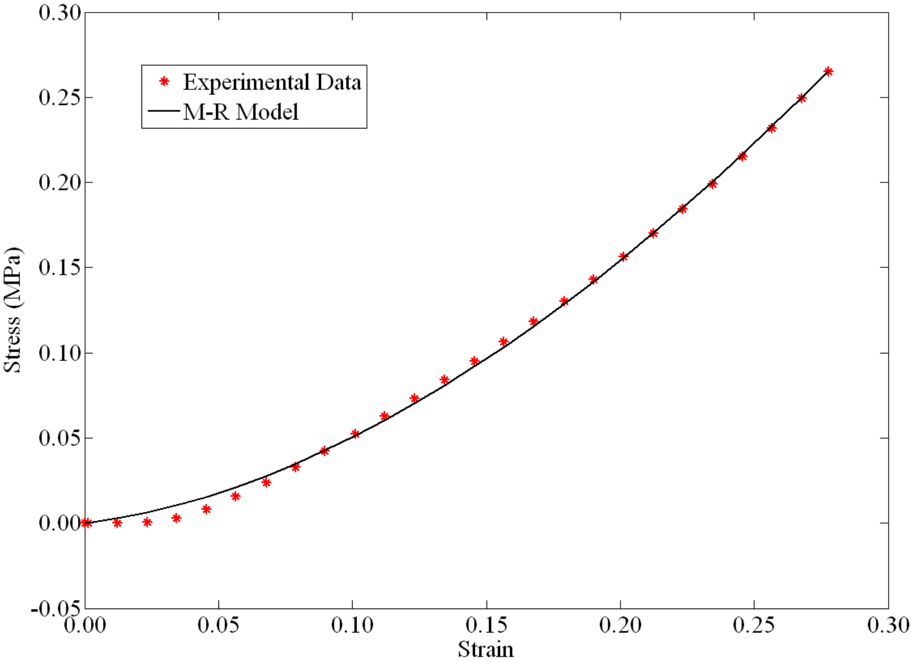

Figure 4-5: Comparison of the experimental data and the M-R model's stress-strain data obtained by a uniaxial compression test for 20-A material at C_{10} = 604.989 kPa and C_{01} = -573.343 kPa.

The results confirm that 20-A is harder than 30-OO and 30-OO is harder than 10-OO. The derived material constants were used to develop the sensor-tissue interaction finite element model. The developed model is shown in Figure 4-6. To study the effects of a tissue embedded inside the background tissue, a lump with the radius of R is located at a known x, and y position with respect to the shown coordinate system.

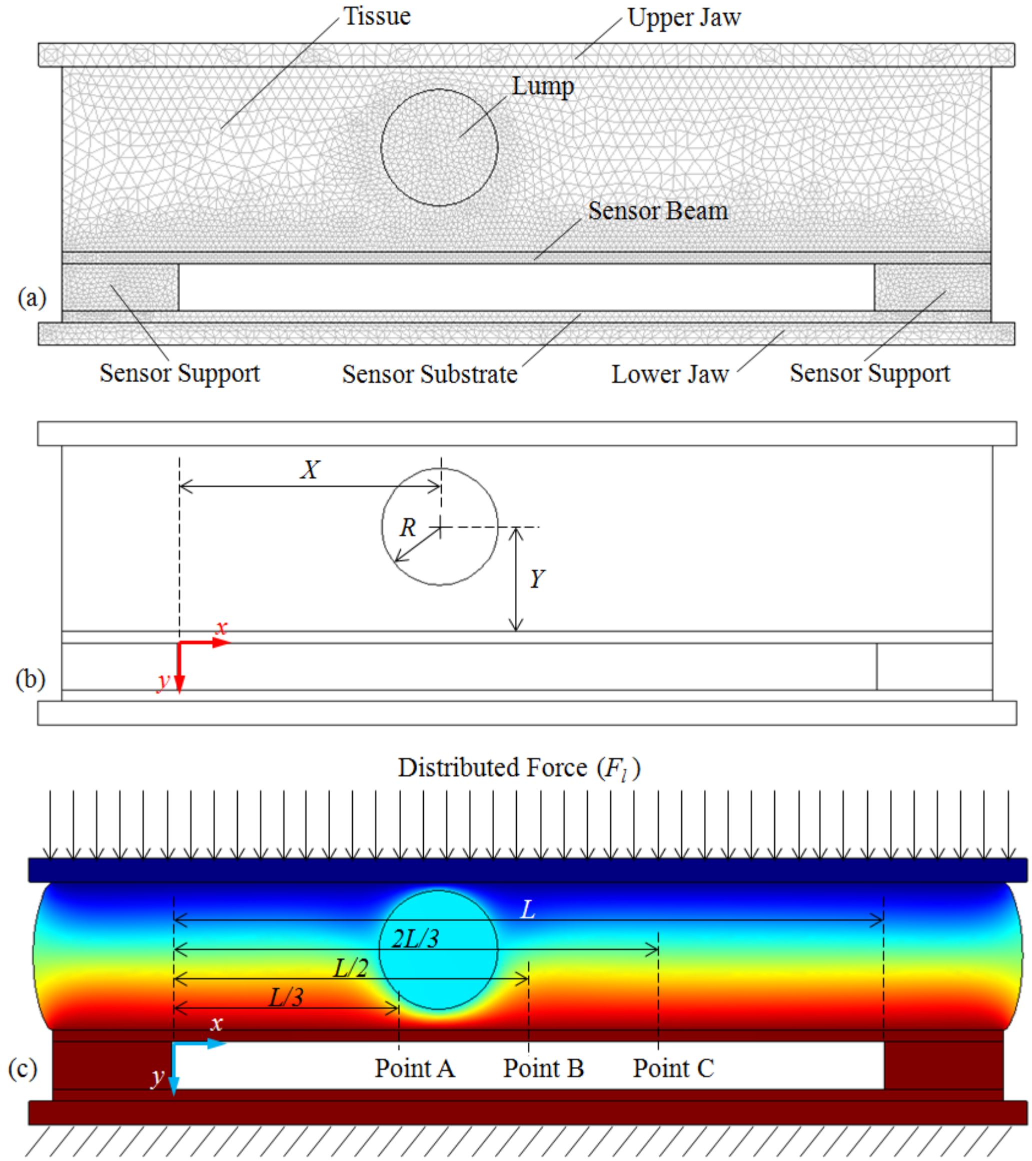

Figure 4-6: The finite element model of the interaction between the sensor and a background tissue containing a lump with a known position and geometry in different configurations: (a) the meshed

structure of the model; (b) the radius and the position of the lump are shown with respect to a Cartesian coordinate system; (c) the deformed structure of the model is shown when a distributed load is applied to the upper jaw and when the lower jaw is fixed. In (c), the color field shows the *y*-displacement.

In the experimental tests, it was observed that the friction between the elastomeric materials and the upper jaw of the test instrument as well as the friction between those materials and the sensor beam is large enough to avoid any lateral sliding movement between them. Because of this friction, the same conditions were implemented in the FE model. In this model, a Lagrange-quadratic triangular element was chosen since this type of element has hyperelasticity, a large degree of deformation, and large strain capability, all three of which are required for our purposes. This element has two degrees of freedom at each node. The boundary conditions of the problem were considered as follows:

- As shown in Figure 4-6-c, the lower boundary of the lower jaw was fixed in all directions
- The lower boundary of the sensor was glued to upper boundary of the lower jaw
- The lower boundary of the tissue was glued to the upper boundary of the sensor beam
- The upper boundary of the tissue was glued to the lower boundary of the upper jaw
- The circular boundary of the lump was glued to the tissue
- The right and left boundaries of the tissue had free boundary conditions.
- As shown in Figure 4-6-c, a distributed force of the amount F_l (N/mm) was applied to the upper boundary of the upper jaw by using the parametric solver of

COMSOL as the negative F_l (force per unit length). As a result, the lower jaw was lowered and the tissue was compressed towards the sensor.

To simplify the model, it was assumed that the sensor was fixed and the interacting force was applied through the tissue to the sensor. However, in real surgical conditions, the tissue is fixed and the contact force is applied from the sensor to the tissue. Although the conditions used in this simulation were different from real surgical conditions, the simulated results remained constant because of Newton's third law.

4.4 Materials and Methods

The number of parameters has a significant effect on the sensor output. Such parameters are defined by the material properties of the background tissue and by any potential embedded tissue inside the background tissue (i.e. lump, blood vessel, ureter, etc.) as well as by the size and the location of any embedded tissue. Practically, during minimally invasive surgical tasks, these parameters are very important for the surgeons. In fact, changing the mentioned parameters causes variations in the degree of deflection of the sensor beam. The proposed sensors measure such variations in the beam deflection. This is the reason why the sensors are set so as to measure these parameters. Basically, there could be some combination of these parameters that might result in similar sensor beam deflections. Consequently, some restrictive simplifications should be assumed to formulate the sensor response. More pointedly, these restrictive assumptions are also important for the development of an inverse model to reconstruct the parameters using the information measured by the sensor.

To reduce the complexity of the problem, a reduction of the parameters is applied to the material properties of the background tissue as well as to the size, location, and material properties of the model of the embedded tissue inside the background tissue. As an example of this parameter reduction, consider that the embedded tissue can generally be a lump, a blood vessel, a ureter, etc., having different sizes. Since all of these embedded tissues can be approximated as spherical features in a 2-D cross section, the number of parameters defining the size of these different embedded tissues is reduced to a single parameter that is the lump radius, R. As another example, the number of parameters characterizing the material properties of the background tissues is reduced to the value of their degree of hardness on the Shore scale. The moduli of elasticity of the embedded lumps are chosen as the only parameter that characterizes their material properties. To characterize the position of the lump, the X and Y parameters are defined as shown in Figure 4-6-b. Another important parameter is the amount of contact force during sensor-tissue interaction. As shown in Figure 4-6-c, this parameter is defined by the amount of force applied on a given unit length of the upper boundary of the upper jaw, F_l.

In brief, such parameters are categorized as (1) the hardness/softness of the tissue, (2) the location of the lump, (3) the modulus elasticity of the lump, (4) the size of the lump, (5) the depth of the lump, and (6) the amount of contact force.

In addition to these parameters that depend on the characteristics of the contact tissue, the effect of one important sensor parameter that depends on the sensor characteristics is also studied. This parameter is the Young's modulus of the sensor beam. In general, it is assumed that the sensor is made of silicon with a Young's modulus of 170 GPa, which is similar to that of the fabricated sensors presented in the discussion in Chapter 5 to Chapter 9. However, the presented sensor in Chapter 2 is made of a Hi-Impact PolyStyrene material with a Young's modulus of 3000 MPa. As a result, the effect of such changes in the Young's modulus of the sensor beam on the hardness/softness measurement is also studied in the present chapter.

4.5 Results and Discussions

In this section, the simulation results are presented and discussed whereas the experimental data are explained in each chapter. In the model, the size of the sensor beam is considered the same as the size of the beam presented in Chapter 9. This beam measures 30 mm, 4 mm, and 500 µm in length, width, and thickness respectively. Using the geometrical parameters of the sensor beam, an inverse model of the sensor output versus the parameters of the contact tissue can be developed based on the simulation results. In all simulations, the height of the tissue was set at 8 mm, and silicon with a Young's modulus of 170 GPa was chosen to be the material out of which the sensor beam was made except in one of the cases for which plastic was used.

4.5.1 The Effect of Tissue Hardness/Softness

The mechanical properties of biological tissues are one of their important characteristics by which surgeons distinguish between organs and abnormal tissue. In fact, the hardness of tissue indicates its degree of softness. The lower a tissue's degree of hardness, the softer the tissue. To show the effect of tissue hardness/softness on the sensor beam deflection, the interaction of the sensor with various artificial tissues (without any embedded lump) was studied. As summarized in Table 4-1, the artificial tissues are 10-OO, 30-OO, and 20-A. Moreover, to investigate the effect of the Young's modulus of the sensor beam on the sensor sensitivity, the material of the beam was selected as two different materials: silicon and Hi-Impact PolyStyrene with a Young's moduli of 170 GPa and 3000 MPa respectively. From the results shown in Figure 4-7, it can be concluded that the softer the object, the greater the beam deflection. Also it is observed that sensor sensitivity to the measurement of the relative hardness can be improved by decreasing the Young's modulus of the sensor beam.

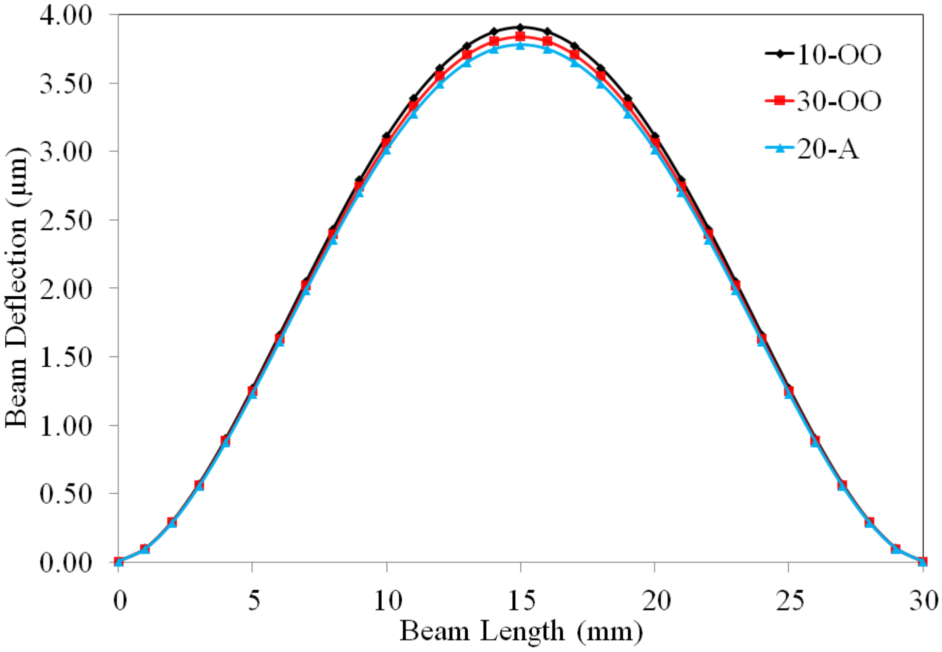

(a)

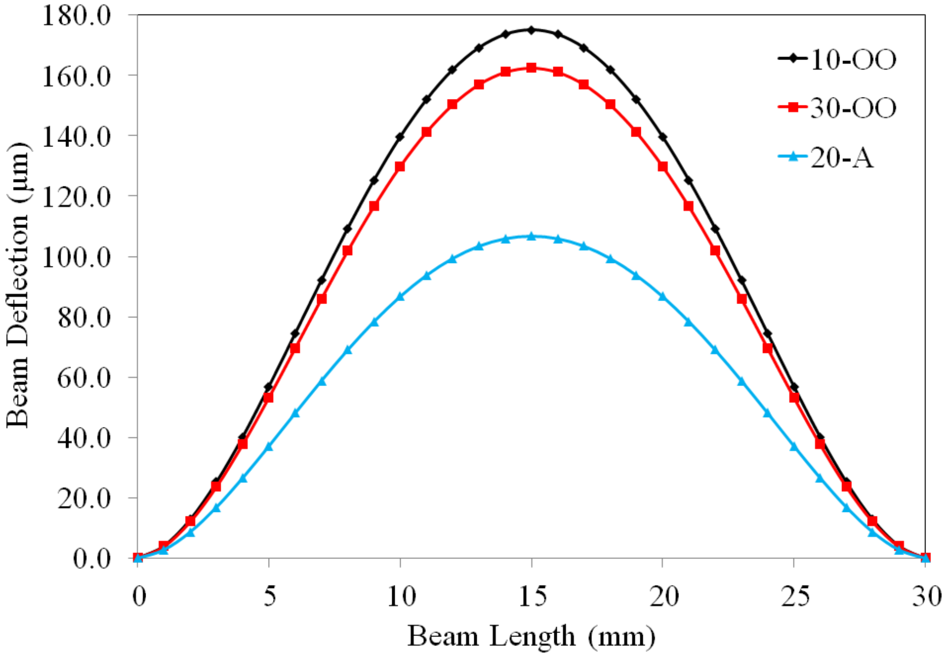

(b)

Figure 4-7: The effect of tissue hardness/softness on sensor beam deflection (a) when the beam was silicon and (b) when the beam was Hi-Impact PolyStyrene. The Hi-Impact PolyStyrene beam has approximately 46 times more deflection than the silicon beam.

In this set of simulations, the magnitude of the applied distribution force, F_l, was 0.011 N/mm for the sensor with the silicon beam and 0.01 N/mm for the sensor with the PoylStyrene beam. The magnitude of the distribution force was chosen in such a way that resulted in a few millimeters of tissue deformation as under real surgical conditions. As shown in the graphs, the Hi-Impact PolyStyrene beam had approximately 46 times more deflection than the silicon beam. Hence, the optical fiber bending sensing principle [49] presented in Chapter 2 is more suitable to measuring the PolyStyrene beam deflection whereas the optical fiber coupling loss sensing principle presented in Chapters 5 to 9 is more suitable to measuring the silicon beam deflection.

4.5.2 The Effect of Lump Location

Detecting the location of any potential hidden lump is crucial for surgeons. Assuming that the sensor was small by comparison with the size of the lumps, it was decided that only one lump was potentially located on the sensor beam. To show the effect of the location of the lump on the sensor beam deflection, a set of simulations was performed while the lump position was varied with respect to the *x*-axis as shown in Figure 4-6-b. In this set of simulations, the applied distributed load was 0.011 N/mm and the vertical location of the lump, *Y*, was 3 mm. The lump was configured with a radius of 2.5 mm and a modulus of elasticity equal to 15 MPa. Also the background tissue was 10-OO. Under such conditions, Figure 4-8 shows the simulated sensor beam deflection when the horizontal location of the lump, *X*, varies.

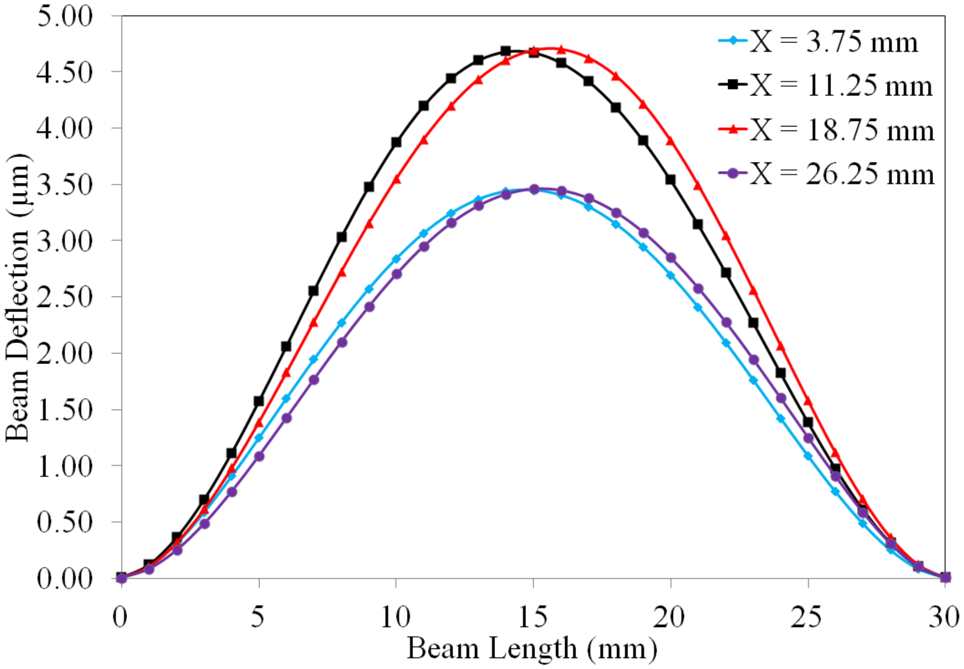

Figure 4-8: The effect of the lump lateral position on the sensor beam deflection. The modulus of elasticity of the lump was 15 MPa, and that of the tissue was 10-OO. The radius of the lump was 2.5 mm. *Y* was 3 mm.

The simulation results show that the position of the lump affects the beam deflection. The proposed sensors measured such changes in the beam deflection to detect the position of the lump.

In three of the proposed sensors in this thesis presented in Chapters 2, 6, and 9, the deflection of the sensor beam is measured at Point A, Point B, and Point C as shown in Figure 4-6-c. To show the effect of the lump location on the beam deflection at these three points, a set of simulations was performed while the horizontal lump location, X, was varied from 0 to 30 mm with 1 mm intervals with respect to the x-axis. Figure 4-9 shows the sensor beam deflection for such a set of simulations. The results confirm that the proposed algorithms in Chapter 2 and Chapter 6 can be used to detect the location of the lump. In this set of simulations, it was assumed that the radius of the lump (R) and the vertical position of the lump from the contact boundary (Y) are 2.5 mm and 3.0 mm respectively. The modulus of elasticity of the lump was 15 MPa, and that of the background tissue was 10-OO. Also the applied distributed load was 0.006 N/mm.

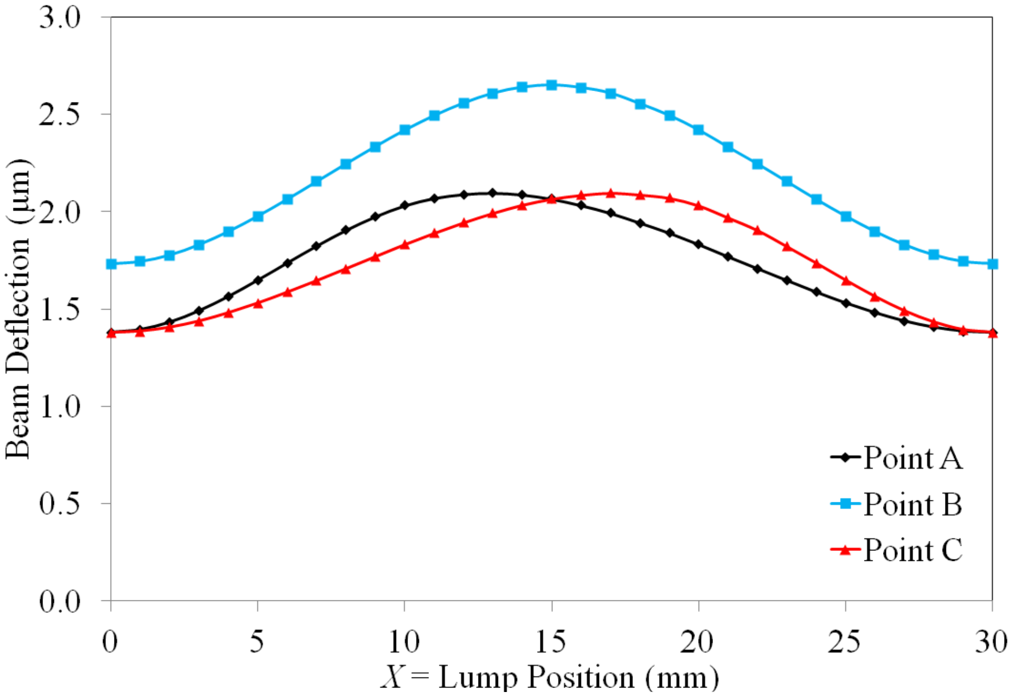

Figure 4-9: The effect of the lump lateral position on the beam deflection at Points A, B, and C. The modulus of elasticity of the lump was 15 MPa, and that of the tissue was 10-OO. The radius of the lump was 2.5 mm. *Y* was 3 mm.

4.5.3 The Effect of the Lump Modulus of Elasticity

The mechanical properties of the embedded lump and also the background tissue are also important parameters that affect the sensor output. To examine the effect of such parameters, the modulus of elasticity and the degree of hardness were chosen to characterize the mechanical proprieties of the embedded lump and of the background tissue respectively. The lump's modulus of elasticity was considered similar to that reported for typical tissues [91]. It was set at four different values starting from 15 kPa with a tenfold increase for each following value. The degrees of harness for the background tissues were considered as 10 in Shore OO and 20 in Shore A. Table 4-2: Moduli of elasticity for the background tissues summarizes the values of the moduli of elasticity obtained from the compression tests performed on 10-OO and 20-A artificial tissues. As confirmed in the table, 10-OO is softer than 20-A.

Table 4-2: Moduli of elasticity for the background tissues

$E_{10\text{-}OO}$	0.0453 MPa
$E_{20\text{-}A}$	0.8901 MPa

In this set of simulations, the lump radius (R) was chosen as 2.5 mm. The lateral position (X) and the vertical position (Y) of the lump were chosen as 15 mm and 3 mm respectively. The applied distributed load (F_l) was set as 0.006 N/mm. Under such conditions, the sensor beam deflection is shown while the background tissue was selected as 10-OO (Figure 4-10-a) and 20-A (Figure 4-10-b).

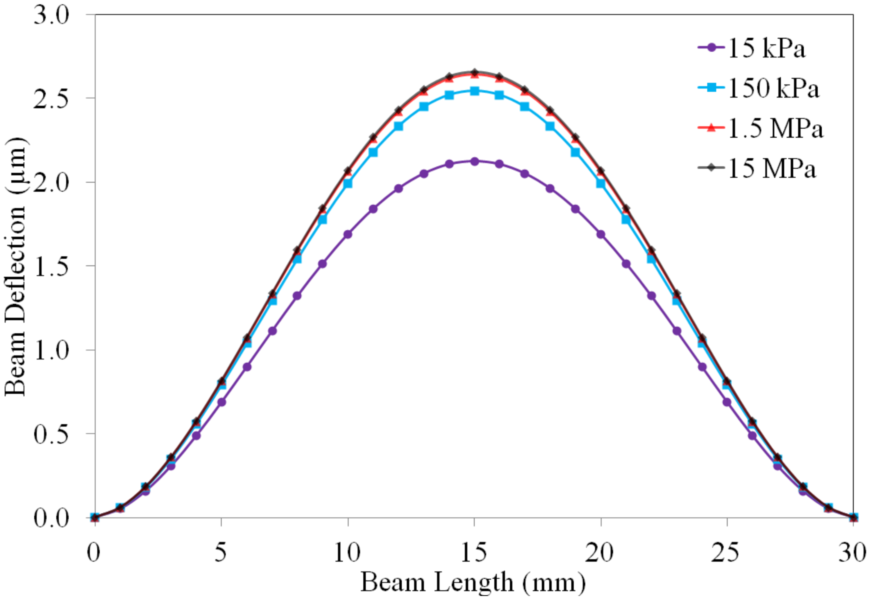

(a)

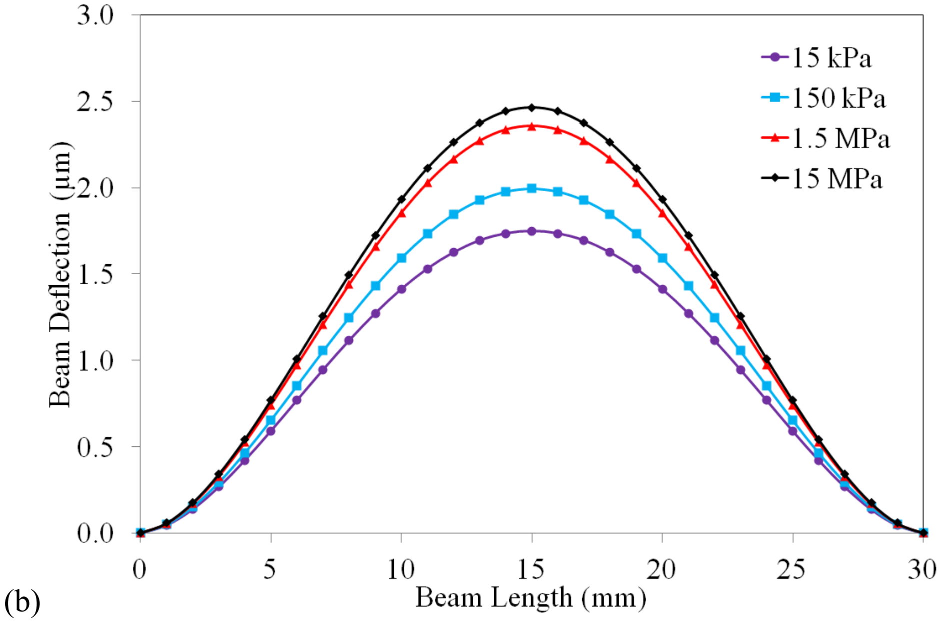

Figure 4-10: The effect of the lump's modulus of elasticity on the beam deflection: in (a), the background tissue is 10-OO; in (b), the background tissue is 20-A.

The simulation results show that the greater the lump's modulus of elasticity (E_{lump}), the greater the beam deflection. However, the sensitivity of the sensor is decreased as the value of E_{lump} is increased. In addition, as can be seen in Figure 4-11, the sensitivity is increased as the background tissue becomes softer.

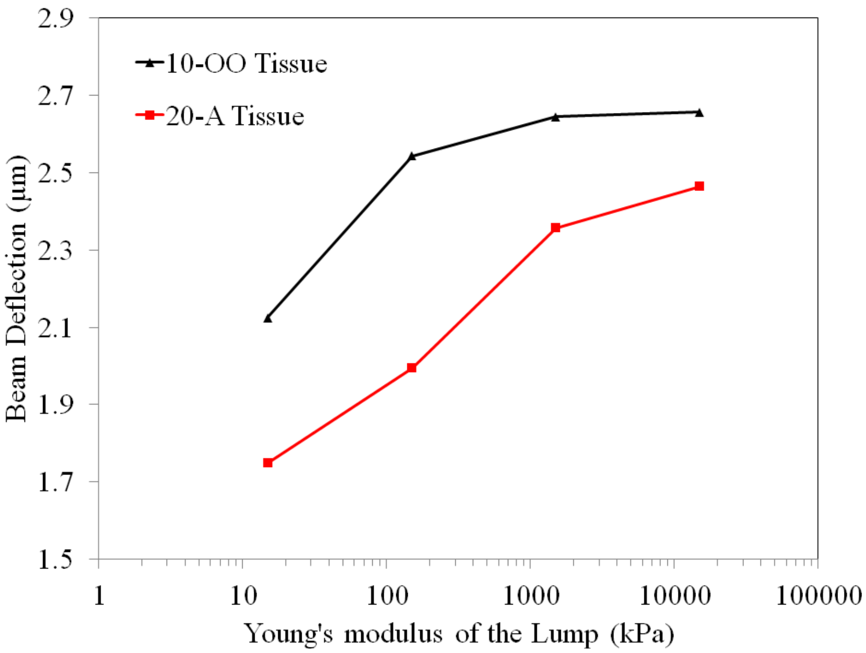

Figure 4-11: Sensor beam deflection versus the lump's modulus of elasticity for softer (10-OO) and harder (20-A) background tissues.

4.5.4 The Effects of Lump Size

The lump size is one of the key parameters of great importance for surgeons. For instance, the size of a cancerous lump plays an important role in diagnosing the phase of a disease. Moreover, detecting a cancerous lump at its earliest stage of development increases the chance of treatment for patients. To investigate the effect of lump size on sensor beam deflection, an embedded lump with different radiuses was assumed inside 10-OO tissue. The modulus of elasticity, the lateral position (*X*), and the depth (*Y*) of the lump were set as 1.5 MPa, 15 mm, and 4 mm respectively. Moreover, the applied distributed load was selected as 0.006 N/mm. Under such conditions, Figure 4-12 shows the simulated beam deflection while the lump radius changes from 0 to 3.5 mm.

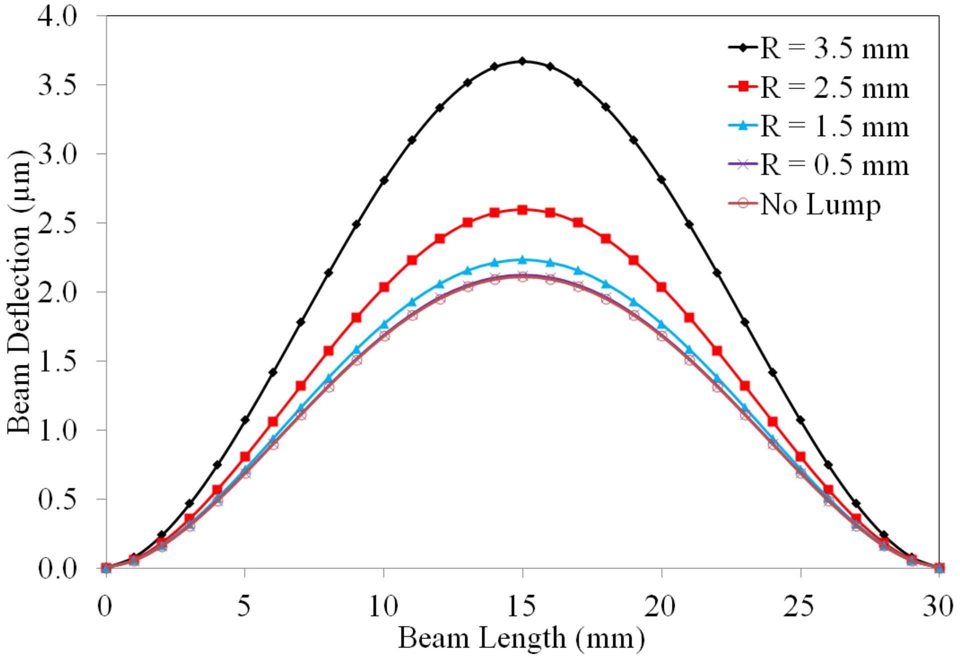

Figure 4-12: The effects of lump radius (*R*) on the beam deflection with a background tissue of 10-OO. The lump is located at *X*=15 mm and *Y*=4 mm with respect to the coordinate system as shown in Figure 4-6-b. The lump's modulus of elasticity is 1.5 MPa.

For better understanding, the comparison between the sensor beam deflection and the lump radius is shown in Figure 4-13. It can be seen that the sensitivity of the sensor to the lump size increases as the lump size increases. In other words, the early detection of small cancerous lumps (tumours) is more challenging than the detection of larger lumps.

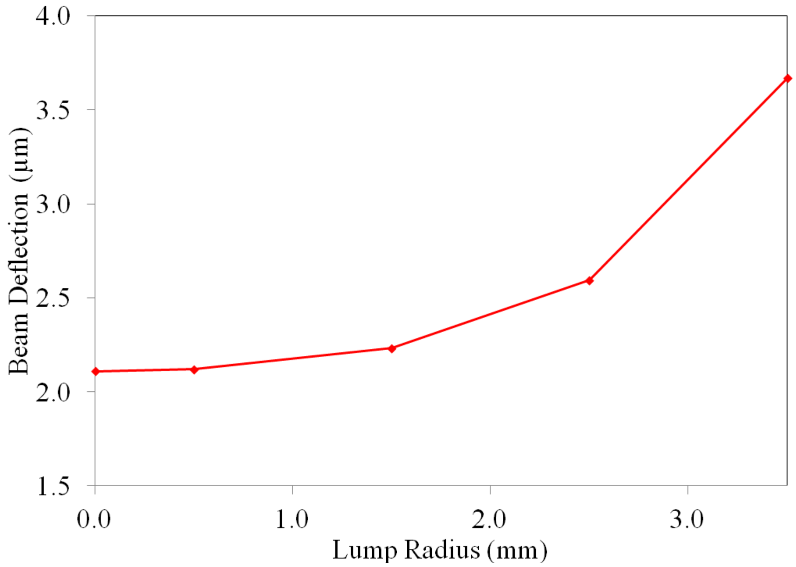

Figure 4-13: Variations of the sensor beam deflection plotted against lump radius for 10-OO background tissue. The lump, with a 1.5 MPa modulus of elasticity, was located on the center of the sensor beam.

4.5.5 The Effect of Lump Depth

To show how the sensor is sensitive to the depth of the lump, a set of simulations was performed while the lump depth (*Y*) was varied from 0.5 mm to 4.5 mm with 2 mm intervals. In this set of simulations, a lump with a radius of 2.5 mm and a modulus of elasticity equal to 15 MPa was assumed at the middle point of the beam in the *x* direction inside a 10-OO background tissue. The height of the tissue was chosen as 12 mm. Moreover, a distributed load with a magnitude of 0.006 N/mm was set to be applied to the upper jaw. Figure 4-14 shows the effect of the lump depth on the beam deflection under such conditions. The simulation results show that the sensor sensitivity to the lump depth is relatively low. To allow further evaluation, the variations of the sensor beam deflection plotted against the lump depth are given in Figure 4-15. As depicted in this graph, the sensitivity decreases as the lump depth increases. As a result, the detection of deep lumps is especially challenging during surgical tasks.

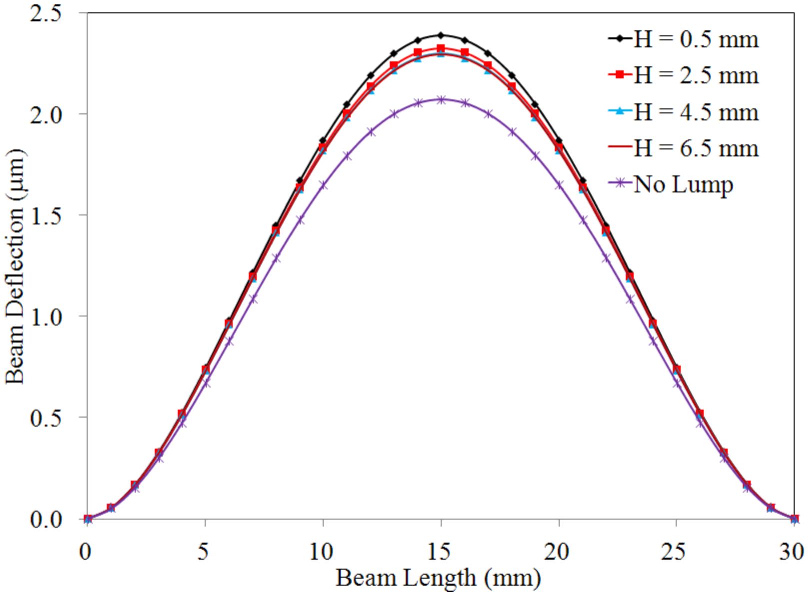

Figure 4-14: The effect of lump depth (*Y*) on the sensor beam deflection. *R*, *X*, E_{lump} and F_l were chosen as 2.5 mm, 15 mm, 15 MPa, and 0.006 N/mm respectively. The height of the background tissue was set as 12 mm. The background tissue was selected as 10-OO.

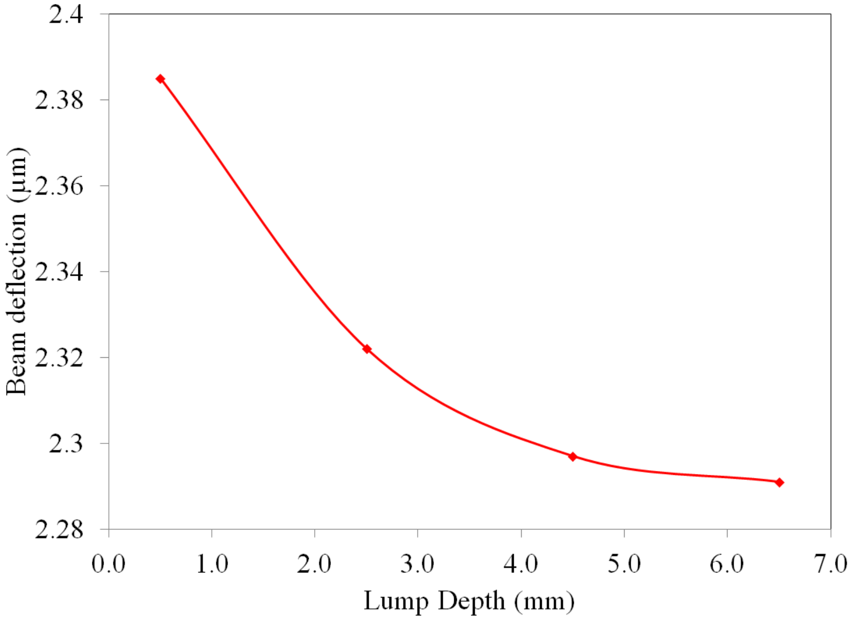

Figure 4-15: Comparison between the sensor beam deflection and the lump depth.

4.5.6 The Effect of the Applied Load

The magnitude of the contact load while the sensor is interacting with tissue also affects the sensor beam deflection. The sensor should measure this contact force in order to measure the important parameters mentioned above. To characterize the effect of the contact force on the sensor output, it was assumed that the beam-type sensor interacts with 10-OO tissue without the presence of any lump inside the tissue. The contact load was defined by the magnitude of the applied distributed load (F_l). In a set of simulations, F_l was varied from 0.002 N/mm to 0.010 N/mm at 0.002 N/mm intervals. Based on such conditions, the data in Figure 4-16 show the effects of the applied load on the sensor beam deflection. As predicted, the relation between the applied load and the beam deflection is linear. As described in Chapter 5, the sensor should be calibrated to measure the load accurately.

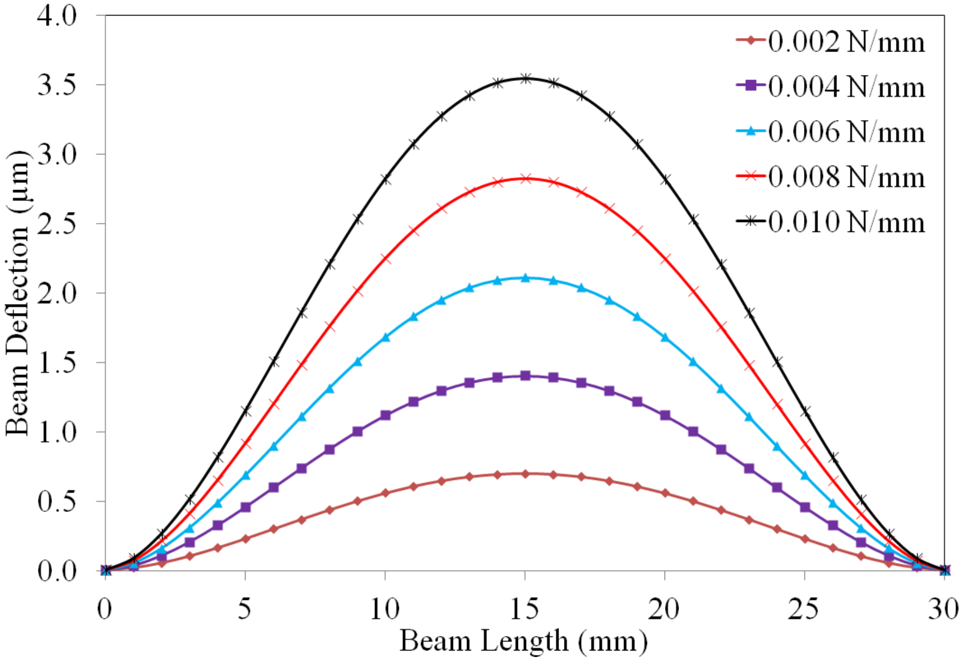

Figure 4-16: The effect of an applied distributed load (F_l) on the sensor beam deflection. 10-OO background tissue without any embedded lump was chosen.

4.6 Conclusions

The main purpose of this chapter is to provide theoretical considerations necessary for modeling the response of the proposed sensors presented in this thesis while they are interacting with biological tissues. To do so, a theoretical formulation for modeling the behavior of soft tissues has been proposed in this chapter. Based on the proposed theory, a finite element model of sensor-tissue interaction was developed in COMSOL Multiphysics software. The modeled sensor was chosen as a beam structure with boundary conditions and a size similar to those of the sensors proposed in the present thesis. The sensing elements of the proposed sensors measure the variations in the beam deflection of the sensors. Consequently, the effects on the sensor beam deflection of important parameters involved in minimally invasive surgical application were studied in the present chapter. To study these effects, various sets of simulations were performed to investigate the effects of important parameters on the sensor beam deflection. Such important parameters include the mechanical properties of tissues as well as the size, the location, and the mechanical properties of lumps embedded inside background tissues.

In order to simplify the problem, various assumptions were applied to reduce the number of important parameters. For instance, the time-dependent mechanical behaviors of tissues were not implemented in this work. In fact, the tissue was modeled as a hyperelastic material that undergoes large deformation without showing any viscoelastic properties. Based on the simulated results, an inverse model can be developed to reconstruct the tissue's degree of softness as well as the size and location of any potential tissue such as a lump, blood vessels, ureter, etc., embedded inside the background tissue.

Chapter 5: Fully Optical High Sensitive Force Sensing

In the present chapter, a novel miniaturized optical force sensor is introduced for use in medical devices such as minimally invasive robotic-surgery instruments. The sensing principle of the sensor relies on light transmission in optical fibers. Although the sensor is designed for use in surgical systems, it can be used in various other applications due to its unique and innovative features. Among the unique features of the sensor are the high accuracy/resolution, the magnetic resonance compatibility, the electrical passivity, and the absence of drift in the measurement of continuous static force. Using microsystems technology, the proposed sensor was micromachined, and then tested. The sensor measures 18 mm, 4 mm, and 1 mm in length, width, and thickness, respectively. The sensor was calibrated and its performance under both static and dynamic loading conditions was investigated. The experimental test results demonstrate a 0.00–2.00 N force range with an rms error of approximately 2% of the force range. Its resolution is 0.02 N. The characteristics of the sensor such as its size, its measurement range, and its sensitivity are easily tunable.

5.1 Introduction

Recently, the fast-paced growth rate in the use of bio-sensing technology has encompassed almost all the areas dealing with the medical device industry. Sensing the mechanical interaction between medical instruments and skins/organs is one such area. More pointedly, minimally invasive surgery (MIS) and minimally invasive robotic surgery (MIRS) systems are among the common examples of medical devices in which small-sized force sensors are requisite in providing surgeons with force feedback during tool-tissue interaction [1]. Such force feedback allows surgeons to recognize how hard they are pushing or pulling tissues with surgical tools such as graspers.

In fact, MIRS techniques offer a wide-range of advantages for both patients and surgeons [2, 3]. As a result, they are becoming more and more widely accessible in hospitals around the world [4]. More specifically, the da Vinci Surgical System, which was introduced by Intuitive Surgical Inc. (Sunnyvale, CA, USA), is one common example of such surgical systems. The da Vinci does not provide the surgeon with force/haptic feedback during tissue manipulation [6, 48]. The Canadian competitor of the da Vinci is the Amadeus Surgical Robot, which was introduced by Titan Medical Inc. (Toronto, ON, Canada). In these MIRS systems, force sensors are useful in measuring the interaction forces between surgical tools and tissues [8].

In general, providing surgeons with force feedback results in a better performance in robotic surgical systems [3, 12, 13]. It is experimentally verified that such feedback reduces the grasping force in operations performed by the da Vinci [14]. Therefore, the development of a sensor with the ability to measure the force is crucial for use in robotic surgical platforms such as the da Vinci and the Amadeus. For this sensor, various aspects should be taken into account.

First, the sensor should measure the static loads as well as the dynamic. The reason is that in MIS and MIRS, surgeons sometimes need to keep a continuous static contact between surgical tools and tissues. In such a case, static measurement is required to satisfy two important conditions: 1) maintaining a stable contact during tool-tissue interaction, and 2) avoiding damage to the interacted tissue caused by an excessive amount of contact force [17]. In other words, a suitable sensor for this application must measure the static contact force as well as the dynamic one. However, currently available tactile sensors are mainly electrical-based such as capacitive-based [92], piezoelectric-based [18, 93], or piezoresistive-based [94] sensors. Such electrical-based sensors perform mostly only under dynamic loading conditions. Consequently, there is a need to develop a tactile sensor that also performs under static loading conditions. Secondly, the sensor must be magnetic resonance compatible because surgeons sometimes need to perform MIS or MIRS in the presence of magnetic resonance imaging (MRI) devices [21, 22, 95]. Thirdly, the sensor must be electrically-passive for specific types of operations such as minimally invasive cardiovascular operations [23]. Due to the inherent properties of optical fiber technology, fiber-based sensors are one of the few choices that can address these three requirements [24].

Because of the narrow space available at the tips of surgical tools used in MIS and MIRS, size constraint is another important parameter in the design of the force sensor. With the advances of micro electro-mechanical system (MEMS) technology, a new opportunity has been created to develop the miniaturized force sensors [25]. Optical fiber technology is compatible with MEMS technology. The sensing principles of optical fiber sensors are mainly divided into three subdivisions: fiber Bragg grating (FBG) sensors, interferometry-based optical fiber sensors, and intensity-modulated optical fiber sensors [26]. Among these three sensing principles, the intensity-modulated principle offers unique advantages such as less expensive equipment, less complexity, and less sensitivity to thermal-induced strain [27]. In addition, using this principle, sensors can perform both static and dynamic measurements.

In recent years, a large number of force and tactile sensors have been introduced for use in MIS and MIRS. Some of these force sensors were designed to measure tactile/cutaneous information. Others have been designed to measure force/kinesthetic information [11, 96]. Nevertheless, each of the developed sensors has its own practical restrictions. As an example, in 2009, Sokhanvar et al. [18] proposed a MEMS endoscopic tactile sensor that uses a piezoelectric-based sensing principle. Their sensor is electrically passive, but not magnetic resonance compatible. Their developed sensor also does not perform under static loading conditions. As another example, recently, King et al. [6] integrated a commercial FlexiForce force sensor into the graspers of the da Vinci surgical system to provide surgeons with force feedback. The sensing principle of this commercially available force sensor is based on a piezoresistive material. Such material is not electrically passive.

Recently, optical fiber-based sensors, which address both being magnetic resonance compatible and being electrically passive, have been widely used in surgical applications. In fact, such optical sensors are mostly used in catheterization procedures [32-35, 97]. However, a very limited number of these force sensors have the capability of being integrated into surgical graspers. Although these sensors easily can be integrated into the tips of catheters, their specific design is not suitable for integration into surgical graspers. For instance, recently, an FBG sensor was proposed to measure micro-deformations of a catheter tip [33]. This sensor was integrated into a TactiCath ablation catheter developed by Endosence SA (Geneva, Switzerland). Moreover, and more recently, Althoefer et al. [34, 35] have proposed miniaturized MRI-compatible optical fiber sensors for use in surgical applications. Although their proposed sensors are optical-fiber based, they are not specifically designed to be integrated into surgical graspers. As another example of force sensors for use in MIS and MIRS, Peris et al. [19] have developed a tri-axial micro optical fiber sensor to measure force feedback during MIRS. However, their developed sensor measures only the kinesthetic information. Most recently, in 2010, Howe et al. [71] fabricated and tested an optical fiber force sensor for use in surgical applications. The sensing principle of this sensor is based on intensity-modulated optical fiber sensors, thereby satisfying the previously mentioned conditions. However, in the first place, it is not designed to be integrated into graspers, but it is suitable for catheterization procedures.

In fact, the key feature of the proposed sensor is its capability of measuring the tool-tissue interaction force with the following characteristics: first, it can perform measurements under both static and dynamic loading conditions; second, it is MRI-compatible and electrically passive; third and most significantly, it can measure the force by using only one single moving part. Thanks to the first characteristic of the sensor, surgeons can maintain contact stability between surgical tools and tissues while at the same time avoiding tissue damage because of the undesirable excessive force applied from surgical tools to tissues. In addition, due to the second characteristic, the sensor can function in the presence of MRI devices that are currently in widespread use in surgical rooms. Moreover, the sensor can be used in environments where electrically-active sensors are undesirable. The third characteristic of the sensor simplifies its integration into the limited space available at the tips of surgical instruments.

Initially in the present chapter, the design and the theoretical modeling of the proposed sensor are addressed. Then the MEMS fabrication process of the sensor is discussed. Afterwards, the experimental setup and the tests performed to characterize the sensor are explained. Finally, the characterization and the performance of the sensor are also investigated.

5.2 Sensor Design and Modeling

5.2.1 Concept Design

Figure 5-1 illustrates the structure of the force sensor. As shown in this figure, a silicon beam with fixed-fixed boundary conditions is attached to four supports. The supports are fixed on the substrate of the sensor. The beam, the supports, and the substrates are made of silicon. These parts can be diced from a silicon wafer. On the lower surface of the beam, a v-groove is micromachined using MEMS technology. Two optical fibers are integrated into the v-groove. On the one hand, Fiber A is introduced into the v-groove from the left side. On the other hand, Fiber B is introduced into the v-groove from the right side of the sensor. At the middle point of the beam, a narrow gap is introduced between the bare ends of Fiber A and Fiber B. These bare ends of the fibers are cleaved and polished to have a perfectly flat surface. On the left side, the other end of Fiber A is connected to a laser light source. On the right side, the other end of Fiber B is connected to a photo-detector. The light source injects the light into Fiber A. At the mid-point of the beam, the light couples from Fiber A to Fiber B through the gap. The coupled light entering Fiber B is detected by the photo-detector, which is connected to the right end of Fiber B. For better visualization, the beam is transparent and translucent in Figure 5-1-b and Figure 5-1-c respectively.

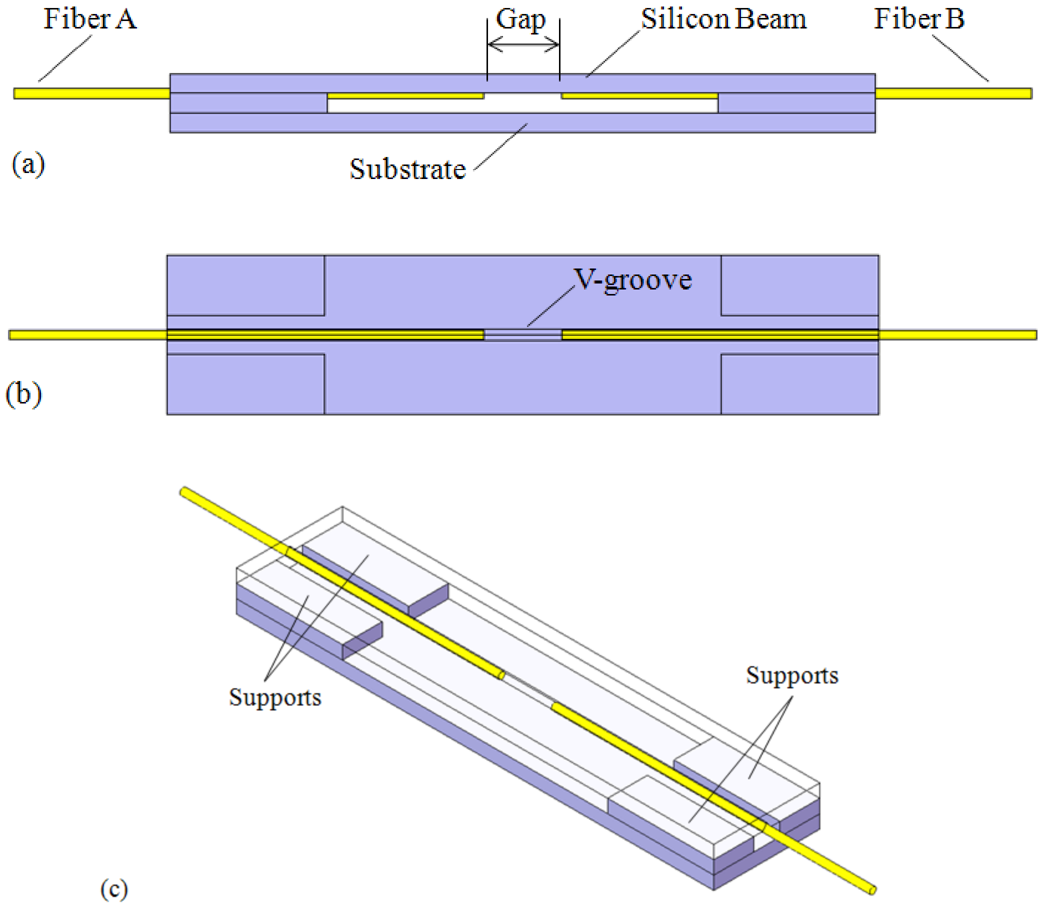

Figure 5-1: The structure of the force sensor in different views: (a) front view; (b) top view in which the beam is transparent for better visualization; (c) 3D view in which the beam is translucent for better visualization.

In this design, the sensing principle relies on measuring the coupling loss, which is an intensity-modulated method. In Chapter 2, based on a different technique, another intensity-modulated force sensor was proposed by the present authors. The earlier work is a single-mode optical fiber sensing based on a bending principle [49, 52], which has its own disadvantages. For instance, the earlier design cannot easily be micromachined with MEMS technology. In fact, the v-grooved design of the present sensor simplifies its miniaturization by using low-cost anisotropic silicon-based micro-machining techniques such as wet etching techniques.

Basically, the force applied to the sensor beam results in the deflection of the beam. The deflection of the beam alters the coupled light. In other words, the deflection of the beam results in light coupling loss between Fiber A and Fiber B. The sensor measures the force applied to the sensor beam. The sensor measures the force whether it is a concentrated force or a distributed force.

5.2.2 Sensor Modeling: Parametric Analysis

Coupling loss (dB) due to angular misalignment between Optical Fiber A and Optical Fiber B of the sensor is modeled theoretically. In addition, the relation between the angular misalignment and the force applied to the sensor beam is also modeled. Therefore, the theoretical aspect of the relation between the contact force and the resulting sensor output is investigated.

Coupling efficiency caused by the misalignment between Fiber A and Fiber B of the sensor can be defined as η [98, 99]:

$$\eta = 4\frac{D}{B}\exp(-A\frac{C}{B}) \tag{5.1}$$

where

$$A = \frac{(kw_A)^2}{2} \tag{5.2}$$

$$B = G^2 + (D+1)^2 \tag{5.3}$$

$$C = D(G^2 + D + 1)\sin^2(\Delta\theta) \tag{5.4}$$

$$D = (\frac{w_B}{w_A})^2 \tag{5.5}$$

$$G = 2\frac{Q}{kw_A^2} \tag{5.6}$$

in which k is the propagation constant of the gap medium between Fiber A and Fiber B. w_A and w_B are the Gaussian mode field-radius of Fiber A and Fiber B respectively. $\Delta\theta$ is the angular misalignment between the axis of Fiber A and Fiber B. In other words:

$$k = \frac{2\pi n_0}{\lambda} \tag{5.7}$$

$$w_A = a(0.65 + \frac{1.619}{V^{3/2}} + \frac{2.879}{V^6}) \tag{5.8}$$

$$w_B = w_A \tag{5.9}$$

$$V = \frac{2\pi a}{\lambda}\sqrt{n_{core}^2 - n_{cladding}^2} \tag{5.10}$$

$$\Delta\theta = \left|\theta_B - \theta_A\right| \tag{5.11}$$

in which n_0, n_{core}, and $n_{cladding}$ are the refractive index of the media, the core of the fibers, and the cladding of the fibers respectively. a is the radius of the core of the fiber. λ is the wavelength of the light. The V parameter is derived by Equation 10. θ_A and θ_B are derived from the Euler-Bernoulli equations for a beam with fixed-fixed boundary conditions [72]:

$$\theta(x) = \frac{f_L}{12EI}(-L^2x + 3Lx^2 - 2x^3) \tag{5.12}$$

$$\theta_A = \theta(x) \text{ where } x = \frac{L-Q}{2} \tag{5.13}$$

$$\theta_B = \theta(x) \text{ where } x = \frac{L+Q}{2} \tag{5.14}$$

where f_L is the force per length applied to the sensor beam; E is the modulus of elasticity of the sensor beam; I is the moment of inertia of the beam's cross section around its neutral axis; L is the length of the sensor beam; Q is the gap between Fiber A and Fiber B; x is the position on the sensor beam. Now, based on the coupling efficiency and the power of the light source, P_A, the power of the coupling light into Fiber B, P_B, can be obtained:

$$P_B = \eta P_A \tag{5.15}$$

Fiber B is coupled to a photodetector. The photodetector converts the light intensity of Fiber B into the electric voltage, V_{OUT}. Consequently, the output of the sensor is the electric voltage, which is linearly proportional to P_B. In other words, the sensor output voltage can be calculated as follows:

$$V_{OUT} = R(\lambda, LOAD)P_B \tag{5.16}$$

in which $R(\lambda, LOAD)$ is the multiplication of the spectral responsivity of the photodetector and the resistance of an external load. The spectral responsivity, which is a function of the light wavelength, can be obtained from the specifications of the photodetector. The external load resistance, which defines the sensitivity of the voltage measurement, can be finely tuned. Finally, using a DAQ, the output voltage is ready to be observed with the LabVIEW software.

Based on these theoretical considerations, increasing the gap between the fibers (Q) has two different effects on the sensor output. On the one hand, the optical coupling between the fibers decreases as Q increases. This effect reduces the output performance of the sensor. On the other hand, the sensitivity of the beam slope measurement improves as Q increases within a specific range. In other words, increasing the value of the gap, Q, has two opposite effects on the sensor output: (a) it degrades the sensor performance from optical point of view whereas (b) it improves the sensor performance from mechanical point of view. As a result, the value of Q can be optimized to obtain the best possible sensor performance.

5.3 Sensor Micro-fabrication

Anisotropic wet etching techniques were used to make the v-groove on the sensor beam. An N-Type <100> silicon wafer was used for the micro-fabrication process. First, using the thermal oxidation method, a thin silicon dioxide (SiO_2) layer, with a thickness of 525 nm, was deposited on the silicon wafer. Second, a photoresist layer was coated on the wafer and was then baked (a soft bake). Third, using a photolithography technique and a glass mask, the photoresist mask was patterned. The glass mask was designed to make v-grooves of different sizes on the silicon wafer. Fourth, the patterned photoresist was baked (a hard bake). Fifth, the unprotected oxide layer was etched with a buffered oxide etch (BOE). Finally, the v-grooves were micromachined using Tetramethylammonium hydroxide (TMAH) wet etching. After making the v-grooves on the silicon wafer, a dicing saw was used to dice the sensor beam. The other components of the sensor such as the supports and the substrate were diced using another N-Type <100> silicon wafer.

Figure 5-2-a shows the sensor beam and the integrated optical fibers that lead into the v-groove of the beam. Figure 5-2-b shows the whole sensor structure after assembling the components of the sensor. Although three v-grooves were micromachined on the beam, only the middle one was used for fiber integration. Using a dicing saw machine (ECSE 8003), the silicon beam and the supports were cut from the micromachined silicon wafer and a raw silicon wafer respectively. A UV curing optical adhesive from Norland Products Inc. (NJ, USA) was used to assemble the optical fibers inside the v-groove. This adhesive was cured by exposure to a UV light. This method allows the perfect alignment of Fiber A and Fiber B inside the v-groove before bonding them with the adhesive.

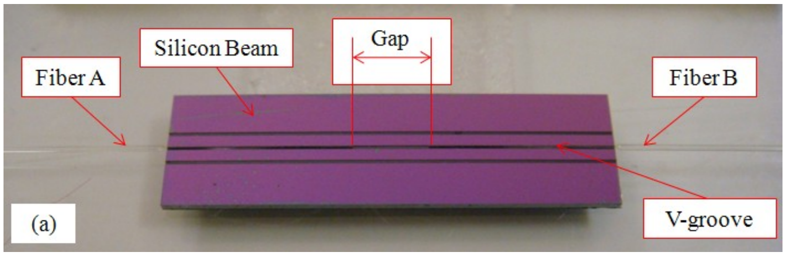

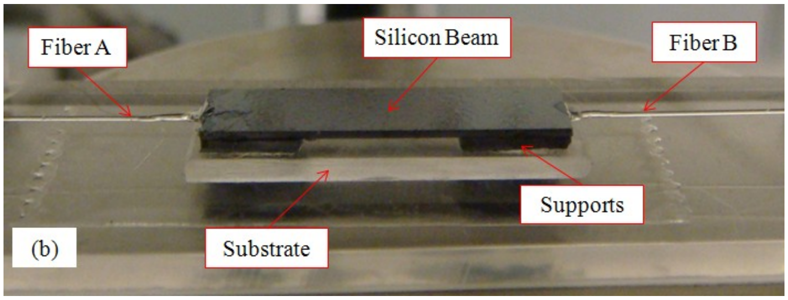

Figure 5-2: The photograph of the sensor: (a) the lower surface of the sensor beam, which includes two integrated optical fibers leading into the v-groove; (b) the whole structure of the assembled sensor.

Figure 5-3 illustrates the scanning electron microscopy (SEM) images of the micromachined v-groove and the integrated optical fibers. Using a fiber cleaver, the tips of the optical fibers were cleaved. As shown in Figure 5-3-b, the cleaved tip of the fiber has a flat surface. Such a flat surface is necessary to have a symmetrical light coupling between the fibers. The optical fibers are single-mode with an 8.2 µm core diameter, a 125 µm cladding diameter, and a 245 µm coating diameter. The coatings on the integrated portion of the fibers into the v-grooves were stripped off. Therefore, the diameters of the fibers shown in the Figure 5-3 are 125 µm. However, the coatings were left on the rest of the fibers that are outside of the v-grooves. The coating ensures the flexibility of the fibers.

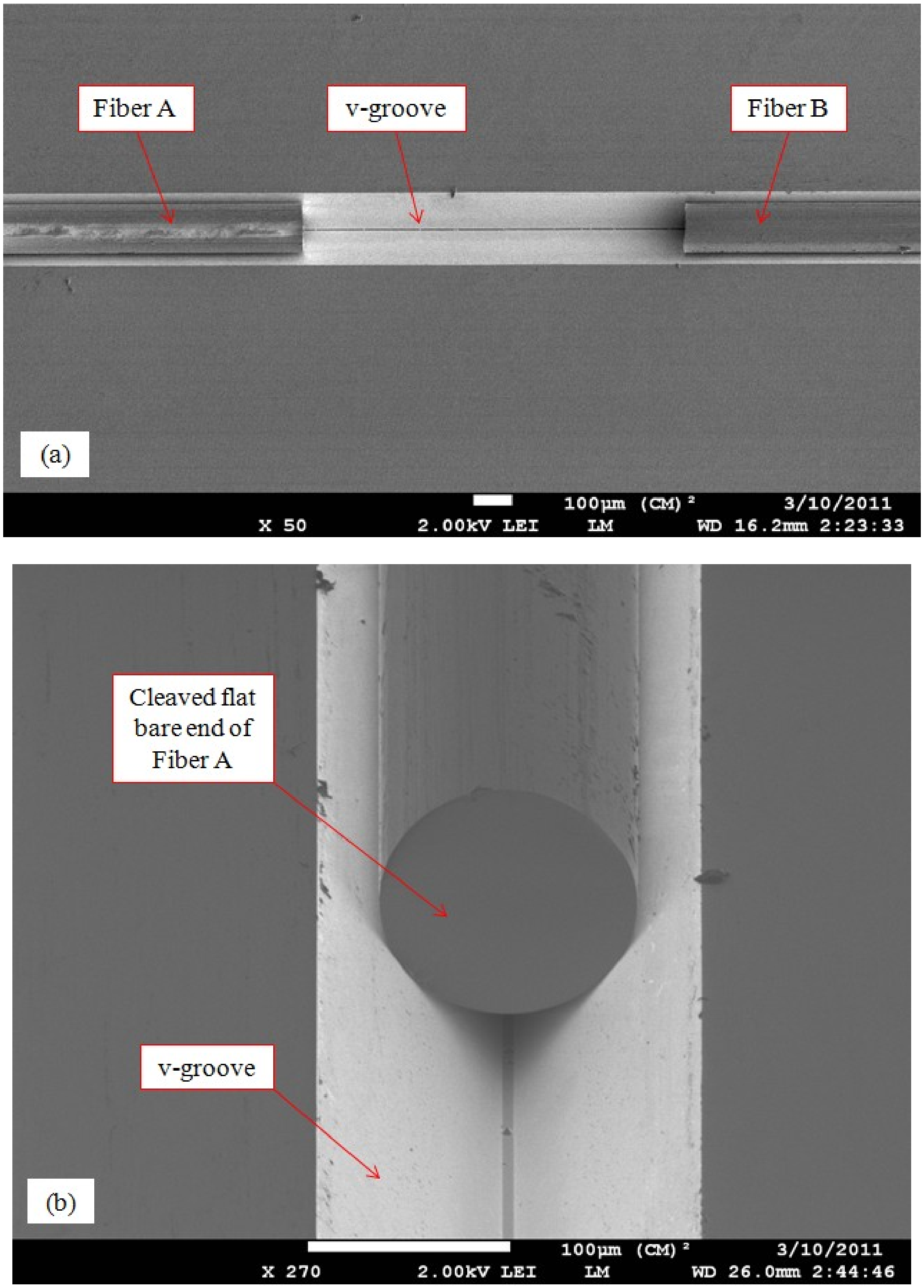

Figure 5-3: The SEM image of the integrated optical fibers into the micromachined v-grooves: (a) the top view of the lower surface of the sensor beam; (b) the flat and cleaved surface of one of the fibers inside the v-groove.

After assembling, the sensor was tested under various experimental conditions to evaluate its performance.

5.4 The Experimental Setup

The sensor was tested experimentally to verify the performance of force measurement. Two different experimental conditions were used: (a) a test with a concentrated force; and (b) a test with a distributed force applied from an artificial tissue. Figure 5-4-a shows the sensor under the test with a concentrated force. The test with the concentrated force was performed to calibrate the sensor. Moreover, in order to simulate the performance of the sensor while interacting with biological tissues during the robotic-assisted surgical tasks, a series of tests with an artificial tissue were also performed. Figure 5-4-b shows the sensor during the test with the artificial tissue. The artificial tissue was made of a Dragon Skin® series of silicone rubber material from Smooth-On Inc. (PA, USA) with a degree of hardness equal to 20 shore A.

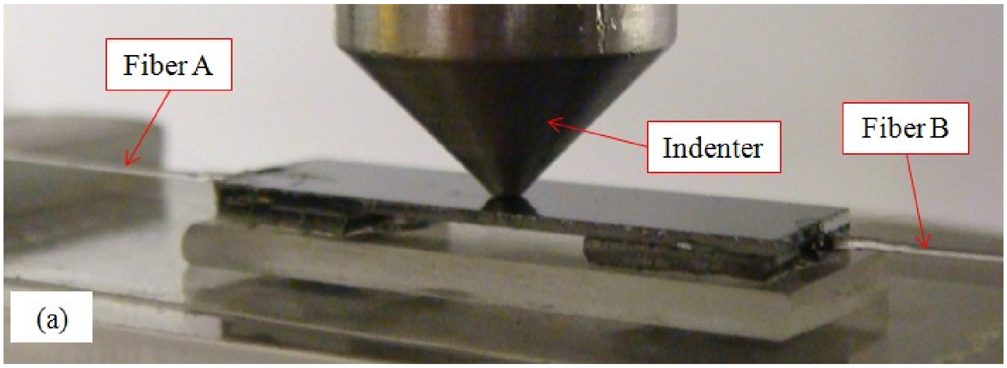

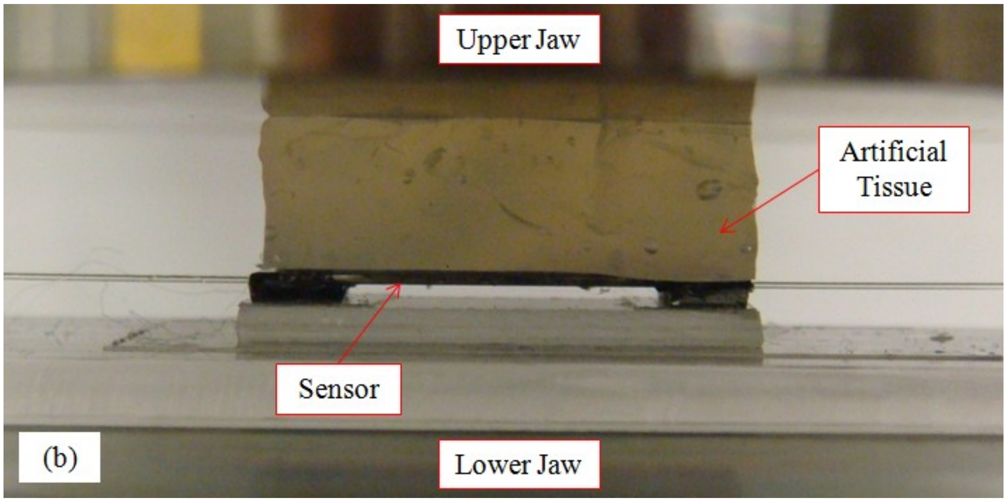

Figure 5-4: The sensor during the tests with (a) concentrated force, and (b) the artificial tissue.

Figure 5-5 shows the diagram of the experimental setup. A light source injects the laser light into Fiber A. The force applied to the sensor beam modifies the intensity of the coupled light into Fiber B. The photodetector converts the intensity of the coupled light into the voltage. Via a DAQ, the output voltage is processed on a computer.

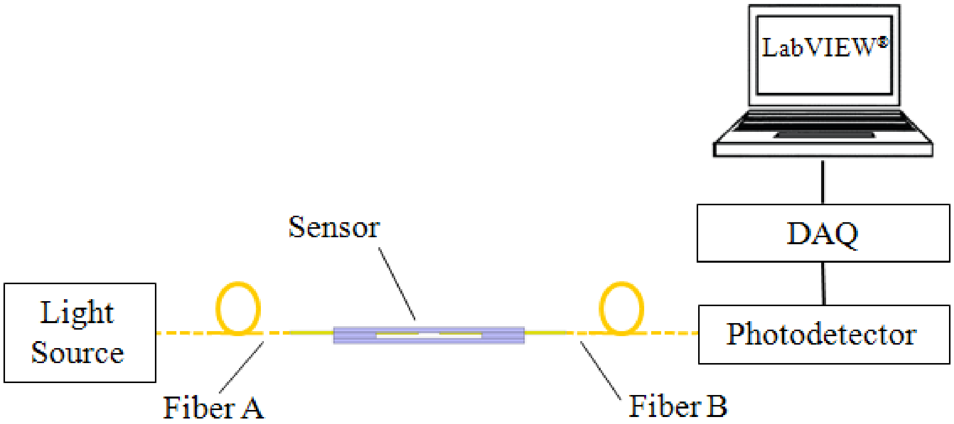

Figure 5-5: The diagram of the experimental setup

In this design, Fiber A and Fiber B were introduced to the sensor structure from two different directions. Such configuration would make the integration of the sensor into the surgical graspers a bit challenging. An alternative design can be used to simplify this integration. As the alternative design, micro mirrors can be used in the structure of the sensor to reflect back the light from one fiber to another. As another option, gold-coated fiber ends can be used to do so. Thanks to these alternative designs, the fibers can be introduced to the sensor from one direction. Such a configuration will facilitate the integration of the sensor into the surgical tools. As can be seen in Figure 5-6, a circulator is required to inject the source light into the sensor and also to direct the reflected light from the sensor into the photodetector.

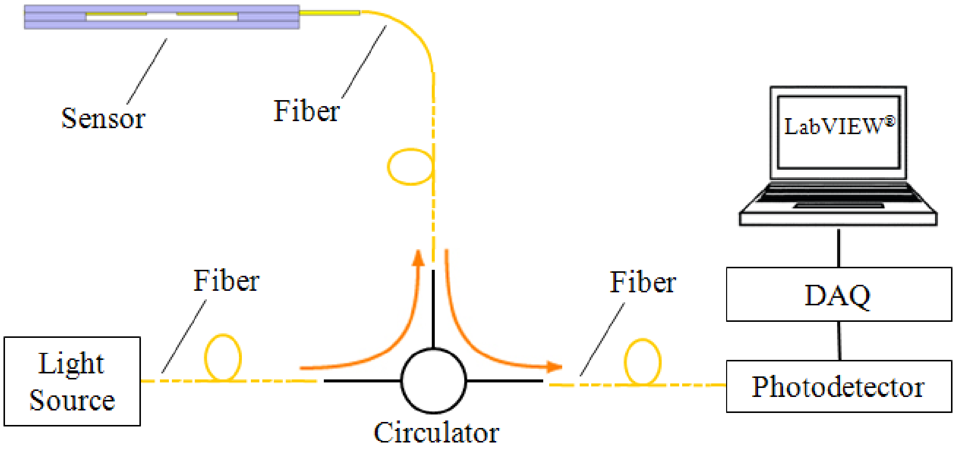

Figure 5-6: The alternative design in which the optical fibers are introduced to the sensor from one direction using micro-mirrors in the sensor beam.

Figure 5-7 shows the photograph of the experimental test setup. The light source is a superluminescent diode (SLD). It is a HP-371 from SUPERLUM DIODES Ltd. (Ireland). At its full-width-half-maximum (FWHM), the spectral bandwidth of the SLD is 53 nm with a center wavelength of 843 nm. The photodetector is a DET02AFC, with a wavelength range of 400 nm to 1100 nm, from Thorlabs Inc. (NJ, USA). The DAQ is an NI PCI-6225. Using an ElectroForce 3200 test instrument from Bose Corp. (MN, USA), known input force functions are applied to the sensor. The input reference force functions can be customized on the WinTest software. This software provides a user-friendly interface to control the parameters of the test. On the one hand, the input force is measured with WinTest. On the other hand, the output voltage of the photodetector is measured on LabVIEW software. After performing the calibration process, which is explained in Section 5.5, the output signal is processed on LabVIEW. The processes signal gives the force as measured by the micromachined sensor.

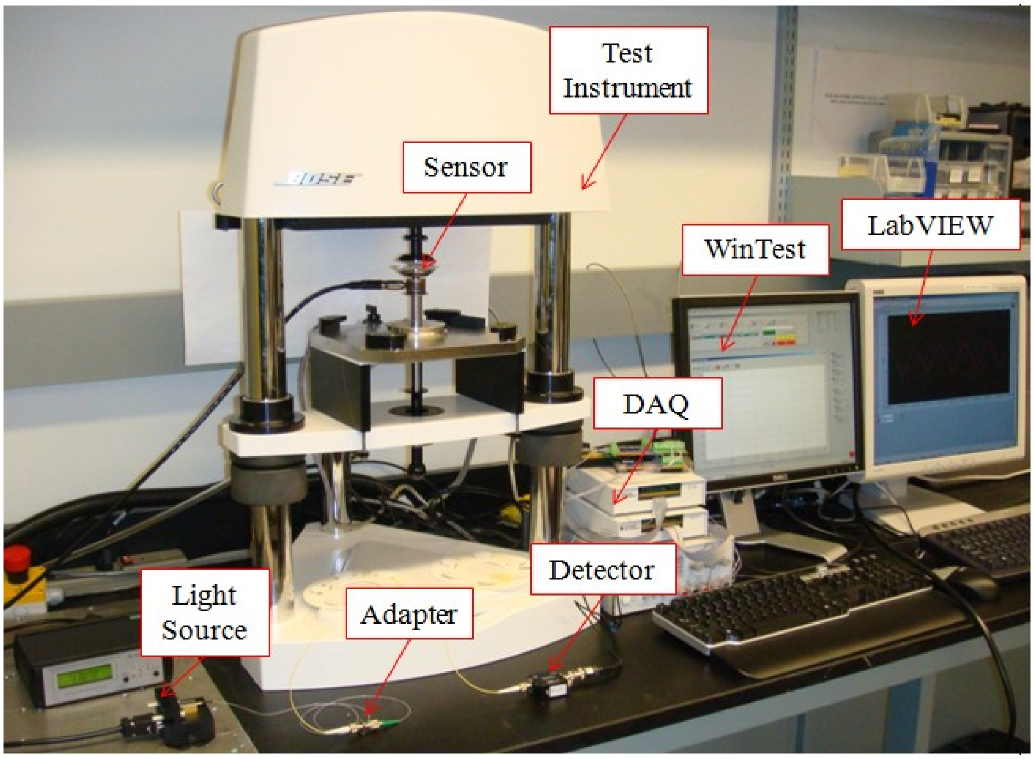

Figure 5-7: The photograph of the experimental setup.

5.5 Experimental Results: Sensor Calibration and Sensor Characterization

5.5.1 Sensor Calibration

A linear calibration is required for the sensor. The response equation of the sensor is defined in LabVIEW as follows:

$$F = AV_{OUT} + B \tag{5.17}$$

where *A* is the constant gain and *B* is the constant bias. The input force applied to the sensor is measured by a 225 N (50 lb) calibrated load cell embedded in the ElectroForce test instrument. WinTest software version 4.0 is installed on the test instrument computer to control the test parameters. The input force, *F*, is recorded with the WinTest software. The output voltage of the sensor, V_{OUT}, is recorded by LabVIEW. Now, by taking Equation 17 into account, *A* and *B* constants can be found. The sampling rates on LabVIEW and WinTest for both sensors were selected as 500 Hz to record the changes in the force as fast as possible. In order to attenuate the high-frequency noise, a low-pass filter was applied to the output signal on the LabVIEW.

5.5.2 Sensor Characterization

In order to characterize the performance of the sensor, various experimental tests were performed. These experimental tests were designed to evaluate the following characterizations of the sensor: first, the sensitivity of the sensor; second, the dynamic response of the sensor; third, the capability of the sensor to perform under static loading conditions; fourth, the rms error of the sensor; and fifth, the resolution of the analog output of the sensor.

First of all, in order to address the sensitivity of the sensor, the ratio between the output voltage of the sensor (V_{OUT}) and the input force (*F*) is obtained before applying the calibration equation to the output signal. Figure 5-8 depicts the output voltage of the sensor for a loading/unloading cycle ranging from 0.0 to 4.9 N. A trend-line, which shows the sensitivity of the sensor, is fitted to the graph. The negative trend of the output voltage against the input force results from the nature of the optical sensing principle. In fact, the greater input force results in greater coupling loss, which causes the smaller output voltage. This is why by applying the greater force to the sensor its output voltage is decreased. However, this negative trend is compensated for in the calibration algorithm applied to the sensor output by the LabVIEW software. The graph also shows the negligible effect of hysteresis associated with the sensor characteristics.

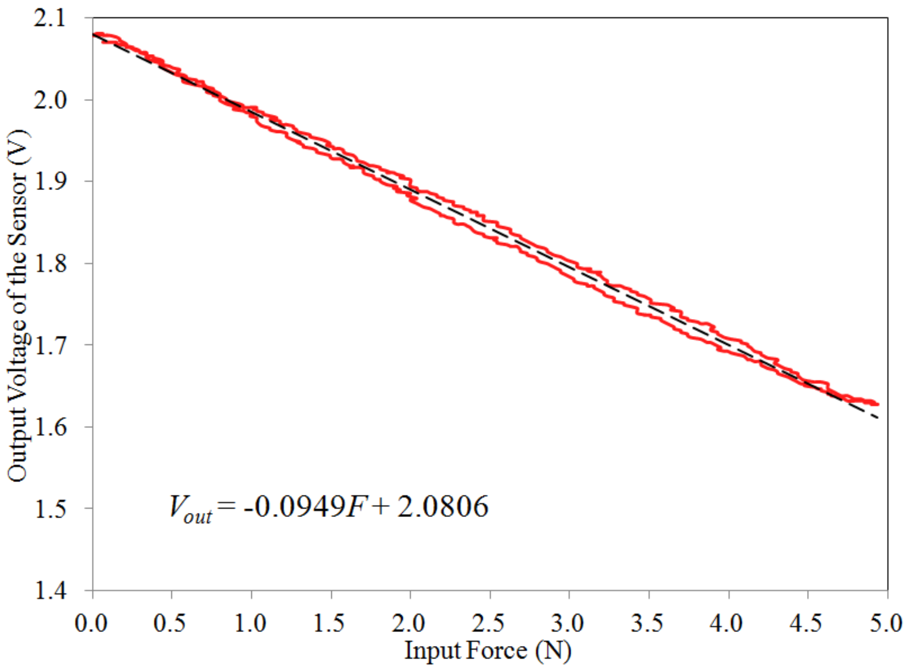

Figure 5-8: The ratio between the output voltage of the sensor and the input force before applying the calibration algorithm to the output signal. The solid line shows the sensor output for a loading/unloading cycle. The dashed line depicts the fitted trend-line.

Secondly, the dynamic response of the sensor is determined. Figure 5-9 compares the response of the sensor and an input linear chirp force from 0 to 5 Hz. For the first 25 seconds of this test, the value of the rms error of the sensor is 0.041 N, which is 2.05% of the force range. In this test, a first-order low-pass filter with a 20 Hz cut-off frequency was applied to the output signal of the photodetector. In robotic assisted surgical tasks, the frequency of mechanical interaction between surgical tools and tissues is usually less than a few hertz. Therefore, the 20 Hz cut-off frequency does not eliminate any useful information from the output signal. However, it eliminates the non-desirable high-frequency noise from the signal. Although the sensor was tested for the 0-2 N range, more tests confirmed the capability of the sensor to measure forces of up to 5 N. For the wider range of force measurement (i.e. more than 5 N), the dimensions of the sensor beam as well as the gap between the fibers can be modified to suit the requirements.

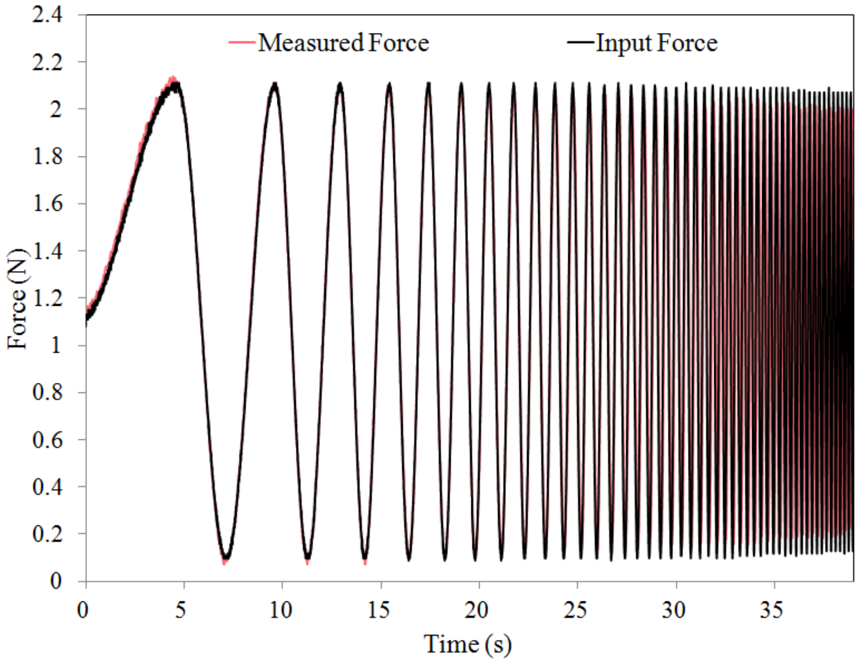

Figure 5-9: The dynamic response of the sensor: comparing the input force and the measured force for a linear chirp force from 0 to 5 Hz.

Thirdly, the performance of the sensor in the measurement of static loads is investigated. In doing so, a square concentrated force with an amplitude of 1.0 N and a frequency of 0.02 Hz was applied to the sensor. Figure 5-10 compares the sensor response with such an input force. In this test, a first-order low-pass filter with 10 Hz cut-off was applied to the output signal. As can be seen in the test results, the sensor has a negligible drift during a period of 25 seconds. This characteristic of the sensor is one of its key features for use in robotic-assisted surgical tasks where surgeons need to keep a continuous stable contact while grasping tissues.

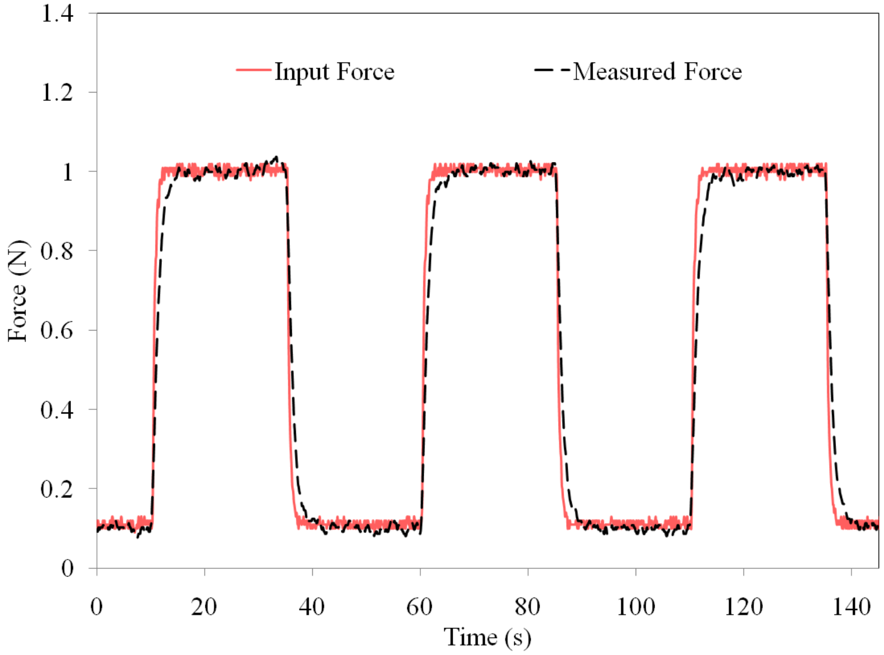

Figure 5-10: The performance of the sensor to measure static loads: Comparing the input force and the measured force for a square function between 0.1 N to 1.0 N with the frequency of 0.02 Hz.

Moreover, Figure 5-11 shows the input force versus the measured force for a square function with linear amplitude increments. In this test, a third-order low-pass filter with a 25 Hz cut-off frequency was applied to the output signal. This test was performed to characterize the hysteresis of the sensor. The amplitude of each increment is 0.1 N and the frequency is 1 Hz. As can be seen in the test results, the sensor shows a low hysteresis effect in the middle section of the graph. This effect can be eliminated by using more solid adhesive materials to bind the components of the sensor together.

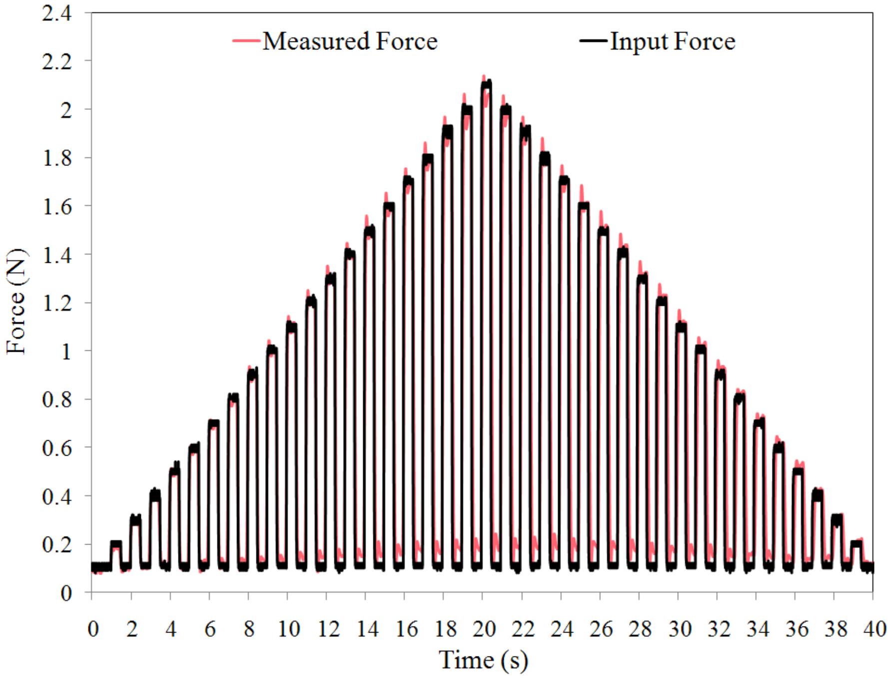

Figure 5-11: Input force versus measured force for a square function with linear amplitude increments.

In addition, in order to evaluate the resolution of the sensor, a square force function with 0.02 N step increments was applied to the sensor. Under such conditions, Figure 5-12 compares the input force and the measured force. In this test, the filter applied to the output signal is a first-order low-pass with a 10 Hz cut-off frequency. As shown in the graphs, the results confirm that the resolution of the sensor is at least 0.02 N. In addition, as can be seen in Figure 5-12-b, the noise level of the fabricated sensor is lower than the noise level of the reference force sensor. The reference sensor is a relatively expensive and relatively large-size load cell that is a part of the ElectroForce test instrument. However, the fabricated sensor in this work is more cost-effective with relatively smaller size and with relatively better performance. Moreover, the reference load is electrical-based, which is neither electrically-pass nor magnetic resonance (MR) compatible.

However, the fabricated sensor is optical-based, being both MR compatible and electrically passive.

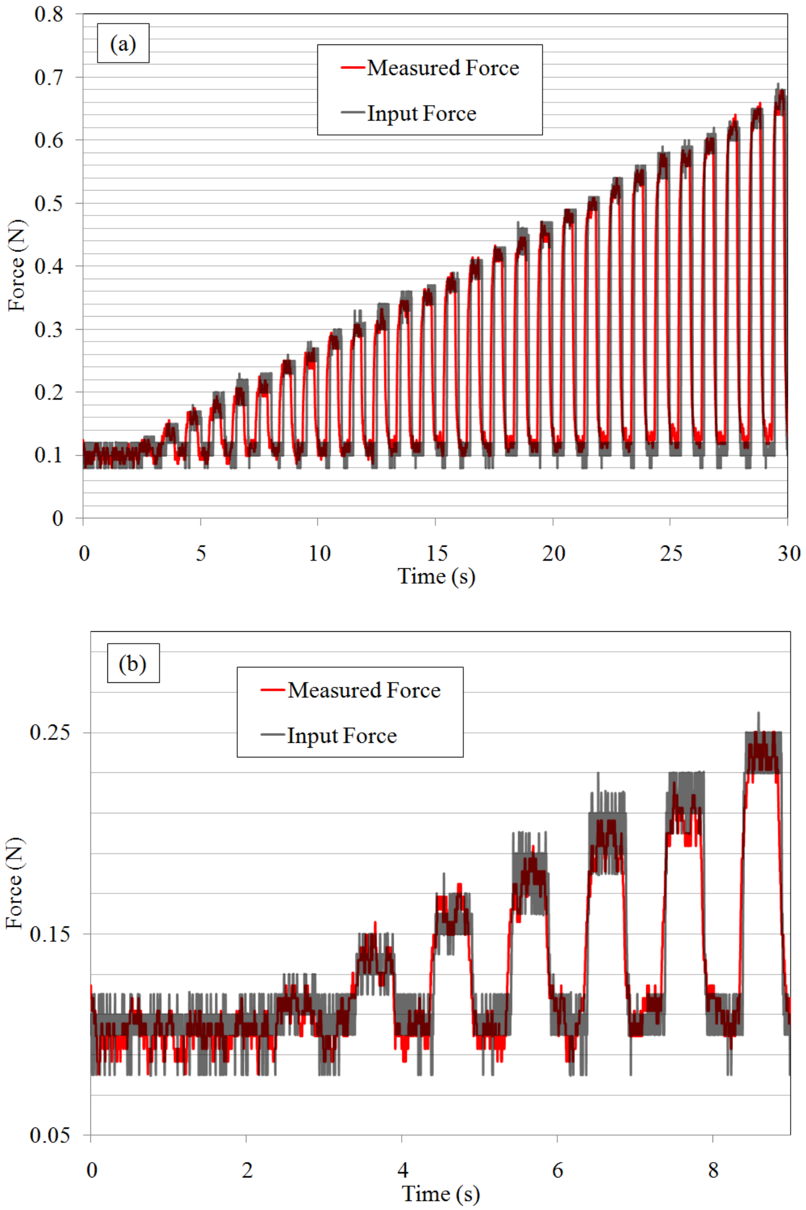

Figure 5-12: (a) Input force versus measured force to evaluate the resolution of the sensor. (b) The magnified graph, which shows that the noise level of the prototyped sensor is lower than the reference commercial force sensor.

Finally, Figure 5-13 shows the dynamic response of the sensor to a triangle force with the amplitude between 0.1 N and 2.0 N and with a 1 Hz frequency. In this test, the cut-off frequency of the order and the cut-off frequency of the low-pass filter was one and 20 Hz respectively. This test was performed to characterize the linearity of the sensor as well as its hysteresis. As can be observed in the graph, the output of the sensor is linear within the tested range. Also in this test, there is no hysteresis effect associated with the sensor.

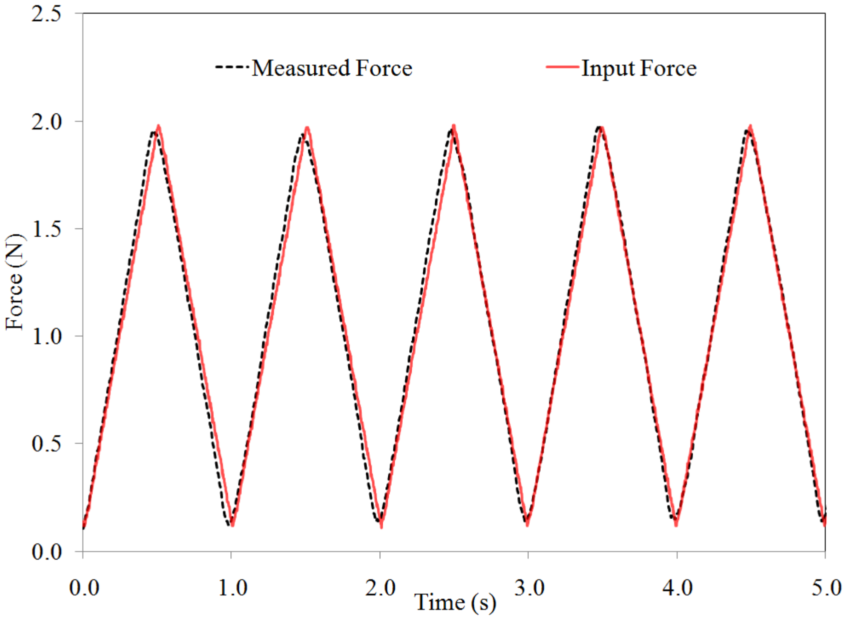

Figure 5-13: Input force against measured force for a triangle force with 1 Hz frequency.

5.6 Conclusions

In this research, an innovative optical force sensor was designed, prototyped, and tested. The performance of the sensor such as its rms error and resolution was characterized. The experimental test results show that the performance of the prototype sensor is better than the commercially-available counterparts of the sensor. Compared to the commercially available force sensors, the prototyped sensor has a relatively smaller size. Due to the simple design of the sensor, it was micromachined with a relatively low cost. In fact, this cost can also be lowered by taking the advantage of the batch fabrication provided by MEMS technology. In addition, the proposed sensor has various unique features: (1) it is magnetic resonance compatible; (2) it is electrically passive; (3) it performs under static and dynamic loading conditions; (4) it is ultrasound-friendly, and (5) it has a high resolution. Thanks to these innovative features of the sensor, there are numerous applications for the sensor not only in the robotics, automation, and medical device industry, but also in many other fields where accurate and highly sensitive static and dynamic force sensing in a harsh environment is required. However, in the first place, the sensor has been designed to be integrated into surgical graspers. This is why the sensor has a rectangular and narrow shape. Such a shape easily allows the sensor to be integrated into the limited space available on grasper jaws.

More pointedly, the prototype sensor has a relatively better performance than some of the commercially available electrical-based ones, which are relatively expensive. In fact, an ElectroForce test instrument from BOSE Corp. was used to determine the performance of the sensor. During the experimental tests, it was observed that the noise level of the prototyped sensor was lower than the noise level of the force sensor of the ElectroForce device. To enhance the performance of the sensor, its design parameters such as the dimensions of the sensor beam and the length of the gap between the fibers can be altered accordingly.

Chapter 6: Optical Array-based Force Distribution Sensing Suitable for Lump/Artery Detection

Surgeons who perform robotic-assisted surgical tasks need to investigate the hidden tissue structures when contacting them using surgical tools. Such an investigation can be addressed with a sensor integrated into the end-effectors of surgical systems. Due to limited space, such a sensor must be miniaturized in size. In the present work, the optical microsystems technology is utilized to develop a miniature force distribution sensor for integration into the surgical end-effectors. The sensing principle of the sensor is based on the mechanism of splice coupling. As the device is fully optical, the sensor is magnetic-resonance compatible and is also electrically passive. The experimental results performed on the developed sensor confirm its ability to measure the distributed force information. Such information is used to detect different tissue structures such as lumps, arteries, or ureters during robotic-assisted surgical tasks.

6.1 Introduction

In recent years, the field of robotics has affected various aspects of people's lives. Among these aspects, the presence of robots in hospitals has affected the lives of many individuals in the need of medical assistance [100]. Surgeons' hands are being rapidly replaced by the end-effectors of sophisticated robotic-assisted surgical platforms [101]. However, unlike the fingertips of surgeons' hands, the robotic end-effectors do not provide surgeons with useful force distribution perception [6, 14]. Although a large number of sensors have been proposed to mimic surgeons' fingertips, there are still unsolved challenges associated with such sensors [96]. Among those challenges, it is important for the sensors to be magnetic-resonance (MR) compatible, electrically passive, ultra-sound friendly, and miniaturized, and these sensors must carry out their functions under static loading [11, 71].

In terms of the sensing principle, available force distribution sensors that have been proposed by researchers or industries can be basically categorized into two groups [11]: the first group is electrical-based sensors; the second group is optical-based sensors. Some of the developed electrical-based sensors, such as those that are piezoelectric based [18], are electrically passive. However, they cannot address MR compatibility since they produce electro-magnetic interference (EMI) [21, 22]. In fact, optical-based sensors offer a number of advantages over electrical-based ones. For instance, they are insensitive to and do not produce EMI [11, 32, 35]. Also they are electrically passive and ultrasound friendly [71]. It is for this reason that they are suitable for use in medical applications where MR compatibility is important and introducing electrical signals into the patient's body is not desired.

Despite the disadvantages of electrical-based sensors, such sensors can be used in surgical applications where MR compatibility and electrical passivity are not required. For instance, Sokhanvar et al. [18, 93] have proposed piezoelectric-based sensors for use in minimally invasive surgery systems. However, because of the characteristics of the piezoelectric sensing element used in their sensor, the sensor does not work under static loading conditions. In another example, King et al. [6, 14] have integrated a commercially available piezoresistive force sensor (FlexiForce) with the end-effectors of the da Vinci surgical systems to provide surgeons with feedback from the contact force between the robot end-effectors and tissues. Their study shows that such force feedback reduces grasping forces during the robotic-assisted surgical tasks performed by the da Vinci robots.

The remarkable advantages of optical fibers [24] have created new possibilities for developing small and low-cost sensors for use in medical applications [102]. In recent years, a large number of such sensors have been proposed to assist surgeons to perform robotic-assisted surgical tasks more reliably [11]. The optical fiber sensors can be categorized as fiber Bragg grating (FBG) sensors, interferometry-based sensors, and intensity-modulated sensors [26]. For instance, for use in surgical tools, Taniguchi et al. [103] have recently developed a force-measurement device using FBG. Also in 2011, two interferometry-based sensors have been proposed [104, 105] for use in surgical applications where surgeries are performed in the presence of magnetic resonance imaging (MRI) devices. Among the three categories of the optical fiber sensors, intensity-modulated sensors offer exclusive features such as less complexity, less expensive equipment, and less sensitivity to thermal-induced strain [27]. In addition, they are typically compatible with micro electro mechanical systems (MEMS) technology.

The present chapter discusses the design, modeling, microfabrication, and testing of an intensity-modulated optical force distribution sensor for integration into the end-effectors of robotic-assisted surgical platforms. The sensor measures the distributed force information by using a single moving part. As a result, it is not necessary to use an array of sensors to measure the distributed force information. Therefore, the sensor can be more easily integrated into small spaces available at the tips of robotic end-effectors. In addition, the developed sensor is MR compatible, electrically passive, ultrasound friendly, and sensitive to both static and dynamic loading conditions. Another feature of the sensor is that it is compatible with cost-effective MEMS batch-fabrication techniques. Such a unique combination of sensor features attracts a large number of applications in the medical device industry. Among them, robotic-assisted surgical platforms have a significant potential for the use of such a sensor.

6.2 Sensor Design

Figure 6-1 shows the structural design of the sensor. The sensor consists of a substrate, four supports, a beam and three pairs of optical fibers. The beam, the supports, and the substrate are made of silicon. The beam is attached to the supports. Three v-grooves are micromachined on the bottom surface of the beam. Three pairs of optical fibers are integrated into the v-grooves of the beam. Figure 6-1-d shows in detail the configuration of the three pairs of fibers inside the v-grooves. A small gap is introduced between the left fiber and right fiber of each pair. The center of the gap between each pair of the fibers A, B, and C is positioned at distances equal to $L/3$, $L/2$, and $2L/3$ (point A, point B, and point C) respectively from the left side of the beam along the x axis (Figure 6-3-a). For each pair, the left fiber and the right fiber are connected to a light source and a photodetector respectively. The sensing principle of the sensor depends on measuring the deflection of the beam at points A, B, and C. To carry out this type of measurement, single-mode optical fibers are integrated into the micromachined v-grooves. In previous works [49, 52], a single-mode optical fiber sensor based on a bending principle was proposed to measure the distributed force information. However, the present design, which is based on coupling loss, is more compatible with MEMS technology than the previous design, which is based on the bending principle. Consequently, the sensor based on the present design can be micromachined at a smaller size to allow integration into the limited space that is available at the tips of the robotic end-effectors.

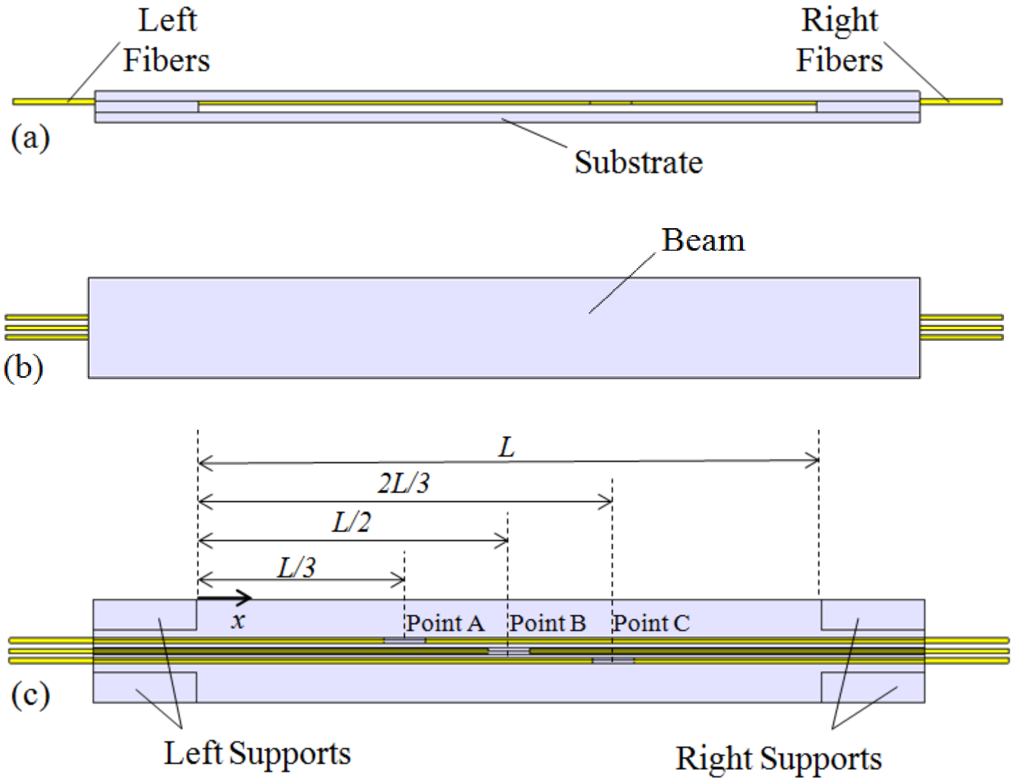

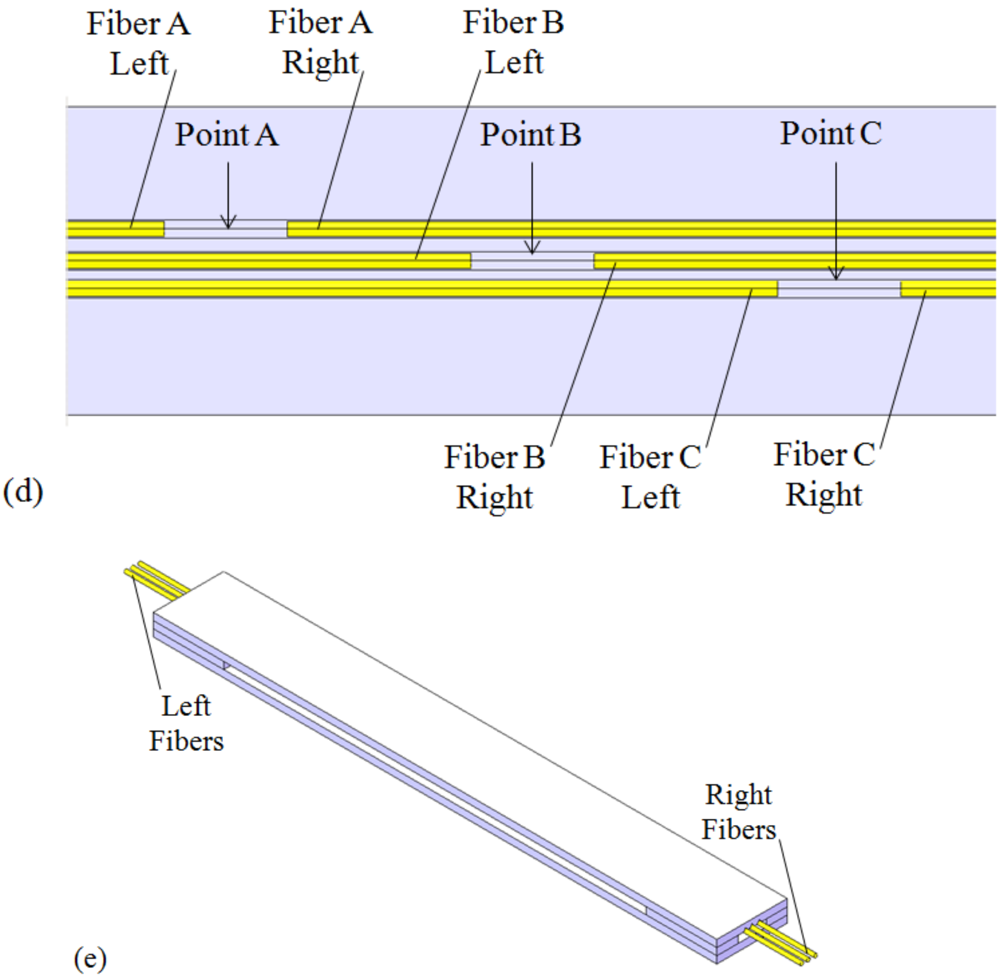

Figure 6-1: The structure of the sensor at different views: (a) front view; (b) top view; (c) top view in which the beam is translucent; (d) the magnified view of the lower surface of the sensor beam; and (e) 3D view.

Generally, the load applied to the sensor beam results in deflection of the beam. The deflection of the beam results in the angular misalignment between both pairs of fibers at points A, B, and C. Figure 6-2 depicts such misalignment between Fibers B Left and B Right at Point B. The angular misalignment results in a coupling loss between each fiber pair. The coupling loss results in the change of the output voltage of each photodetector connected to the right fibers. By processing the output of the photodetectors, the distributed force information can be measured.

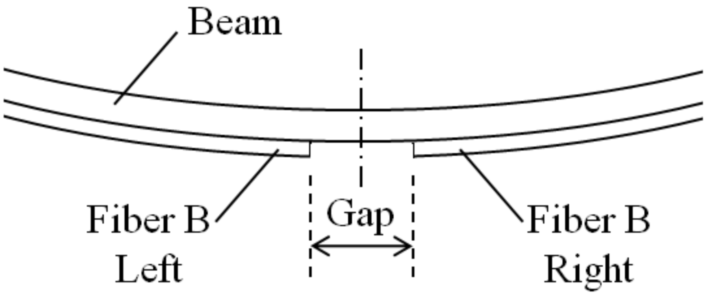

Figure 6-2: Schematic view of the deformed structure of the sensor beam and corresponding optical fibers in the middle part of the sensor beam. Such deformation causes a misalignment between fibers.

Figure 6-3 shows different views of the interaction between the sensor and a soft object containing a hidden solid lump. As depicted, the solid lump is located at position *X* to the left side of the beam. *L* is the length of the beam.

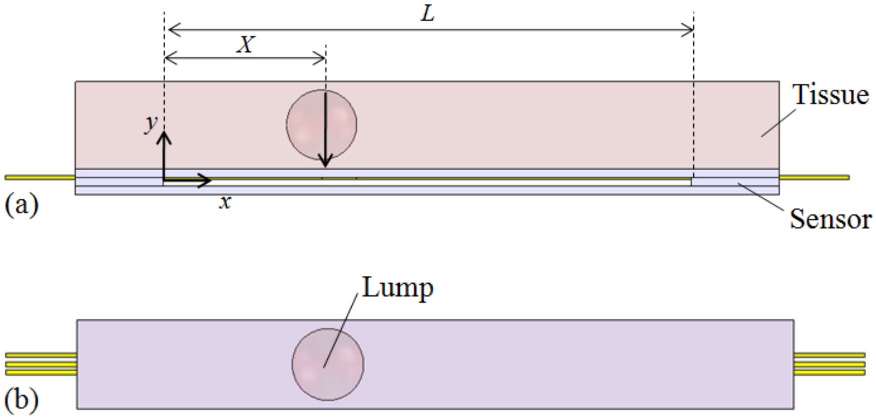

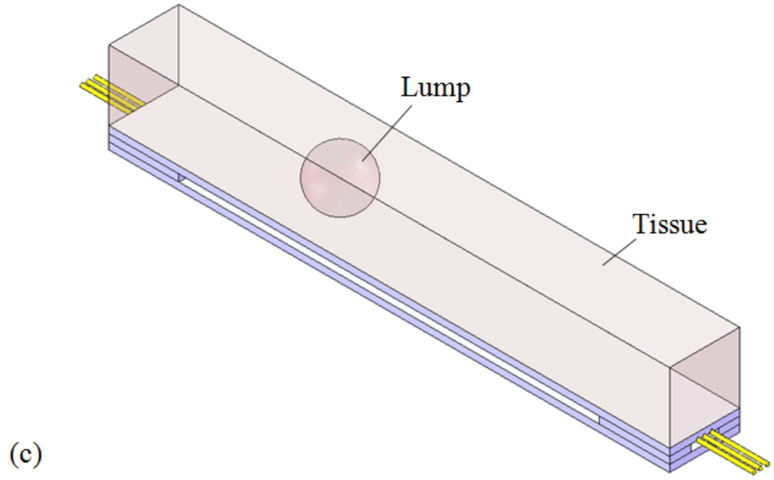

Figure 6-3: The sensor measures the position of a solid lump embedded inside a soft contact object. Interaction between the sensor and a tissue containing a lump shown in (a) front view, (b) top view, and (c) 3D view

Using an algorithm described in Section 6.3, the sensor measures the distributed force information. Measuring such information, the sensor senses the local discontinuities in the hardness of the contact object. In fact, hardness indicates the degree of softness for biological tissues.

6.3 Sensor Modeling

Based on the theoretical formulation for a Euler Bernoulli beam under fixed-fixed boundary conditions [72], the relation between the angular misalignment of each pair of fibers (the slope of the beam at points A, B, and C) and the position of a concentrated force applied to the sensor beam at point X is determined. Moreover, based on theoretical models [98, 99], the relation between the angular misalignment and the resulting coupling loss on each pair of fibers is also determined. In fact, the greater the angular misalignment, the greater the coupling loss and the smaller the output voltage from the photodetector. Figure 6-4 shows the simulated slope of the sensor beam detected by the optical fibers at points A, B, and C caused by a concentrated force applied to point X on the sensor beam. The parameters of this simulation are considered similar to those parameters used in the experimental tests performed on the micromachined sensor. In the simulated model, the modulus of elasticity of the silicon beam is 170 GPa. In real conditions, the silicon beam of the micromachined sensor contains a thin layer of silicon dioxide (SiO_2) with the thickness of 525 nm. However, because of such narrow thickness, this oxide layer has negligible effect on the mechanical properties of the sensor beam. This is why the oxide layer is not considered in the model. The length, the width, and the thickness of the beam are 30 mm, 5 mm, and 500 μm respectively. The gap between each pair of fibers is 1 mm. The concentrated force is 1 N.

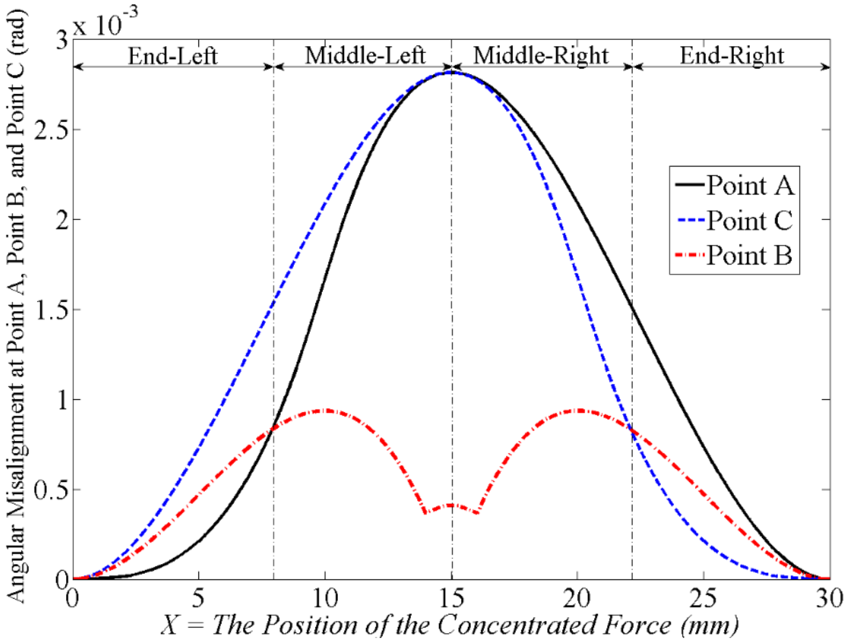

Figure 6-4: Simulation results show the slope of the sensor's beam detected by the optical fibers at point A, point B, and point C caused by a concentrated force applied at point *X*. The 1st, 2nd, 3rd, and 4th quarters of the beam are named End-Left, Middle-Left, Middle-Right, and End-Right in the algorithm.

Based on the simulated results shown in Figure 6-4, an algorithm can be used to measure the position of the concentrated force. This algorithm is illustrated in Figure 6-5. The *VA*, *VB*, and *VC* represent the output voltage from the photodetectors connected to fibers A, B, and C respectively. In fact, the greater the slopes of the beam at points A, B, and C, respectively, the smaller the *VA*, *VB*, and *VC*. By using this algorithm, the position of a concentrated force or an embedded lump can be detected in the four parts of the beam of the sensor: End-Left, Middle-Left, Middle-Right, and End-Right. More pointedly, as illustrated in Figure 6-5, by finding the difference between *VB* and *VA* as well as the difference between *VB* and *VC*, the exact position of the force can be found within each of the four parts of the sensor beam. Now, the position of the concentrated force is known for a specific pre-defined part. In each of these parts, the *VB* gives the magnitude of the contact force. Theoretically, for each pre-defined part, the greater the *VB*, the greater the magnitude of the contact force applied to the sensor. The locations of Point A, Point B, and Point C are selected in such a way that results in the four pre-defined parts of the sensor beam having approximately equal lengths. Using such configuration, the distributed force information can be discretely sensed on these four equal-length parts of the sensor beam.

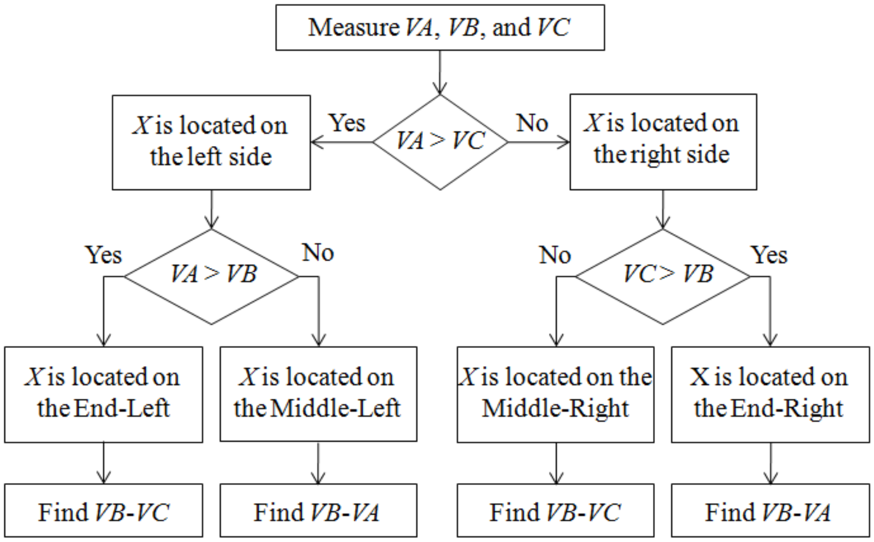

Figure 6-5: The block diagram of the algorithm to measure the position of the concentrated force (*X*).

In fact, the position of the concentrated force corresponds to the location of the solid lump embedded inside the soft background tissue. For the use of the sensor in robotic-assisted surgical platforms, knowing the amount of the interaction force between the sensor and the tissue, which is a combination of concentrated and distributed forces, helps surgeons avoid tissue damage. This force can be determined by processing the output of the sensor from Fiber B. Under the specific conditions of different types of surgical application, the required range of force measurement and the required resolution may vary. However, the specifications of the sensor, such as its range and its resolution, can be tuned accordingly by modifying the dimensions of the sensor beam and also by changing the configuration of the integrated optical fibers. Such configurations include the position of the gaps between each pair of fibers on the beam, the length of each gap, and the number of optical fiber pairs.

6.4 Sensor Microfabrication

In order to evaluate the performance of the sensor, a prototype was developed. MEMS technology was used to microfabricate the components of the sensor. Figure 6-6 shows the components of the sensor before the assembly. Using a dicing saw machine (ECSE 8003), the substrate and the supports were cut from an N-Type <100> silicon wafer. Using an anisotropic silicon wet etching technique, three v-grooves were microfabricated on the bottom surface of the sensor beam. In doing so, a thin layer of silicon dioxide (SiO_2) with the thickness of 525 nm was first of all deposited on the silicon wafer. The thermal oxidation method was used to grow the oxide layer on the silicon wafer. Secondly, using a SpinBall Spin Station from SITE Services, Inc. (Santa Clara, CA, USA), a photoresist layer (1813 Shipley resist) with the thickness of 1.4 µm was deposited, using spin-coating, on the wafer and was then baked at 115°C for 60 seconds. Third, using an EVG620 Automated Mask Alignment System (EV Group GmbH, Austria) with a mask, the photoresist layer was patterned according to the design of the mask. The mask is designed so as to microfabricate various sizes of v-grooves with a variety of combinations on the silicon wafer. Fourth, the patterned photoresist layer was baked at 90°C for 90 seconds (a hard bake). Fifth, the unprotected oxide layer was etched inside a wet bench containing a 6:1 buffered oxide etch (BOE) solution, containing six parts of 40% ammonium fluoride (NH_4F) and one part of 49% hydrofluoric acid (HF) in water. Finally, using the Tetramethylammonium hydroxide (TMAH) wet etching at 85ºC with 25% concentration, the v-grooves were microfabricated on the silicon wafer. Afterwards, a dicing saw machine (ECSE 8003) was used to cut the sensor beam precisely out of the silicon wafer respecting the dimensions. The other components, such as the sensor substrate and the sensor, supports were cut from an unprocessed N-Type <100> silicon wafer using the same dicing saw machine.

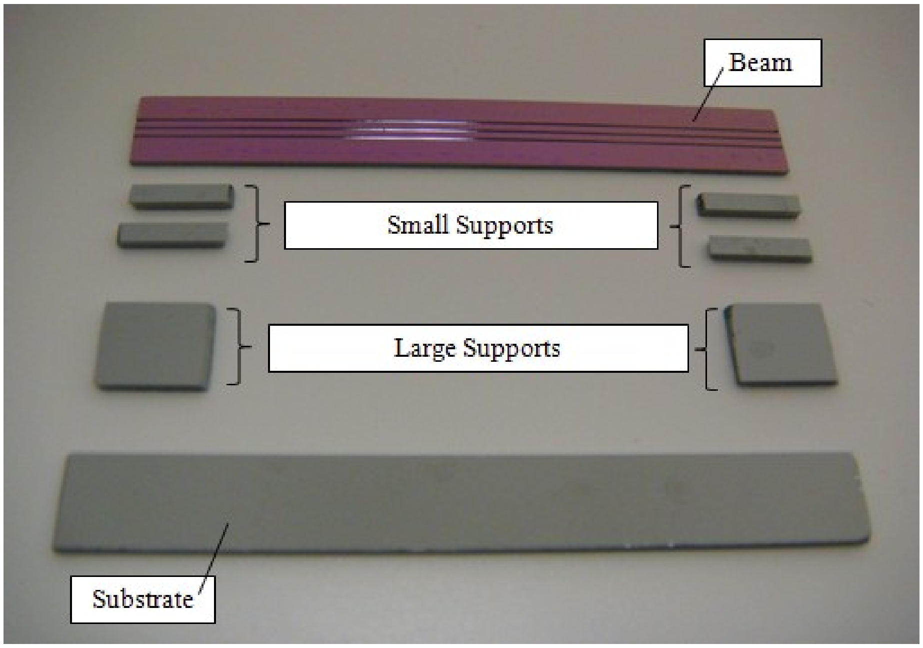

Figure 6-6: The components of the sensor before assembly.

Figure 6-7 shows the beam of the sensor after integrating the optical fibers into the microfabricated v-grooves. The general view of the bottom surface of the beam with the integrated optical fibers is illustrated in Figure 6-7-a. In order to fix the optical fibers inside the v-grooves, an optical adhesive from Norland Products (NJ, USA) was used. The adhesive was cured by exposure to an ultra-violet (UV) light. This method allowed the perfect alignment between the pairs of optical fibers inside the v-grooves before fixing them. Figure 6-7-b shows the magnified view of the middle of the beam under the microscope. As can be seen in this view, there is a gap in the middle of the beam of 1 mm between the bare ends of Fiber B-left and Fiber B-right.

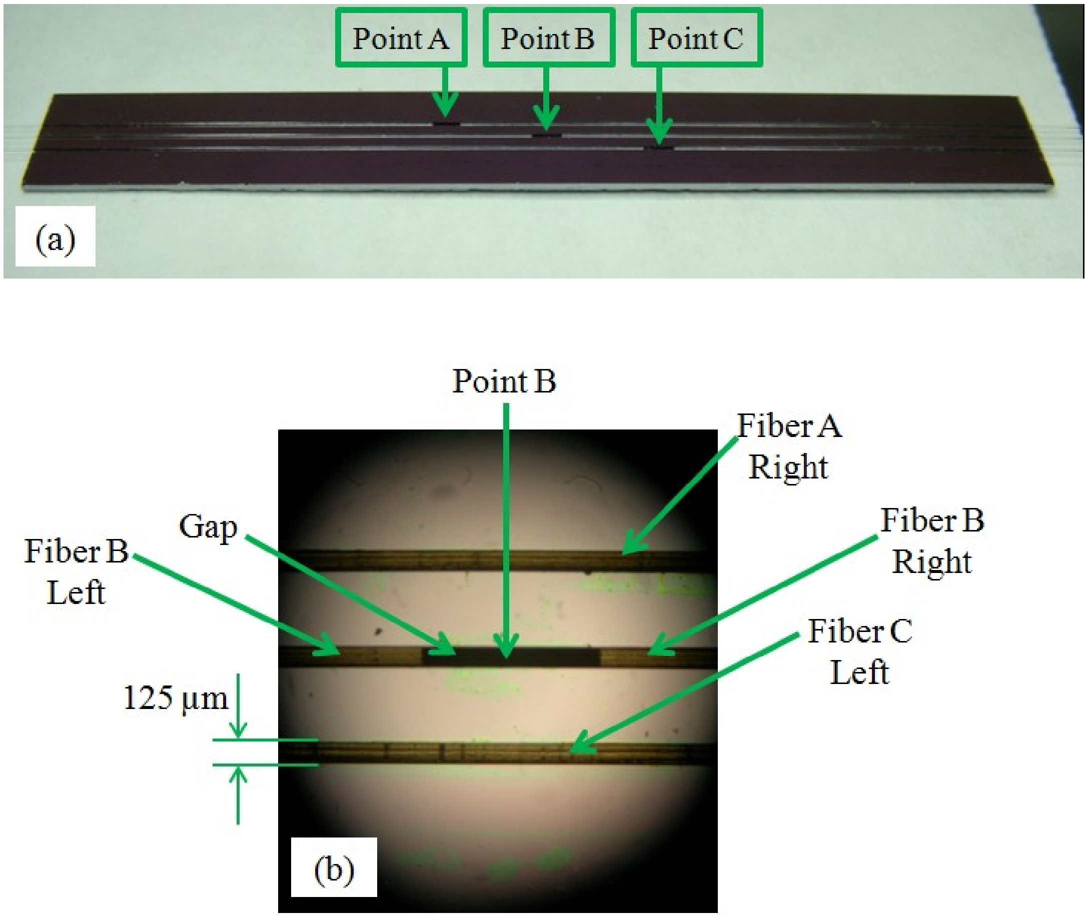

Figure 6-7: The beam of the sensor: (a) bottom surface of the beam; (b) the magnified view of the middle of the beam under the microscope.

A JSM-7600TFE filed emission-scanning electron microscope (JEOL Ltd., Japan) was used to investigate the quality of the microfabricated v-grooves by examining the Scanning electron-microscopy (SEM) images. Figure 6-8 shows the SEM images of the microfabricated sensor beam. The view of the bottom surface of the sensor beam is shown in Figure 6-8-a. The angled view of the edge of the sensor beam is shown in Figure 6-8-b. As can be seen in these SEM images, the surface quality of the (111) plane of the silicon beam is considerably smooth so as to allow the uniform insertion of the optical fibers inside the v-grooves. The width of each v-groove is approximately 150 µm.

The optical fibers are single-mode with 8.2 μm, 125 μm, and 245 μm for core, cladding, and coating diameters respectively. Along the portion of the fibers integrated into the v-grooves, the fiber coating layers were stripped away. Such conditions resulted in fibers with 125 μm diameters integrated into the v-grooves with 150 μm widths. The bare ends of each pair of optical fibers were precisely cleaved by a fiber cleaver. The cleaving produces a flat surface at the bare end of each fiber, thereby ensuring a symmetrical light coupling between the corresponding optical fibers. To ensure the flexibility of the optical fibers that were attached to the sensor, the coating layers were left along the other portions of the fibers outside of the v-grooves.

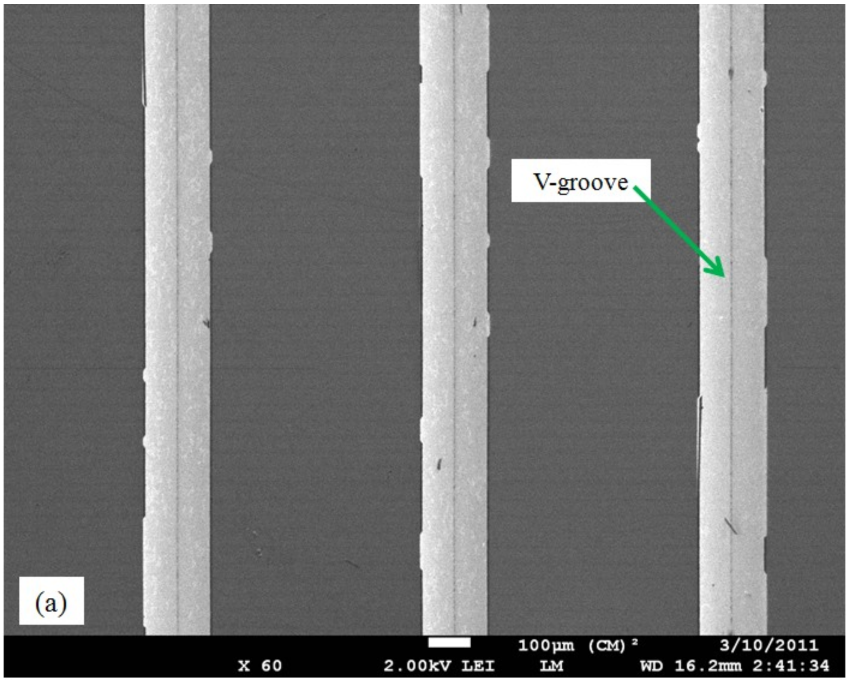

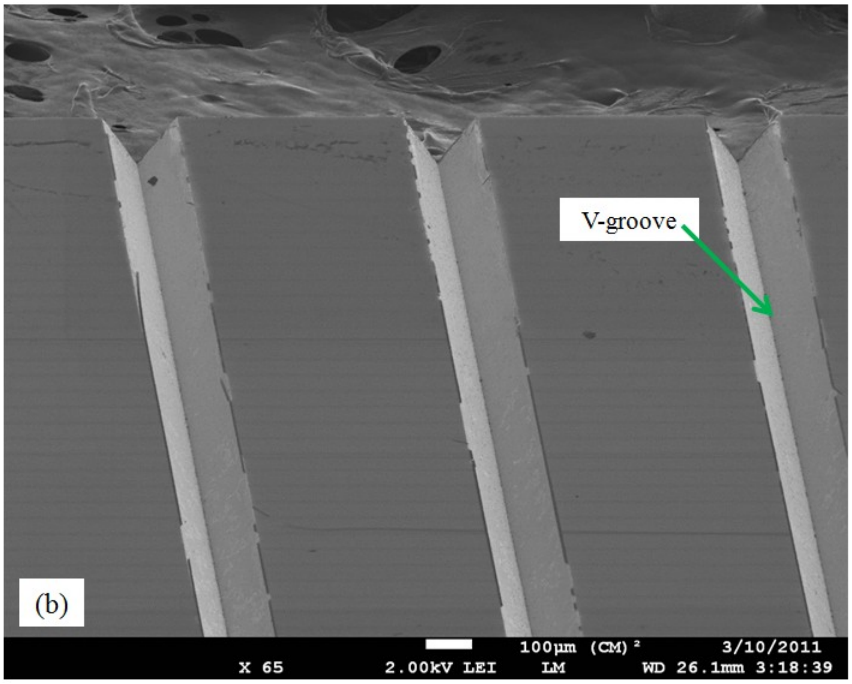

Figure 6-8: The SEM images of the v-grooves made along the lower surface of the sensor beam: (a) top view; (b) angled view of the beam edge.

6.5 Experimental Setup

In order to examine the performance of the sensor, it was tested under different experimental test conditions. Figure 6-9 shows the microfabricated sensor under different experimental test conditions. Figure 6-9-a, Figure 6-9-b, and Figure 6-9-c show the sensor in a test with a concentrated force, with an embedded lump in an artificial tissue under uniform loading, and with an embedded artery in an artificial tissue under uniform loading respectively.

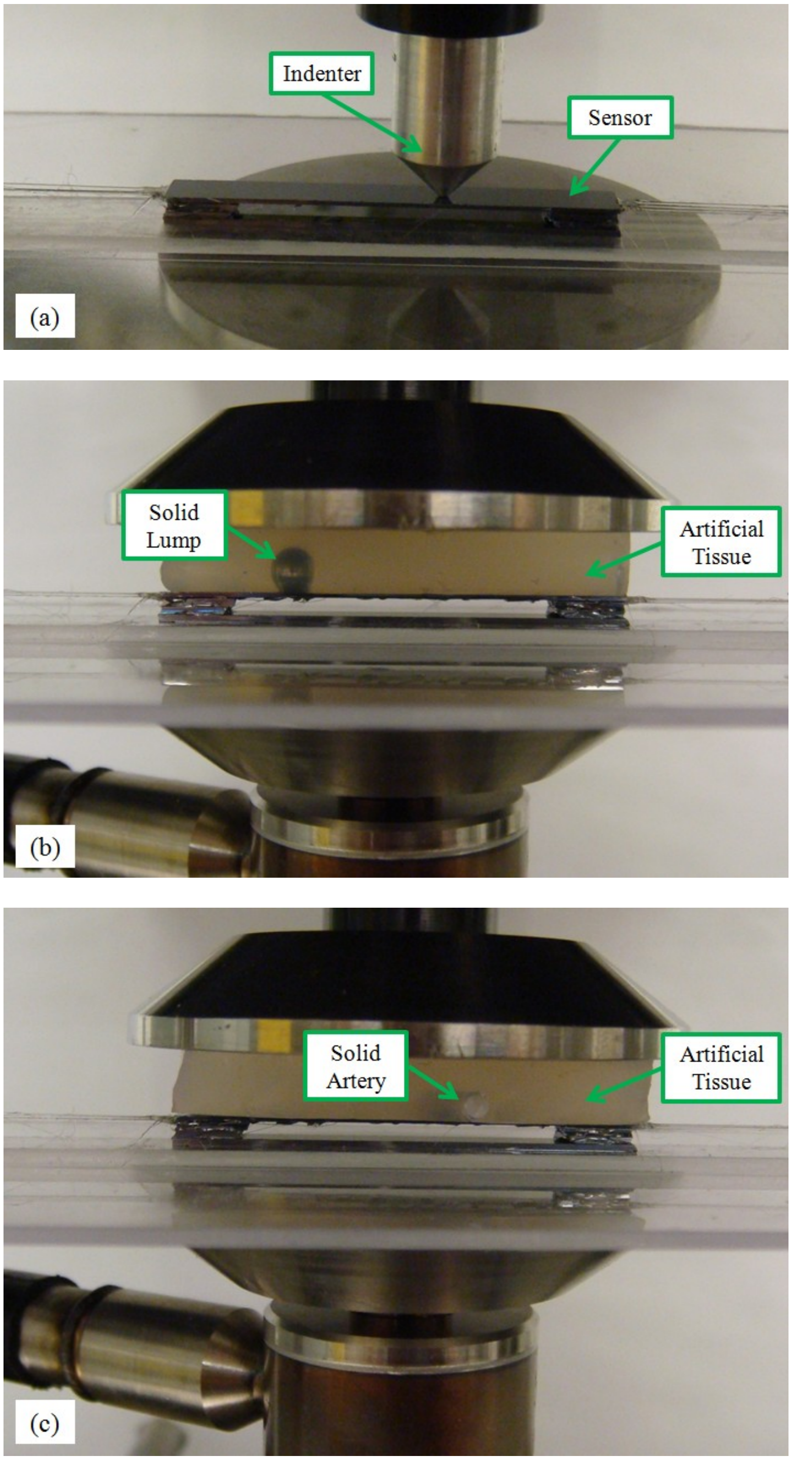

Figure 6-9: The sensor under different experimental conditions to measure the position of: (a) a concentrated force, (b) an embedded lump in an artificial tissue under uniform loading, and (c) an embedded artery in an artificial tissue under uniform loading.

Figure 6-10 shows the photograph of the experimental setup. The light source is a HP-371 superluminescent diode (SLD) made by Superlum Inc. in Ireland. It injects a narrow-band light spectrum with a central wavelength of 843 nm into the left parts of fibers A, B, and C. At full-width-half-maximum (FWHM) of the SLD light source, its spectral bandwidth is 53nm. Through the gaps between the corresponding fibers inside the v-grooves, the light couples into the right parts of the optical fibers. Separately, the ends of the right parts of the fibers are coupled into three photodetectors. The photodetectors are DET02AFC from Thorlabs Inc. (NJ, USA), with a wavelength range of 400 nm to 1100 nm. A DAQ is used to transfer the output voltage of the photodetectors to a computer using LabVIEW software. The DAQ is a PCI-6225 from National Instruments. The sensor is fixed on the lower jaw of an ElectroForce 3200 test instrument from Bose (MN, USA). Through the upper jaw of this test instrument, various known input loads are applied under different experimental conditions of concentrated force test and distributed force test with artificial tissue. To control the input parameters such as applied load and displacement, a software interface is connected to the test instrument. This software, which provides an object-oriented environment to control the parameters, is WinTest. The input loads are customized on the WinTest software connected to the test instrument. These input loads are measured on the WinTest. The sensor output from the photodetectors connected to Fibers A, B, and C is measured with LabVIEW software. Using the algorithm represented in Figure 6-5, the output signals are processed with LabVIEW to measure the distributed force information on the sensor beam.

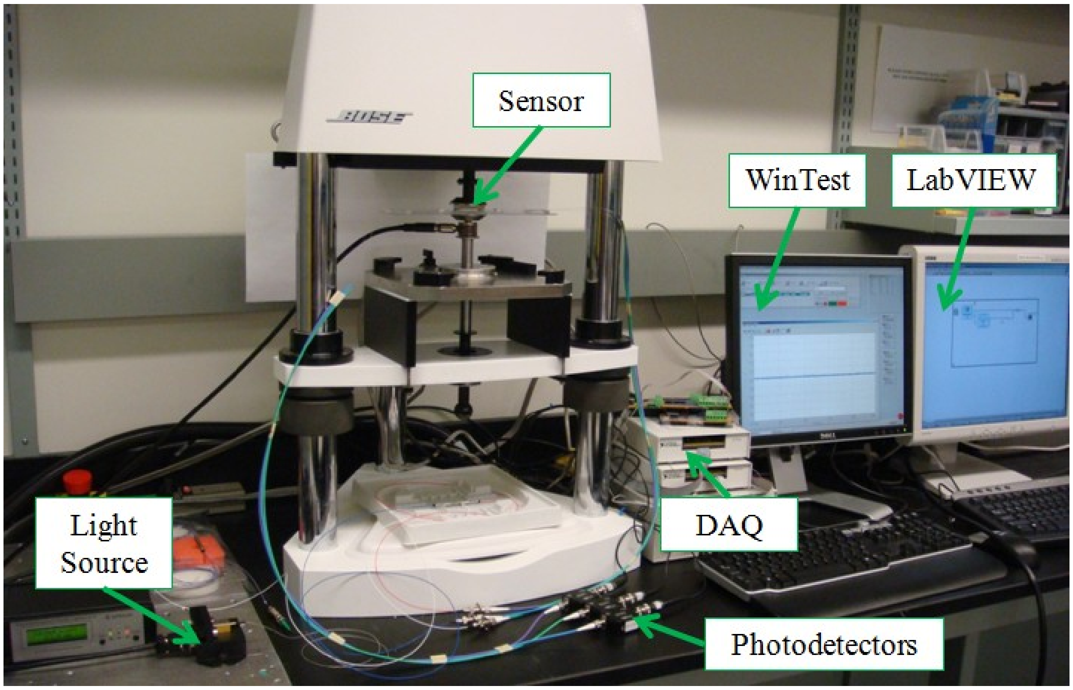

Figure 6-10: Photograph of the experimental setup.

6.6 Experimental Results

To confirm the performance of the sensor, different experimental tests were performed. In the first test, the response of the sensor to a concentrated force was examined. A triangle force function with an amplitude between 0 to 2 N and the frequency of 1 Hz was selected for this test. A triangle function was selected to examine the linearity and the hysteresis of the sensor. Also the selected 1 Hz is a reasonable frequency for the interaction between surgical tools and tissues. For instance, in beating heart surgery [71] such frequency is in the range of beating frequency of the heart, which is approximately 1 Hz. The main purpose of this test is to measure the position of the concentrated force by processing the sensor output. Figure 6-11 shows the sensor response while a concentrated force is applied to the Middle-Right part of the beam. As can be seen in the graph, the relation between the output voltage of the sensor for Fibers A, B, and C is: *VA<VC<VB*. Knowing this relation and using the proposed algorithm given in Figure 6-5, the position of the concentrated force can be obtained. Under such conditions, the algorithm determines that the Middle-Right part is the position of the concentrated force. This position is the same as the real position of the applied force. Consequently, this test confirms the ability of the sensor to measure the position of a concentrated force. Such a concentrated force can be produced by a hidden lump or artery embedded in a soft background tissue. Although the linearity and the hysteresis of the sensor output have not quantitatively characterized, visual characterizations of the results confirm a reasonable linearity and a low hysteresis effect for the sensor.

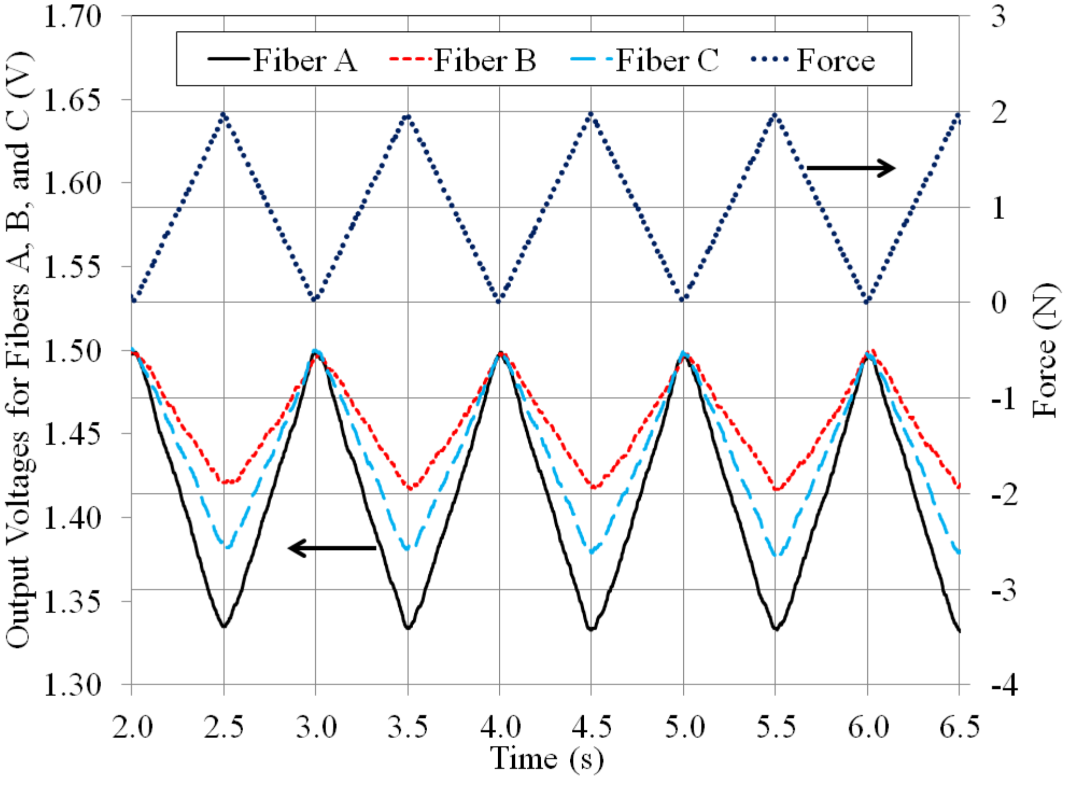

Figure 6-11: The response of the sensor to a concentrated triangle force with the frequency of 1 Hz applied to the Middle-Right part of the sensor beam.

In order to characterize the drift of the sensor output, a square concentrated force with an amplitude between 0 to 2 N and the frequency of 0.05 Hz was applied to the Middle-Left part of the sensor. Figure 6-12 shows the sensor response to such force function. This test validates two important sensor characteristics. First, the sensor measures the location of the force applied on the Middle-Left part by using the algorithm. Second, the sensor undergoes negligible amount of drift under static loading conditions. The second characteristic ensures a stable tool-tissue interaction when surgeons need to maintain the contact.

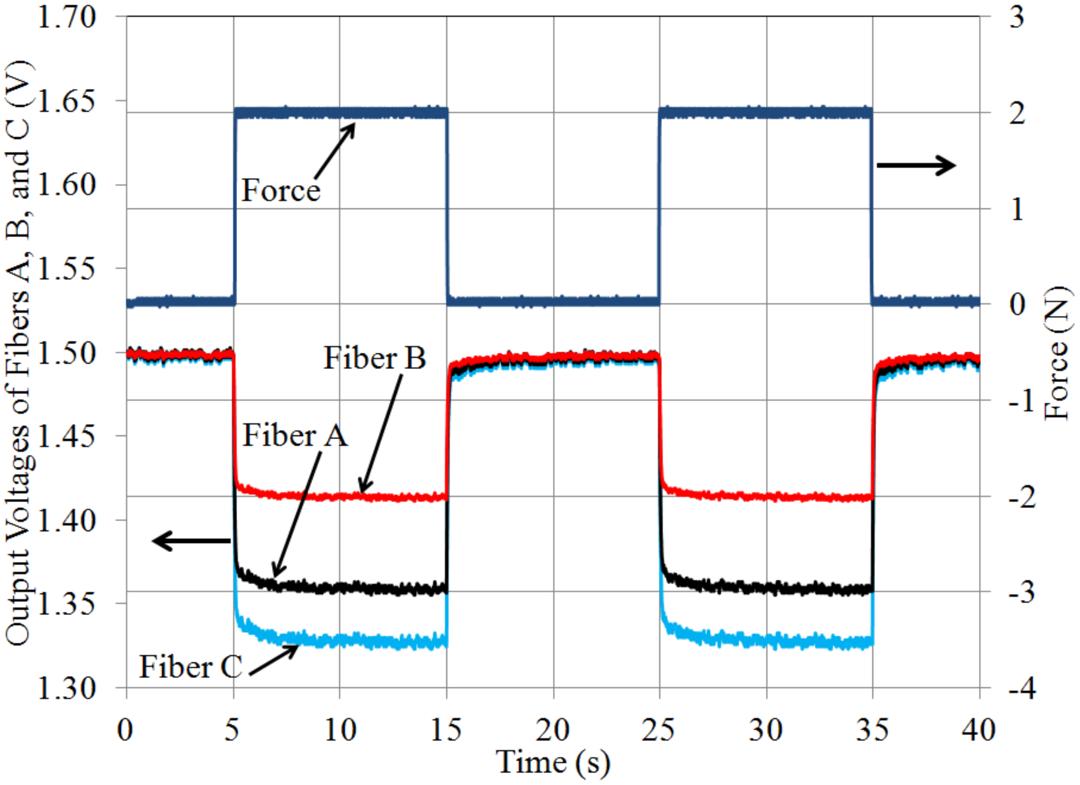

Figure 6-12: The response of the sensor under static loading conditions. A concentrated square force with the frequency of 0.05 Hz applied on the Middle-Left part of the sensor.

Another test scenario was applied to investigate the ability of the sensor to detect the position of a hidden hard lump/artery embedded inside soft background tissues. In this test, a silicone rubber material with the degree of hardness equals to 10 shore OO was used as an artificial tissue. As shown in Figure 6-12, a solid cylindrical-shape artery was embedded inside the artificial tissue on the right part of the sensor. Under such conditions, Figure 6-12 shows the response of the sensor to a square force with amplitude between 0 to 10 N and the frequency of 0.02 Hz. The results show that *VA* is greater than *VC*. Based on the algorithm, it means that the artery is located on the right side of the sensor, which is correct. Moreover, the sensor output has a negligible drift during the 25 seconds of static sensor-tissue interaction.

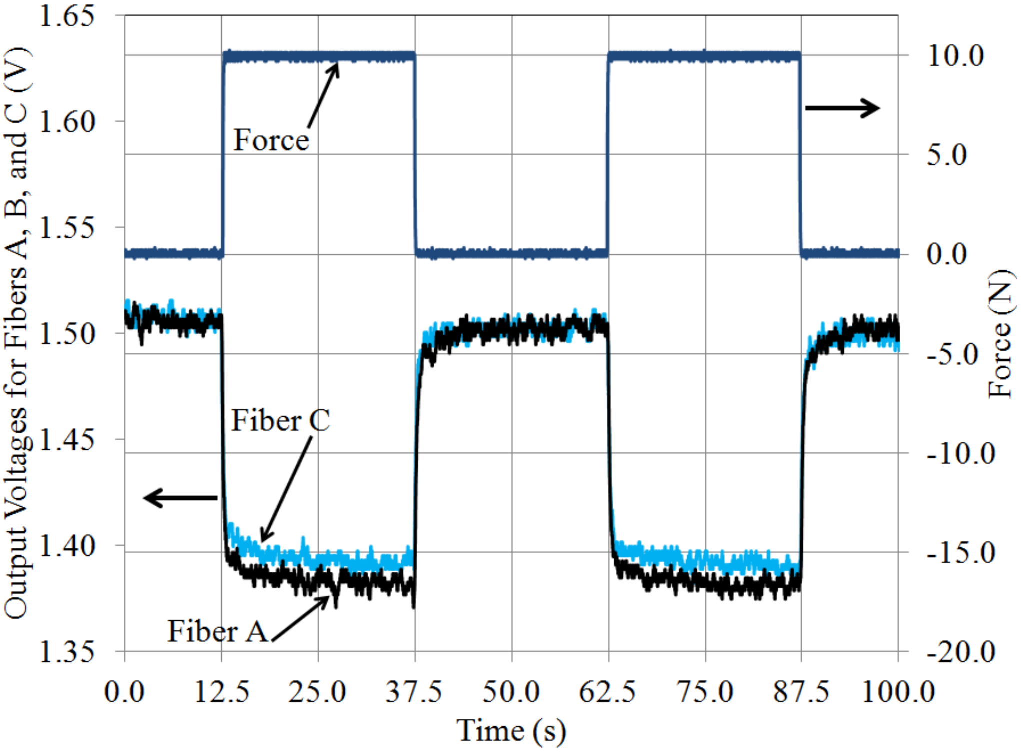

Figure 6-13: The sensor measures the location of an artificial artery embedded on the right part of the sensor in an artificial tissue.

Finally, Fiber A was chosen to compare the experimental results with the simulation results. Fiber A and Fiber B have symmetry with respect to the middle point of the sensor beam. This is why only Fiber A was selected for this test. Figure 6-14 shows the average values and error bars of the experimental output for Fiber A as well as the simulated out when a concentrated force is applied to the sensor at twelve different points starting 1.25 mm from the left side of the sensor beam at 2.5 mm intervals. For each point, the test was repeated 20 times. As can be seen in the graph, the repeatability of the sensor for each point is in a reasonable range. This graph also shows a very important characteristic of the sensor for measuring the position of a concentrated force. Comparing this graph with Figure 6-4 shows that instead of using all three output channels of the sensor, only two channels (Channels A and B) can be used to measure the position of a concentrated force on only the half-left part or only the half-right part of the sensor beam. Such measurement reduces the complexity of the sensor design as well as of the post-processing software. However, as a trade-off, it limits the range of measurement to half of the sensor beam length. In other words, to achieve this simpler sensor configuration, although only two pairs of optical fibers are needed, a sensor twice as long is needed to measure the same range compared to the sensor with three pairs of fibers.

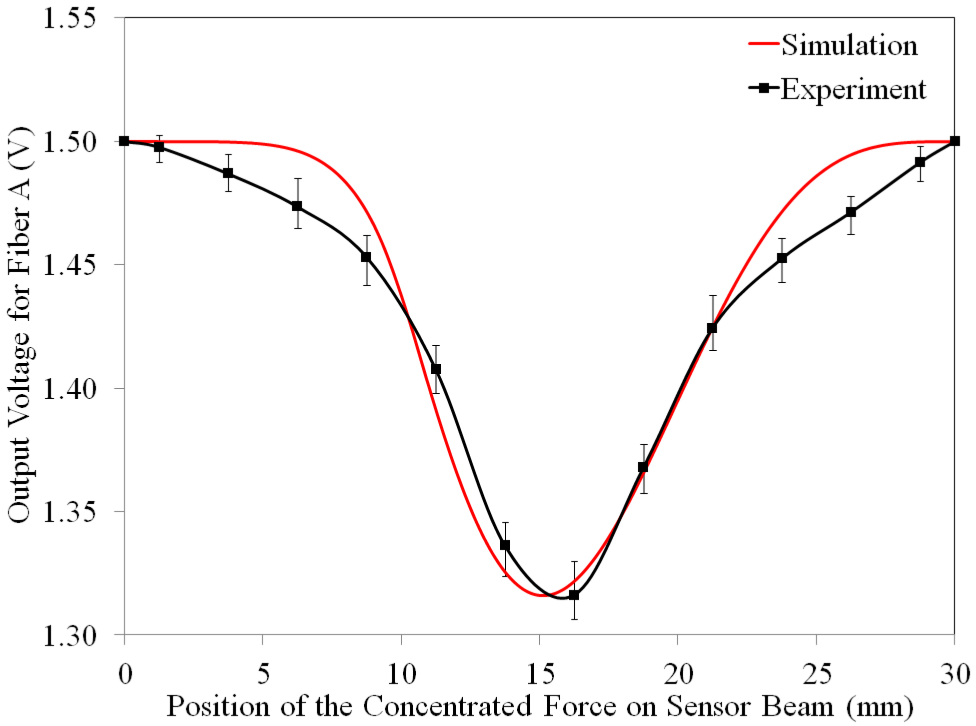

Figure 6-14: Comparison between the experimental and simulated sensor output for Fiber A when a concentrated force is applied to different points on the sensor beam. The error bars indicate the range.

6.7 Conclusions

In brief, the feasibility and the performance of an innovative beam-type optical fiber force sensor for use in surgical applications were investigated in the present work. The novelty of the proposed sensor lies in its measuring the distribution of force information by using only one single moving part, which is a beam. The sensor can be fitted into any narrow space available at the tips of surgical tools. More importantly, unlike the available electrical-based sensors, the proposed sensor performs under static loading conditions. In addition, it is insensitive to electromagnetic interference and it is also electrically passive. The proposed sensor was fabricated and then tested using microsystems technology. In the use of this technology, the slope of the single moving part of the sensor is measured in different points. Based on this multi-point measurement, an innovative idea is then applied to sense the distributed force information applied to the moving part of the sensor. A theoretical model of the sensor was developed. This theoretical model was utilized to develop an algorithm. The algorithm was applied to the sensor output to measure the distributed force information. The test results confirm the ability of the sensor to measure local discontinuities in the hardness/softness of contact objects. Such contact objects can be biological tissues and such local discontinuities can be arteries, ureters, or hidden tissue abnormalities such as cancerous lumps inside the tissues.

Chapter 7: Fully Optical Microsystem for Static and Dynamic Relative Hardness Sensing

The present chapter discusses the designing, prototyping, and testing of an innovative tactile sensor. The proposed tactile sensor measures the degree of hardness of soft objects such as biological tissues. It performs such measurements under both static and dynamic loading conditions. More significantly, it is magnetic resonance (MR) compatible, electrically passive, and ultra-sound friendly. These unique characteristics of the sensor make it a practical choice for use in robotic-assisted surgical platforms. The prototype version of the sensor was developed by using optical microsystems technology. The experimental test results performed on the prototyped sensor have validated its ability to measure the relative hardness of artificial tissues.

7.1 Introduction

In recent years, the presence of high-tech medical devices in surgical rooms has increased at a fast pace. Robotic-assisted surgical platforms are one of the common examples of such devices. In fact, the success of these surgical platforms, such as the da Vinci, has demonstrated the advantages of such platforms over traditional open-surgery techniques. Despite the advantages of such systems, they still suffer from a number of inadequacies. The lack of reliable force sensors capable of measuring contact information between surgical tools and tissues is one of the causes of such inadequacy [4, 6]. In order to respond to this inadequacy, tactile sensors are needed that mimic the palpation performed by surgeon's fingertips. In doing so, robots with force-feedback capabilities [11, 106] have been proposed recently for use in minimally invasive surgery (MIS).

In the present chapter, an optical MEMS tactile sensor is proposed to measure the relative hardness of soft objects. Such soft objects can be biological tissues. The application of the sensor is in minimally invasive surgery (MIS) systems, minimally invasive robotic surgery (MIRS) systems, and catheter-based techniques (CBT) to perform cardiovascular surgery. The proposed sensor was microfabricated and has been tested. The results of the tests confirm that the sensor can distinguish between three artificial tissues with different degrees of hardness. These artificial tissues can be three different biological tissues in real surgical situations. In addition, compared to the existing sensors, the proposed tactile sensor in this study has extensive innovative and unique features. Such innovative features mean that it is MRI-compatible, electrically passive, ultrasound-friendly, able to perform under both static and dynamic loading conditions, has very high resolution, and has high accuracy.

7.2 Sensor Design

The proposed sensor measures the contact force as well as the relative hardness of a contact soft object. Such soft objects could be biological tissues interacting with surgical tools during MIS and MIRS. Figure 7-1 illustrates the structural design of the sensor from different views.

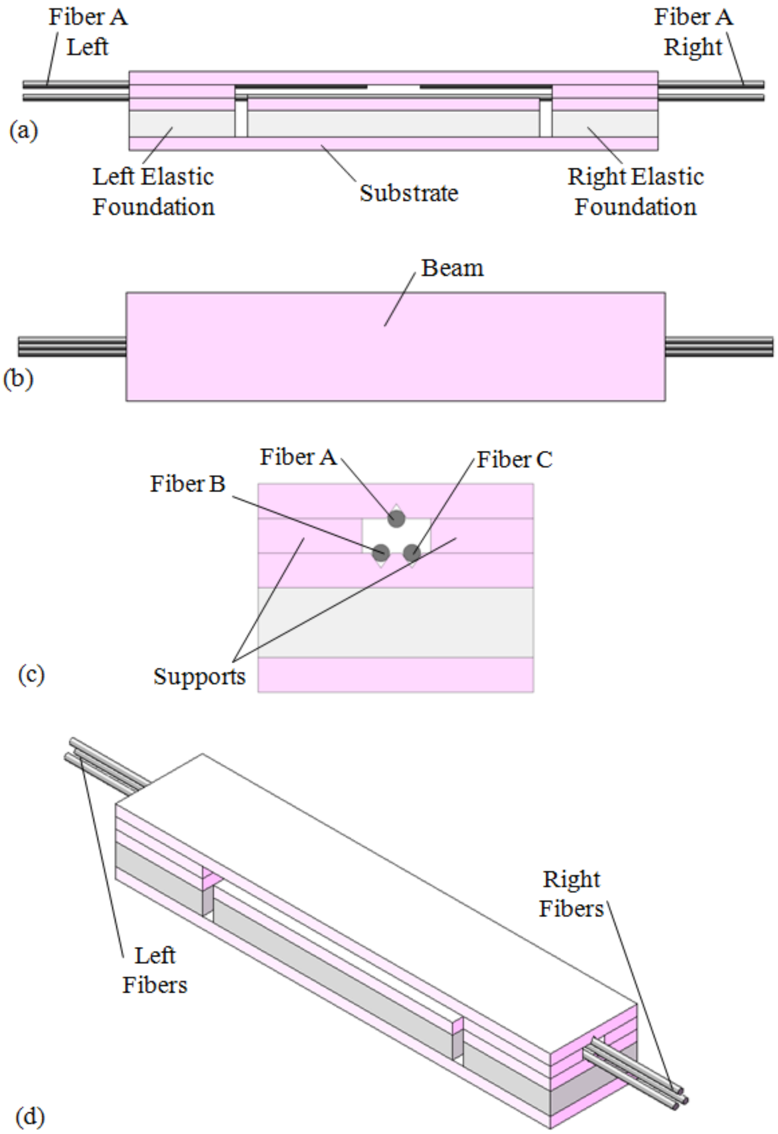

Figure 7-1: The structural design of the sensor: (a) front view; (b) top view; (c) side view; and (d) 3D view.

The sensor consists of nine silicon parts, three elastomeric foundations, and three pairs of optical fibers. The nine silicon parts include one substrate, three v-grooved chips, four supports, and one v-grooved beam. The substrate and four supports are cut from an N-Type <100> silicon wafer. On the beam and on three chips, v-grooves are micromachined. The elastic foundations are made of Polydimethylsiloxane (PDMS) material. The optical fibers are single-mode. The sequences of the sensor assembly are dealt with in the design phase. As can be seen in Figure 7-1, the elastic foundations are mounted on the substrate. Three v-grooved chips are mounted on the elastic foundations. Two pairs of optical fibers (Fibers B Left/Right and C Left/Right) are integrated into the v-grooves of the chips. Four supports are mounted on the chips. The beam is fixed on the supports. Hence the beam has fixed-fixed boundary conditions. A pair of optical fibers (Fibers A Left/Right) is integrated into the v-groove of the beam.

In Figure 7-2, the arrangement of optical fibers inside the v-grooves is demonstrated. This figure demonstrates the top view of the sensor in which the beam is shown transparent, thereby allowing the visualization of the arrangement of the fibers. Three pairs of fibers are shown in this view. Fiber A Left and Fiber A Right are integrated into the v-groove of the beam. This v-groove is made on the bottom surface of the beam. In the middle of the beam, there is a gap between the bare ends of Fiber A Left and Fiber A Right.

Fiber B Left is integrated into the left v-grooved chip and is terminated at the edge of the chip. Fiber B Right is integrated into the v-grooves of the right chip and the middle chip and is terminated at the left edge of the middle chip. This fiber is terminated at the right edge of the middle chip. Fiber C Left is integrated into the v-grooves of the left chip and the middle chip. It is terminated at the right edge of the middle chip. Fiber C Right is integrated into the v-groove of the right chip and is terminated at the left edge of this chip. Having such configurations, small gaps are located between the left parts and the right parts of Fiber B and Fiber C.

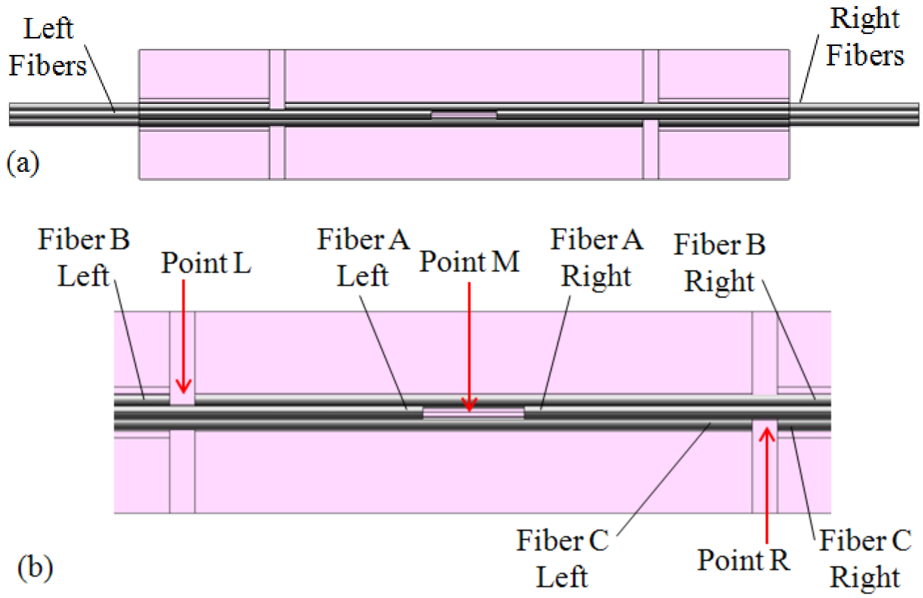

Figure 7-2: The configuration of the optical fibers on the silicon parts of the sensor: (a) the top view in which the sensor beam is transparent for better visualization; and (b) the magnified version of the top view.

The sensor measures the relative hardness of a contact soft object such as a tissue (Figure 7-3). To do so, the amplitude of the interacting load between the sensor and the tissue as well as the resultant deformation of the tissue must be measured simultaneously. In fact, the proposed sensor measures both of these data at the same time.

The load applied to the sensor results in the compression of the left and right elastic foundations (PDMS layers in this case) at both sides of the sensor. As a result, on the left side, optical misalignment occurs between Fiber B-Left and Fiber B-Right at Point L. Similarly, on the right side, optical misalignment occurs between Fiber C-Left and Fiber C-Right at Point R. By measuring the amount of loss at Point L and Point R, the amplitude of the load can be measured. On the other hand, at Point M (Figure 7-3), by measuring the coupling loss between Fibers A-Left and A-Right, the angular deflection of the beam at its central point can be measured. This angular deflection of the beam represents the resultant deformation of the contact tissue. In fact, as shown in Figure 7-4, for the same amount of force measured by Fibers B and C, the greater the hardness of the contact object, the smaller the deflection of the beam. In other words, for the same amount of contact force, the smaller the hardness of the object, the greater the angular misalignment between the Fiber A-left and Fiber A-Right. The hardness of tissue indicates its degree of softness, which is an important parameter to characterize biological tissues during MIS, MIRS, and CBT.

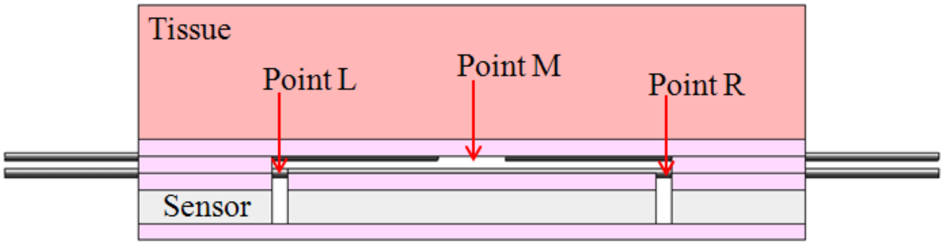

Figure 7-3: The sensor is contacting a soft object to measure the degree of hardness.

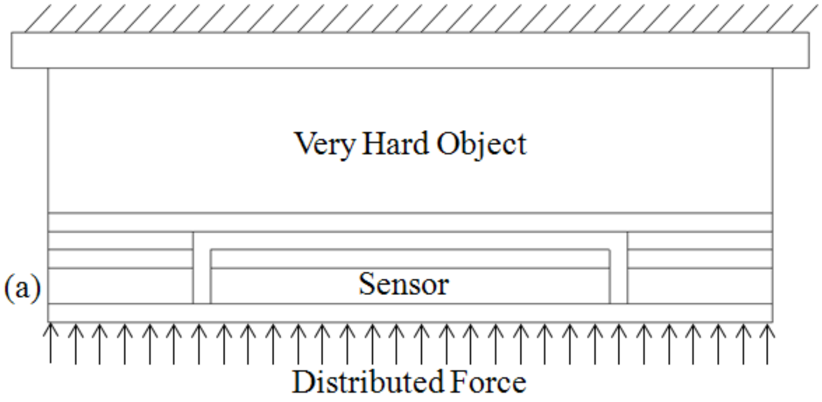

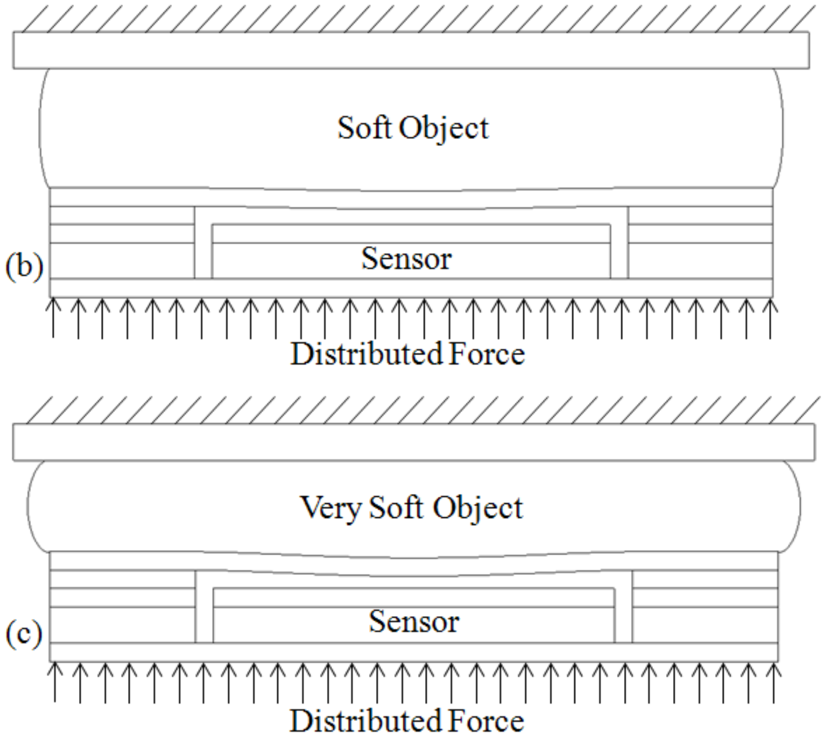

Figure 7-4: For the same amount of distributed of force applied to the tissue from the sensor, the greater the greater the object's degree of softness, the greater the deflection of the sensor beam. In (a), contact object is very hard. The contact object in (b) is relatively harder than that in (c).

7.3 Sensor Modeling

When the sensor interacts with a soft object, it measures the contact force as well as the resulting deformation of the soft object. The contact force is measured by Fibers B and C whereas the resulting deformation is measured by Fibers A. The sensing principle relies on measuring the coupling loss between each pair of fibers. For the force measurement, the contact force results in a lateral misalignment between each pair of fibers. This lateral misalignment results in coupling loss. However, for the deformation measurement, the deformation of the contact object results in the deflection of the sensor beam, and the deflection results in the angular misalignment between the pairs of Fiber A. This angular misalignment results in the coupling loss. The theoretical considerations involved with the force measurement and the deformation measurement are slightly different.

7.3.1 Force Measurement

Coupling loss (dB) due to the lateral misalignment between Fiber B-left and Fiber B-right is modeled theoretically. Moreover, the relation between the contact force, the resulting lateral misalignment, and the sensor output is modeled. Based on that, the theoretical explanation of the relation between the contact force and the sensor output is investigated.

The coupling efficiency caused by the misalignment of Fiber A left and Fiber A right of the sensor can be defined as η_{Force} [98, 99]:

$$\eta_{Force} = 4\frac{D}{B}\exp(-A\frac{C}{B}) \tag{7.1}$$

where

$$A = \frac{(kw_{BL})^2}{2} \tag{7.2}$$

$$B = G^2 + (D+1)^2 \tag{7.3}$$

$$C = (D+1)F^2 \tag{7.4}$$

$$D = (\frac{w_{BR}}{w_{BL}})^2 \tag{7.5}$$

$$G = 2\frac{Q}{kw_{BL}^{2}} \tag{7.6}$$

$$F = 2\frac{\Delta\ell}{kw_{BL}^{2}} \tag{7.7}$$

in which k is the propagation constant of the gap media between Fibers. w_{AL} and w_{AR} are the Gaussian mode field radius of Fiber A left and Fiber A right respectively. Q is the gap between Fiber A-left and Fiber A-right. $\Delta\ell$ is the lateral displacement between the axis of Fiber A Left and Fiber A Right.

$$k = \frac{2\pi n_0}{\lambda} \tag{7.8}$$

$$w_{BL} = a(0.65 + \frac{1.619}{V^{3/2}} + \frac{2.879}{V^{6}}) \tag{7.9}$$

$$w_{BR} = w_{BL} \tag{7.10}$$

$$V = \frac{2\pi a}{\lambda}\sqrt{n_{core}^{2} - n_{cladding}^{2}} \tag{7.11}$$

in which n_0, n_{core}, and $n_{cladding}$ are the refractive indexes of the media, of the core of fibers, and of the cladding of fibers respectively. a is the radius of the core of the fiber. λ is the wavelength of the light. $\Delta\ell$ is derived due to the linear elastic behavior of the elastic foundation [72]. In fact, the PDMS is modeled as a linear elastic material since the deformations applied to the elastic foundation are small in this case.

$$\Delta\ell \qquad \genfrac{}{}{0pt}{}{\ell}{EA} \tag{7.12}$$

where ℓ is the initial thickness of the PDMS layer; *E* is the modulus of elasticity of the PDMS; *A* is the area of the small chip, which is mounted on the small PDMS layer; and *F* is the contact force. Now, based on the coupling efficiency and the power of the light source (P_{BL}) the power of the coupled light from Fiber B Left into Fiber B Right (P_{BR}) can be obtained as:

$$P_{BR} = \eta_{Force} P_{BL} \tag{7.13}$$

Fiber B Right is coupled to a photodetector. The photodetector converts the light intensity of Fiber B Right into the electric voltage, V_{BR}. Consequently, the output of the sensor is the electric voltage, which is linearly proportional to P_{BR}. In other words, the sensor output voltage can be calculated as follows:

$$V_{BR} = R(\lambda, LOAD) P_{BR} \tag{7.14}$$

in which $R(\lambda, LOAD)$ is the multiplication of the spectral responsivity of the photodetector and the resistance of an external load. The spectral responsivity, which is a function of the light wavelength, can be obtained from the specifications of the photodetector. The external load resistance, which defines the sensitivity of the voltage measurement, can be tuned. Ultimately, using a DAQ, the output voltage is ready to be observed on the LabVIEW software. Such theoretical formulations provide the contact force on the left side of the sensor. The same theory is applied between Fiber C Left and Fiber C Right so as to model the contact force applied on the right side of the sensor.

7.3.2 Deformation Measurement

Coupling loss (dB) due to the angular misalignment between Optical Fiber A Left and Optical Fiber A Right of the sensor is proportional to the deformation of the soft contact object. It should be restate that for the same amount of contact force, the greater the tissue softness, the greater the beam deflection, hence, the greater angular misalignment between Fibers A Left and A Right. Here, the relation between the angular misalignment and the sensor output is modeled. The coupling efficiency caused by the misalignment between Fiber A Left and Fiber A Right of the sensor can be defined as $\eta_{Deformation}$ [98, 99]:

$$\eta_{Deformation} = 4\frac{D}{B}\exp(-A\frac{C}{B}) \tag{7.15}$$

where

$$A = \frac{(kw_{AL})^2}{2} \tag{7.16}$$

$$B = G^2 + (D+1)^2 \tag{7.17}$$

$$C = D(G^2 + D + 1)\sin^2(\Delta\theta) \tag{7.18}$$

$$D = (\frac{w_{AR}}{w_{AL}})^2 \tag{7.19}$$

$$G = 2\frac{Q}{kw_{AL}^2} \tag{7.20}$$

in which w_{AL} and w_{AR} are the Gaussian mode-field radius of Fiber A Left and Fiber A Right respectively. Q is the gap between Fiber A Left and Fiber A Right. $\Delta\theta$ is the angular misalignment between the axis of Fiber A Left and Fiber A Right.

$$k = \frac{2\pi n_0}{\lambda} \tag{7.21}$$

$$w_{AL} = a(0.65 + \frac{1.619}{V^{3/2}} + \frac{2.879}{V^6}) \tag{7.22}$$

$$w_{AL} = w_{AR} \tag{7.23}$$

$$V = \frac{2\pi a}{\lambda}\sqrt{n_{core}^2 - n_{cladding}^2} \tag{7.24}$$

Now, based on the coupling efficiency and the power of the light source, P_{AL}, the power of the coupling light into Fiber A Right, the P_{AR}, can be obtained:

$$P_{AR} = \eta P_{AL} \tag{7.25}$$

Fiber A Right is coupled to a photodetector. The photodetector converts the light intensity of the fiber into the electric voltage, V_{AR}. Consequently, the output of the sensor is the electric voltage, which is linearly proportional to P_{AL}. In other words, the sensor output voltage can be calculated as follows:

$$V_{AR} = R(\lambda, LOAD)P_{AL} \tag{7.26}$$

where $R(\lambda, LOAD)$ is the multiplication of the spectral responsivity as described in Section 7.3.1. Similar to sensor output from Fibers B and C, the output voltage for Fiber A (V_{AR}) is recorded on LabVIEW. In fact, the smaller the hardness of the contact object, the more $\Delta\theta$ and the less V_{AR}.

7.4 Sensor Prototyping

7.4.1 Sensor Micro-fabrication

The photograph of the sensor components are shown in Figure 7-5. The substrate (Layer A) and the four supports (Layer D) of the sensor were diced precisely from an N-Type <100> silicon wafer. The elastic foundations (Layer B) were made of PDMS films. A SYLGARD 184 silicone elastomer kit (Dow Corning Co., MI, USA) with the ratio of 10:1 was used to make the PDMS films. The thickness of this layer was 500 μm. In order to achieve a uniform layer with a smooth surface quality, a spin coater was used to coat the PDMS layer on a silicon wafer. Then the layers were diced into small strips with the required dimensions. Another N-Type <100> silicon wafer was used to make the v-grooved parts of the sensor, which are Layer C and Layer E. An anisotropic wet-etching with buffered hydrofluoric acid (BHF) and Tetramethylammonium hydroxide (TMAH) was used to micromachine the v-grooves on the silicon wafer. Then a wafer-dicing machine was used to cut out the chips and the beam from the micromachined silicon wafer.

7.4.2 Sensor Assembly

After the micro-machining of the sensor components, they are assembled. First, the v-grooved chips were placed on the elastic foundations (Figure 7-5-b). Then they were mounted on the substrate. Afterwards, the optical fibers were placed and glued appropriately inside the v-grooves of the chips. The supports were fixed on the chips. The fibers were integrated into the middle v-groove of the beam. Finally, the beam was accordingly placed and fixed on the supports.

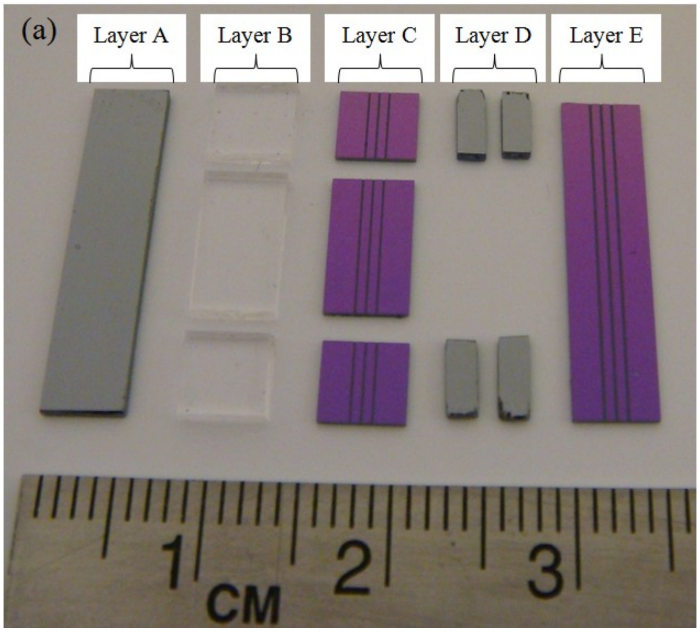

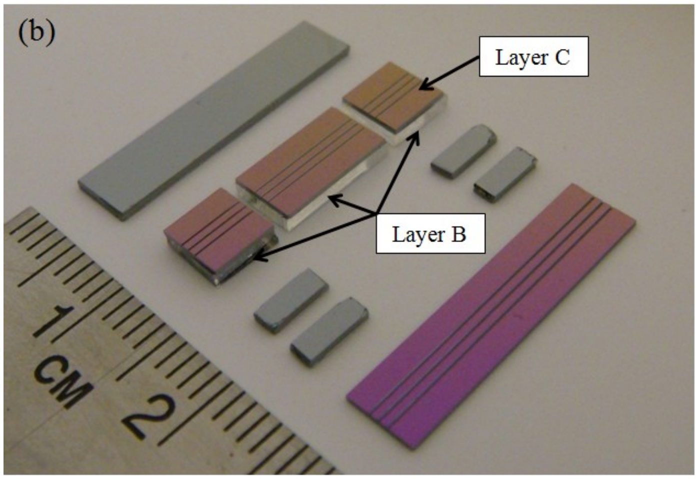

Figure 7-5: The components of the sensor before assembly.

Scanning electron-microscopy (SEM) imaging techniques were applied to examine the size and the surface quality of the v-grooves and also to evaluate how accurately the fibers were integrated into the v-grooves. Figure 7-6-a illustrates the SEM images of the micromachined v-grooves at the edge of the middle chip with only one fiber integrated into the chip. The adjacent v-groove was intentionally left empty to visualize the cross section of the micromachined v-groove. Figure 7-6-b demonstrates the terminated end of the fiber at the edge of the middle chip.

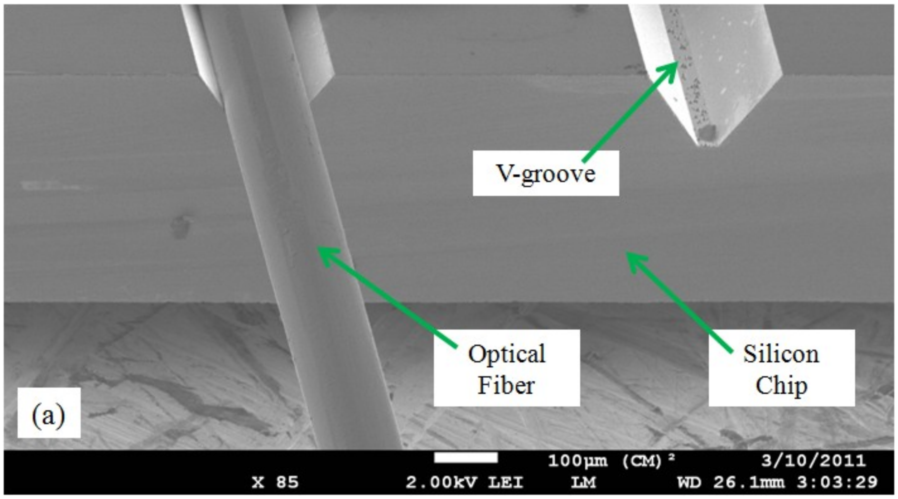

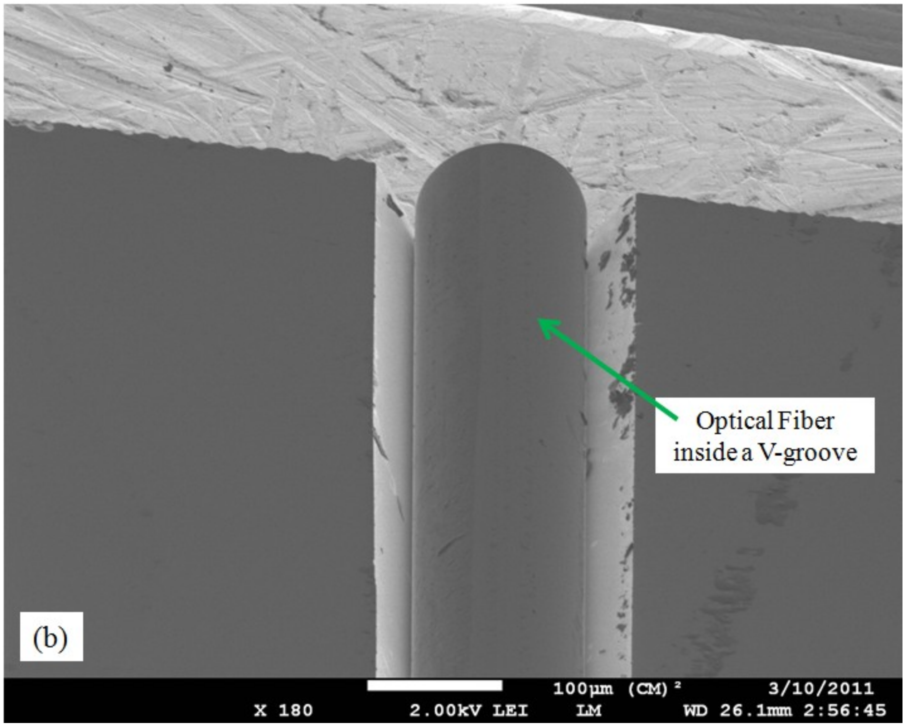

Figure 7-6: The SEM images of the optical fibers integrated into the v-grooves

7.5 Experimental Setup

To examine the sensor performance, an experimental setup was designed for the relative hardness measurement of artificial tissues and also for the measurement of local discontinuities in the hardness of these tissues. Figure 7-7 illustrates the photograph of the experimental setup. The light source is connected to Fibers A Left, B Left, and C Left. Fibers A Right, B Right, and C Right are connected to three photodetectors. The light source is an HP-371 superluminescent diode (SLD) from Superlum (Ireland). At the full-width-half-maximum (FWHM) of the SLD, its spectral bandwidth and center wavelength are 53 nm and 843 nm respectively. The photodetectors are DET02AFC with the wavelength range of 400 nm to 1100 nm, from Thorlabs (NJ, USA). Using a DAQ, the electrical output signals of the photodetectors are converted into a computer. The

DAQ is an NI PCI-6225 from National Instruments. Using an ElectroForce 3200 test instrument from Bose (MN, USA), the sensor was tested experimentally. The test instrument comes with a software interface called WinTest. This software provides a user-friendly environment to control the test parameters such as force and displacement. Known reference force/displacement functions, customized on the WinTest software, were applied to the test setup. The output voltage of the photodetectors was measured on the LabVIEW software.

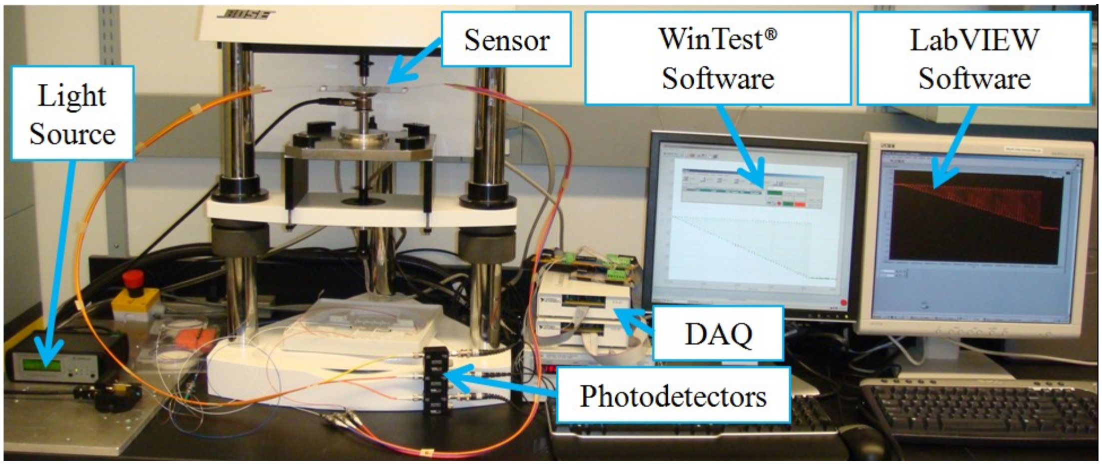

Figure 7-7: The photograph of the experimental setup.

Figure 7-8 shows the sensor under experimental tests. A number of test setup scenarios were used. The sensor was placed on the low jaw of the Bose test instrument. In the first scenario, the sensor was tested under a concentrated force applied to the sensor beam whereas in the second scenario, the sensor was tested while interacting with artificial tissues. The first scenario was chosen to examine the response of the sensor under static loading conditions. On the other hand, the second scenario was set up to validate the sensor ability to measure the relative hardness. In Figure 7-8-a, the sensor was tested with concentrated forces applied from an indenter to different points on the sensor beam. In Figure 7-8-b, the sensor was measuring the hardness of an artificial tissue.

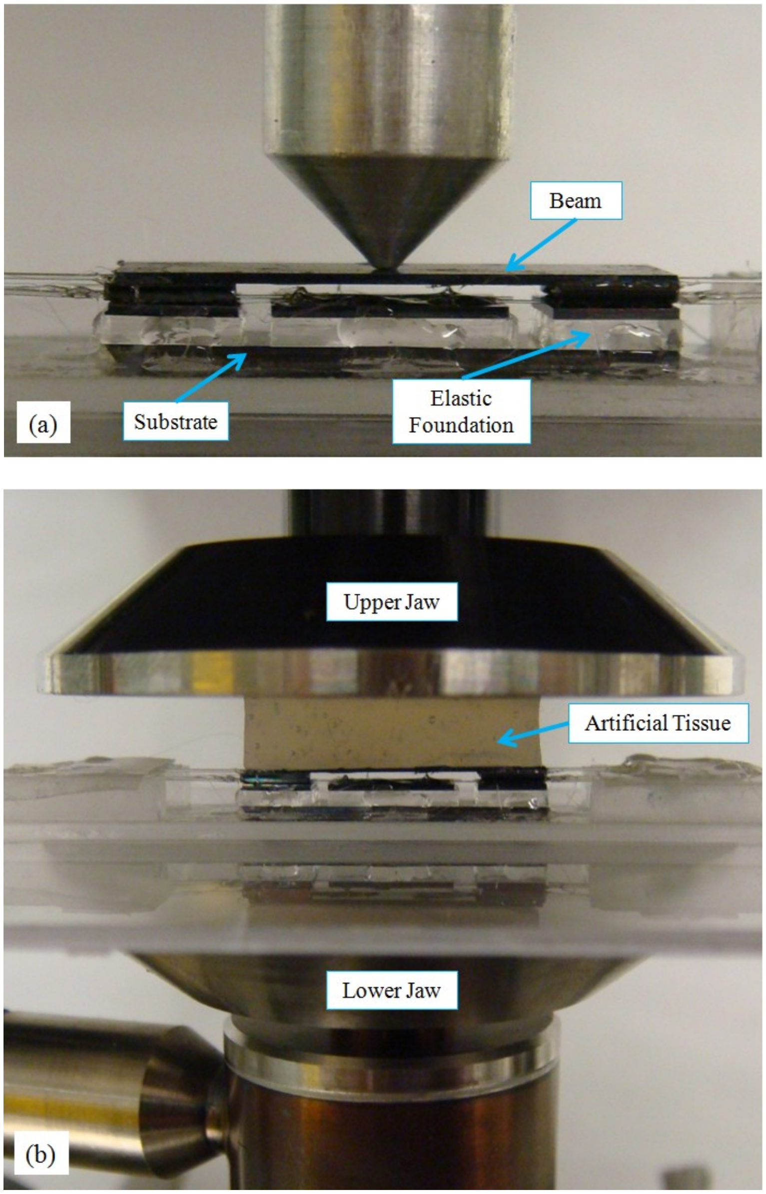

Figure 7-8: The photograph of the sensor under the experimental tests: (a) test with concentrated force; (b) test with distributed force.

7.6 Experimental Results

To evaluate the performance of the sensor in measuring the relative hardness of tissues, the sensor was tested with three artificial tissues with different degrees of hardness. Figure 7-9 shows the output of the sensor while contacting the artificial tissues. In this test, the setup is the same as the test configuration shown in Figure 7-8-b. Three silicone rubber materials with different degrees of hardness were used as artificial tissues. Those silicone rubber materials were the following: (1) the 10 OO with the degree of hardness equal to 10 Shore on scale OO, which is the softest, (2) the 30 OO with the degree of hardness equal to 30 Shore on scale OO, which is harder than the first material, and (3) the 20 A with the degree of hardness equal to 20 Shore on scale A, which is the hardest among these three materials. During the tests, the lower jaw was fixed. A triangle force with the frequency of 0.1 Hz was applied from the upper jaw. This condition was repeated for three silicone rubber materials. A triangle function was chosen to examine the linearity and hysteresis of sensor outputs. For the frequency of force function, the relatively slow rate of 0.1 Hz was chosen to observe any potential relaxation of the artificial tissues.

As shown in Figure 7-9, Fibers B and C measure the force while Fiber A measures the degree of hardness/softness of the contact objects. For three tested materials, Fibers B and C measure the same force. However, the output of Fiber A varies in the three tested materials. The more the voltage drops for Fiber A, the softer the tested material is. Using this concept, the results show that the 10 OO is softer than the 30 OO, and 20 A is hardest. This comparison confirms the capability of the sensor to measure relatively the hardness/softness of soft contact objects. These artificial tissues can represent three biological tissues in real surgical conditions. As an example, they can represent left atrium tissue, mitral valve annulus tissue, and mitral valve leaflet tissue in cardiovascular mitral valve repair surgery. Among them, the leaflet is the softest one, the annulus is the harder one, and the atrium has the moderate degree of softness. In terms of the linearity, Fiber A has a linear behavior whereas Fibers B and C do not show linear behaviors. However, in terms of hysteresis, sensor output from all three Fibers A, B, and C show a negligible hysteresis. Even though the linearity and hysteresis of the sensor outputs have not been quantified, a qualitative analysis of these characteristics can be observed in Figure 7-9.

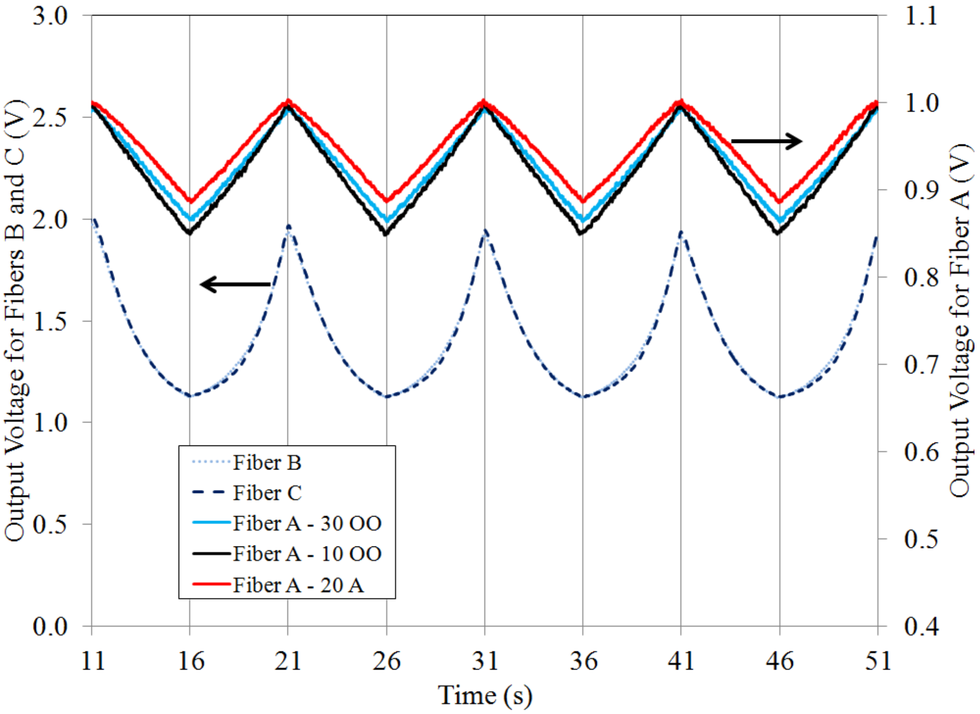

Figure 7-9: The output of the sensor during the interaction with three artificial tissues with different degrees of hardness/softness. The sensor distinguishes between such artificial tissues.

In the second test, the ability of the sensor to detect the location of an embedded lump/artery was investigated. The conditions of the test are similar to Figure 7-9 except that there was an embedded solid lump inside the artificial tissue on the left-half part of the sensor. A triangle force with the amplitude between 0.1 N to 2.5 N and with the frequency of 0.1 Hz was applied through the upper jaw of the test instrument. Figure 7-9 shows the sensor response to such test conditions from Fibers B and C. As can be seen, the output voltage of Fiber B is less than the output voltage of Fiber C. It means that the deformation of the left elastic foundation is more than the deformation of the right elastic foundation. In other words, it confirms that the lump is located on the left-half part of the sensor beam.

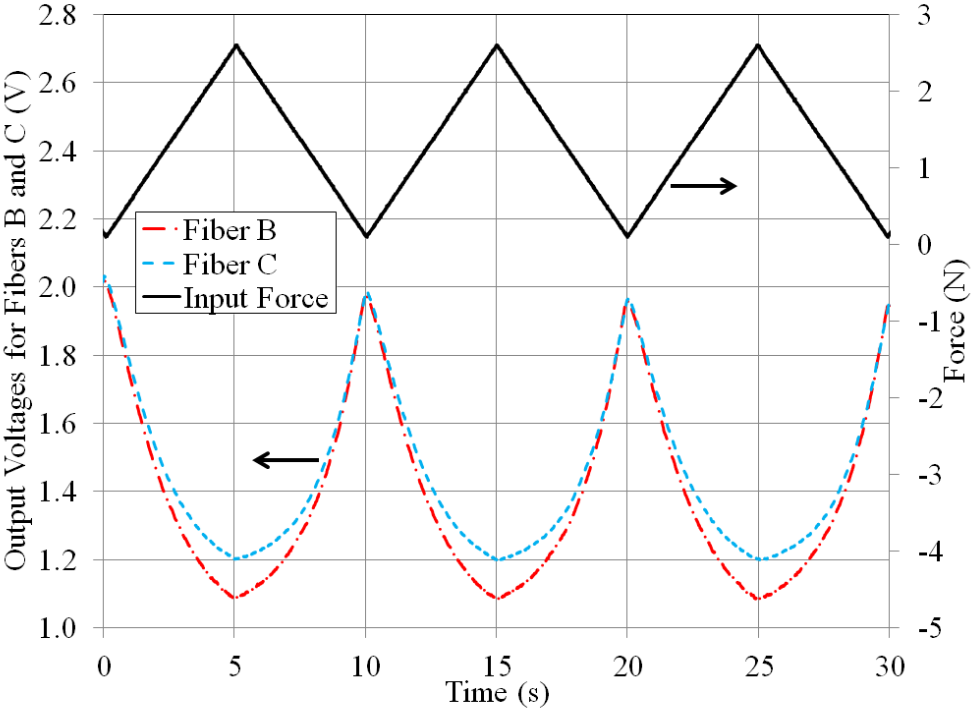

Figure 7-10: Sensor output to detect the location of an embedded lump on the left part of the sensor inside the tissue.

In the last test, the capability of the sensor to perform under static loading conditions was examined. To do so, a square concentrated force function, as shown in Figure 7-9, with the amplitude between 0.1 N to 1.0 N with the frequency of 0.025 Hz was applied on the sensor. Figure 7-9 shows the response of the sensor to such force function from Fibers A and B. Since Fiber B and Fiber C show similar behaviors, only one of them, Fiber B, was considered in this test. Because Fiber A is attached to a rigid silicon structure, its output has negligible drift. However, Fiber B has more drift since it is indirectly attached to the elastic foundation. In fact, the time-dependent mechanical properties of PDMS elastic foundation (such as its relaxation and creep) result in the drift in the outputs of Fiber B and C. This drift can be minimized by changing the material of the elastic foundation to an elastic material with the minimum of viscoelastic properties. Moreover, proper calibration algorithms can be also applied to the sensor outputs to minimize the drift effects.

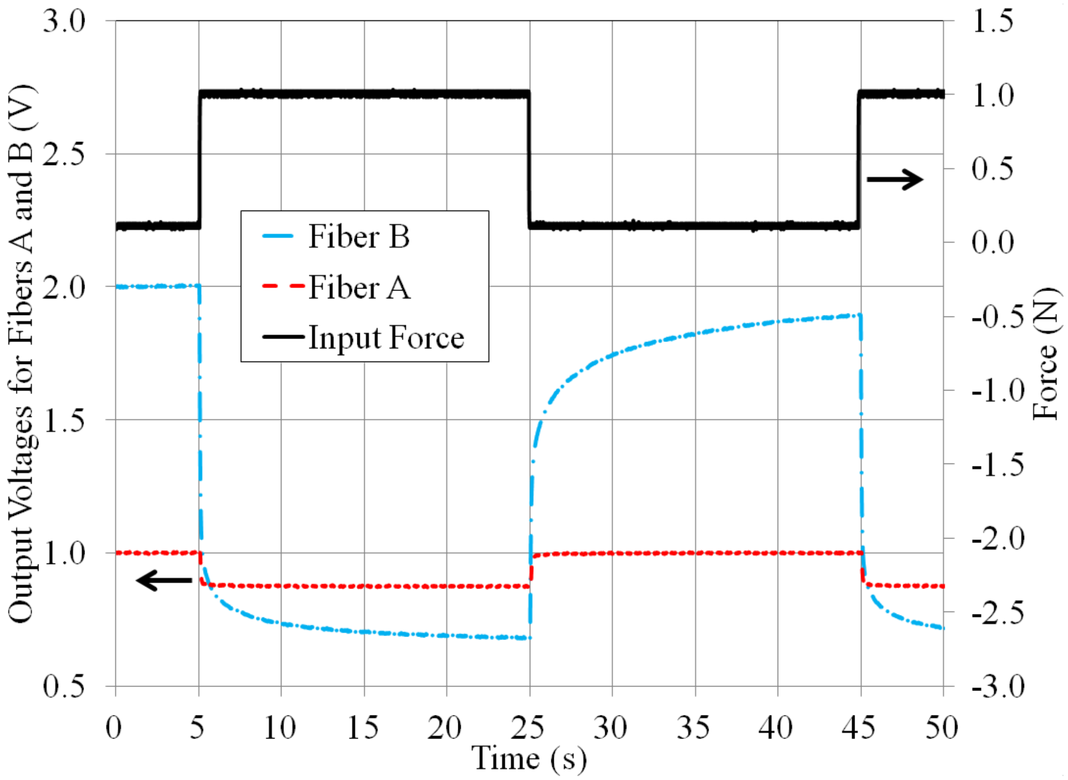

Figure 7-11: Response of the sensor from Fibers A and B to a square input force function with the frequency of 0.025 Hz.

7.7 Conclusions

In the present work, an innovative concept is proposed to measure the relative hardness of soft objects under both static and dynamic interactions. Based on the proposed concept, a prototype version of the sensor was micromachined using microsystems technology. To examine the sensor ability to measure the relative hardness and the local discontinuities in the hardness of soft objects, a number of experimental tests were performed using soft objects as artificial tissues. Experimental test results demonstrate that the sensor measures the relative hardness of soft contact objects. Such objects can be different biological tissues contacting surgical tools in surgical applications.

Chapter 8: Optical-Piezoresistive Hybrid Relative Hardness Sensing

In the present chapter, an innovative optical-piezoresistive hybrid sensor is introduced to measure the mechanical properties of soft contact objects. While the sensor interacts with biological tissues, it measures the contact force as well as the relative resulting deformation of the tissue simultaneously. Measuring both force and deformation results in tissue characterization. On the one hand, the finite element model of the sensor-tissue interaction was developed. On the other, the prototype version of the sensor was micro machined. Comparing the simulation results of the model with the experimental results of the prototype, the performance of the sensor was validated.

8.1 Introduction

In this study, a hybrid version of the sensor proposed in Chapter 7 is proposed. The hybrid sensor takes advantages of two state-of-the-art sensing principles. These are piezoresistive-base and optical-based principles. The sensor is designed to measure the relative hardness of tissues. While interacting with tissues, the piezoresistive sensing element of the sensor measures the contact force. In the mean time, the optical sensing principle of the sensor performs a relative measurement of the resulting deformation in the tissue.

8.2 Sensor Design

Figure 8-1 illustrates different views of the structure of the hybrid tactile sensor. The sensor consists of eight parts made of silicon, two piezoresistive elements, and one pair of optical fibers. The eight silicon parts include one substrate, two chips, four supports, and one beam. A v-groove is micromachined on the bottom surface of the beam. On the left and right sides of the sensor, the piezoresistive elements are sandwiched between the substrate and the chips. Two supports are fixed on top of each chip located on both sides of the sensor. Two optical fibers are integrated into the v-groove of the beam in a way that a narrow gap is placed between them in the middle of the beam. The beam is fixed on the supports.

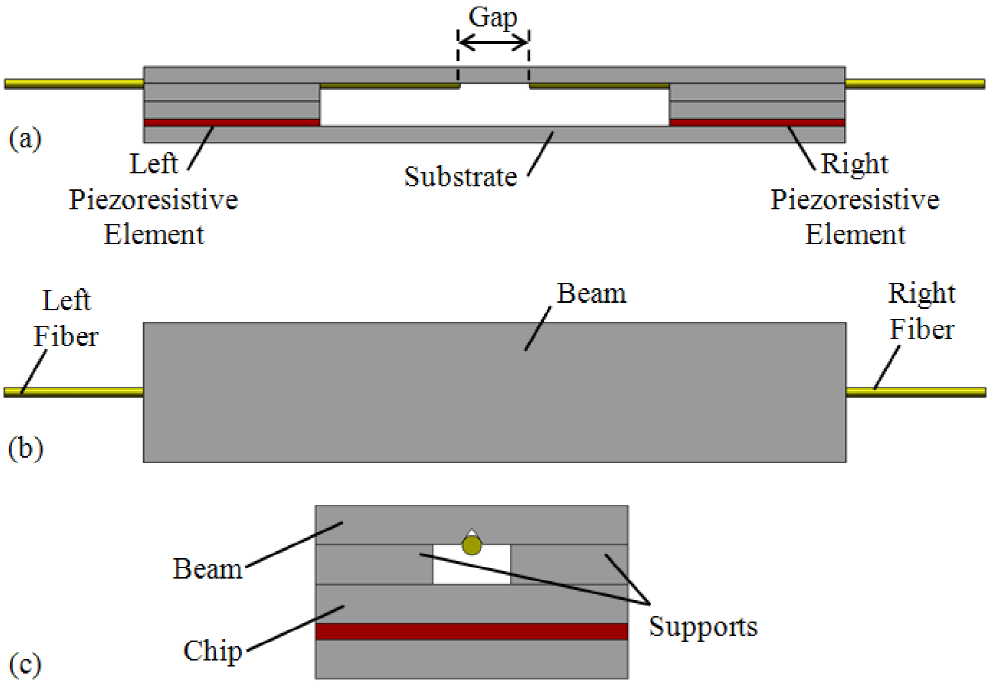

(d)

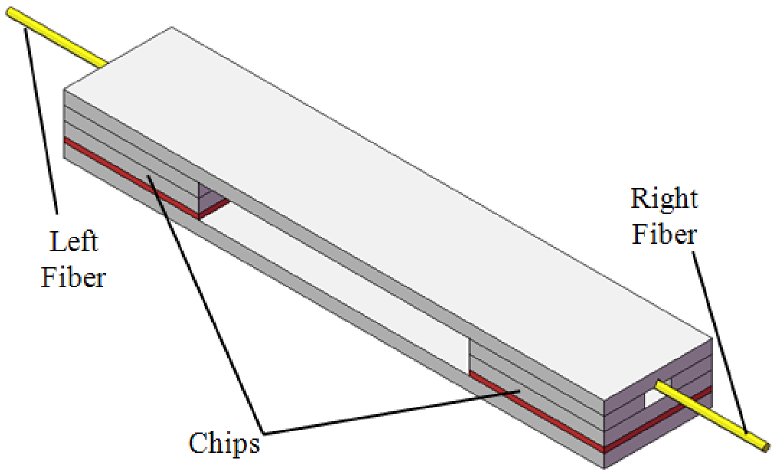

Figure 8-1: The structural design of the hybrid sensor in different geometrical views: (a) front view; (b) top view; (c) side view; (d) 3D view.

Each piezoresistive element consists of one piezoresistive film and two thin electrodes made of copper. Through electric wires, the electrodes are connected to an electric circuit and then to a computer. The left fiber and the right fiber (Figure 8-1-d) are connected to a light source and a photodetector respectively. The output voltage of the photodetector is connected to the computer.

8.3 Sensor Modeling

8.3.1 Modeling the Sensor-Tissue Interaction

In order to model the interaction between the sensor and tissue, first, the tissue should be modeled. In the present work, three silicone rubber materials with different degrees of hardness are selected as the artificial tissues to model the sensor-tissue interaction. The mechanical properties of the selected artificial tissues are similar to the properties of biological tissues. During the tool-tissue interactions involved in surgical applications, such materials undergo large deformation. Consequently, their behaviour can be described by nonlinear elasticity theory. Hyperelastic models are one of the common choices used to model the elastic materials with large deformations [74]. Hyperelastic materials are described by a strain energy function, *W*, which is a scalar function. The stress component of the material as a result of applied strain is obtained from the following equation [75].

$$\mathbf{S} = \frac{\partial W(\mathbf{F})}{\partial \mathbf{F}} \tag{8.1}$$

where **F** is the deformation gradient tensor and **S** is the first Piola-Kirchhoff stress tensor. In order to describe the strain energy function, a Neo-Hookean (N-H) [75] model is chosen. The N-H model is widely acceptable to model silicone rubber materials as well as biological tissues. In this case, the artificial tissue is assumed as an isotropic and a nearly-incompressible material. Based on the N-H model, the strain energy function of an isotropic/nearly-incompressible hyperelastic material is defined by the following equation [75, 89].

$$W = \frac{1}{2}\mu(I_1 - 3) + \frac{1}{d}(J-1)^2 \tag{8.2}$$

where I_1 is the first deviatoric strain invariant, J is the determinant of the elastic deformation gradient tensor (**F**); μ is the initial shear modulus of the material, and d is the material incompressibility parameter. The initial shear modulus and the incompressibility parameter are derived from the following equations [89, 90].

$$\mu = 2(C_{10} + C_{01}) \tag{8.3}$$

$$d = \frac{1-2\nu}{C_{10} + C_{01}} \tag{8.4}$$

where C_{10} and C_{01} are the constants of the Mooney-Rivlin (M-R) model for the hyperelastic material. These constants are calculated using curve fitting techniques applied to the stress strain data of the material obtained in the compression experimental tests. ν is the Poisson's ratio of the material, which, in this case, is assumed to be 0.49 for the nearly-incompressible material. The initial bulk modulus of the material is defined by Equation 8.5.

$$\kappa = \frac{2}{d} \tag{8.5}$$

In the experimental setup, three different silicone rubber materials, named 10-OO, 30-OO, and 20-A, made by Smooth-On, Inc. (PA, USA), were used to represent the biological tissues. These three materials have different mechanical properties. An ElectroForce 3200 test instrument (Bose, Minnesota, USA) was used to obtain the stress-strain data for these three materials under uni-axial compression tests. Based on the obtained experimental data, the M-R material constants for these materials were derived by using curve-fitting methods [76]. Table 8-1 gives the derived material constants for the artificial tissues that are used in the experimental setup. Accordingly, the dimensions of the tested artificial tissues were selected with respect to the dimensions of the prototype sensor. Based on the derived material constants and taking into consideration the dimensions of the tested artificial tissues, the finite element model of the artificial tissues were developed in COMSOL Multiphysics software. In this model, the 2-D space dimension mode of the structural mechanics module of the software was used. For the model, the plain strain mode with parametric analysis and large deformations was selected. The Lagrange-Quadratic triangular elements were chosen. This type of element addresses the hyperelasticity, large deflection, and large strain capabilities. Comparing the simulated stress-strain behavior with the real behavior of the artificial tissues obtained by the experiments verify that the derived material constants are quite accurate. Results show that 20-A is harder than 30-OO and the 30-OO is harder than the 10-OO.

Table 8-1: Mooney-Rivlin parameters of the artificial tissues

	C_{10} (kPa)	C_{01} (kPa)
10-OO Material	27.147	-25.776
30-OO Material	85.157	-80.385
20-A Material	604.989	-573.343

Afterwards, the derived material constants of the artificial tissues were used in the modeling. Figure 8-2 illustrates the finite element model of the sensor-tissue interaction. In this model, the conditions are the same as those applied in the experimental tests. The material properties of the sensor are assumed similar to the fabricated one. As depicted in Figure 8-2-b, the sensor is mounted on the bottom jaw of the ElectroForce test instrument. As under the test conditions, the silicone rubber material, which represents biological tissue, is located on the sensor beam. Using the parametric solver of the software, the upper jaw is lowered by applying a distributed force to the tissue through this upper jaw. In the experimental tests, it was observed that the considerable friction between the artificial tissues and the beam of the sensor prevented any lateral sliding movements between them. Therefore, in the model the upper and lower boundaries of the tissue are glued to the lower boundary of the upper jaw and to the upper boundary of the sensor beam respectively.

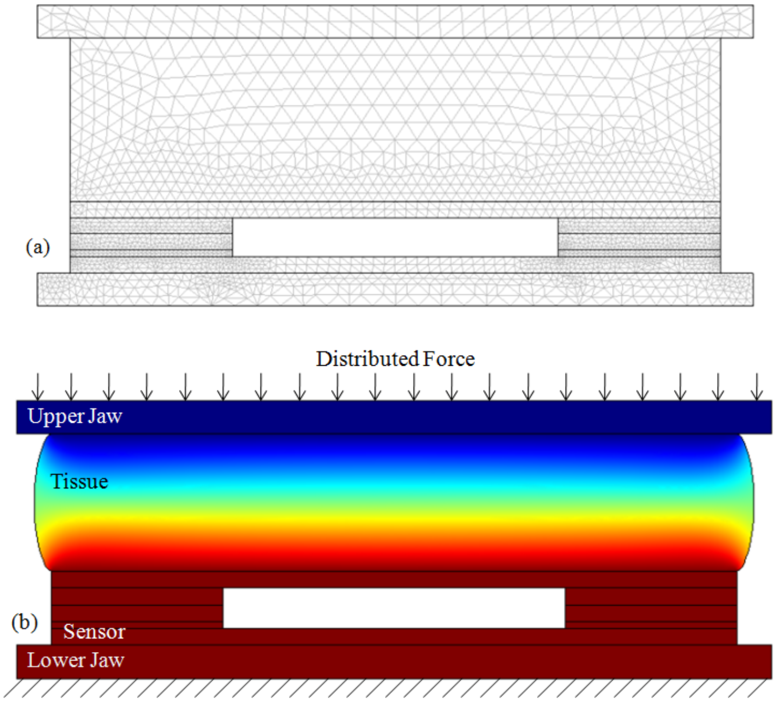

Figure 8-2: The finite element model of sensor-tissue interaction: (a) meshed structure of the model; (b) the deformation of the tissue and the components of the sensor. The tissue is modeled as a hyperelastic material. Simulation results show that the sensor measures the relative hardness of contact tissues.

As shown in Figure 8-3, for the same amount of the distributed force applied to tissue through the upper jaw, the deflection of the sensor beam varies for tissues with different degrees of hardness. Based on this information, the softness of contact tissue can be measured. In this case, for the same amount of contact force, the beam deflection for the 10-OO material is greater than that for the 30-OO material. Also the beam deflection for the 20-A material is less than for the others. This shows that the 10-OO is softer than the 30-OO and the 30-OO is softer than the 20-A. The results of this finite element analysis verify the concept of the relative hardness measurement obtained with the proposed design of the sensor.

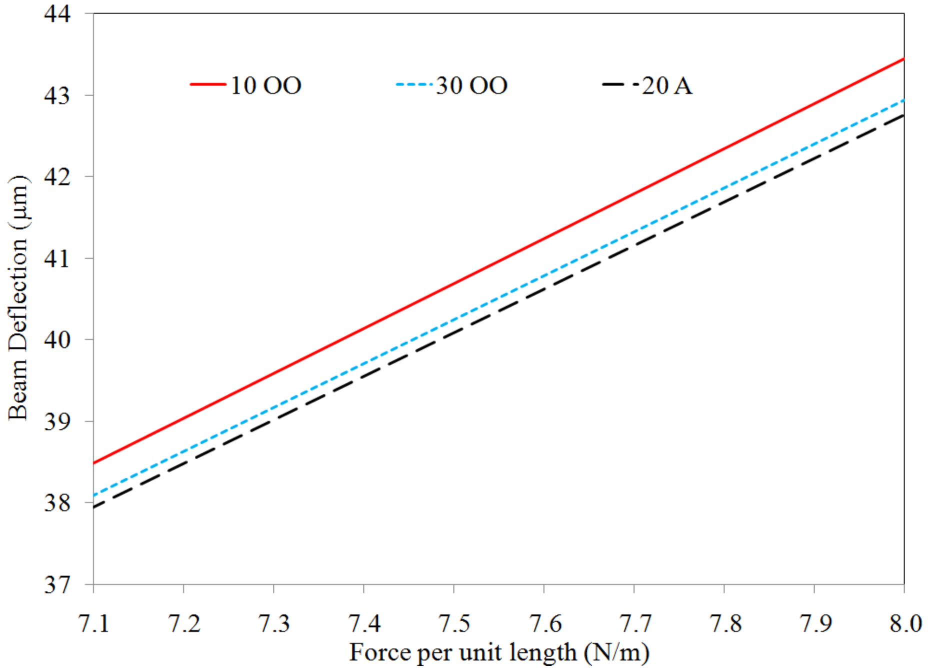

Figure 8-3: For the same amount of force, the deflection of the sensor beam varies during the interaction with tissues with different degrees of hardness. Based on this information, the softness of contact tissue can be measured.

8.3.2 Modeling the Optical Element of the Sensor

As discussed, the sensor measures the contact force as well as the resulting deformation in the contact objects. Since the difference between the resulting deformations of different tissues under the same contact loads is very small, a highly sensitive sensing element is needed. In the present work, for measuring such deformations, an optical-based sensing element is utilized to satisfy the required sensitivity.

As discussed in Section 8.2, the sensing element relies on measuring the coupling loss between two single-mode adjacent optical fibers. The theoretical considerations [98, 99] for modeling the relation between the angular misalignment and the resulted coupling loss on the optical fibers have been investigated in Chapter 5 of the present thesis.

8.3.3 Modeling the Piezoresistive Element of the Sensor

When it comes to force sensing, the piezoresistive materials have numerous advantages such as low ratio of noise, quick response time, and small dimensions. In the present work, the piezoresistive sensing element is selected because of its thin thickness, which addresses the miniaturization requirements for this specific application. A semiconductive polymer composite, which is a force sensitive resistor (FSR) material, was chosen as the piezoresistive sensing element of the sensor. This composite is a carbon-filled polyethylene film, named Linqstat (from CAPLINQ Corporation, Canada) with the thickness of approximately 200 μm. The relationship between the electrical resistance of the piezoresistive element and the force applied to it is characterized experimentally. In fact, the performance of the piezoresistive element has been addressed in [59, 107].

In order to convert the output voltage of the piezoresistive elements into the sensed force, a calibration procedure was applied to the sensor. Experimental test results confirm that the conductance of the sensing element has a linear relation with the contact force [59, 107].

8.4 Sensor Fabrication

The sensor was micromachined by using micro electro mechanical systems (MEMS) technology. An N-Type <100> silicon wafer was used to develop different parts of the sensor. An anisotropic wet etching technique was used to make v-grooves on the silicon wafer. First, the growth of thermal silicon oxide was used to deposit a thin layer of silicon oxide on the silicon wafer. The thickness of the oxide layer was approximately 525 nm. Due to such thin thickness, this layer has a negligible effect on the mechanical properties of the sensor beam. This is why the oxide layer was not considered in the model presented in Section 8.3.1. The oxide film was used as a mask. The oxide layer was patterned by a photo-resist. Then the exposed parts of the oxide layer were etched in a buffered hydrofluoric acid (BHF) or a Buffered Oxide Etch (BOE) 6:1 solution for approximately six minutes. During this process, the exposed parts of the oxide layer were removed. Then the photo-resist layer was removed and the wafer was cleaned. Then the wafer was etched in Tetramethylammonium hydroxide (TMAH) for approximately six hours. After etching the v-grooves on the silicon wafer, the components of the sensor were precisely cut to the required sizes using a wafer sawing machine.

The v-groove provides a foundation to integrate the optical fibers. As a result, their surface quality and their size are very important factors. For examining these factors, scanning electron microscopy (SEM) imaging was used to obtain a qualitative observation of the v-groove and the fibers integrated into them. Figure 8-4 shows the SEM images of the microfabricated components of the sensor. As can be seen, the smooth surface quality of the v-groove provides a rugged foundation to attach the fibers to the sensor beam structure and at the same time to precisely align Left Fiber and Right Fiber with respect to each other.

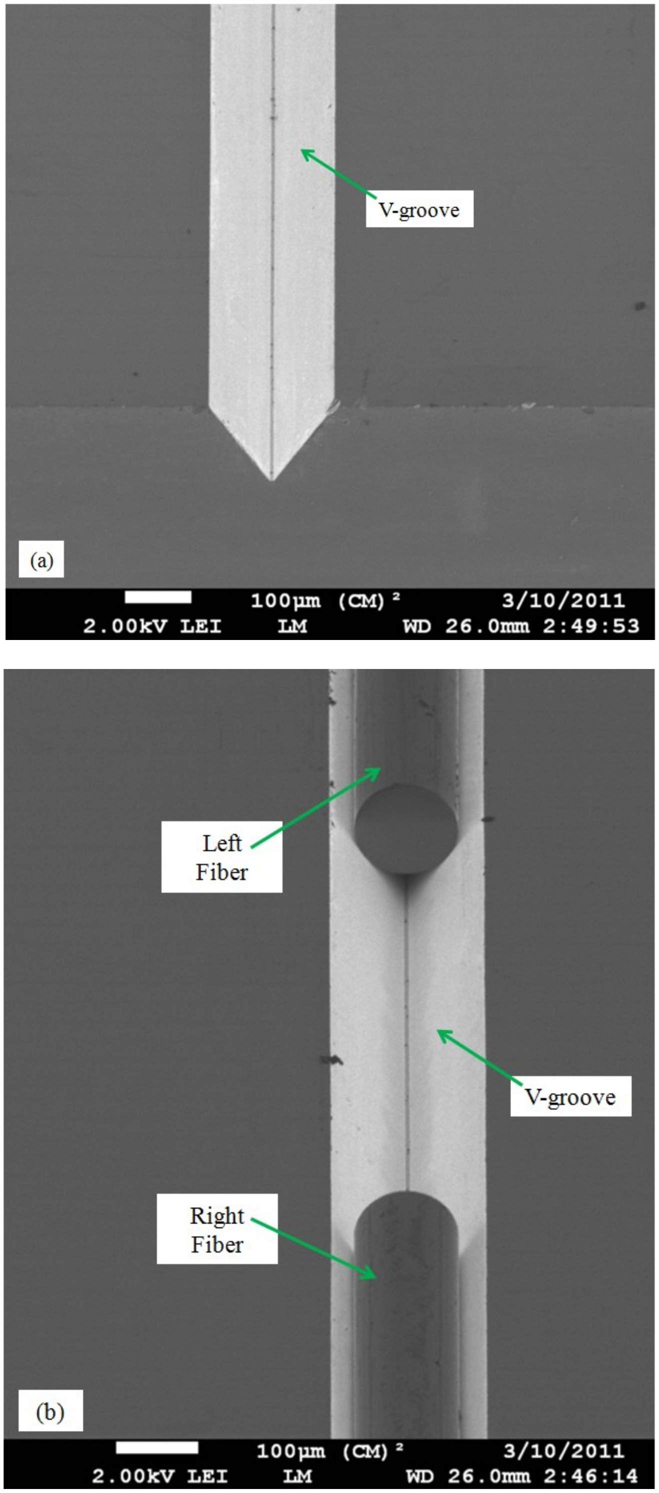

Figure 8-4: The SEM images of: (a) the v-groove on the lower surface of the sensor beam, and (b) a pair of optical fibers integrated on that v-groove. The v-groove provides a rugged foundation to precisely align the fibers attached to the sensor beam.

Figure 8-5 shows the photograph of the components of the sensor before the assembly. The silicon substrate, the silicon chips, and the silicon supports were cut from an N-Type <100> silicon wafer with a thickness of 500 µm. The substrate provides a rigid base to assemble the other components of the sensor. In order to make the piezoresistive force sensors, two square parts were precisely cut out of the piezoresistive Linqstat film. Also the electrodes were cut from a copper sheet with a thickness of 200 µm. The Linqstat films were sandwiched between the electrodes on each side of the sensor. The size of the piezoresistive films was 5 mm by 5 mm. The size of the square parts of the electrodes was 4 mm by 4mm.

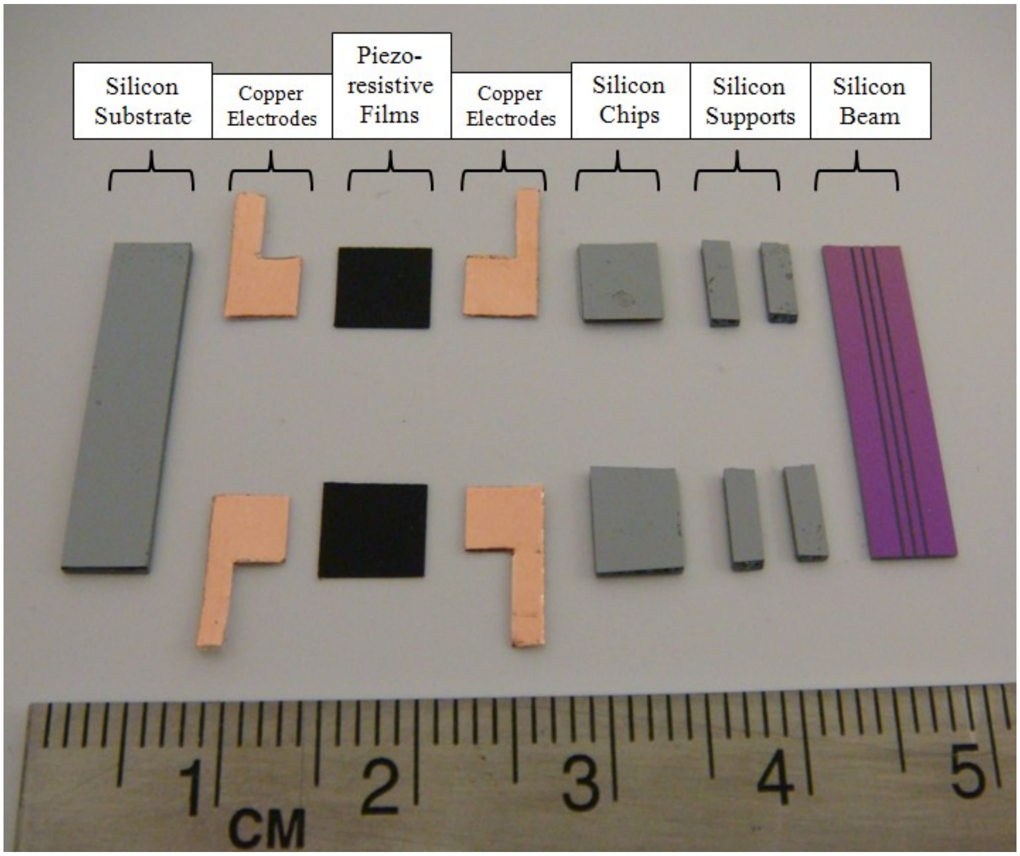

Figure 8-5: The photograph of the components of the sensor.

Figure 8-6 shows the photograph of the final assembled sensor structure. In order to assemble the components of the sensor, the sandwiched piezoresistive elements were, first of all, fixed on the sides of the substrate (rigid base) and the electric wires were soldered to the electrodes. Secondly, the silicon parts were fixed to the piezoresistive elements and the supports were fixed on top of the silicon parts. Thirdly, the pairs of optical fibers were integrated and bonded inside the middle v-groove of the silicon beam. Finally, the silicon beam with the integrated fibers was aligned and then fixed on top of the supports.

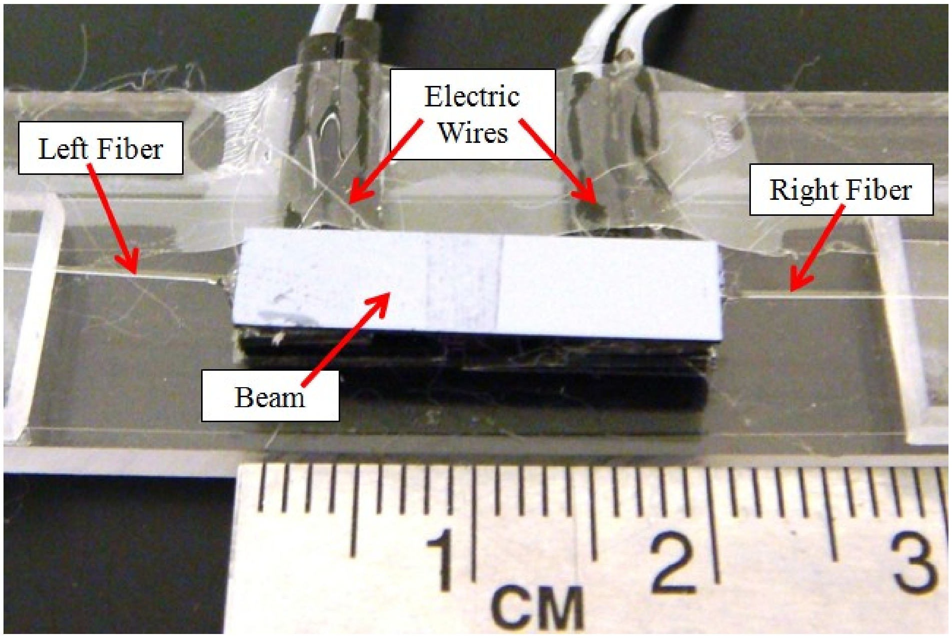

Figure 8-6: The photograph of the assembled sensor.

8.5 Experimental Setup

An experimental setup was used to test the performance of the sensor. Figure 8-7 demonstrates the block diagram of the experimental setup. A light source is connected to the input fiber on the left side of the sensor. On the other side, the output fiber is connected to a photodetector. The light source is a superluminescent diode (SLD) with Model HP-371 from Superlum Co. (Ireland). The central wavelength of the SLD is 843nm. The photodetector is DET02AFC from Thorlabs (NJ, USA). Its wavelength range is between 400 nm and 1100 nm. The photodetector is connected to the LabVIEW software via a DAQ. The DAQ is an NI PCI-6225.

In order to convert the output voltage of the piezoresistive films into the force, an electric circuit described in [62] was used. Also based on the described technique in [62], the output of the piezoresistive films was calibrated to measure the contact force. The electric wires of the piezoresistive sensing element are connected to the same DAQ through a buffered electric circuit. The buffered circuit is brought into play to minimize the loading effects of the piezoresistive elements on the amplifiers of the DAQ. Such a circuit reduces the cross-talk effect within the channels of the DAQ. Having such a configuration, the output voltage of the piezoresistive sensing elements is converted to LabVIEW via the buffered circuit and the DAQ.

An ElectroForce 3200 test instrument from Bose (MN, USA) was used to test the sensor. As depicted in Figure 8-7, the sensor was placed on the lower jaw of the test instrument. Different artificial tissues were placed between the sensor and the upper jaw of the test instrument. The test instrument was connected to the WinTest software. WinTest provides a user-friendly interface to control the test parameters such as force and displacement between the jaws of the test instrument. On the one hand, the test scenarios applied to the sensor-tissue interaction were customized in the WinTest environment. On the other, in the LabVIEW environment, the output voltages of the photodetector as well as the output voltage of the piezoresistive elements were processed to measure the relative hardness of the artificial tissues. In the LabVIEW code, first-order low-pass filters with 25 Hz, and 15 Hz cut-off frequencies were applied to the output signal of the photodetector and piezoresistive elements respectively. These cut-off frequencies were chosen to provide adequate attenuation for the 60 Hz noise. Compared to the output voltage of the piezoresistive films, the output voltage of the photodetector has a lower noise-to-signal ratio. This is why the cut-off frequency of the filter implemented for the piezoresistive elements is lower than that implemented for the photodetector. In surgical application, the rate of tool-tissue interactions is basically less than few Hertz. Consequently, the 15 Hz cut-off frequency does not filter any important data related to sensor-tissue interactions. However, it results in a better signal output.

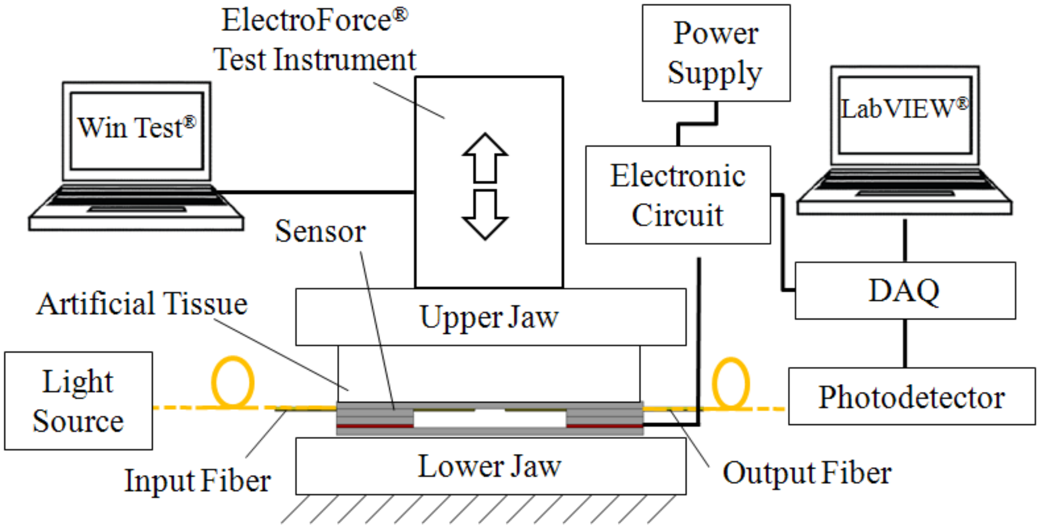

Figure 8-7: The block diagram of the experimental setup.

8.6 Experimental Results

To evaluate the sensor performance, the test results were compared. First, the piezoresistive elements were calibrated to measure the contact force. To measure the contact force, a linear calibration with a constant gain and a constant bias was implemented to the voltage output of the piezoresistive sensing elements. To characterize the performance of the sensing elements, their response to a known input force was investigated. Figure 8-8 shows the calibrated output of the piezoresistive elements located on the left and the right sides of the sensor. The input is a square force with the amplitude of 0.1 N to 2.6 N and the frequency of 1 Hz. The force range and the frequency were chosen in a way that they are in accordance with the tool-tissue interactions during real surgical operations [29, 77]. The force is a concentrated force applied to the middle point of the sensor beam. In fact, this is the output of the sensor after applying the calibration process on the output signal in LabVIEW. As can be seen in this graph, for a symmetrical loading condition, the left and the right piezoresistive sensing elements of the sensor measure the same force. As discussed later on in the present section, the piezoresistive sensing elements also recognize unsymmetrical loading conditions. Such measurement helps surgeons to investigate the distributed force information that results in detecting the position of a lump/artery.

To attenuate the high-frequency noise of the voltage output, 15 Hz first-order low-pass filter was applied to the output signals of piezoresistive elements. 15 Hz was chosen since the frequency of tool-tissue interaction is usually less than few hertz in real surgical tasks. Figure 8-9 compares the non-filtered and the filtered output of one of the piezoresistive elements. The filtered signal has a lower range of noise. However, the filter increases the response time of the sensor.

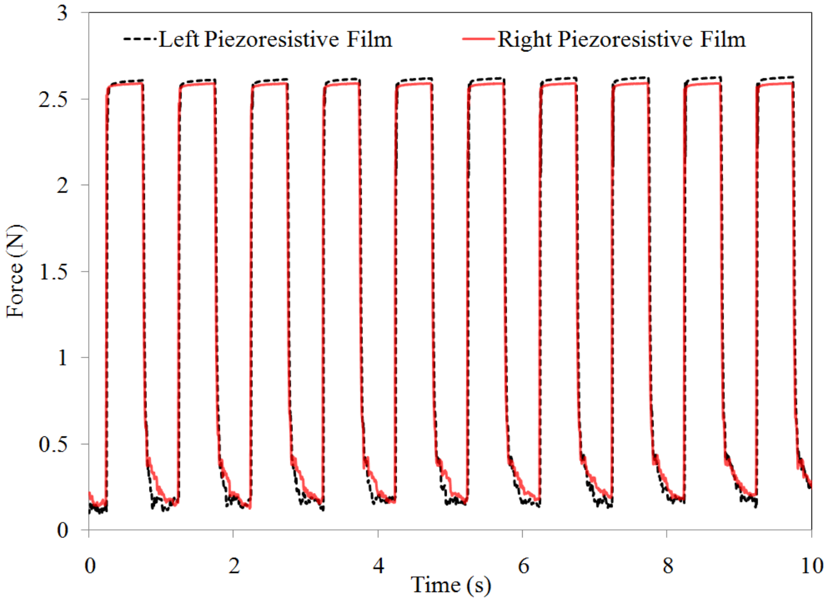

Figure 8-8: The calibrated output of the piezoresistive films sandwiched under the left and the right supports of the sensor. The input is a square force with the amplitude of 0.1 N to 2.6 N and the frequency of 1 Hz. The force is a concentrated force applied to the middle point of the sensor beam.

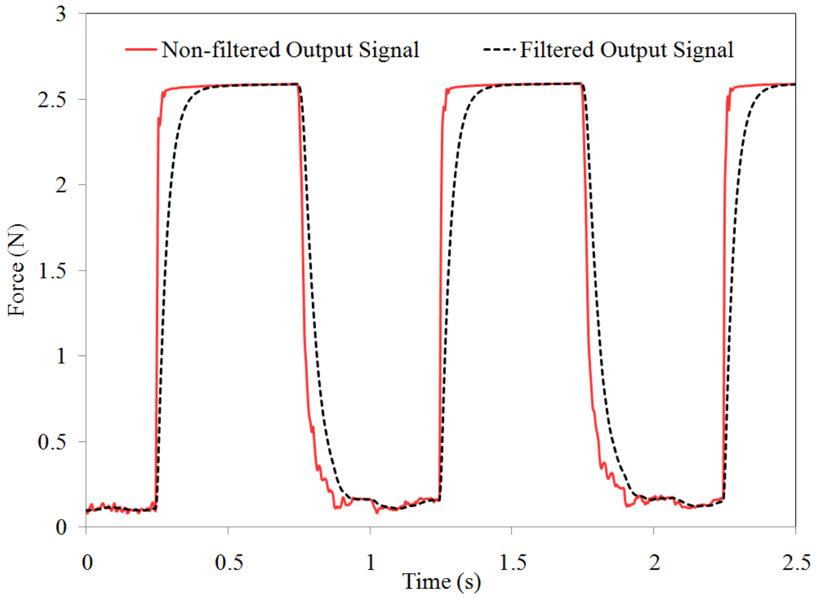

Figure 8-9: Comparison between the non-filtered and the filtered output of one of the piezoresistive films. The filter is low-pass. The filtered signal has a lower range of noise. However, the filter increases the response time of the sensor.

To ensure that the sensor is capable of measuring the relative hardness degree of tissues, a test with artificial tissues was performed on the sensor. The artificial tissues were chosen with three different degrees of hardness: shore OO 10 (10 OO), shore OO 30 (30 OO), and shore A 20 (20 A). These artificial tissues represent three different biological tissues in real surgical scenarios. Figure 8-10 displays the output of the sensor from the piezoresistive sensing elements and also from the optical fiber while interacting with these tissues. The piezoresistive sensing elements measure the amount of interacting force between the sensor and the artificial tissues. For the same amount of interacting force, the amount of change in the output voltage of the fiber is proportional to the softness of the contact object. Based on this principle, the results of the test show that 10 OO is softer than 30 OO and it is softer than 20 A. These experimentally obtained results are exactly the same as those in the real situations. Hence this test verifies the sensor's capability to measure the relative hardness of tissues.

In addition, another test was performed to examine the ability of the sensor to detect lump/artery. In this test, an artificial tissue sample containing an embedded solid lump was used. Figure 8-11 shows the output of the sensor while interacting with such tissue sample. The lump was located on the right-half part of the sensor-tissue's contact area. Such conditions will result in an unsymmetrical load distribution on the sensor beam since more force is applied to the area underneath the solid lump than to the rest of the contact area. As shown in the test results, the right sensing element of the sensor shows more force than its left counterpart does. This information tells the surgeon that the hardness of the tissue on the right side of the contact area is more than the hardness of the tissue on the left side of the contact area. Such non-uniformity in the degree of hardness can be caused by an embedded hidden harder tissue located inside the softer background tissue. Such harder tissue represents an artery, a ureter, or an abnormal tissue e.g. a cancerous lump.

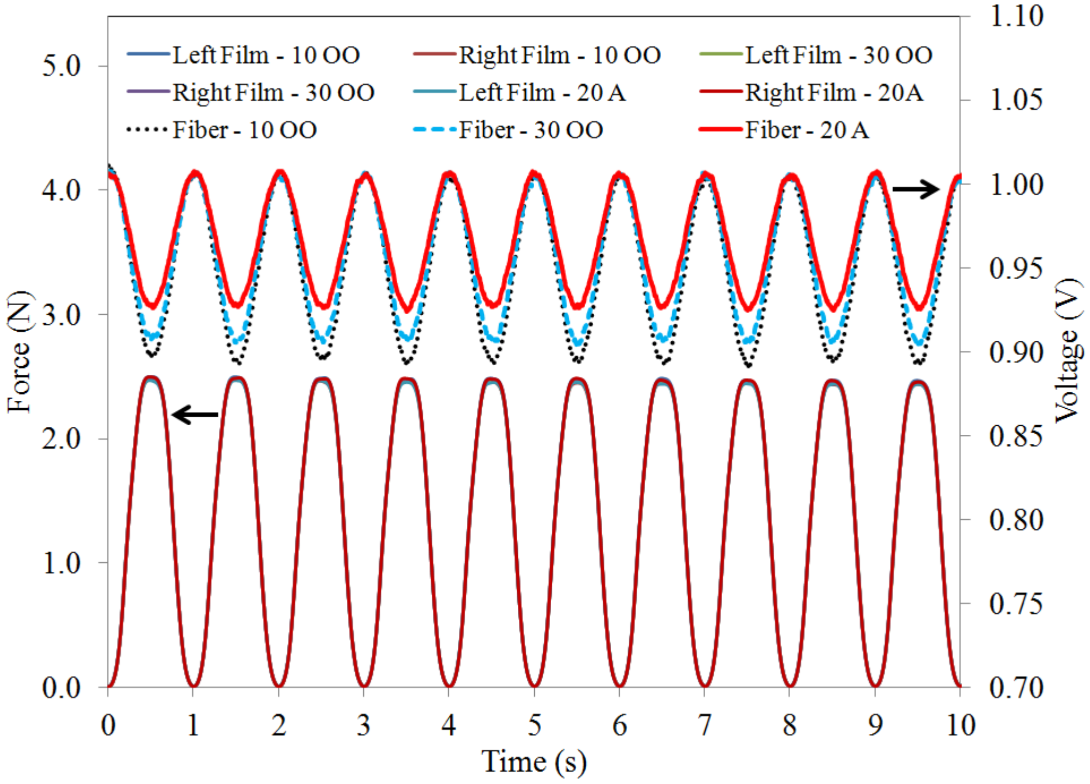

Figure 8-10: The output of the sensor from the piezoresistive films and also from the optical fiber while interacting with artificial tissues with different degrees of hardness. Piezoresistive films show the amount of interacting force between the sensor and the artificial tissues. For the same amount of interacting force, the amount of change in the output voltage of the fiber is proportional to the softness of the contact object.

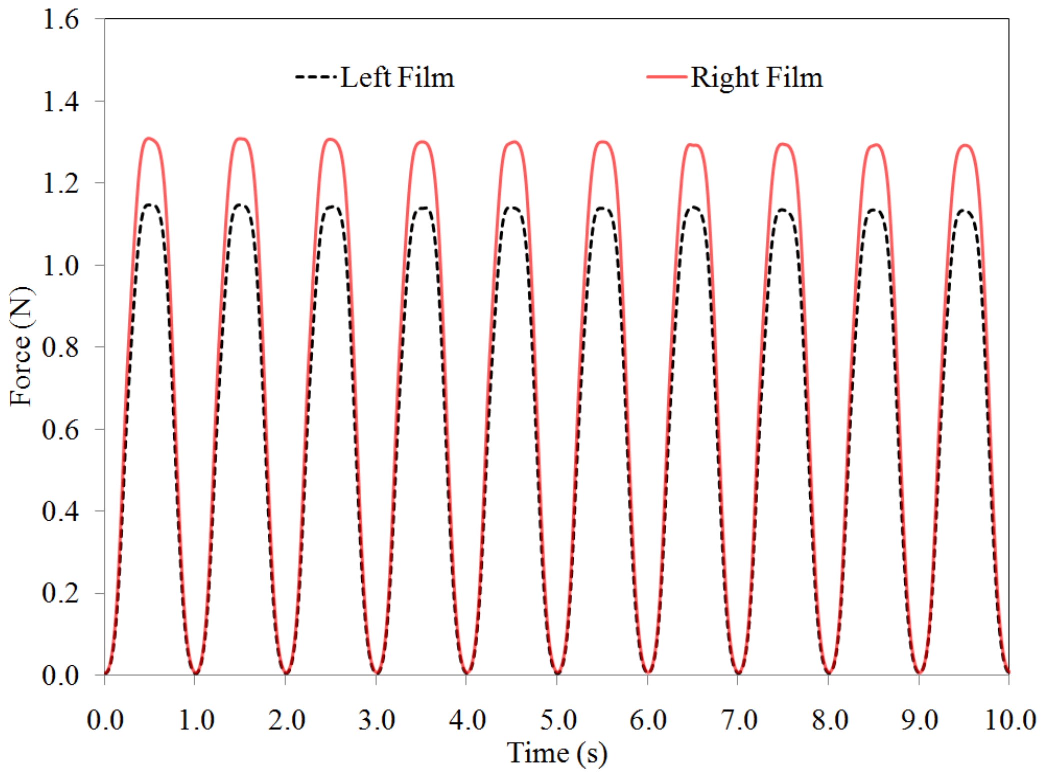

Figure 8-11: The output of the sensor while interacting with an artificial tissue containing an embedded solid lump on the right side of the contact area.

8.7 Conclusions

In the present study, an innovative optical-piezoresistive hybrid sensing principle is proposed to measure tactile information during the tool-tissue interaction in surgical applications. The sensing principle relies on measuring the contact force by using piezoresistive-based methods and by measuring the resulting displacement by using optical-based methods. In order to validate the proposed concept, a finite element model of the interaction between the sensor and tissues was developed. In addition to the modeling, a prototype version of the sensor was microfabricated and also tested. Both the simulation results of the developed model and the experimental results of the fabricated sensor confirm the ability of the sensor to measure the local hardness of soft samples. One of the main applications of such measurement is in the medical device industry. Although this would be the main application of the proposed device, the sensor can have numerous applications in other industries such as the robotics and automation industry.

Chapter 9: Multi-Purpose Optical Microsystem for Static and Dynamic Tactile Sensing

To perform minimally invasive surgical tasks, surgeons need artificial touch perception to characterize tissues via surgical instruments. In the present study, a sensor with capabilities similar to the fingertip perceptions of surgeons is designed, modeled, simulated, prototyped, and tested. Comprehensive experimental tests were performed on the prototype version of the sensor. The test results confirmed that the proposed sensor, being similar to human fingers, measures the amount of contact force, the position of a concentrated force, the local variations in force distribution along the length of the sensor, and the relative hardness as well as the local discontinuities in the hardness of soft objects. The sensing element of the sensor relies on optical microsystems technology. Due to the inherent characteristics of this technology, the sensor encompasses a large number of enhanced features. Such features are that it is magnetic resonance compatible, electrically passive, and performs under static/dynamic loading conditions, which are essential in performing a wide-range of minimally invasive surgical tasks.

9.1 Introduction

The use of minimally invasive surgical techniques in performing surgical procedures offers significant advantages for both surgeons and patients. In recent years, this field has rapidly expanded from conventional endoscopic devices to the sophisticated computer-controlled robotic-assisted surgical platforms. The da Vinci® surgical system developed by Intuitive Surgical Inc. [5] in the USA and its Canadian counterpart, Amadeus®, developed by the Titan Medical Inc. [15], are among the most popular examples of such surgical platforms. In these surgical platforms, tactile sensors are required in order to let surgeons know the tactile information at the contact area between surgical tools and tissues.

Up to the present, a diverse number of sensors have been proposed for use in minimally invasive surgical tasks whether they are conventional endoscopic tasks or complicated robotic-based tasks. However, to the best of the authors' knowledge, the proposed sensor is the only one that encompasses all the following characteristics in one single small-size package: first, the sensor measures the amplitude as well as the position of a concentrated force; second, the sensor measures the local variations in force distribution along its length; third, it measures the relative hardness of soft objects such as tissues; fourth, it measures local discontinuities in the hardness of soft objects along the contact area; fifth, it is magnetic resonance compatible; sixth, it is electrically passive; seventh, it performs under both static and dynamic loading conditions; eighth, the design of the sensor is based on microsystems technology, which allows the miniaturization necessary for it to fit into the limited narrow space on the end-effectors of surgical tools; and ninth, using the low-cost micro electro mechanical systems (MEMS) batch fabrication techniques, it can be produced in a cost-effective way, thereby addressing the economic requirements of the medical device industry.

The present study discusses the designing, modeling, simulating, prototyping, and testing of the proposed tactile sensor. After the explanation of its design, the theoretical model of the sensing principle of the sensor as well as the finite element model of the sensor-tissue interaction is discussed. The prototype version of the sensor was fabricated and tested by using micro-systems technology. The experimental test results prove that the sensor measures the relative hardness of artificial tissues as well as the local discontinuities in the force and hardness distribution along the contact area between the sensor and tissues.

9.2 Sensor Design

In the design of the sensor, the objectives as well as the constraints should be considered. The objective is to measure the amplitude/position of force, the variations in force distribution, the relative hardness, and the discontinuities in the hardness. Consequently, the sensor must comprise various sensing elements to address the required objectives. In the structure of the sensor, multiple sensing elements should be reserved for sensing the force distribution and force position. However, such elements are not enough to satisfy the hardness measurement requirements. In fact, for the hardness measurement of the soft objects, the contact force as well as the resulting deformation must be measured simultaneously. As a result, another sensing element is required to measure the resulting deformation. In the structural design of the proposed sensor, two sensing layers are incorporated. One sensing layer measures the contact force whereas the other layer performs relative measurements of the resulting deformation. Moreover, the multiple sensing elements integrated into the sensor structure measure the variations in force distribution and the discontinuities in hardness.

More pointedly, the design constraints should also be taken into account. Such constraints consist of the following: (a) the constrained size of the available space at the tips of surgical end-effectors; (b) the interference with magnetic resonance imaging (MRI) and ultra-sound devices commonly available in surgical rooms; (c) the electrical disruption of the organs of the body such as the heart; and (d) the performance under dynamic and also static loading conditions. In fact, the MEMS-compatible design of the sensor addresses the first constraint. Choosing the optical fiber sensing principle addresses the second, the third, and the fourth constraints. In the design phase, each component and the whole assembled structure of the sensor are dealt with.

9.2.1 Sensor Components

As shown in Figure 9-1, the sensor comprises five narrow layers and five pairs of optical fibers. The first, the third, the fourth, and the fifth layers, counting from the bottom, are made of silicon whereas the second layer is made of polydimethylsiloxane (PDMS) material. The first layer, which is a single part, is the substrate of the sensor. The second layer, which consists of three separate parts with the same thickness, is the elastic foundation of the sensor. The third layer consists of three separate parts cut from a micromachined silicon wafer. On the top surfaces of these three parts, two rows of v-grooves are micromachined. The fourth layer includes four silicon chips cut from a silicon wafer. Each two of these four chips is located one on the left side and one on the right side of the sensor. The fifth layer, which is a single part, is a beam cut from a micromachined silicon wafer. On the bottom surface of the beam, three parallel rows of v-grooves are micromachined. All of the optical fibers of the sensor are single-mode. They are integrated into the v-grooves of the third layer and the fifth layer. Whereas two pairs of fibers are integrated into the third layer, three pairs of them are integrated into the fifth layer.

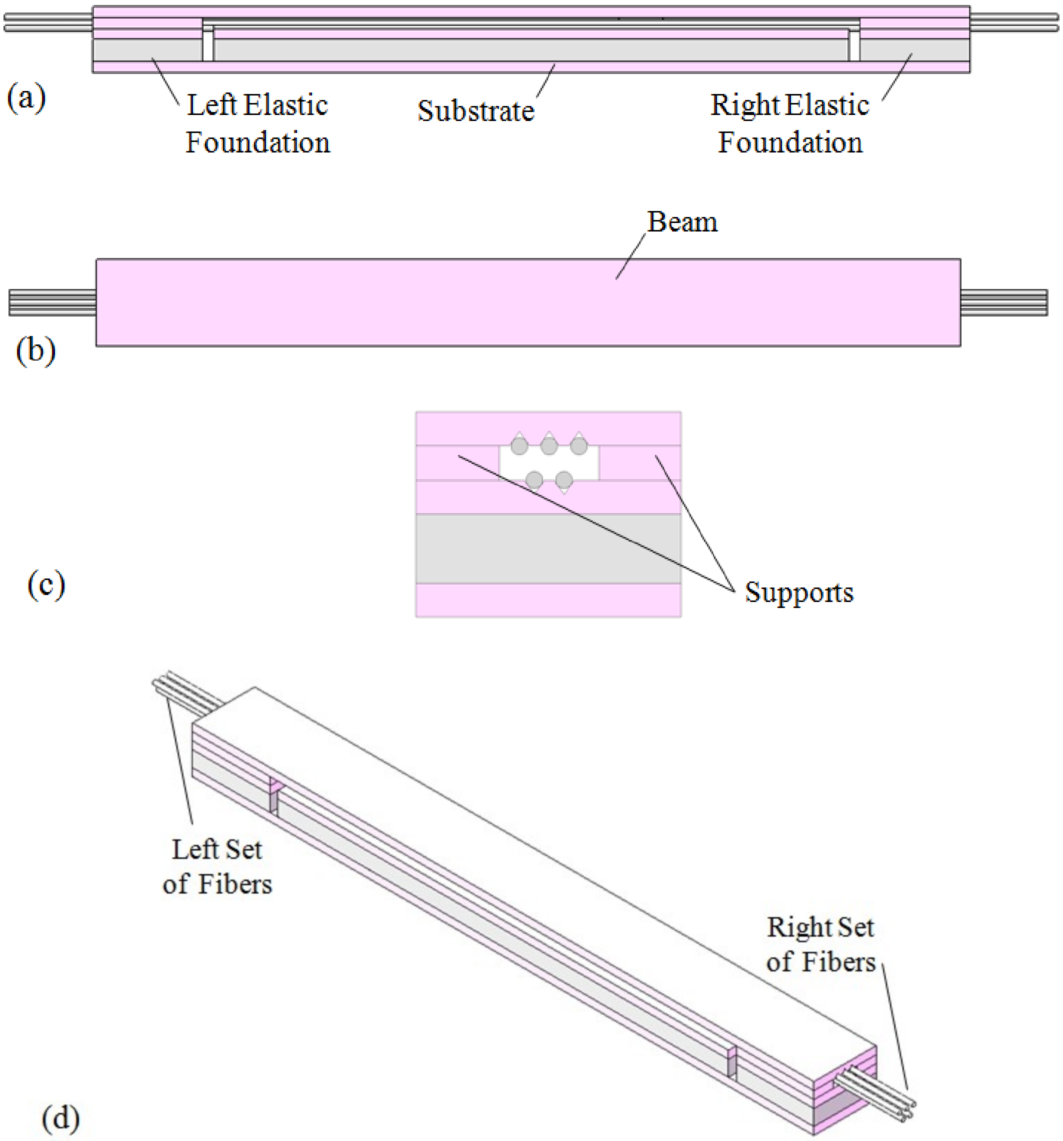

Figure 9-1: The design of the sensor in various geometrical views: (a) front view; (b) top view; (c) side view; and (d) 3D view.

9.2.2 Sensor Assembly

The five layers of the sensor are mounted on top of each other. Between the layers, the optical fibers are integrated with a specific configuration. Figure 9-1 shows the assembled structure of the sensor in different views whereas Figure 9-2 illustrates the detailed design of the integration of the optical fibers inside the v-grooves on the silicon parts of the sensor. In fact, the optical fibers, which are integrated into the third and fifth layers of the sensor, provide two sensing layers for the sensor. The third layer measures the force whereas the fifth layer performs relative measurements of the resulting deformation.

In the sensor assembly, the first three layers are assembled. Then the optical fibers of the third layer are assembled. In the next step, the fourth layer is assembled. Before assembling the fifth layer, the optical fibers are integrated in this layer. Finally, the fifth layer is assembled.

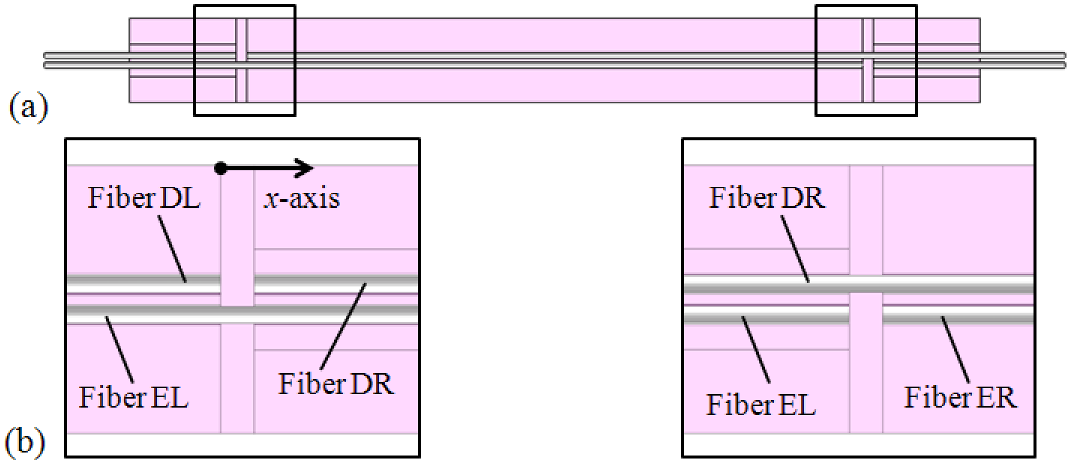

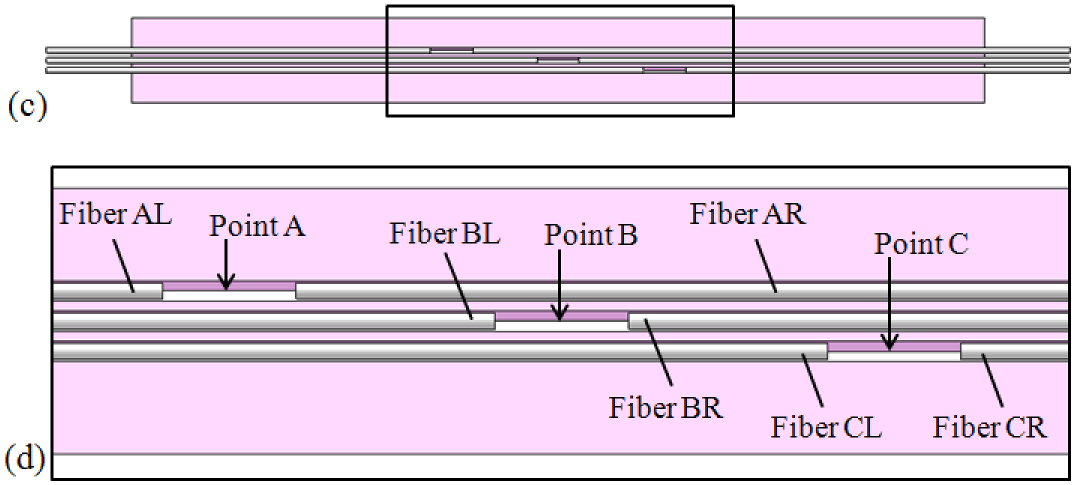

Figure 9-2: The detailed design of the integration of optical fibers inside the v-grooves on the silicon parts of the sensor: (a) shows the fibers integrated into the third layer of the sensor; these fibers measures the force; (b) shows the magnified view of (a); (c) shows the fibers integrated into the fifth layer, which is the beam of the sensor; (d) illustrates the magnified view of the (c).

As depicted in Figure 9-2-b, on the left side of the third layer, the Fiber DL and the Fiber DR are aligned in front of each other along their axis. A gap of 500 µm is provided between these two fibers. This gap is continued through the third and the second layers of the sensor. On the right side of the sensor, in a similar configuration, Fiber EL and Fiber ER are aligned in front of each other with a 500 µm gap. This gap is extended through the third and second layers up to the substrate. On the fifth layer, as depicted in Figure 9-2-d, Fiber AL and Fiber AR are aligned inside one of the v-grooves with an approximately 1 mm gap. The same configuration is applied between Fibers BL/BR and Fibers CL/CR. The middle point of the gaps between the pairs of Fibers A, B, and C is spaced at points that are one third (Point A), one half (Point B), and two thirds (Point C) of the distance down the sensor beam respectively with respect to the *x*-axis shown in Figure 9-2-b. A light source is connected to the left fibers whereas the right fibers are coupled to photodetectors.

9.3 Sensor Modeling

Three aspects should be taken into consideration in the modeling. The first aspect is the theoretical considerations of the optical loss between the fibers. The second aspect is the relation between the loading conditions applied to the sensing component of the sensor and the resulting output of the fibers. The third aspect is the relation between the degree of hardness of the contact tissue and the resulting loading conditions during the sensor-tissue interaction.

9.3.1 Optical Modeling

The sensing component of the sensor is the sensor beam. The total contact force applied to the sensing component is measured by the pair of Fibers D on the left side and the pair of Fibers E on the right side of the sensor. The sensing component is modeled as an Euler-Bernoulli beam with fixed-fixed boundary conditions. Through the fourth layer and the third layer, the force applied to the beam is applied to the left part and the right part of the second layer, which is the elastic foundation. The elastic foundation, which is made of PDMS, is modeled as a linear elastic material with a modulus of elasticity equal to 3.639 MPa obtained from experimental results. The applied force results in the compression of the PDMS layer, thereby reducing the coupling loss between the pairs of fibers. The theoretical aspects of the coupling loss between the fibers are discussed in Section 5.2.2 and Section 7.3.

9.3.2 Sensor-Tissue Interaction Modeling

Figure 9-3 shows the finite element model of the sensor and the contacting tissue in COMSOL software. At the top, the tissue interacts with the upper jaw of a test instrument whereas at the bottom, the tissue interacts with the sensing component of the sensor, which is the sensor beam. A controlled distributed load is applied to the tissue via the upper jaw of the test instrument. The resulting beam deflection as well as the resulting deformation in the elastic foundation of the sensor is simulated during the sensor-tissue interaction.

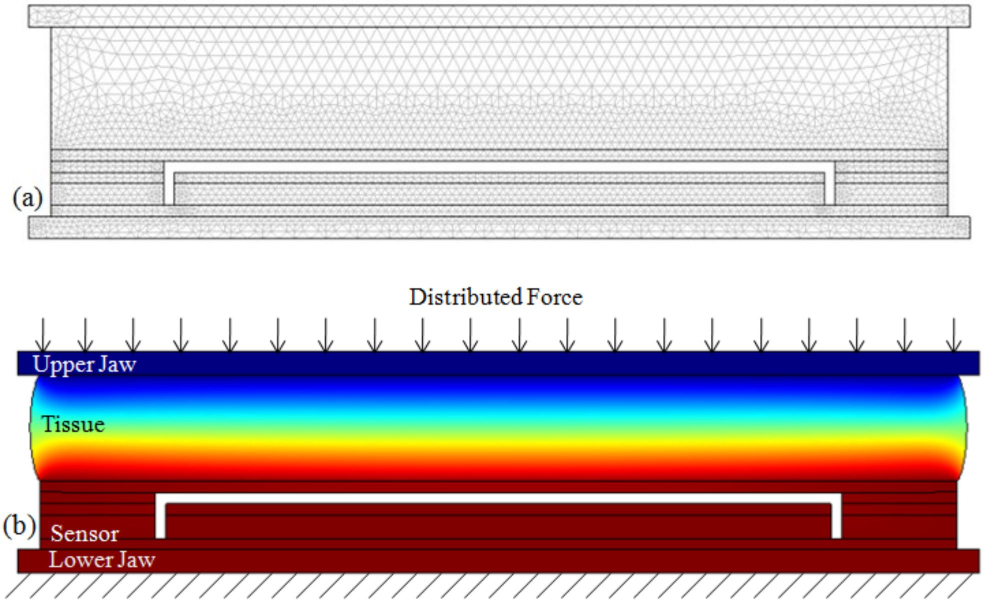

Figure 9-3: The finite element model of the tool-tissue interaction: (a) meshed structure of the model; (b) the deformation of the tissue and the components of the sensor. The tissue is modeled as a hyperelastic material. Simulation results show that the sensor measures the relative hardness of contact tissues.

In order to develop the finite element model of the tissue, compression tests were first performed on the artificial tissues with different degrees of hardness. Then, the obtained stress-strain data from the experiments were used to derive the material properties that are implemented in the model. The tissues were modeled as Neo-Hookean [75, 89] hyperelastic materials. The aspects of the hyperelastic model as well as the interaction model between the sensor and the tissue are discussed in Chapter 4 and Section 8.3. Table 9-1 summarizes the obtained material constants for three different artificial tissues with different degrees of hardness.

Table 9-1: Neo-Hookean parameters of the artificial tissues

	μ (kPa)	κ (kPa)
10-OO Material	2.743	137.149
30-OO Material	9.542	477.123
20-A Material	63.293	3164.638

Although a comprehensive parameter study for the model of sensor-tissue interaction is presented in Chapter 4, another simulation results is also discussed in this section. Figure 9-4 shows that, for the same amount of force, the deflection of the sensor beam varies during the interaction with tissues with different degrees of hardness. Based on this information, the softness of the contact tissue can be measured. For the same value of contact force per unit length of the upper jaw, the greater the degree of hardness, the smaller the beam deflection. The simulated results show that there is a reverse relation between the degree of hardness of the contact object and the deflection of the beam. This relation will be used to perform the relative measurements of the hardness of tissues in the experiments.

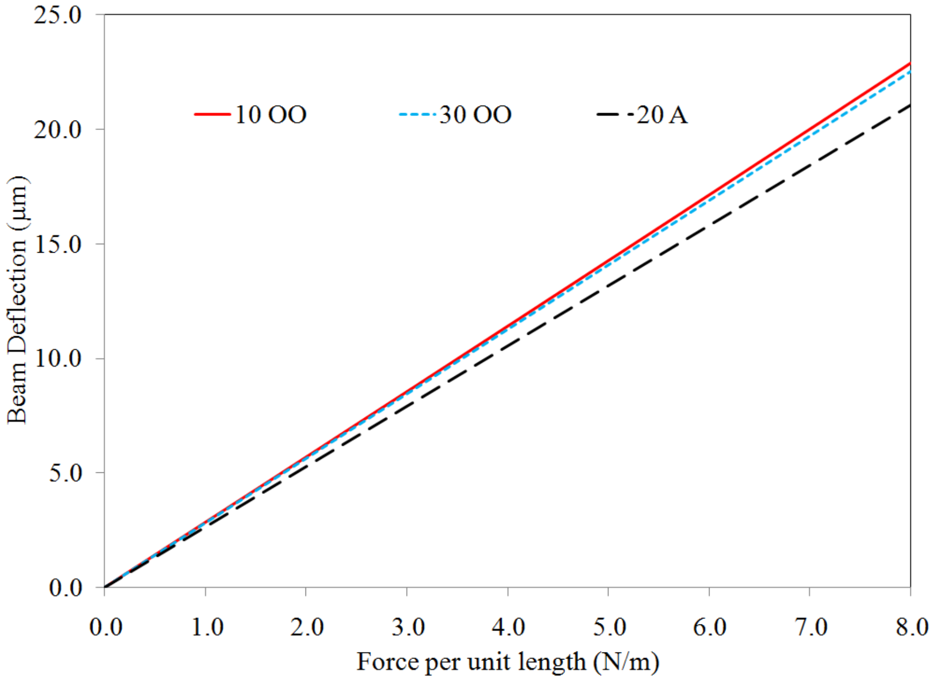

Figure 9-4: For the same amount of force, the deflection of the sensor beam varies during the interaction with tissues with different degrees of hardness. Based on this information, the softness of contact tissue can be measured.

For the same simulation, Figure 9-5 compares the contact force against the *y*-displacement of the left and the right elastic foundations. For the same amount of force applied to the tissue through the upper jaw of the test instrument, the simulation results verify that, while the beam deflection varies for the three contact tissues, the *y*-displacement of the PDMS layers remains constant. The PDMS *y*-displacement is measured by the integrated fibers on the third layer of the sensor.

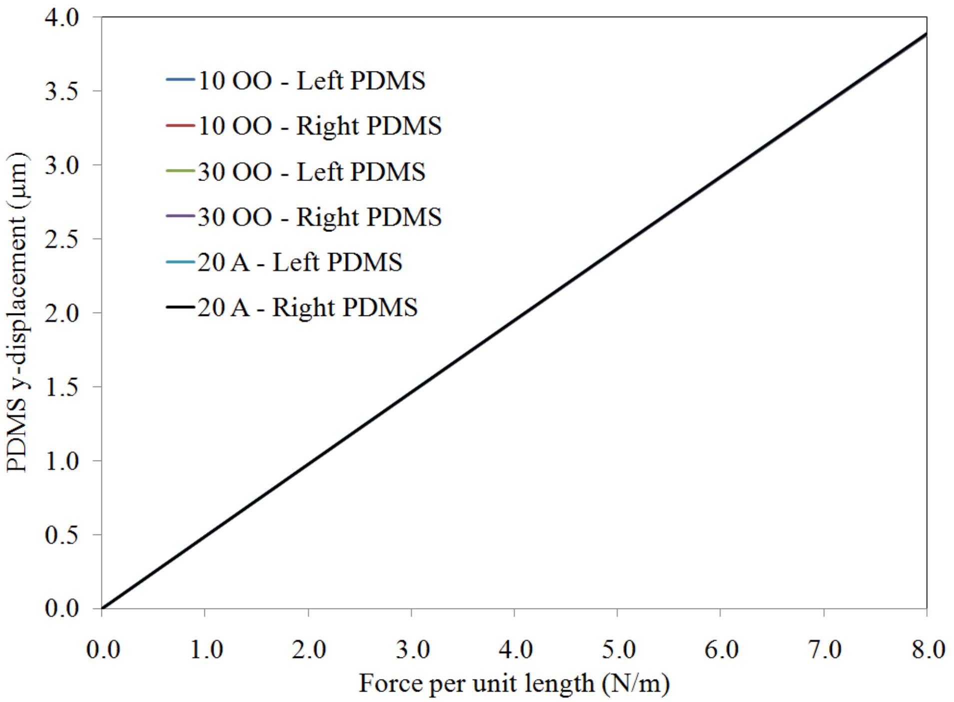

Figure 9-5: Contact force versus the y-displacement of the left and the right elastic foundations for three soft materials with different degrees of hardness.

Figure 9-6 shows the finite element model of the sensor and a tissue with an embedded solid lump using COMSOL software.

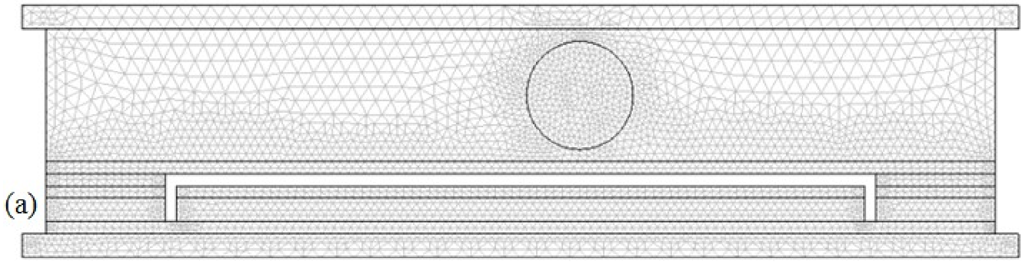

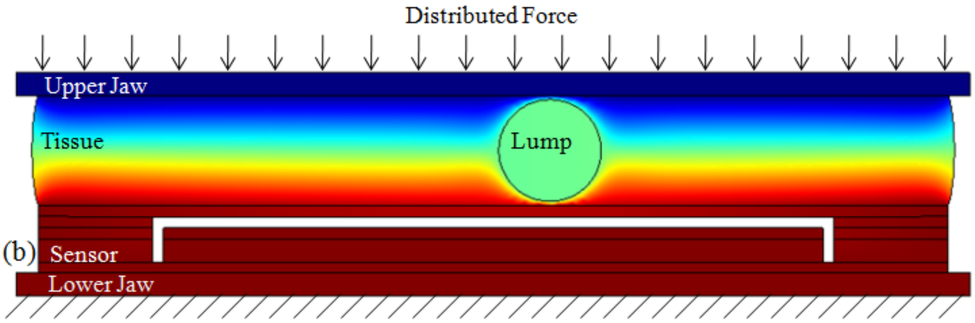

Figure 9-6: The finite element model of tool-tissue interaction. The tissue contains an embedded lump at position *X*. (a) the meshed structure of the model; (b) the deformation of tissue, embedded lump, and the components of the sensor. The model undergoes large deformations. The tissue is modeled as a hyperelastic material.

The effects of the lump’s size and location as well as its modulus of elasticity on the sensor’s beam deflection are studied in Chapter 4, Section 4.5.

9.4 Sensor Micro-fabrication

Isotropic wet etching techniques were utilized to micro machine the v-grooves on an N-Type <100> silicon wafer. The micro fabrication process has been described in Section 5.3. Figure 9-7 shows the design of the mask that was used to micromachined the v-grooves on the silicon wafer.

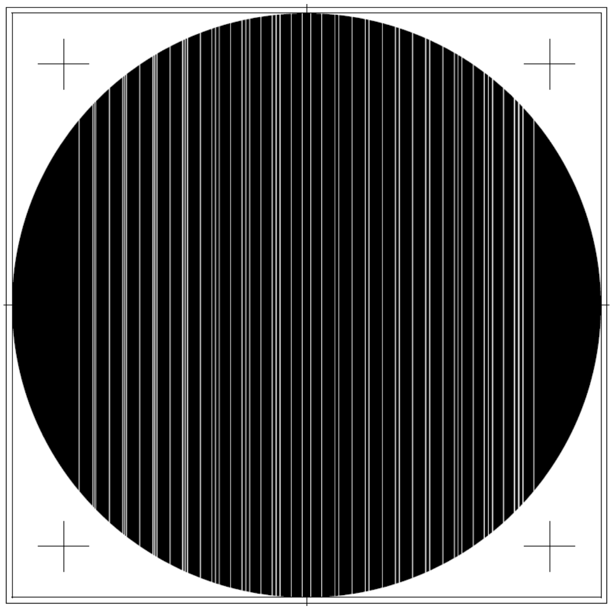

Figure 9-7: The design of the mask used to micromachine the v-grooves on silicon wafers.

Figure 9-8 shows the photograph of the micromachined silicon wafer. Figure 9-8-a shows the wafer before cutting the sensor components whereas Figure 9-8-b shows it after cutting the sensor component. A blade with 120 µm thickness was used to cut the sensor components out of the wafer.

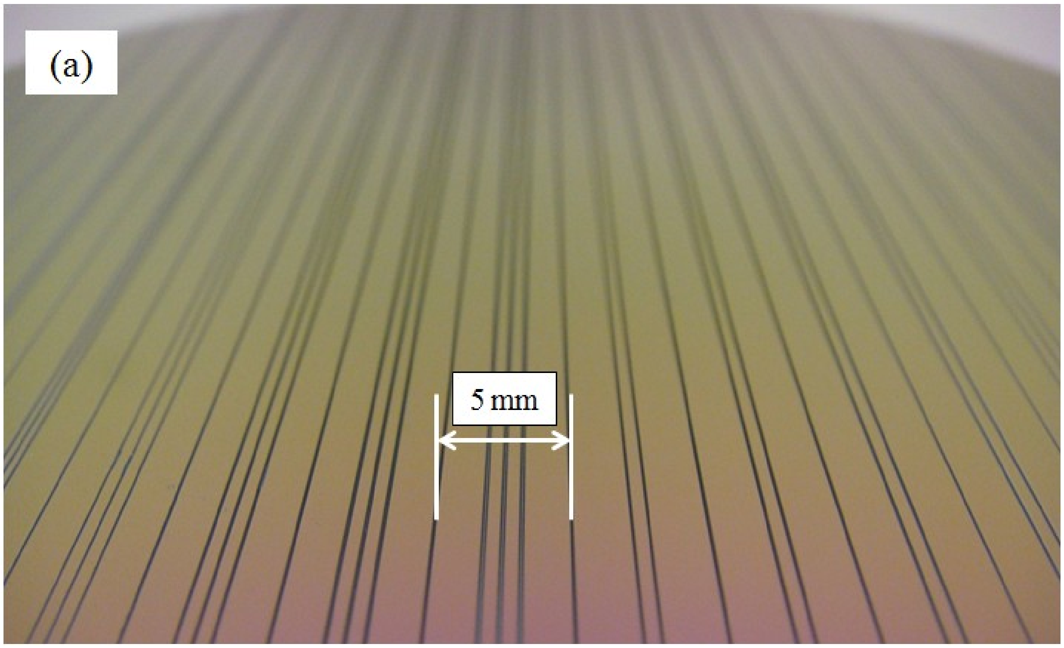

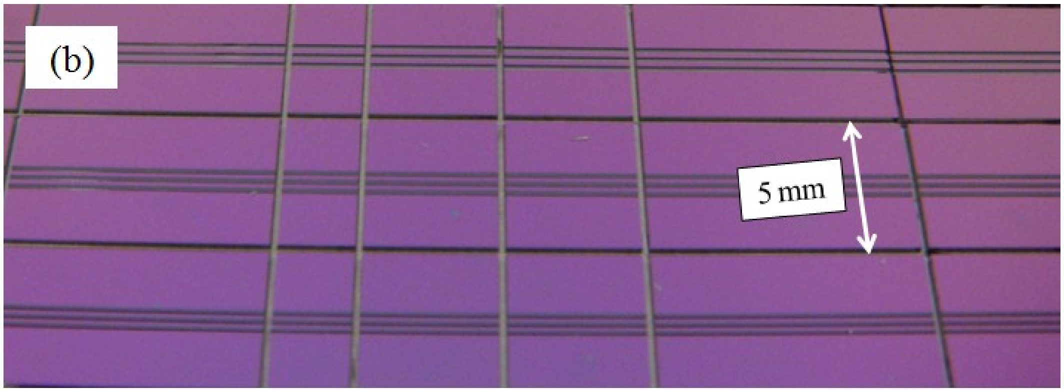

Figure 9-8: The photograph of the micromachined silicon wafer: (a) before cutting the sensor components; (b) after cutting the sensor components.

Figure 9-9 shows the configuration of the assembled optical fibers integrated into the v-grooves on the bottom surface of the sensor beam under the microscope. Where *L* is the length of the beam, the position of Point A, B, and C are located at a distance of *L*/3, *L*/2, and 2*L*/3 respectively from the left edge of the beam with respect to the coordinate system shown in Figure 9-2.

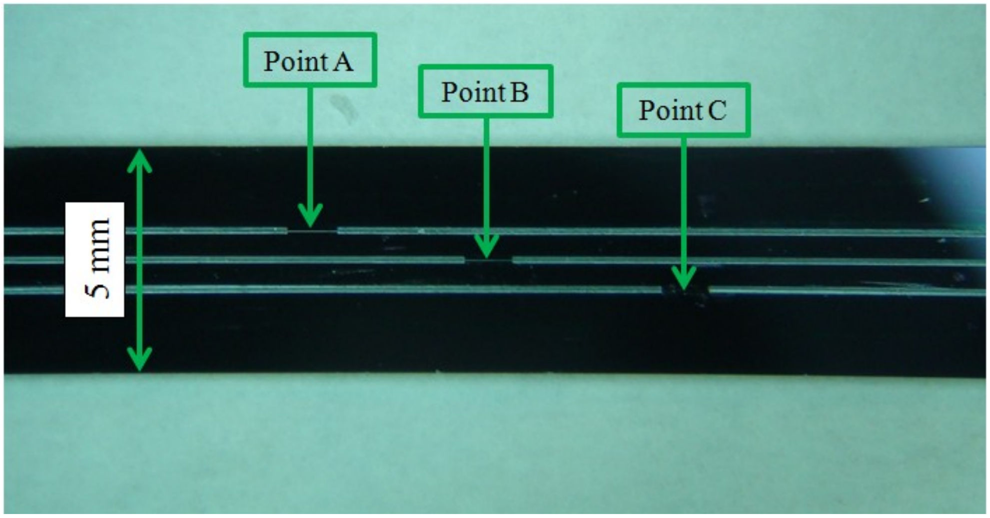

Figure 9-9: The configuration of optical fibers integrated into the v-grooves on the lower surface of the sensor beam under the microscope.

To qualify the surface quality and the size of the v-grooves, scanning electron microscopy (SEM) techniques was used to observe the v-grooves and the integrated fibers inside them. Figure 9-10 illustrates the SEM images of the three micromachined v-grooves on the bottom surface of the sensor beam. The top view of the bottom surface of the beam and the angled view of the beam edge are shown in Figure 9-10-a and Figure 9-10-b respectively. The smooth etched surfaces of the v-grooves provide a foundation for aligning the pairs of optical fibers, accurately.

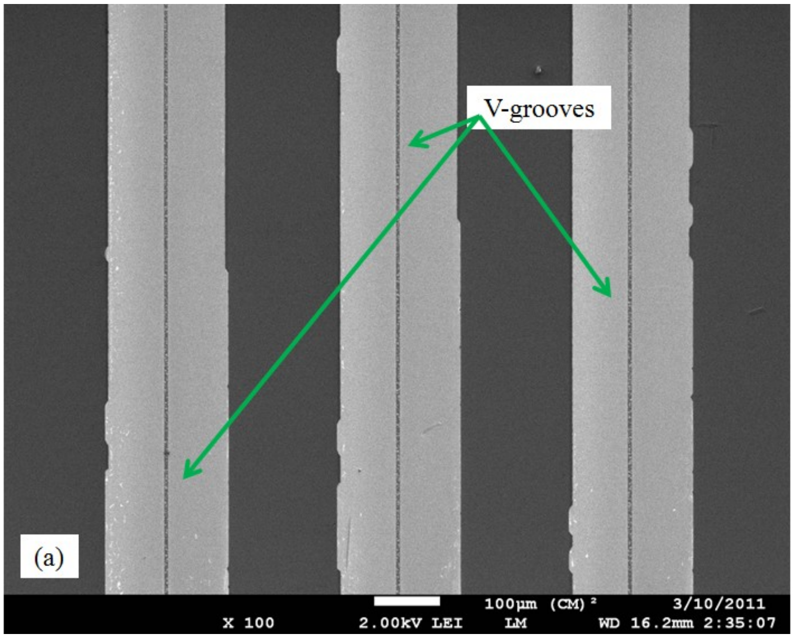

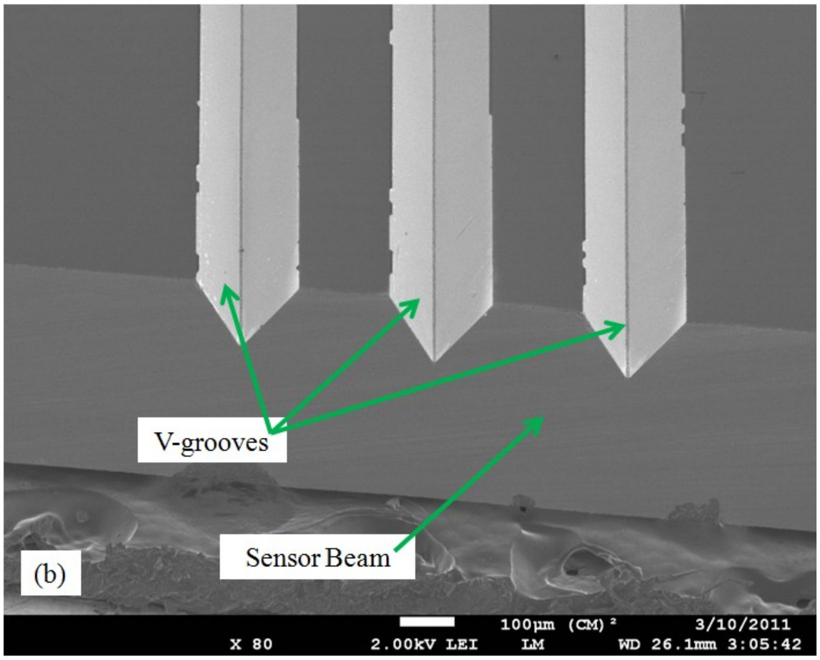

Figure 9-10: The SEM images of three v-grooves micromachined on the bottom surface of the sensor beam: (a) top view of the beam bottom surface; (b) angled view of the beam edge.

Figure 9-11 shows the SEM images of the integrated optical fibers inside the v-grooves on the sensor beam. In Figure 9-11-a, Fiber CL and Fiber CR are integrated into the corresponding v-groove whereas the v-groove for Fibers BL/BR is left empty for demonstration purposes. Figure 9-11-b is the magnified view of the gap between Fiber CL and Fiber CR. As can be seen, the smooth surface quality of the v-grooves results in precise alignments between each fiber pairs.

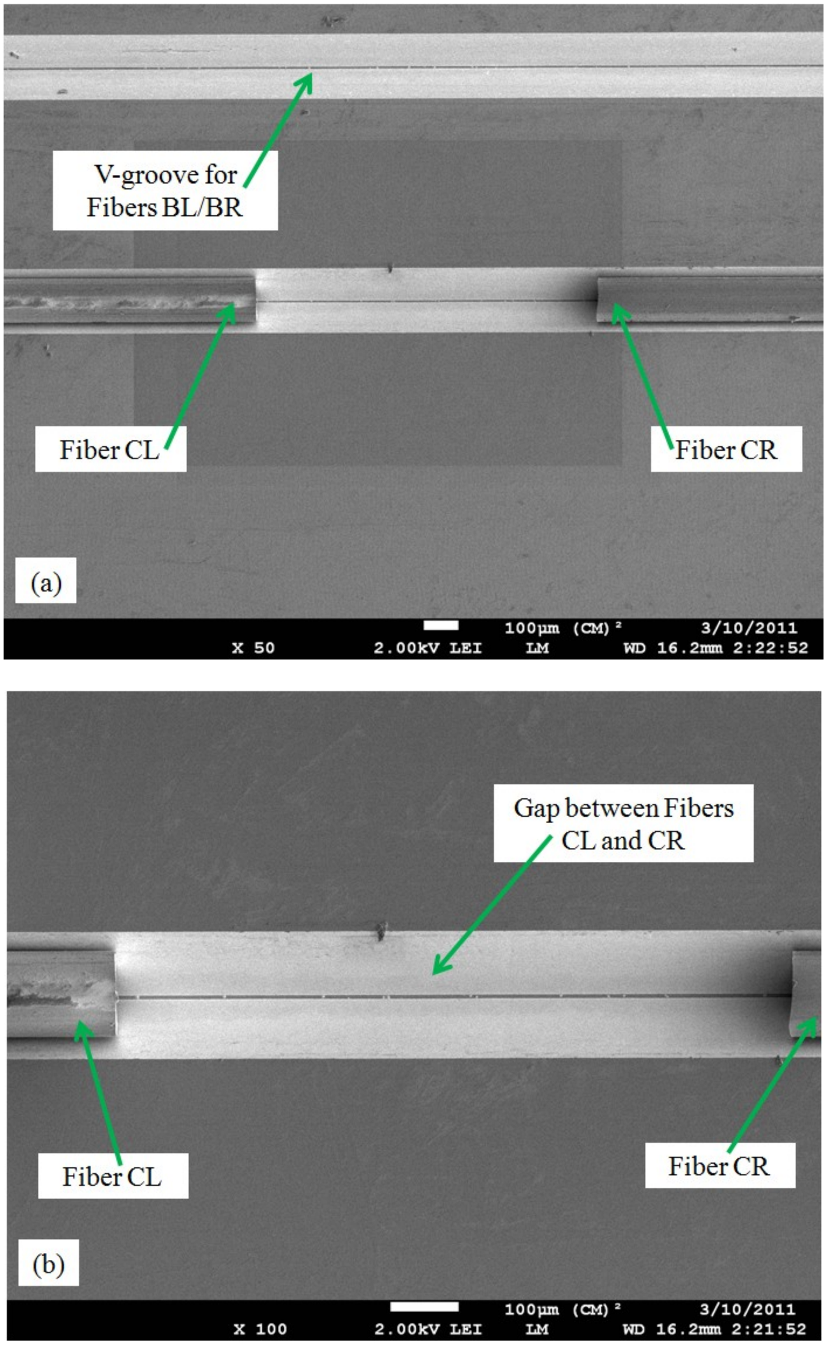

Figure 9-11: The SEM images of the integrated optical fibers inside the v-grooves on the sensor beam.

Figure 9-12-a shows the SEM images of Fiber DR on the right side of the sensor while Figure 9-12-b shows Fiber DL on the left side of the sensor both integrated into the third layer of the sensor. As can be seen, the v-grooves are neatly micromachined to provide a reliable foundation for the fibers integrated into the third layer of the sensor.

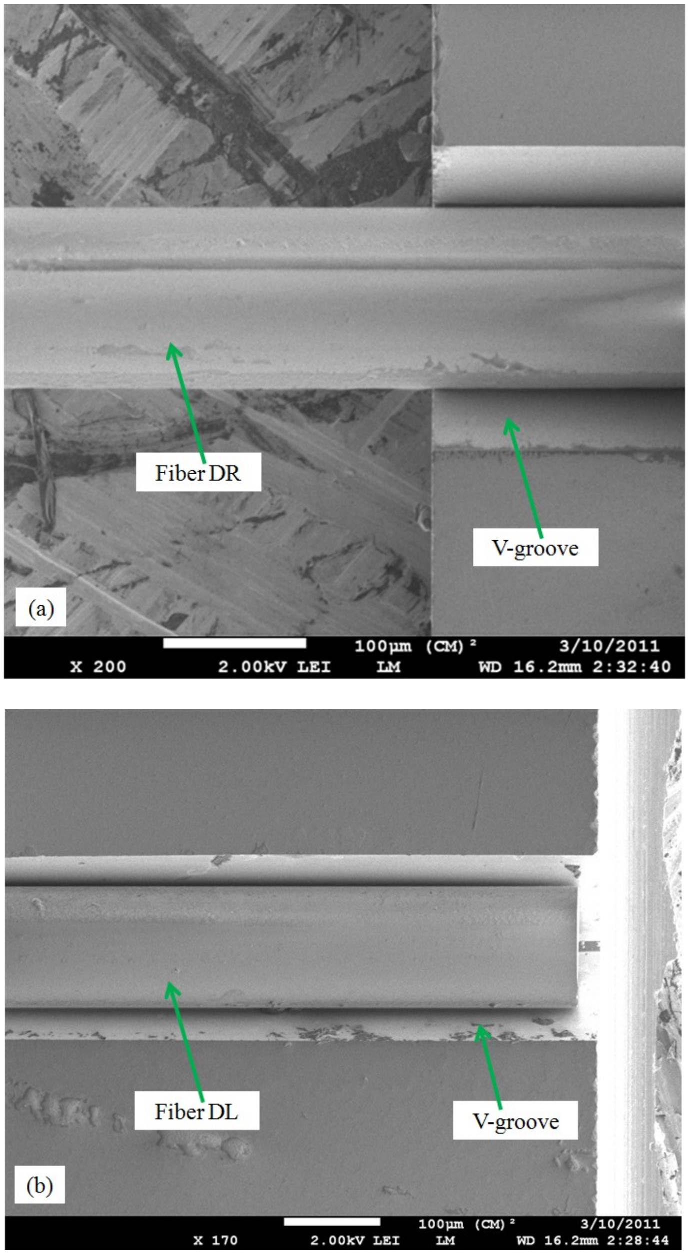

Figure 9-12: The SEM images of: (a) Fiber DR integrated into the right part of the third layer on the right side of the sensor; (b) Fiber DL integrated into the left part of the third layer on the left side of the sensor.

9.5 Experimental Setup: the Proof of Concept by Performing Experimental Tests

As mentioned before, using the finite element method (FEM), sensor-tissue interaction models were developed to prove the concept. In addition to the simulation results, in order to prove the concept, the sensor was fabricated and was tested. Figure 9-13 shows a photograph of the sensor components before the assembly. In this figure, the five layers of the sensor are placed next to each other. The optical fibers are not yet integrated into the v-grooves.

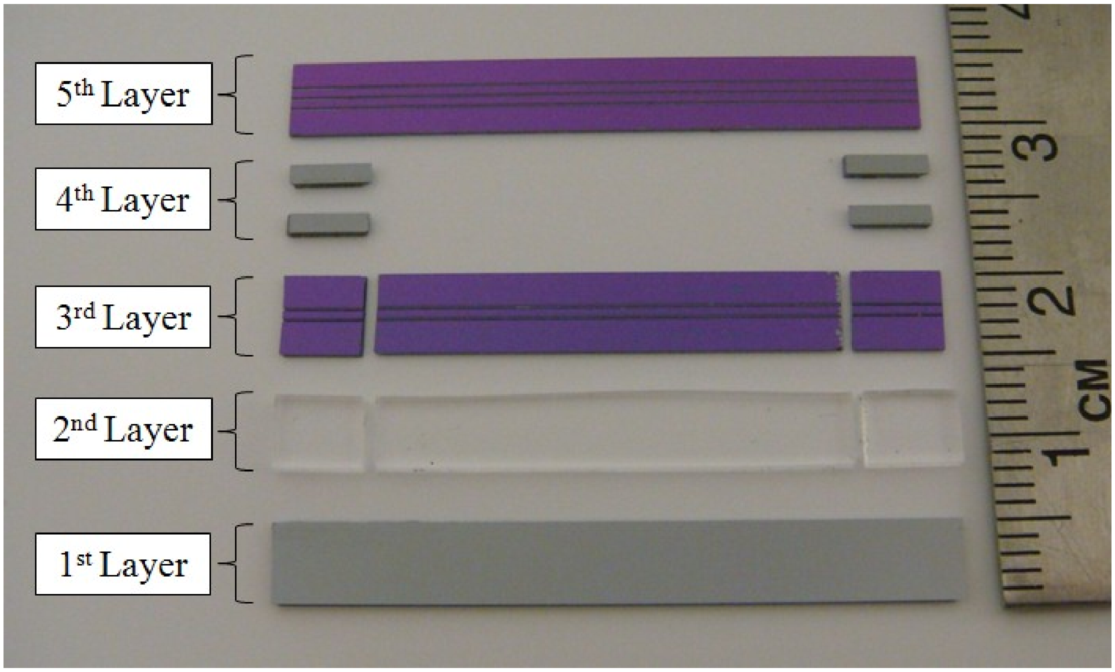

Figure 9-13: The components of the sensor before assembly.

Figure 9-14 shows the first three layers of the sensor assembled together. At the beginning of the sensor assembly steps, the second layer, which is the elastic foundation, is placed on the first layer, which is the sensor substrate. This substrate provides a rigid base for the other sensor components. The second layer comprises three separate parts, which are the left, middle, and right parts. Then the third layer, which consists of three separate parts (the left part, middle part, and right part), is placed on the second layer. A narrow gap is provided between the left part and the middle part as well as between the right part and the middle part in the second and third layers.

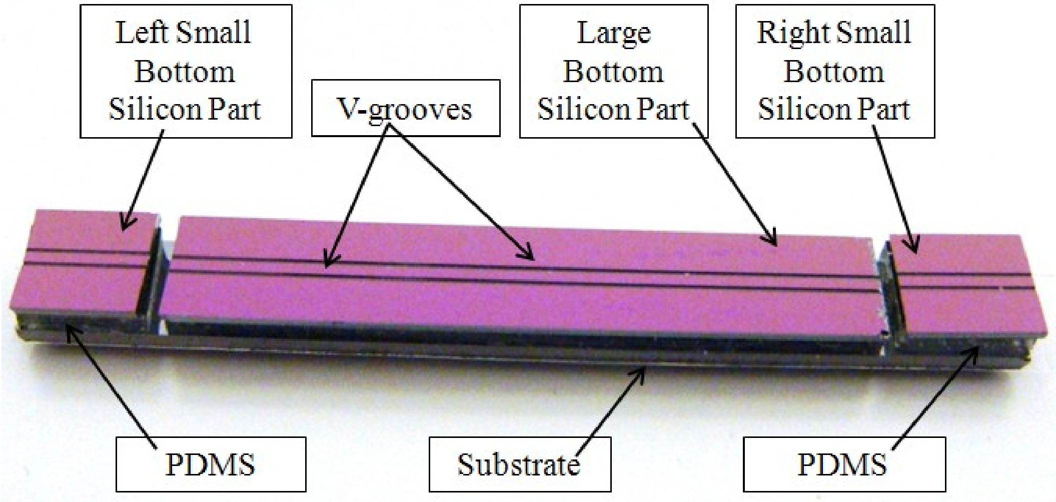

Figure 9-14: The first, second, and third layers of the sensor assembled together. The fourth and the fifth layer as well as the optical fibers are not yet assembled.

Figure 9-15 shows the progress made on the assembly steps of the sensor after fixing the fourth layer as well as after integrating Fibers DL/DR and EL/ER into the v-grooves of the third layer. The fourth layer included four separate parts, two of which were mounted on the left part of the third layer and the other two were mounted on the right part of the third layer.

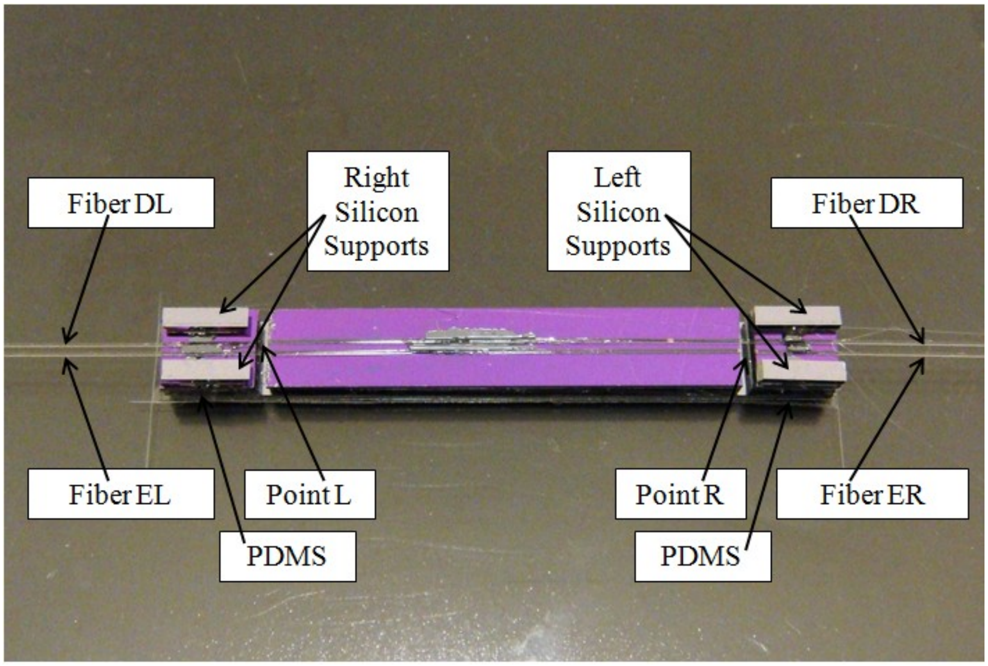

Figure 9-15: The lower part of the sensor integrating the optical fibers and the supports.

Figure 9-16 illustrates the photograph of the final assembled sensor. On the one hand, a light source is connected to the left set of fibers. On the other, the right fibers are connected to five photodetectors.

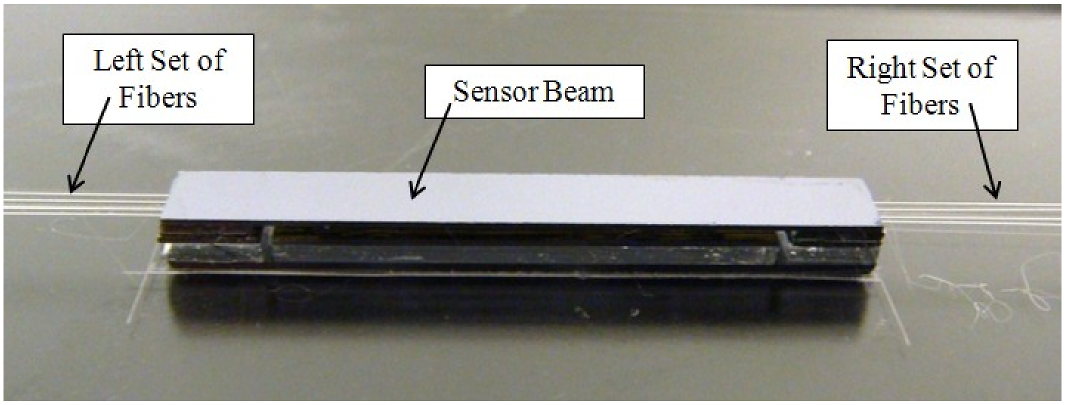

Figure 9-16: The photograph of the final assembled sensor.

Afterwards, several experimental tests were performed to validate the proposed concept. These experimental tests were performed under different conditions. First, the ability of the sensors to measure the softness/hardness of various soft artificial tissues was tested. The tested artificial tissues are three different silicone rubber materials with different degrees of hardness. These materials are listed in Table 9-2.

Table 9-2: Silicone rubber materials used as artificial tissues for the experimental tests.

Name of the Material	**Shore Hardness**
Ecoflex® 00-10	10 OO
Ecoflex® 00-30	30 OO
Dragon Skin® 20	20 A

Then, the capability of the sensors to locate the position of an embedded hard object in a soft object was tested. The hard object can be a potential lump, a blood vessel, a ureter, etc., surrounded by a background tissue (soft object in our case). Moreover, the ability of the sensor to perform under both static and dynamic loading conditions was investigated.

9.6 Experimental Results

Experimental testes performed to validate the sensor performance in measuring the softness/hardness of tissues with different degree of hardness as well as detecting lump/artery. Figure 9-17 shows the schematic diagram of the experimental setup. An ElectroForce test instrument from Bose Company (Minnesota, USA) was used to apply an input force to the sensor. The sensor was placed on the lower jaw of the Bose device. Different silicone rubber materials were placed between the sensor and the upper jaw of the test device.

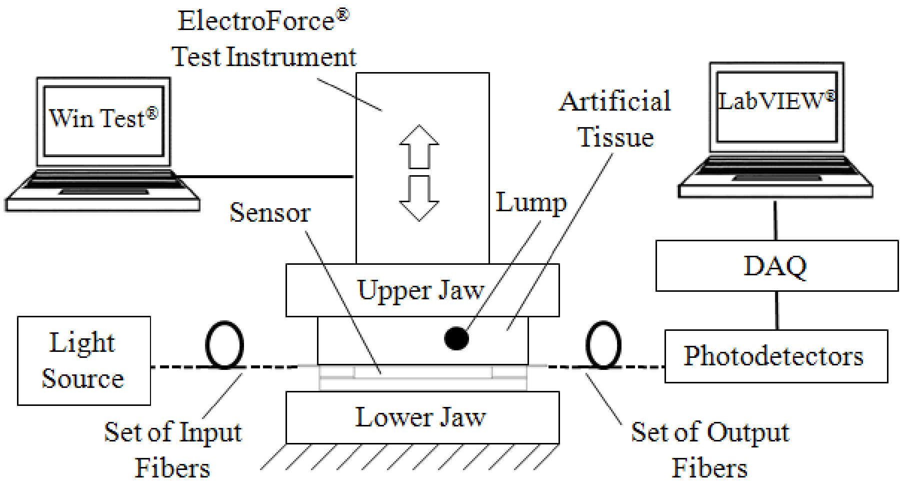

Figure 9-17: The block diagram of the experimental setup.

Figure 9-18 shows the photograph of the sensor in the various experimental tests. In the first step (a), the sensor was tested under a concentrated force applied through an indenter that is connected to the actuator of the ElectroForce tests instrument. This test was performed to calibrate the sensor outputs from its channels with respect to the concentrated applied force. In the second step (b), the sensor was tested while interacting with artificial tissues with different degrees of hardness. In this test, the capability of the sensor to measure the relative hardness of tissues was examined. In the third test (c) and the fourth test (d), the sensor was tested while it was interacting with artificial tissues containing an embedded artificial solid lump and an artificial solid artery respectively. These two tests evaluate the ability of the sensor to detect the position of a hidden lump/artery inside embedded soft background tissues.

In fact, a concentrated force applies to the sensor beam where the lump/artery is located. In addition to this concentrated force, distributed force applies to the sensor beam because of the interaction between the beam and the tissue. Because of the superposition principle for the deflection of the beam [72], this added distributed applied force will not affect the relative slope of the beam at Point A, Point B, and Point C. Consequently, proposed algorithm in Figure 6-5 can be used to measure the position of the lump/artery in real surgical scenarios. To examine this, tests (c) and (d) were performed on the sensor.

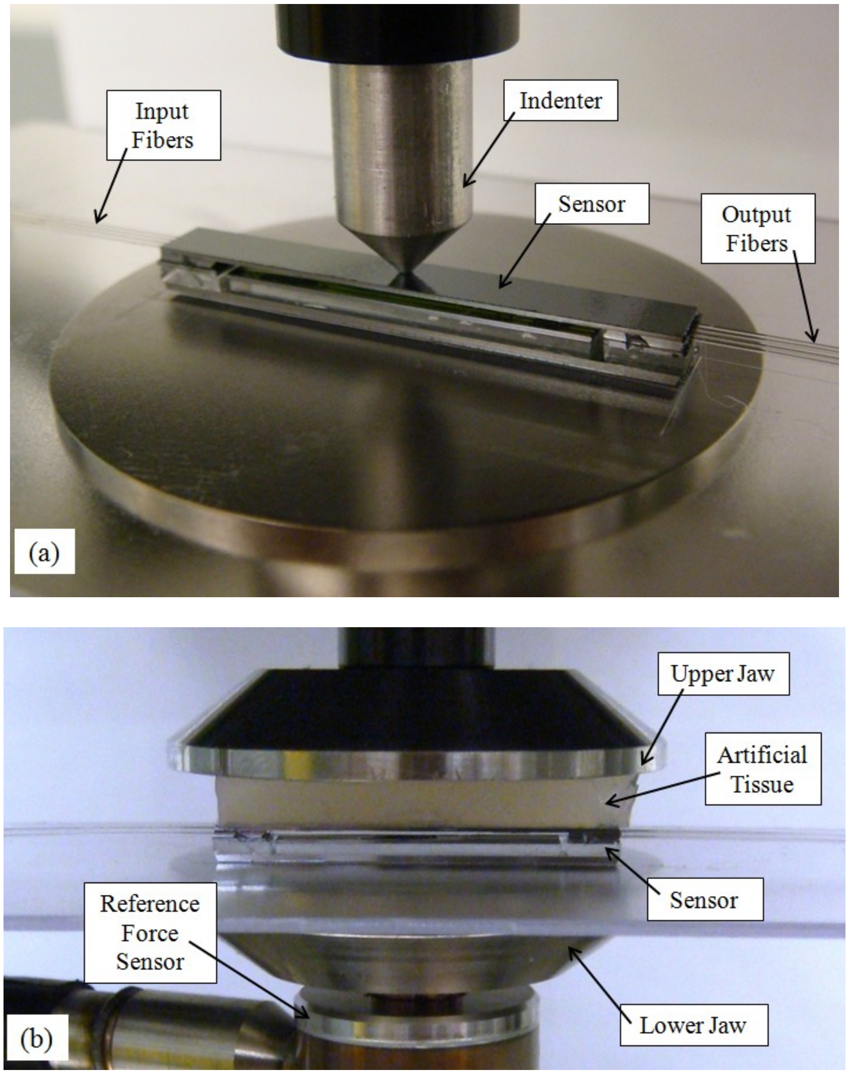

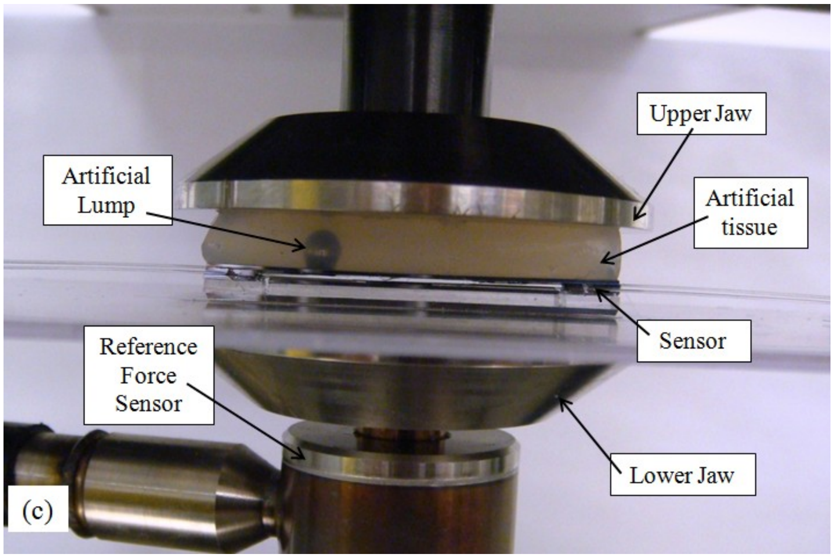

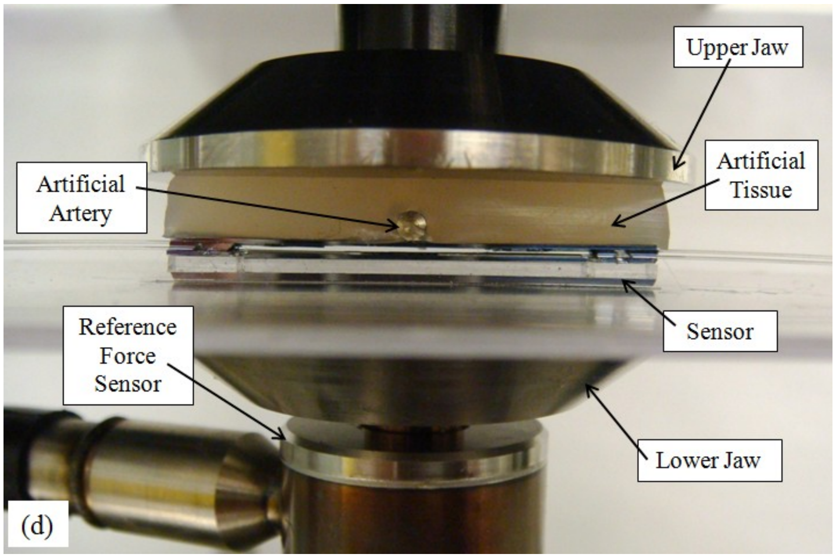

Figure 9-18: The photograph of the sensor in various experimental tests.

In order to validate the sensor performance to measure the relative hardness, the output of the sensor while interacting with the three artificial tissues was evaluated. The configuration of this test is shown in Figure 9-19-b. Through the upper jaw, a square force with the frequency of 0.1 Hz was applied to the tissues. This frequency was chosen to observe any potential relaxation or creep of the artificial tissues during the 5 seconds of stable sensor-tissue interaction during each period. Another reason for choosing such frequency was to study the sensor response under static loading conditions. Under such test conditions, Figure 9-19 shows the output of the sensor. As can be seen in the results, for the same contact force observed by the output of Fibers D and E, the resulting deformation of the samples vary based on their degree of hardness. In fact, as discussed in Section 9.3.2, the resulting deformation changes the output of Fiber B. In other words, the smaller the degree of the hardness of the tissue, the greater the voltage drop in the output of Fiber B. Considering this fact, the results of this test verify that the 10 OO, 30 OO, and 20 A tissues relatively have the smallest degree of hardness, the medium degree of hardness, and the greatest degree of hardness.

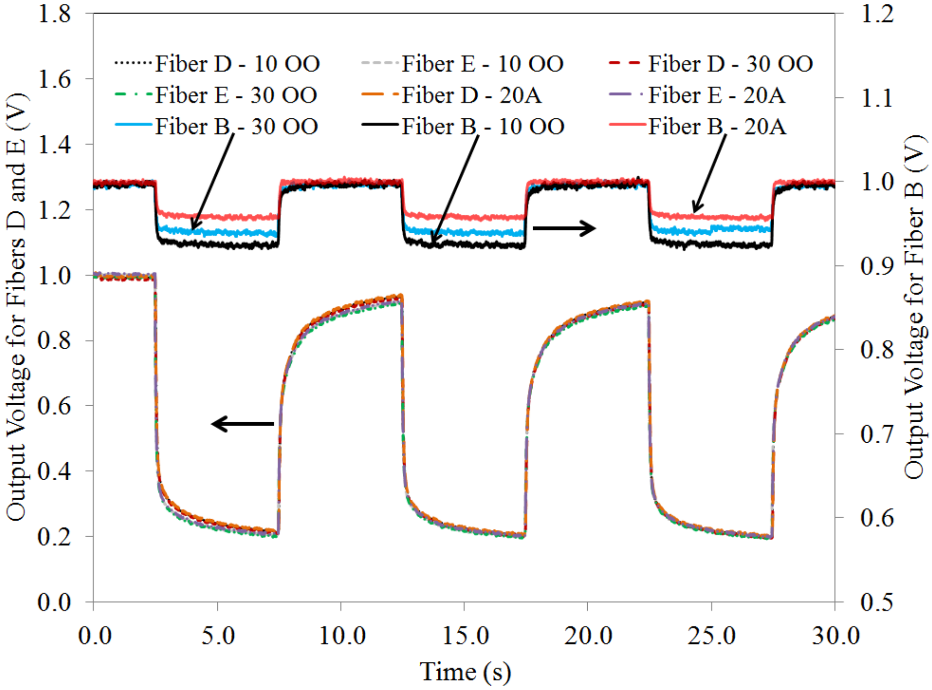

Figure 9-19: The output of the sensor to measure the relative hardness of three different artificial tissues.

The purpose of the next tests is to investigate the ability of the sensor to detect lump/artery under static loading conditions. To do so, a square force function with the amplitude of 0.1 N to 1.0 N and the frequency of 0.025 Hz was applied through the upper jaw as shown in Figure 9-23. Such low frequency was chosen to observe the sensor performance during the measurements under static loading conditions. With the chosen frequency, a constant force is applied for the duration of 20 seconds, which is long enough to address the needs of static interactions in real surgical tasks. Under described test conditions, Figure 9-23 shows the sensor output from Fibers A and C while a solid lump is embedded on the left-half part inside the tissue similar to shown photograph in Figure 9-23-c. Results show that the output voltage for Fiber C is less than the output voltage for Fiber A. Using the algorithm, it means that the lump is located on the left-half part. Consequently, this test confirms the lump detection ability of the sensor. Moreover, the sensor output from Fiber A and C undergoes negligible drift during the 20 seconds of constant interaction. This also confirms the sensor ability to perform under static loading conditions.

Again, to verify the sensor ability to detect a lump, a similar test to the previous one was performed. In this test, however, the lump was located on the right-half part instead of the left-half part. Figure 9-23 shows the sensor output from Fiber A and C under such test conditions. As can be seen, the output voltage for Fiber A is less than the output voltage for Fiber C. It means that the lump is located on the right-half part. Moreover, the outputs show negligible drifts under static loading conditions

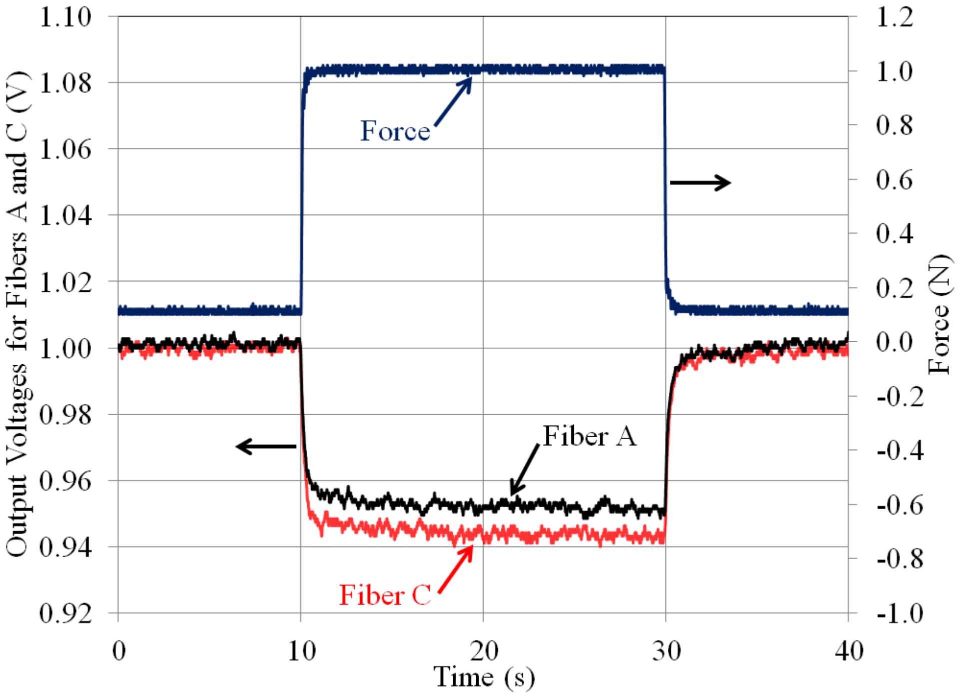

Figure 9-20: The output of the sensor while interacting with a tissue containing a lump located on the left-half part of the sensor as shown in Figure 9-18-c.

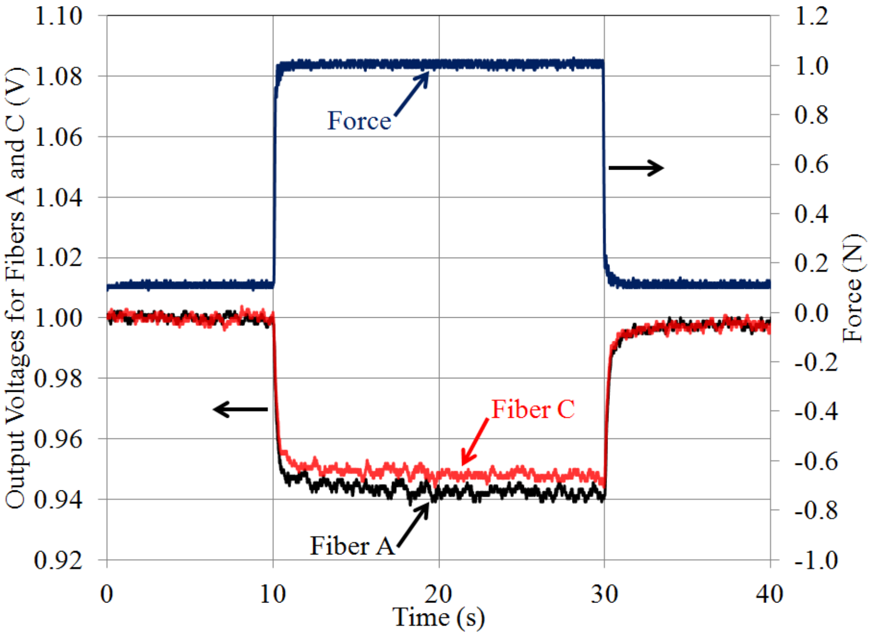

Figure 9-21: The output of the sensor while interacting with a tissue containing a lump located on the right-half part of the sensor.

In the next test, a solid cylindrical artery was embedded inside the tissue on the middle part of the sensor. Other parameters and conditions are similar to those used for the two previous tests. For this test, Figure 9-23 shows the sensor output form Fibers A and C. Once again, the static measurement ability of the sensor was verified. Since the artery is located on the middle point, there is not any difference between output voltages of Fibers A and C. It means two fibers are not enough to detect a lump/artery located on the middle point of the sensor. This is one of the limitations of the proposed sensor. This effects of this limitation can be minimized if surgeons examine at least two close positions during the tool-tissue interaction and compare the results.

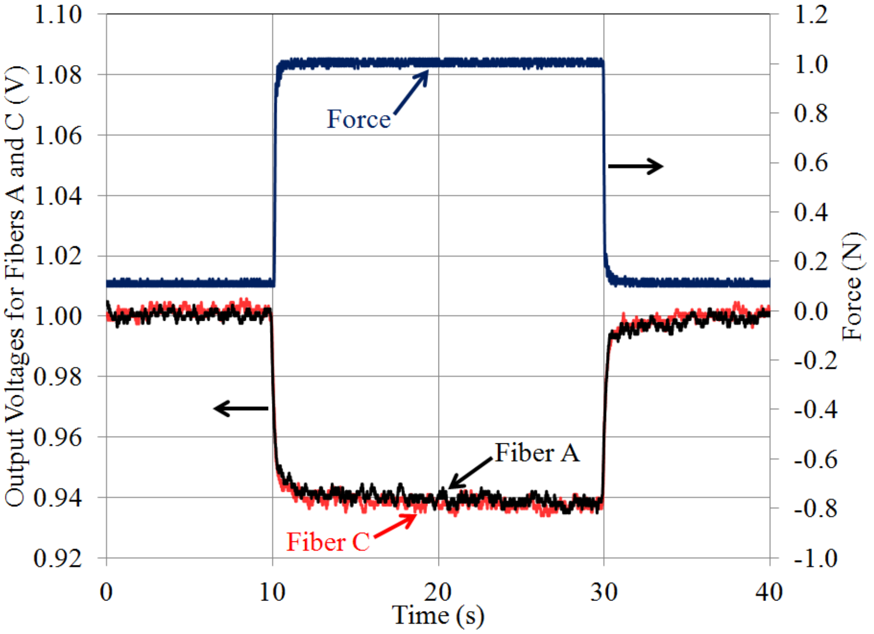

Figure 9-22: The output of the sensor while interacting with a tissue containing an artery located on the middle part of the sensor as shown in Figure 9-18-d.

Although by processing the outputs of Fibers A, B, and C the position of a hidden lump/artery can be detected, outputs of Fibers D and E can also be used to obtain further tactile information during sensor-tissue interaction. For instance, when a lump/artery is located on the left or right half part of the sensor, it causes an unsymmetrical force distribution to be applied to the sensor beam. Figure 9-23 shows the output of the sensor from Fiber D and Fiber E while interacting with a tissue containing a lump located on the left-half of the beam. In such testing conditions, the voltage drop for Fiber D is more than the voltage drop for Fiber E.

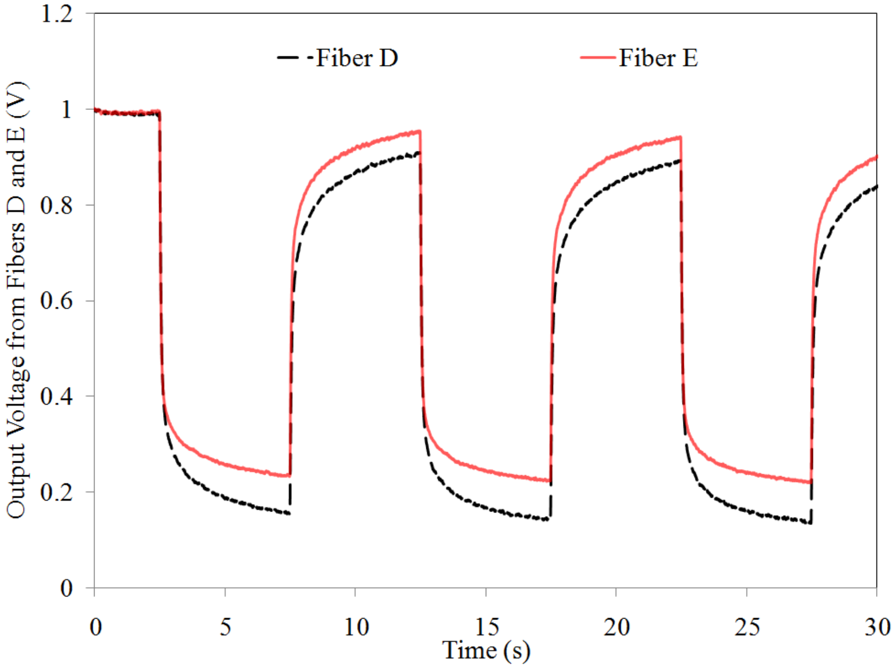

Figure 9-23: The output of the sensor from Fiber D and Fiber E when interacting with a tissue containing a lump on the left-half side of the sensor.

This information confirms that the applied force has an unsymmetrical distribution with the greater density on the left-half of the sensor beam. In other words, it tells surgeons that the lump/artery is located on the left-half part. This information will be added to the distributed force information observed by Fibers A, B, and C. Hence it helps surgeons to sense a more reliable tactile perception during tool-tissue interactions. As shown in the graph, the input force was a square function with the frequency of 0.1 Hz in this test.

Although the outputs of Fibers D and E have drifts, they can still perform measurements under static loading conditions. In other words, during the 5 seconds of static loading periods, Fibers D and E show reasonable outputs that can be used to detect unsymmetrical applied loads.

9.7 Conclusions

In the present study, an innovative concept is applied to develop a multi-functional tactile sensor for use in the robotics, automation, and medical device industries. The developed sensor measures the contact force as well as the mechanical properties of contact objects. On the one hand, the contact force can be a concentrated force, a distributed force, or any combination. On the other hand, the mechanical properties can be the degree of hardness/softness, stiffness, hyper-elastic properties, or viscoelastic properties of the materials. Such materials can be biological tissues for applications in the medical device industry, or any other soft materials in the automation and robotics industry. In addition to the innovative design of the sensor, it has other important novel features. For instance, (1) the sensor is immune to electromagnetic fields; (2) it is electrically passive; (3) it is ultra-sound friendly; and (4) it performs under both static and dynamic interacting conditions. Due to the first feature, the sensor performs in the presence of magnetic resonance imaging (MRI) devices, which are in widespread use in surgical rooms these days. Due to the second feature, the sensor is compatible with cardiovascular operations because it does not disrupt the normal electrical activities of the heart. Because of the third feature, the sensor can be utilized in specific types of operations where surgeons must use ultra-sound imaging techniques for whatever reason during surgical operations.

More importantly, due to the fourth feature, surgeons can perform the measurement while maintaining a stable static contact between surgical tools and tissues while at the same time avoiding tissue damage resulting from excessive interacting force between surgical tools and tissues. In fact, such surgical tools can be catheters in cardiovascular operations or can be surgical graspers in minimally invasive operations.

The sensor was modeled and the responses of the sensor to various conditions were simulated. Using microsystems technology, the sensor was miniaturized. In order to investigate the performance of the miniaturized sensor, various experimental tests were performed. The results of the experimental tests confirmed the capability of the sensor to measure force distribution data as well as the mechanical properties of artificial tissues. Moreover, test results showed that the sensor performed the measurements during both static and dynamic interactions between the sensor and the sample materials.

Chapter 10: Conclusions

10.1 Summary and Conclusions

In the present thesis, seven different configurations of sensors have been proposed for minimally invasive surgical tasks. In the first chapter, an introduction to tactile sensing for use in surgical applications was presented. In the second chapter, a sensing principle based on the bending of optical fibers has been used for designing and prototyping a tactile sensor for use in minimally invasive surgery (MIS) systems and minimally invasive robotic surgery (MIRS) systems. This sensor measures the distributed force information along the length of the sensor. However, it cannot measure the degree of hardness of the contact tissue. In the third chapter, a catheter-tip tactile sensor was designed and fabricated for use in catheter-base cardiovascular surgery. This sensor measures the force and the relative degree of hardness of the tissue interacting with the tip of the catheters. However, it is not suitable for integration into a robotic assisted surgical instrument such as graspers. The sensors proposed in the second and the third chapters were not miniaturized by using micro-systems technology. However, the sensors proposed in the next five chapters were miniaturized by taking the advantage of optical microsystems technology.

In the fourth chapter, the designing and prototyping of a very high-sensitive force sensor was discussed. This sensor was miniaturized by using microsystems technology and was based on the sensing principle of the optical fiber coupling loss. This sensor is the first generation of the microsensors proposed in the present thesis. Although this sensor measures the contact force, it cannot measure other tactile information such as force distribution or the mechanical properties of the contact object. In the fifth chapter, the second generation of the micro-sensor was proposed. The second generation measures not only force but also the distribution of the force along the length of the sensor. In the sixth chapter, the third generation of the micro-sensor was proposed. This sensor measures the contact force as well as the degree of hardness while interacting with the tissue. In the seventh chapter, the fourth generation of the micro-sensor was based on a hybrid sensing principle. In terms of the types of measurements, this sensor is similar to the third generation. However, it uses a combination of optical fiber and piezoresistive based sensing principles, which relatively simplify its structure compared to the third generation. As a trade-off for its less-complex design, it has a lower performance than the third generation. In the eighth chapter, the fifth generation of the micro-sensor, which is fully optical and most complete, was proposed. In fact, the fully optical sensor encompasses all the features of the previous generations of the micro-sensor. This fully optical microsystem based tactile sensor has been studied, fabricated, and tested under different conditions. In short, the key features of this micro-sensor are listed as follows:

a. The sensor measures contact force whether it is a concentrated force, distributed force, or any combination of them.
b. The sensor measures the mechanical properties of contact objects such as the relative degree of hardness.
c. The sensor measures the local discontinuities in the mechanical properties of the contact objects along the length of the contact area.

d. Unlike the electrical-based sensors, the sensor performs such measurements under both static and dynamic loading conditions. Due to such advantages of fully optical sensing principle in nature, surgeons can perform the measurement when maintaining a stable static contact between surgical tools and tissues while at the same time avoiding tissue damage resulting from an excessive force interacting between surgical tools and tissues.

e. The sensing principle of the sensor is insensitive to electro-magnetic fields; hence it is magnetic resonance compatible. Hence, this sensor can potentially perform in the presence of magnetic resonance imaging (MRI) devices, which are in widespread use in surgical rooms.

f. The sensor is also electrically-passive due to its fully optical configuration. As a result, it is compatible with cardiovascular operations because it does not disrupt the normal electrical activities of the heart.

g. The sensor can also be utilized in specific types of operations where surgeons must use ultrasound imaging techniques during surgical operations as it is ultrasound friendly due to rugged mechanical configuration.

h. Due to above inherent advantages, the sensor has vast applications in robotic, automation, material testing, and medical device industries.

i. The configuration of the design is such that the performance of the sensor such as its accuracy, resolution, and measurement range can be tuned for different requirements.

j. The performance of the prototype sensor such as its resolution and its noise-to-signal ratio are much better than the commercially available electrical-based force sensors that are neither MRI-compatible nor electrically-passive.

10.2 The Future Study

The objective of the present thesis was to develop tactile sensors for integration into the end-effectors of surgical platforms. In doing so, based on seven innovative concepts, different tactile sensors have been developed in the present work. However, there are still a number of considerations that can be implemented for the further improvement of the presented work. Ultimately, such improvements are discussed in the following categories:

a. In the current fabricated versions, two sets of optical fibers are introduced to the sensors from two opposite sides of the sensor. In future versions, optical fibers with gold-coated bare ends can be used to omit one of the two sets of fibers. As an alternative, micro-mirrors can be used in the micromachined silicon structure of the sensors to reflect the light 180 degrees into the output fibers. Using such designs, the optical fiber sets will be introduced to the sensor from only one side. As a result, the integration of the sensor into surgical graspers will be easier.

b. Instead of using an external large-size light source, a very small-size light source can be integrated into the structure of the sensor. Hence only one set of fibers will be connected to the sensor. Such a configuration will facilitate the integration of the sensor into the surgical instruments.

c. In the present work, the relative measurement of the hardness was investigated. In future work, the sensor can be calibrated to measure the absolute degree of hardness of soft objects. The application of such measurements will be in the area of material testing to characterize soft materials.

d. The experimental results performed on the sensors proved that the sensor measures the force and the resulting deformation with a high performance. Due to the high-sensitive performance of the sensor, the time-dependant mechanical properties of the tissues such as their visco-elastic material properties can also be characterized with the sensor.

e. In the future, *in-vivo* clinical tests should be performed on the sensors to assess the risk management of processes based on, e.g., the Food and Drug Administration (FDA) protocols.

f. Finally, for commercialization purpose, the platform of the sensor can be made of non-conductive polymeric materials such as SU-8 in order to ensure the absolute MRI-compatibility of the sensor material.

Bibliography

[1] D. B. Camarillo, T. M. Krummel, and J. K. Salisbury, “Robotic technology in surgery: past, present, and future,” *Am. J. Surg.*, vol. 188, no. 4A, pp. 2–15, 2004.

[2] M. Mack, “Minimally invasive and robotic surgery,” *J. Am. Med. Assoc.*, vol. 285, no. 5, pp. 568–572, 2001.

[3] A. K. Okamura, “Methods for haptic feedback in teleoperated robot-assisted surgery,” *Ind. Robot*, vol. 31, no. 6, pp. 499–508, 2004.

[4] Vanja Bozovic, *Medical Robotics*, I-Tech Education and Publishing, Vienna, Austria, January 2008, pp. 491–498.

[5] *http://www.intuitivesurgical.com*, Last visited on December 05, 2011.

[6] C.-H. King, M. O. Culjat, M. L. Franco, C. E. Lewis, E. P. Dutson, W. S. Grundfest, and J. W. Bisley, “Tactile feedback induces reduced grasping force in robot-assisted surgery,” *IEEE Trans. Haptic*, vol. 2, no. 2, pp. 103–110, 2009.

[7] G. C. Burdea, *Force and Touch Feedback for Virtual Reality*, John Wiley & Sons, Inc., 1996, pp. 3–4.

[8] S. Schostek, M. O. Schurr, and G. F. Buess, “Review on aspects of artificial tactile feedback in laparoscopic surgery,” *Med. Eng. Phys.*, vol. 31, pp. 887–898, 2009.

[9] A. L. Trejos, J. Jayender, M. T. Perri, M. D. Naish, R. V. Patel, and R. A. Malthaner, “Robot-assisted tactile sensing for minimally invasive tumor localization,” *Int. J. Robot. Res.,* vol. 28, no. 9, pp. 1118–1133, 2009.

[10] B. Kuebler, R. Gruber, Ch. Joppek, J. Port, G. Passig, J.H. Nagel, and G. Hirzinger “Tactile feedback for artery detection in minimally invasive robotic surgery-preliminary results of a new approach,” in *Proc. IFMBE*, vol. 25, no. 6, 2009, pp. 299–302.

[11] P. Puangmali, K. Althoefer, L. D. Seneviratne, D. Murphy, and P. Dasgupta, “State-of-the-art in force and tactile sensing for minimally invasive surgery,” *IEEE Sens. J.*, vol. 8, no. 4, pp. 371–381, April 2008.

[12] C. R. Wagner, N. Stylopoulos, and R. D. Howe, “The role of force feedback in surgery: analysis of blunt dissection,” in *Proc. 10th Symp. on Haptic Interfaces for Virtual Envir. and Teleoperator Systs.*, Orlando, FL, March 2002.

[13] C. R. Wagner, N. Stylopoulos, P. G. Jackson, and R. D. Howe, “The benefit of force feedback in surgery: examination of blunt dissection,” *Presence-Teleoper. Virtual Env.*, vol. 16, no. 3, pp. 252–262, 2007.

[14] C.-H. King, M. O. Culjat, M. L. Franco, J. W. Bisley, G. P. Carman, E. P. Dutson, and W. S. Grundfest, "A multielement tactile feedback system for robot-assisted minimally invasive surgery," *IEEE Trans. Haptic*, vol. 2, no. 1, pp. 52–56, January-March 2009.

[15] *http://www.hansenmedical.com*, Last visited on December 05, 2011.

[16] *http://www.titanmedicalinc.com*, Last visited on December 05, 2011.

[17] J. Stoll, and P. Dupont, "Force control for grasping soft tissue," in *Proc. 2006 IEEE International Conference on Robotics and Automation*, Orlando, FL, May 2006, pp. 4309–4311.

[18] S. Sokhanvar, M. Packirisamy, and J. Dargahi, "MEMS endoscopic tactile sensor: toward in-situ and in-vivo tissue softness characterization," *IEEE Sens. J.*, vol. 9, no. 12, pp. 1679–1687, 2009.

[19] J. Peirs, J. Clijnen, D. Reynaerts, H. V. Brussel, P. Herijgers, B. Corteville, and S. Boonea "A micro optical force sensor for force feedback during minimally invasive robotic surgery," *Sens. Actuator A-Phys.*, vol. 115, no. 2–3, pp. 447–455, 2004.

[20] K. Cleary, A. Melzer, V. Watson, G. Kronreif, and D. Stoianovici, "Interventional robotic systems: applications and technology state-of-the-art," *Minim. Invasive Ther. Allied Technol.*, vol. 15, pp. 101–113, 2006.

[21] K. Chinzei, and K. Miller, "MRI guided surgical robot," in *Proc. 2001 Australian Conference on Robotics and Automation*, Sydney, November 2001, pp. 50–55.

[22] K. Chinzei, R. Kikinis, and F. A. Jolesz, "MR compatibility of mechatronic devices: Design criteria," in *Proc. 2nd Int. Conf. Med. Image Computing and Computer-Assisted Intervention*, 1999, pp. 1020–1031.

[23] S. G. Yuen, M. C. Yip, N. V. Vasilyev, D. P. Perrin, P. J. del Nido, and R. D. Howe, "Robotic force stabilization for beating heart intracardiac surgery," in *Proc. 12th Int. Conf. Med. Image Computing and Computer-Assisted Intervention: Part I*, 2009, pp. 26–33.

[24] J. A. C. Heijmans, L. K. Cheng, and F. P. Wieringa, "Optical fiber sensors for medical applications-practical engineering considerations," in *Proc. 4th European Conference of the International Federation for Medical and Biological Engineering (IFMBE)*, vol. 22, 2008, pp. 2330–2334.

[25] K. J. Rebello, "Applications of MEMS in surgery," in *Proc. IEEE*, vol. 92, Jan. 2004, pp. 43–55.

[26] T. A. Kern, *Engineering Haptic Devices*, Springer, 1st Edition, 2009, pp. 321–347.

[27] P. Puangmali, K. Althoefer, and L. D. Seneviratne, “Mathematical modeling of intensity-modulated bent-tip optical fiber displacement sensors,” *IEEE Trans. Instrum. Meas.*, vol. 59, no. 2, pp. 283–291, February 2010.

[28] S. Sokhanvar, M. Packirisamy, and J. Dargahi, “A multifunctional PVDF-based tactile sensor for minimally invasive surgery,” *Smart Mater. Struct.*, vol. 16, pp. 989–998, 2007.

[29] G. Tholey, and J. P. Desai “A modular, automated laparoscopic grasper with three-dimensional force measurement capability,” in *Proc. 2007 IEEE International Conference on Robotics and Automation,* Italy, April 2007, pp. 250–255.

[30] A. Patriciu, D. Petrisor, M. Muntener, D. Mazilu, M. Schär, and D. Stoianovici, “Automatic brachytherapy seed placement under MRI guidance,” *IEEE Trans. Biomed. Eng.*, vol. 54, no. 8, pp. 1499–1506, August 2007.

[31] N. Takahashi, M. Tada, J. Ueda, Y. Matsumoto, and T. Ogasawara, “An optical 6-axis force sensor for brain function analysis using fMRI,” in *Proc. IEEE International Conference on Sensors*, Toronto, Canada, October 2003, pp. 253–258.

[32] P. Polygerinos, D. Zbyszewski, T. Schaeffter, R. Razavi, L. D. Seneviratne, and K. Althoefer, “MRI-compatible fiber-optic force sensors for catheterization procedures,” *IEEE Sens. J.*, vol. 10, no. 10, pp. 1598–1608, October 2010.

[33] K. Yokoyama, H. Nakagawa, D. C. Shah, H. Lambert, G. Leo, N. Aeby, A. Ikeda, J. V. Pitha, T. Sharma, R. Lazzara, and W. M. Jackman, “Novel contact force sensor incorporated in irrigated radiofrequency ablation catheter predicts lesion size and incidence of steam pop and thrombus,” *Circ.-Arrhythmia Electrophysiol.*, vol. 1, no. 5, pp. 354–362, 2008.

[34] P. Puangmali, P. Dasgupta, L. D. Seneviratne, and K. Althoefer, “Miniaturized triaxial optical fiber force sensor for MRI-guided minimally invasive surgery,” in *Proc. 2010 IEEE International Conference on Robotics and Automation*, Alaska, USA, May 2010, pp. 2592–2597.

[35] P. Polygerinos, P. Puangmali, T. Schaeffter, R. Razavi, L. D. Seneviratne, and K. Althoefer, “Novel miniature MRI-compatible fiber-optic force sensor for cardiac catheterization procedures,” in *Proc. 2010 IEEE International Conference on Robotics and Automation*, Alaska, USA, May 2010, pp. 2598–2603.

[36] *http://www.endosense.com*, Last visited on December 05, 2011.

[37] A. P. Sarvazyan, V. Egorov and J. S. Son, *Tactile breast imager and method for use*, U. S. Patent 2007/0038152 A1, Feb. 15, 2007.

[38] D. Q. Larkin, S. J. Blumenkranz and R. Kumar, *Modulator force sensor*, U. S. Patent 2007/0151391 A1, July 5, 2007.

[39] G. Obinata, K. Oka, H. Miura and N. Moriyama, *Control of object operating force, object gripping force and robot hands*, U. S. Patent 7707001 B2, April 27, 2010.

[40] T. Mizota, K. Kamiyama, H. Kajimoto, N. Kawakami and S. Tachi, *Optical tactile sensor and method of reconstructing force vector distribution using the sensor*, U. S. Patent 2007/0040107 A1, Feb. 22, 2007.

[41] M. R. Fernald, T. J. Bailey, M. B. Miller, J. M. Sullivan, J. R. Dunphy, M. A. Davis, C. J. Wright, A. D. Kersey, M. A. Putnam and R. N. Brucato, *Optical differential pressure sensor*, U. S. Patent 2004/0129083 A1, Jul. 8, 2004.

[42] J. A. Wise, *Robotic sensor*, U. S. Patent 4,651,074, Mar. 17, 1987.

[43] A. W. Thiele, J. S. Schoenwald and D. E. Gjellum, *Crossed fiber optic tactile sensor*, U. S. Patent 4,733,068, Mar. 22, 1988.

[44] P. G. Duncan, S. M. Christian and J. A. Schroeder, *Fiber optic sensor system and method for measuring the pressure of media*, U. S. Patent 6,838,660 B2, Jan. 5, 2005.

[45] N. Aeby and G. Leo, *Catheter having tri-axial force sensor*, U. S. Patent 2008/0009750 A1, Jan. 10, 2008.

[46] G. Leo, N. Aeby and D. Inaudi, *Medical apparatus system having optical fiber load sensing capability*, U. S. Patent 2006/0200049 A1, 2006.

[47] J. Kane, *Optical pressure sensor for measuring blood pressure*, U. S. Patent 4,691,708, 1987.

[48] C. H. King, M. Franco, M. O. Culjat, A. T. Higa, J. W. Bisley, E. Dutson and W. S. Grundfest, "Fabrication and characterization of a balloon actuator array for haptic feedback in robotic surgery," *J. Med. Devices,* vol. 2, no. 4, pp. 041006-1–041006-7, 2008.

[49] R. Ahmadi, M. Packirisamy, J. Dargahi and R. Cecere, "Discretely-Loaded Beam-Type Optical Fiber Tactile Sensor for Tissue Manipulation and Palpation in Minimally Invasive Robotic Surgery," *IEEE Sens. J.,* vol. 12, no. 1, pp. 22–32, 2012.

[50] R. Ahmadi, M. Packirisamy and J. Dargahi, "Optical fiber sensor array for Artery/Lump detection," in *Proc. IEEE 7th International Workshop on Fibre Optics and Optical Passive Components (WFOPC)*, Montreal, Canada, July 2011, pp. 13–15.

[51] R. Ahmadi, J. Dargahi, M. Packirisamy and R. Cecere, "A new hybrid catheter-tip tactile sensor with relative hardness measuring capability for use in catheter-based heart

surgery," in *Proc. IEEE International Conference on Sensors*, Hawaii, USA, November, 2010, pp. 1592–1595.

[52] R. Ahmadi, J. Dargahi, M. Packirisamy, and R. Cecere, "A new MRI-compatible optical fiber tactile sensor for use in minimally invasive robotic surgery systems," in *Proc. Fourth European Workshop on Optical Fiber Sensors*, vol. 7653, September 2010, pp. 2Z-1–2Z-4.

[53] R. Ahmadi, M. Packirisamy and J. Dargahi, "High sensitive force sensing based on the optical fiber coupling loss," *J. Med. Devices,* Under Review, Submitted on October 27, 2011, Paper No. MED-11-1096.

[54] R. Ahmadi, M. Packirisamy and J. Dargahi, "Optical array-based force distribution sensing suitable for lump/artery detection," *IEEE Trans. Biomed. Eng.*, Under Review, Submitted on January 09, 2012, Manuscript ID: TBME-00033-2012.

[55] R. Ahmadi, M. Packirisamy and J. Dargahi, "An Innovative optical microsystem for static and dynamic tissue diagnosis in minimally invasive surgical operations," *J. Biomed. Opt.,* Under Review, Submitted on Dec. 14, 2011, Manuscript #11755SS.

[56] R. Ahmadi, M. Packirisamy and J. Dargahi, "Modeling and parametric study of sensor-tissue interaction for minimally invasive surgical tasks," *Int. J. Med. Robot. Comput. Assist. Surg.,* to be Submitted.

[57] R. Ahmadi, M. Packirisamy and J. Dargahi, "Design and development of an optical-piezoresistive hybrid tactile sensor for use in minimally invasive surgery," *Biosens. Bioelectron.,* to be Submitted.

[58] R. Ahmadi, M. Packirisamy and J. Dargahi, "Multi-purpose optical microsystem: toward hardness measurement and lump/artery detection in minimally invasive surgical tasks," *Biomed. Microdevices,* to be Submitted.

[59] M. Kalantari, M. Ramezanifard, R. Ahmadi, J. Dargahi and J. Kövecses, "A piezoresistive tactile sensor for tissue characterization during catheter-based cardiac surgery," *Int. J. Med. Robot. Comput. Assist. Surg.,* vol. 7, pp. 431–440, 2011.

[60] A. Atieh, M. Kalantari, R. Ahmadi, J. Dargahi, M. Packirisamy and M. H. Zadeh, "FEM analysis of the interaction between a piezoresistive tactile sensor and biological tissues," *World Academy of Science, Engineering and Technology*, vol. 78, pp. 106–110, June 2011.

[61] A. Atieh, R. Ahmadi, M. Kalantari, J. Dargahi and M. Packirisamy, "A piezoresistive based tactile sensor for use in minimally invasive surgery," in *Proc. IEEE 37th Annual Northeast Bioengineering Conference (NEBEC),* Troy, NY, USA, April 2011, pp. 1–2, 2011.

[62] M. Kalantari, M. Ramezanifard, R. Ahmadi, J. Dargahi and J. Kovecses, "Design, fabrication, and testing of a piezoresistive hardness sensor in minimally invasive surgery," in *Proc. IEEE Haptics Symposium,* Waltham, Massachusetts, USA, March 2010, pp. 431–437.

[63] R. Ahmadi, J. Dargahi, M. Packirisamy and R. Cecere, "Catheter-tip tactile sensing for catheter-based techniques," *The Abstract Booklet of McGill Cardiovascular Research Day*, Montreal, Canada, February 2011, pp. 9–9.

[64] R. Ahmadi, M. Kalantari, M. Packirisamy and J. Dargahi, "Modeling and optimal design of an optical MEMS tactile sensor for use in robotically assisted surgery," in *Proc. SPIE Photonics North,* Niagara Falls, Canada, June 2010, pp. 775008.

[65] R. Ahmadi, P. Ashtaputre, J. A. Ziki, J. Dargahi and M. Packirisamy, "Relative hardness measurement of soft objects by a new fiber optic sensor," in *Proc. SPIE Photonics North,* Niagara Falls, Canada, June 2010*,* pp. 77500D.

[66] R. Ahmadi, M. Kalantari, J. Dargahi and M. Packirisamy, ""Catheter-tissue interaction to design an optical MEMS force sensor for use in minimally invasive heart surgery"," *International Conference on Medical Informatics and Biomedical Engineering,* Paris, France, June 2009.

[67] R. Ahmadi, S. Sokhanvar, M. Packirisamy and J. Dargahi, "Wide range force feedback for catheter insertion mechanism for use in minimally invasive mitral valve repair surgery," in *Proc. SPIE Photonics West on Optical Fibers and Sensors for Medical Diagnostics and Treatment Applications IX,* San Jose, CA, USA, January 2009*,* pp. 71730W.

[68] R. Ahmadi, J. Dargahi and M. Packirisamy, "MOEMS sensor for use in computer controlled catheter heart surgery," *AI/GI/CRV/IS Conference,* Poster Presentation, Windsor, Canada, May 2008.

[69] R. Ahmadi, J. Dargahi and M. Packirisamy, "Effects of squeeze-film damping in dynamic vibration response in micro-cantilever structures," *Canadian Society for Mechanical Engineers Forum,* Ottawa, Canada, June 2008.

[70] M. Packirisamy, R. Ahmadi and J. Dargahi, *System for sensing a mechanical property of a sample*, International PCT Patent filed on Oct. 26, 2011, Application Number: PCT/CA2011/001192 and Provisional U.S. Patent filed on Oct. 26, 2010, Serial Number: 61/344,859.

[71] M. C. Yip, S. G. Yuen, and R. D. Howe, "A robust uniaxial force sensor for minimally invasive surgery*,"* *IEEE Trans. Biomed. Eng.*, vol. 57, no. 5, pp. 1008–1011, 2010.

[72] F. P. Beer, and E. R. Johnston, *Mechanics of Materials*, McGraw-Hill, 1981, pp. 396–429.

[73] R. C. Gauthier, and C. Ross, "Theoretical and experimental considerations for a single-mode fiber-optic bend-type sensor," *Appl. Optics*, vol. 36, no. 25, pp. 6264–6273, 1997.

[74] Y. C. Fung, *Biomechanics: Mechanical Properties of Living Tissues*, 2nd ed. New York, USA: Springer-Verlag Inc., 1993.

[75] R. W. Ogden, *Non-Linear Elastic Deformations*, Ellis-Horwood Limited, Chichester, 1984, pp. 213–222.

[76] *COMSOL Multiphysics Software User's Guide for Structural Mechanics Module*, pp. 119–121.

[77] E. P. W. der Putten, J. J. den Dobbelsteen, R. H. M. Goossens, J. J. Jakimowicz and J. Dankelman, "Effect of laparoscopic grasper force transmission ratio on grasp control," *Surg. Endosc.*, vol. 23, no. 4, pp. 818–824, 2008.

[78] A. M. Gillinov and J. R. Liddicoat, "Percutaneous mitral valve repair," *J. of Thoracic and Cardiovascular Surgery*, vol. 18, no. 2, pp. 115–121, 2006.

[79] P. Polygerinos, T. Schaeffter, L. Seneviratne, and K. Althoefer, "A fibre-optic catheter-tip force sensor with MRI compatibility: a feasibility study," in *Proc. IEEE 31st Annual International Conference on Engineering in Medicine and Biology Society (EMBS)*, Minneapolis, Minnesota, USA, September 2009, pp. 1501–1054.

[80] P. Puangmali, H. Liu, K. Althoefer, and L. D. Seneviratne, "Optical fiber sensor for soft tissue investigation during minimally invasive surgery," in *Proc. IEEE International Conference on Robotics and Automation (ICRA),* Pasadena, CA, USA, May, 2008, pp. 2934–2939.

[81] D. Zbyszewski, P. Polygerinos, L. D. Seneviratne, and K. Althoefer "A novel MRI compatible air-cushion tactile sensor for minimally invasive surgery," *IEEE/RSJ International Conference on Intelligent Robots and Systems (IROS)*, St. Louis, MO, USA, October, 2009, pp. 2647–2652.

[82] B. Nilsson, D. Tilert, A. Temun, T. Carlsson, and L. Mattsson, "Fast, low-cost fiber-optic displacement sensor," in *Proc. SPIE 17th International Conference on Optical Fibre Sensors*, vol. 5855, Part II pp. 783–786, 2005.

[83] S. Misra, K. T. Ramesh and A. M. Okamura, "Modeling of tool-tissue interactions for computer-based surgical simulation: a literature review," *Presence-Teleoper. Virtual Env.,* vol. 17, no.5, pp. 463–491, 2008.

[84] G. T. Mase and G. E. Mase, *Continuum Mechanics for Engineers.* CRC Press, 1999.

[85] A. D. Freed, "Natural strain," *J Eng. Mater.-T ASME,* vol. 117, no. 4, pp. 379–385, 1995.

[86] M. Mooney, "A theory of large elastic deformation," *J. Appl. Phys.,* vol. 11, no. 9, pp. 582–592, 1940.

[87] T. Belytschko, W. K. Liu and B. Moran, *Nonlinear Finite Elements for Continua and Structures.* Wiley, 2000.

[88] W. Prager, *Introduction to Mechanics of Continua.* Dover Pubns, 2004.

[89] *Element Reference*, Ansys software, Release 12.0, pp. 37–42, April 2009.

[90] A. N. Gent, *Engineering with Rubber: How to Design Rubber Components.* Hanser Gardner Pubns, 2001.

[91] W. Yu, Y. Li, Y. P. Zheng, N. Y. Lim, M. H. Lu and J. Fan, "Softness measurements for open-cell foam materials and human soft tissue," *Meas. Sci. Technol.,* vol. 17, no. 7, pp. 1785, 2006.

[92] A. Sezen, R. Rajamani, D. Morrow, K. Kaufman and B. Gilbert, "An ultraminiature MEMS pressure sensor with high sensitivity for measurement of intramuscular pressure (IMP) in patients with neuromuscular diseases," *J. Med. Devices,* vol. 3, no. 3, pp. 031006-1–031006-9, 2009.

[93] S. Sokhanvar, M. Ramezanifard, J. Dargahi and M. Packirisamy, "Graphical rendering of localized lumps for MIS applications," *J. Med. Devices,* vol. 1, no. 3, pp. 217–226, 2007.

[94] M. Kalantari, M. Ramezanifard, J. Dargahi and J. Kövecses, "3D graphical rendering of localized lumps and arteries for robotic assisted MIS," *J. Med. Devices,* vol. 5, no. 2, pp. 021002-1–021002-10, 2011.

[95] K. Cleary, A. Melzer, V. Watson, G. Kronreif and D. Stoianovici, "Interventional robotic systems: applications and technology state-of-the-art," *Minim. Invasive Ther. Allied Technol.,* vol. 15, no. 2, pp. 101–113, 2006.

[96] E. P. Scilingo, M. Bianchi, G. Grioli and A. Bicchi, "Rendering softness: integration of kinesthetic and cutaneous information in a haptic device," *IEEE Trans. Haptic,* vol. 3, no. 2, pp. 109–118, 2010.

[97] P. Valdastri, K. Houston, A. Menciassi, P. Dario, A. Sieber, M. Yanagihara and M. Fujie, "Miniaturized cutting tool with triaxial force sensing capabilities for minimally invasive surgery," *J. Med. Devices,* vol. 1, no. 3, pp. 206–211, 2007.

[98] S. Nemoto and T. Makimoto, "Analysis of splice loss in single-mode fibres using a Gaussian field approximation," *Opt. Quant. Electron.,* vol. 11, no. 5, pp. 447–457, 1979.

[99] J. Li, Q. Zhang and A. Liu, "Advanced fiber optical switches using deep RIE (DRIE) fabrication," *Sens. Actuator A-Phys.,* vol. 102, no. 3, pp. 286–295, 2003.

[100] P. Gomes, "Surgical robotics: Reviewing the past, analysing the present, imagining the future," *Robot. Comput. Integrated Manuf.,* vol. 27, no. 2, pp. 261–266, 2011.

[101] H. Yousef, M. Boukallel and K. Althoefer, "Tactile sensing for dexterous in-hand manipulation in robotics-A review," *Sens. Actuator A-Phys.,* vol. 167, no. 2, pp. 171–187, 2011.

[102] T. A. Kern, *Engineering Haptic Devices*, Springer, 1st Edition, 2009, pp. 321–347.

[103] K. Taniguchi, E. Kobayashi, S. Joung, M. Ono, N. Motomura, S. Kyo, S. Takamoto and I. Sakuma, "A force measurement device using optical fiber for surgical tools-basic concept and implementation," *J. of Robotics & Mechatronics,* vol. 23, no. 1, pp. 94–104, 2011.

[104] H. Su, M. Zervas, C. Furlong and G. S. Fischer, "A miniature MRI-compatible fiber-optic force sensor utilizing fabry-perot interferometer," *SEM Annual Conference & Exposition on Experimental and Applied Mechanics*, Uncasville, CT, USA, June 2011.

[105] H. Su, M. Zervas, G. Cole, C. Furlong and G. Fischer, "Real-time MRI-guided needle placement robot with integrated fiber optic force sensing," in *Proc. IEEE International Conference on Robotics and Automation (ICRA),* Shanghai, China, May 2011, pp. 1583–1588.

[106] N. Zemiti, G. Morel, T. Ortmaier and N. Bonnet, "Mechatronic design of a new robot for force control in minimally invasive surgery," *IEEE-ASME Trans. Mechatron.,* vol. 12, no. 2, pp. 143–153, 2007.

[107] M. Kalantari, J. Dargahi, J. Kövecses, M. Ghanbari and S. Nouri, "A New Approach for Modeling Piezoresistive Force Sensors Based on Semiconductive Polymer Composites," *IEEE-ASME Trans. Mechatron.,* pending for publication, DOI: 10.1109/TMECH.2011.2108664, available online on March 2011.